



University of Strathclyde

Department of Pure and Applied Chemistry

**Creating Novel Biofunctionalized Nanorod-Dye
Conjugates as Bright Tags for Surface-Enhanced
Resonance Raman Scattering**

by

Alison McLintock

A thesis presented in fulfilment of the requirements for the degree of Doctor of Philosophy

2013

This thesis is the result of the author's original research. It has been composed by the author and has not been previously submitted for examination which has led to the award of a degree. The copyright of this thesis belongs to the author under the terms of the United Kingdom Copyright Acts as qualified by University of Strathclyde Regulations 3.50. Due acknowledgements must always be made of the use of any material in, or derived from, this thesis.

Acknowledgements

I would like to begin by thanking Dr Alastair Wark for the opportunity to work on such an interesting project, and for his continued help and support over the course of my PhD. Without his expertise and encouragement (and fast turnaround of thesis corrections!) this work wouldn't have been possible. I could not have wished for a better supervisor to guide me through the last three and a half years.

I would also like to express my gratitude to Prof. W. Ewen Smith for his invaluable help, and numerous discussions based on this work.

Thank you to the rest of the group in the centre for Molecular Nanometrology for their help and friendship over the years, in particular, Kirsten, Rachel and Hayleigh.

The cellular imaging work described in Chapter 5 would not have been possible without Carlota Cunha Matos, who prepared the cells, and was responsible for the confocal fluorescence measurements. I would also like to acknowledge Danielle Spence, who assisted in exploring a new version of the USTs described at the end of Chapter 5 as part of her final year research project.

I would like to thank to my family, in particular, my Mum and William, and also my Dad, for both the emotional and financial assistance over the course of my education, it wouldn't have been possible without you. I would also like to say a massive thank you to my friends, in particular, Louise, for keeping me motivated, particularly over the last few months.

My greatest thanks go to Craig, for his support over the last few years, and of course, for all of the cups of coffee that went into writing this thesis, but most importantly for always being there.

Abstract

Gold nanorods have attracted much attention in the literature due to the ability to tune the aspect ratio and hence localized surface plasmon resonance (LSPR) of these materials. When co-assembled with molecular dyes this provides new opportunities yet to be explored for the design of multimodal optical probes compatible with a range of spectroscopies, in particular surface-enhanced resonance Raman scattering (SERRS).

This research describes the preparation and characterization of novel SERRS tags, capable of providing very bright Raman signals whilst remaining non-aggregated and thus hotspot-free. Additional advantages of this approach are the excellent control afforded over the dye surface coverage and surface orientation along with the very high level of stability displayed by these nanotags. An approach enabling a systematic study was developed where both the LSPR of the nanorod and the molecular resonance of the dye adsorbed onto the rod surface were varied with respect to the laser excitation wavelengths. Resonance coupling between dyes and nanorods was found to be a significant factor in the overall SERRS enhancement. Also when directly compared to quasi-spherical gold nanoparticles, significantly higher Raman intensities were obtained. The controlled side-by-side assembly of the nanorod-dye conjugates and subsequent stabilization of the suspended clusters for upwards of eight months was also demonstrated.

A new class of tags, known as *universal SERRS tags* (USTs) were proposed. By co-assembling multiple dyes on the same nanorod, bright Raman signals were obtained at wavelengths ranging from 514 – 1064 nm, without requiring nanoparticle aggregation. In addition, correlated SEM and Raman mapping analysis showed it was possible to perform single particle SERRS, with close to 100% of the nanotags found to be SERRS active. The application of the USTs for cellular imaging was clearly demonstrated and the non-cytotoxicity of this system to dendritic cells was confirmed.

Finally, a new methodology was introduced for the covalent functionalization of both polymer wrapped rod and spherical shaped nanoparticles.

Abbreviations

a.u	absorbance units
AgNO ₃	silver nitrate
CE	chemical Enhancement
CTAB	hexadecyltrimethylammonium bromide
DC	dendritic cell
DCI	1,1'-diethyl-2,2'-cyanine iodide
DDA	discrete dipole approximation
DDCI	1,1'-diethyl-4,4'-dicarbocyanine iodide
DMTMM	4-(4,6-dimethoxy-1,3,5-triazin-2-yl)-4-methylmorpholinium chloride
DNA	deoxyribonucleic acid
DTCI	3,3'-diethylthiacarbocyanine iodide
DTDCI	3,3'-diethylthiadibocarbocyanine iodide
DTTCI	3,3'-diethylthiatricarbocyanine iodide
EDC	<i>N</i> -(3-dimethylaminopropyl)- <i>N'</i> -ethylcarbodiimide hydrochloride
EM	electromagnetic
FACS	fluorescence activated cell sorting
HAuCl ₄	chloroauric acid
IR	infrared
LSPR	longitudinal surface plasmon resonance
MGITC	malachite green isothiocyanate
NaBH ₄	sodium borohydride
NaCl	sodium chloride
NaOH	sodium hydroxide
NHSS	N-hydroxysulfosuccinimide

NIR	near-infrared
NIR-797	near-infrared-797
NIR-1064	near-infrared-1064
nm	nanometer
NR	nanorod
PAA	poly(acrylic acid, sodium salt)
PAH	poly(allylamine hydrochloride)
PBS	phosphate buffered saline
PDDAC	poly(diallyldimethylammonium chloride)
PEG	polyethylene glycol
pMBA	para-mercaptobenzoic acid
PSS	poly-(sodium 4-styrenesulfonate)
Rpm	revolutions per minute
SEM	scanning electron microscopy
SERS	surface enhanced Raman spectroscopy
SE(R)RS	surface enhanced resonance Raman spectroscopy
SPR	surface plasmon resonance
TEM	transmission electron microscopy
T_m	melting temperature
Tris	tris(hydroxymethyl)aminomethane
UST	universal SERRS tag
UV-vis	ultraviolet-visible

Contents

Chapter 1 Introduction	1
1.1 Gold Nanoparticles	1
1.2 Surface Plasmon Resonance (SPR).....	1
1.3 Fabrication of Gold Nanorods.....	8
1.4 Surface Plasmon Enhanced Spectroscopies.....	10
1.4.1 Rayleigh Scattering.....	11
1.4.2 Surface Enhanced Fluorescence	12
1.4.3 Raman Scattering	13
1.4.4 Surface Enhanced Raman Scattering (SERS)	14
1.4.5 Surface Enhanced Resonance Raman Spectroscopy (SERRS)	18
1.5 Nanoparticle-Enhanced Optical Sensing and Imaging	21
1.5.1 Extinction Spectroscopy for Biosensing	21
1.5.2 SERS Spectroscopy for Biosensing	23
1.5.3 Enhanced Molecular Imaging Applications.....	25
1.6 Multimodal Spectroscopic Techniques.....	27
1.7 Research Aims.....	30
Chapter 2 Experimental	32
2.1 Nanorod Synthesis	32
2.2 Preparation of Nanorod-Dye Conjugates.....	33
2.3 Preparation of Citrate Capped Spherical Gold Nanoparticles.	34
2.4 Preparation of Citrate Capped Spherical Gold-DTTCl	34
2.5 Aggregation of Citrate Capped Spherical Gold-DTTCl.....	34
2.6 Controlled Aggregation of Nanorods.....	34
2.7 Preparation of Nanorod Clusters for SERRS Analysis.....	35
2.8 Preparation of Universal SERRS Tags (USTs).....	36
2.9 Cell Preparation	36
2.9.1 Cytometry Studies.....	37
2.10 Preparation of Alternative UST Combination	37

2.11 Multilayer Polymer wrapping of PSS NRs.	38
2.12 DNA Sequences Used Throughout Chapter 6	39
2.13 DMTMM Synthesis.....	40
2.14 Conjugation of DNA to PAA wrapped NRs.....	40
2.15 Preparation of Poly(allylamine hydrochloride) (PAH) Stabilized Quasi-Spherical Gold Nanoparticles.....	40
2.16 Polymer Wrapping of PAH Au nanoparticles.....	40
2.17 Conjugation of DNA to PAA Functionalized PAH Au.....	41
2.18 Bioactivity of DNA Only in Solution.....	41
2.19 Raman Analysis	41
2.20 Raman Mapping of Individual USTs	43
2.21 Raman Mapping of USTs in Cells.....	44
2.22 Confocal Fluorescence Mapping.....	44
2.23 Fluorescence Measurements.....	44
2.24 Scanning Electron Microscopy (SEM)	45
2.25 Zeta Potential.....	45
2.26 Extinction Measurements.....	46
Chapter 3 Preparation and Characterization of Monodisperse Stable Nanorod-Dye Conjugates with Controlled Resonance Coupling.....	47
3.1 Scaled up nanorod preparation	49
3.2 Design and Preparation of Nanorod-dye Probes	50
3.3. Sequestration of Dyes into CTAB Bilayer	53
3.4. SEM Analysis of Conjugates	56
3.5 Observation of Resonance Coupling.....	57
3.6 SERRS Characterization of Nanorod-Dye Conjugate Formation.....	60
3.7 SERRS Control Measurements	63
3.8. SERRS Study of Different Nanorod-Dye Combinations.....	66
3.8.1 Changing laser wavelength	67
3.8.2 Changing the dye resonance.....	67
3.8.3 Quantification of SERRS Intensities.....	68
3.9 Comparison of Nanorod versus Spherical shapes.....	72
3.10 Conclusions	76
3.11 Future Work.....	77

Chapter 4 Preparation and Characterization of Stabilized Nanorod-Dye Clusters.....	79
4.1 Cluster Assembly.....	80
4.2 Controlled Aggregation of NRs	81
4.2.1 Altering the Bulk Concentration of Sodium Citrate Added.....	82
4.2.2. Time-dependent aggregation	83
4.2.3 Dependence of Aggregation on Bulk CTAB Concentration.....	84
4.2.4 Dependence of the Aggregation Process on Presence of DTTCl	86
4.3 Polyelectrolyte Wrapping of Clusters	87
4.4 Preparation and Characterization of SERRS Active Clusters	89
4.4.1 Extinction Analysis	89
4.4.2 SEM Analysis	90
4.4.3 SERRS Analysis 785 nm Excitation.....	92
4.4.4 SERRS Analysis 633 nm	94
4.5 Conclusions	96
4.6 Future Work	96
Chapter 5 Creating a Universal Nanoparticle SERRS Tag for Imaging at Multiple Excitation Wavelengths Ranging From the Visible to the Near-IR.....	97
5.1 Selection of Dyes for Universal SERRS Tags	99
5.2. Characterization of Individual Nanorod-Dye Conjugates	100
5.2.1 Extinction Spectra of Individual-Dye NR Conjugates	101
5.2.2 Raman characterization of Individual Nanorod-Dye Conjugates at a Range of Common Excitation Wavelengths.....	103
5.3 Preparation of Universal SERRS Tags	110
5.4 Addition of Dyes When Preparing Universal SERRS Tags	111
5.4.1 All Three Dyes Added Simultaneously	111
5.4.2 Dyes Added Sequentially with Time Delay	113
5.5 Raman Mapping of Single Universal SERRS Tags at a Range of Wavelengths.	116
5.6 Universal SERRS Tags used to Map Cells at a Range of Wavelengths.....	124
5.6.1 Cytotoxicity Study of USTs	125
5.6.2 Cellular Analysis	126
5.6.3 Control Measurements	130
5.7 Alternative Dye Combination for Universal SERRS Tags to Provide Even Brighter Signal at 785 nm Excitation	133

5.8 Conclusions	138
5.9 Future Work	139
Chapter 6 Functionalization of Polymer-Wrapped Nanoparticles	140
6.1 Planned Route for DNA Functionalization of Polymer Wrapped Nanorods	141
6.2 Polymer Wrapping of Nanorods	142
6.3 Selection of DNA for Conjugation	145
6.4 Reagent for Coupling Chemistry	146
6.5 Covalent Conjugation of DNA to Spherical Nanoparticles	148
6.6 Proof of DNA Surface Attachment and Assay Design	154
6.7 Conclusions	158
6.8 Future Work	159
Chapter 7 Conclusions	160
References	162

Chapter 1

Introduction

1.1 Gold Nanoparticles

The application of metallic nanoparticles in particular, gold, has rapidly expanded over the last decade. There are a number of reasons for this increased interest. A vast array of synthetic methods have been reported, allowing excellent control over the size and shape of the nanoparticles synthesised. Gold nanoparticles have been incorporated into a wide variety of imaging and sensing based applications.¹⁻³ Many of these applications are associated with the unique optical properties of gold (and silver) nanoparticles, which are discussed in more detail in the following sections.

A wide range of well-established surface chemistries have been described in the literature, thereby enabling nanoparticle functionalization. Furthermore, depending on the surface chemistry, gold nanoparticles are biologically inert and therefore suitable for use *in vivo* and *in vitro*. Early work focussed on the use of quasi spherical particles, but many other shapes including nanorods and stars are now possible, with a number of methods reported to synthesise these particles, with excellent control over nanoparticle shape and monodispersity now achievable.^{1, 4, 5}

1.2 Surface Plasmon Resonance (SPR)

The intrinsic optical properties of metallic nanoparticles, such as the intense colour displayed by these materials, are attributed to the unique interaction these particles undergo with incident light. It is this interaction which leads to the phenomenon known as surface plasmon resonance (SPR).⁶ A surface plasmon is the collective oscillation of free conductive band electrons that occurs when a large number of these electrons are disturbed from their equilibrium position. Two types of SPR exist, propagating (PSPR) and localized SPR (LSPR). Propagating SPR occurs on planar surfaces of thin metallic films (<~ 80 nm). Surface plasmon polaritons have been excited in gold films with propagation lengths

of approximately 24 μm when excited by light with a wavelength of 850 nm.⁷ LSPR is observed in metallic nanoparticles and surfaces with nanostructured features, less than approximately 100 nm. A variety of metals have been shown to exhibit SPR, including gold, silver, copper, magnesium, aluminium and alkali metals.⁸ Both PSPR and LSPR are sensitive to changes to the dielectric environment surrounding the metallic structure.

Herein, only LSPR will be considered as the work discussed concerns gold nanoparticles. When electromagnetic radiation interacts with metallic nanoparticles that are smaller than the wavelength of the incident light, the result is the displacement of the free nanoparticle surface electrons and polarization of the surface. This leads to a collective oscillation of these electrons, which is characterized by the resonance band in the extinction spectrum of the nanoparticle. Electron oscillations in turn create a highly localized electric field which is greatest at the interface between the particle and the surrounding dielectric medium. This plasmonic field has been shown to enhance a wide number of electrical and vibrational optical properties including fluorescence, Rayleigh and Raman scattering.⁹ The interaction of light with a spherical metallic nanoparticle is depicted in Figure 1.1.

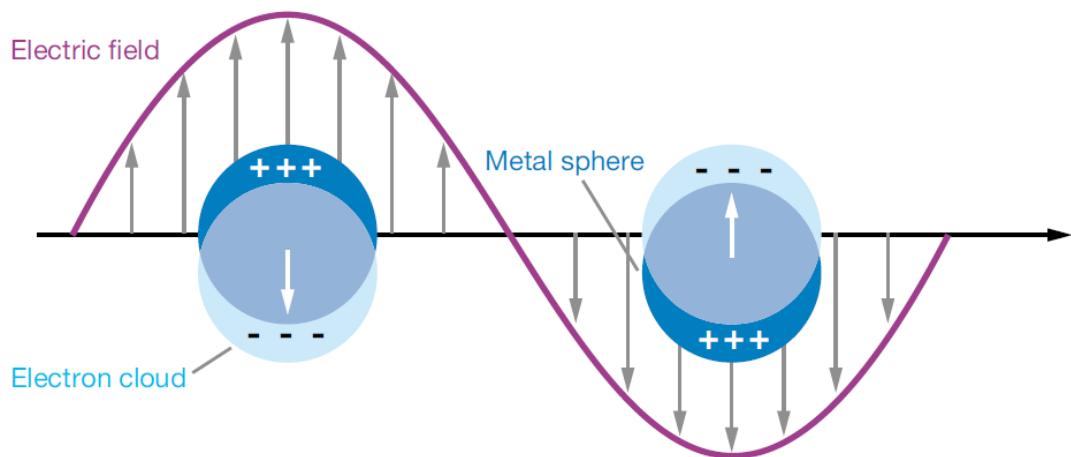


Figure 1.1. Electron displacement under the influence of an electromagnetic field.⁹

The energy of light required to excite LSPR depends on a number of factors, including the particle size and shape, as well as the dielectric constant of the surrounding

media. The interaction of light with solid metal nanoparticles can be described using Mie theory which predicts the scattering and absorbance properties of metal nanoparticles.¹⁰

$$C_{ext} = \left[\frac{24\pi^2 R^3 \epsilon_m^{2/3}}{\lambda} \right] \left[\frac{\epsilon_2}{(\epsilon_1 + 2\epsilon_m)^2 + \epsilon_2^2} \right] = C_{abs} + C_{sca} \quad \text{(Equation 1.1)}$$

where C_{ext} is the extinction cross coefficient, R is the radius of the nanospheres, λ is the wavelength of incident light, ϵ_m is the dielectric constant of the surrounding medium and $\epsilon_1 + i\epsilon_2$ is the complex dielectric function of the material. The extinction coefficient is itself made up of two components, C_{sca} which is the scattering coefficient, and C_{abs} , the absorption coefficient.

Typical extinction coefficients for Au and Ag spherical nanoparticles with a diameter of 30 nm are 5.88×10^9 and $1.85 \times 10^{10} \text{ M}^{-1}\text{cm}^{-1}$ respectively at the LSPR maxima.¹¹ The values obtained here are several orders of magnitude larger than for fluorescent dyes, for example, rhodamine 6G has an extinction coefficient of just 9.3×10^3 .¹² It is possible to use the value for the extinction coefficient to calculate the nanoparticle concentration, using the Beer-Lambert equation Extinction = $C_{eff} l c$, where C_{eff} is the extinction coefficient, l is the path length and c is the analyte concentration.

Equation 1.1 shows that the extinction coefficient varies, depending on the wavelength of incident light and the properties of the substrate material. The higher the value for C_{ext} , the more likely it is that individual nanoparticles can be optically detected. As can be seen in Equation 1, for C_{ext} to be large, the denominator $((\epsilon_1 + 2\epsilon_m)^2 + \epsilon_2^2)$ approaches zero. This occurs if $\epsilon_1 = -2\epsilon_m$ (if ϵ_2 is small). For metals such as gold and silver, ϵ_1 and ϵ_2 are strongly wavelength dependent, with ϵ_2 increasing quickly at longer wavelengths. For spherical gold nanoparticles with a size approximately 10 nm, approximate values for ϵ_1 and ϵ_2 at 633 nm are 0.18 and 3.4 respectively, while at 785 nm, these are 0.15 and -4.8 respectively.¹³

The scattering coefficient is also dependent upon the dielectric constant of the surrounding medium, increasing the value of ϵ_m leads to a decrease in C_{ext} and a red shift in the LSPR.¹⁴

C_{ext} is also strongly influenced by the nanoparticle size. Equation 1.1 contains the component R^3 , where R is the radius of the nanoparticle, meaning that small changes to the size lead to a large change in extinction coefficient. Furthermore, the width distribution of the SPR is dependent upon the size, with an inherent broadening occurring as the particle size increases. The size of the width distribution also provides a good indication of the dispersity of the nanoparticles, with polydisperse samples having broad distributions. For larger particles, C_{sca} dominates, i.e. the particles scatter light more strongly. As the particle size is decreased, the absorption, C_{abs} begins to dominate.¹⁴

Mie theory generally applies to particles that are quasi-spherical, and with a size less than approximately 100 nm. Furthermore, for spherical nanoparticles, plasmon excitation is limited over a fairly narrow excitation range. In order to model these effects in larger nanoparticle sizes and non-spherical shapes, a variety of methods have been described in the literature, including an extension of Mie theory, known as Gans theory,¹⁵ and discrete dipole approximation (DDA)¹⁶ and T-matrix formulation.¹⁷

Dependence on Nanoparticle Size and Shape

Figure 1.2 highlights the areas of the electromagnetic spectrum in which various gold and silver nanoparticles are able to support the excitation of surface plasmons.

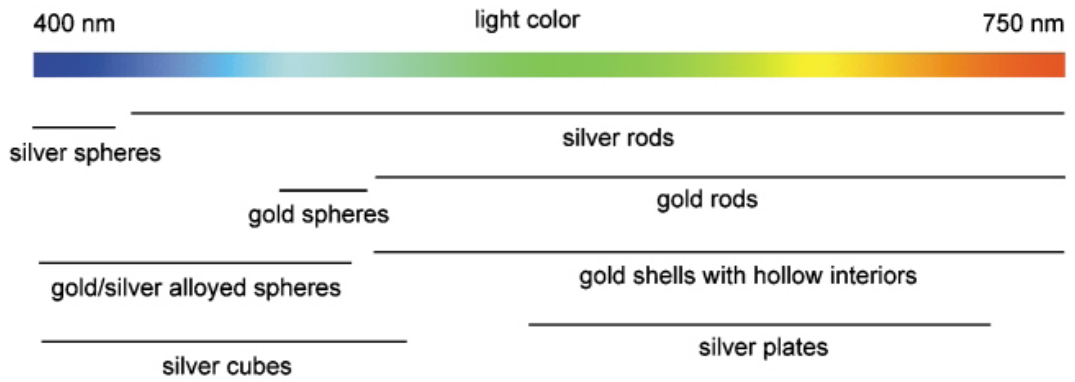


Figure 1.2. Summary comparing regions of the electromagnetic spectrum where various individual or monodisperse gold and silver nanostructures support the excitation of surface plasmons.¹⁸

It can clearly be seen that the both the metal and the shape of the nanoparticle have a dramatic impact on the LSPR position. Typical extinction spectra for gold and silver spheres with different diameters, as well as gold nanorods are depicted in Figure 1.3.

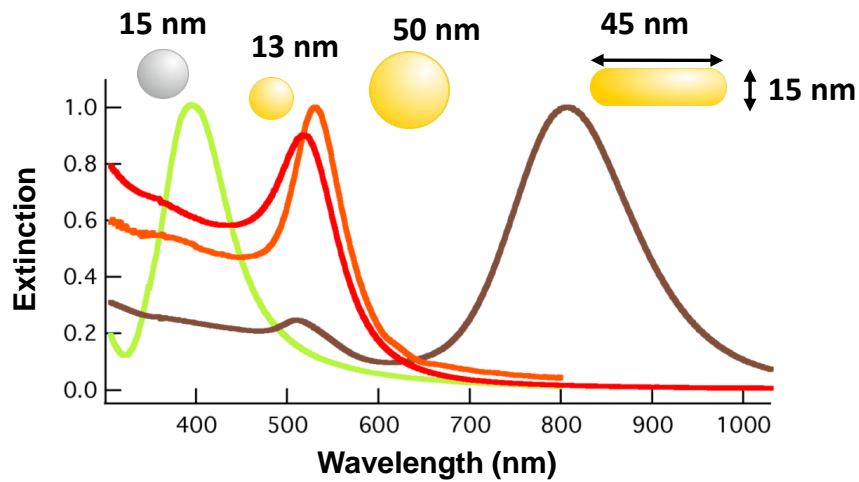


Figure 1.3. Typical extinction spectra obtained for gold and silver quasi-spherical nanoparticles and gold nanorods

Individual spherical nanoparticles only cover a small range of the visible spectrum, in the case of silver, from roughly 380 to 460 nm, and with spherical gold, from approximately 520 to 580 nm. Aggregation of the nanoparticles leads to a large change in

C_{ext} , as bringing metal surfaces into contact with one another results in a significant change in the value of ϵ_m from water to a metal. Alloying the nanoparticles with other noble metals does somewhat increase the range of wavelengths covered, whilst shapes such as cubes and plates allow further spectral coverage. In particular, gold nanorods cover a wide range, typically from approximately 510 nm to the near IR. The longest colloidal preparation method currently available in the literature produces nanorods with plasmon peaks as high as around 1500 nm, and an aspect ratio of approximately 25.^{19, 20}

Optical Properties of Gold Nanorods (NRs)

A typical NR extinction profile, with key features marked, is shown in Figure 1.4.

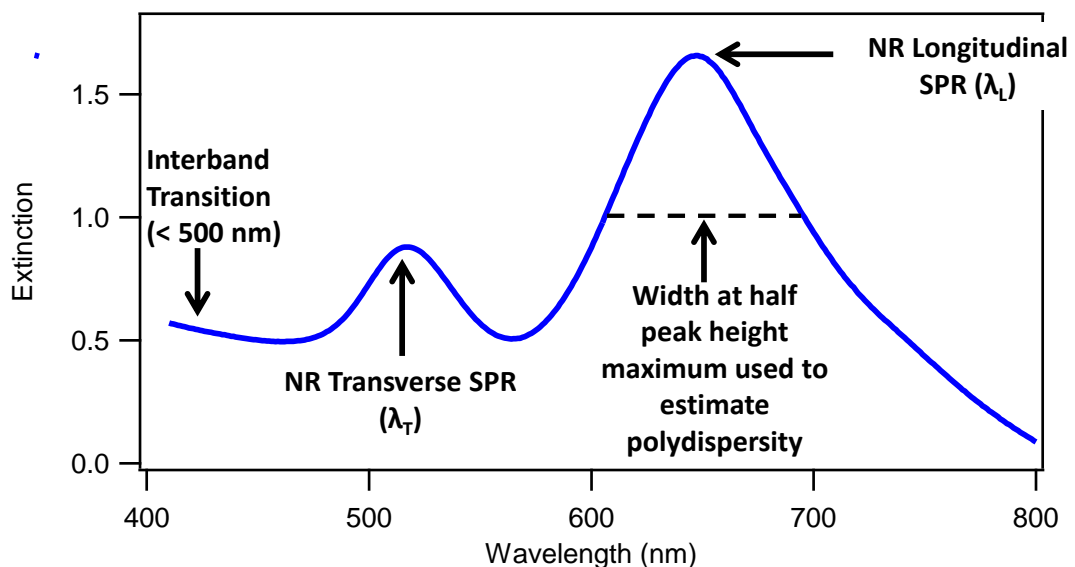


Figure 1.4. Typical extinction profile obtained for NR solution with $\lambda_L = 648$ nm. Key features of the spectra are highlighted.

Gold nanorods have two distinct extinction bands, which represent the two possible plasmon resonances of this material, one due to electronic oscillations along the shorter width axis, leading to the smaller transverse band (peak at λ_T), and oscillations along the length axis, leading to the larger longitudinal band (peak at λ_L). The transverse band is roughly fixed in the region 510-520 nm, whilst the longitudinal band is tuneable

dependent upon the aspect ratio of the nanorods synthesized, allowing gold nanorods to absorb in the visible to the near infra-red region of the electromagnetic spectrum.¹⁸

The full width of the longitudinal peak at half of the maximum peak height is often used as an indicator of particle size dispersity, with narrow peaks indicating a more monodisperse product than broader peaks.

The final key feature highlighted above is the interband transition, which is where a photon had excited an electron from an occupied state in the valence band to an unoccupied state in the conduction band. For gold, this occurs below approximately 500 nm, in this region light is absorbed rather than scattered, and consequently SPR based applications involving gold typically focus on wavelengths above 510 nm.

When describing nanorods, the aspect ratio is commonly used. This is defined as:

$$\text{Aspect ratio} = \text{length}/\text{width} \qquad \text{Equation 1.2}$$

Therefore, longer thinner rods have a larger aspect ratio than shorter thicker rods. In general, increasing the length leads to a red shift of the LSPR, while increases in width result in a blue shift.

The ability to tune the LSPR of nanorods is advantageous, as it allows the preparation of nanorods with a surface plasmon resonance at the desired wavelength. It is more appropriate to consider the aspect ratio than individual lengths or widths, as an increase leads to a greater red shift for λ_L , while λ_T remains unchanged unless the width is increased, which results in a small red shift at ~ 510 nm. This means that suitable nanorods can be prepared for use in a number of plasmon enhanced spectroscopies, such as SERRS and plasmon-enhanced fluorescence.

1.3 Fabrication of Gold Nanorods

The development of methods for the controlled synthesis of colloidal gold nanorods have rapidly progressed since the electrochemical synthesis which were first reported in 1997,²¹ and several approaches now exist for the formation of nanorods in high yield, quality and with high uniformity.

The most established method for nanorod synthesis is the seed-mediated approach, which was described in 2001 by Jana *et al.*²² A growth solution is prepared by the reduction of HAuCl_4 with ascorbic acid, in the presence of the surfactant, cetyltrimethylammonium bromide (CTAB) and silver ions, both of which are required for shape induction. To this, a seed solution of citrate-capped gold nanospheres (3-4 nm) is added. The use of citrate as a stabilizing agent leads to the formation of polycrystalline seeds, and thus impacts the monodispersity of the final product. Citrate is also used as a capping agent in the preparation of several nanoparticle shapes, including nanoplates²³ and nanostars,²⁴ however, it typically results in poorer yields and decreased monodispersity when compared to other methods. In this synthesis, the final aspect ratio of the nanorods obtained is controlled by varying the volume of seed solution added to the growth mixture.

In 2003, two further modifications to this method were introduced by Nikoobakht and El-Sayed.²⁵ The first was in the preparation of the seed solution, by replacing the sodium citrate capping agent with CTAB, which is a stronger stabilizing agent. The reduction of gold by NaBH_4 in the presence of CTAB rather than citrate leads to the formation of single crystalline seed. Since the morphology of the seed is a crucial factor in increasing the yield of nanorods with a well-defined shape, this has led to an increase in the monodispersity of the product. The second modification was to use silver ions in the form of silver nitrate (AgNO_3), to control the final aspect ratio of the nanorods by varying the volume of AgNO_3 added to the growth solution. This method has proved to be the most popular to date, as it produces nanorods in high yield (99%) and allows the formation of NRs with aspect ratios ranging from 1.5 to 4.5.²⁶ Importantly, the rods produced are highly monodisperse, and only a small fraction of spherical nanoparticles are formed, meaning there is no need for repeat centrifugation steps. The growth process is mostly self-limiting, although long term storage or complete termination of growth requires a simple centrifugation step, or it can be halted chemically by the addition of sodium sulphide.²⁷

Growth Mechanism There are a number of contributory steps in the formation of gold nanorods. There are two types of seed which are available for use in the synthesis of NRs; multiply twinned particles (MTP) which are formed from citrate capped gold seeds,²² and single crystalline seeds obtained from CTAB-capped gold seeds. The use of citrate as a capping agent leads to the formation of a polycrystalline seed, which in turn leads to the synthesis of more polydisperse NRs in a low yield.²⁸ The replacement of citrate with CTAB leads to the formation of a single crystalline seed, and high yield, monodisperse NRs.²⁵

CTAB is included in the growth solution as a stabilizing surfactant, however, it also acts to direct the nanoparticle growth via surfactant-based preferential binding.²⁹ High resolution transmission electron microscopy (HRTEM) and electron diffraction patterns were used to show that, in the absence of silver ions, the CTA⁺ head group binds preferentially to the nanorods on the {100} face (i.e. the short axis of the rod), as the spacing of gold atoms on this face is comparable to the size of the surfactant head groups.³⁰ It is commonly accepted that the {110} face, i.e. the longer length axis, has a higher surface energy than other faces. As a result, CTAB binding stabilizes these faces, leading to the prevention of crystal growth on this face, consequently, gold is deposited on the {100} face, promoting rod growth along this axis.

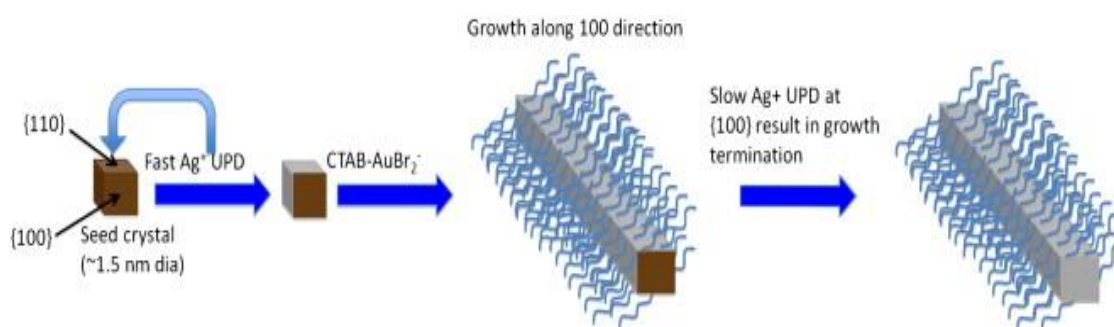


Figure 1.5. Schematic describing the growth of gold nanorods via seed mediated method.³⁰

Silver ions, in the form of silver nitrate, are also known to play an important role in nanorod synthesis. Whilst it is possible to form nanorods in the absence of AgNO₃, the addition of silver ions leads to an increased yield of NRs over other shapes.⁵ The addition of AgNO₃ to aqueous solutions of CTAB results in the formation of silver bromide, AgBr on the

nanorod surface, which is widely thought to play an important role in the growth mechanism of NRs. In the process known as underpotential deposition (UPD), Ag^+ is reduced to Ag^0 , in the form of a metal monolayer, under conditions at which this reduction would not normally occur. This results in the faster deposition of silver ions onto the {110} face than the {100} face, leading to particle growth along this axis, and in turn to the growth of rod-shaped particles. A growth-limiting point is reached when complete silver deposition occurs on the {100} face, which explains why this growth method is unable to produce NRs over 100 nm in length.³¹

The aspect ratio of the resulting nanorods is typically controlled either by altering the concentration of silver nitrate used, with increased concentrations leading to larger aspect ratios, or by altering the volume of seed solution added during the growth stage, with increased volumes leading to decreased aspect ratios.

1.4 Surface Plasmon Enhanced Spectroscopies

Due to the presence of SPR, all forms of optical scattering are enhanced when metallic particles are confined to the nanoscale. This leads to an attractive opportunity to combine metallic nanoparticles with classical spectroscopic techniques in order to develop more sensitive analytical measurements.

Mie theory shows that light scattering efficiency is greatly enhanced under certain resonance conditions. The excitation of surface plasmons creates highly localised intense electric fields close to the nanoparticle surface, which decay exponentially into the dielectric medium, away from the surface. This means that these nanoparticles are able to effectively focus resonantly coupled light. As a result, there is an increase by potentially several orders of magnitude of all radiative properties, such as light absorption, fluorescence, Rayleigh scattering and Raman scattering. The strong scattering displayed by these nanoparticles is the prime reason for increasing interest in utilising these materials for optical applications. A further advantage is that the use of metallic nanoparticles provides the opportunity to go below the diffraction limit, leading to an increase in the optical imaging spatial resolving power. The increased sensitivity afforded by surface plasmon enhanced spectroscopies means that through careful nanoprobe and sensor

design it is possible to achieve localized measurements on the single nanoparticle level, making such probes attractive for imaging and sensing applications.

1.4.1 Rayleigh Scattering

The scattering of light with no change in frequency of the scattered photons is termed Rayleigh, or elastic, scattering. This process is outlined in the Jablonski diagram in Figure 1.6.

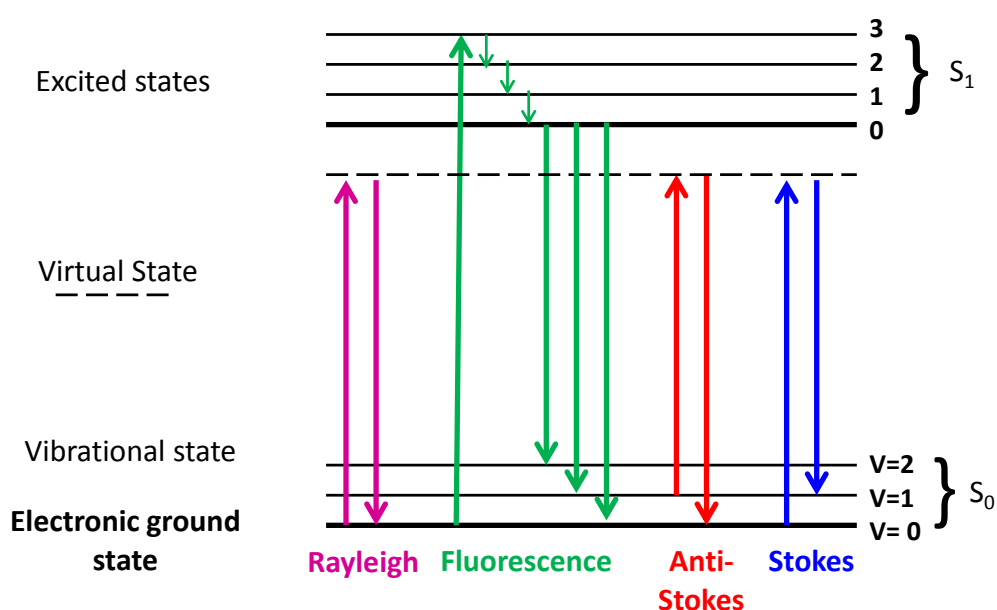


Figure 1.6. Jablonski diagram showing Rayleigh, fluorescence and Raman scattering processes.

Rayleigh scattering is strongly dependent on both the particle size and the wavelength of the incident light, with the intensity of the scattering rapidly increasing as the ratio of particle size to wavelength increases, and also as the overlap of the incident light with the LSPR increases. This means that it is possible to visualise and track individual nanoparticles, overcoming the limitations associated with the diffraction limit. Therefore, the brightness of a single nanoparticle is much greater than an individual fluorescent molecule, and also several hundred times larger than for quantum dots.³²

For gold and silver nanoparticles, which have high scattering efficiencies, it is possible to optically image individual particles as small as 10 nm using a conventional microscope, leading to the development of technologies such as NanoSight, where Rayleigh scattering is analysed to allow the imaging and tracking of nanoparticles in aqueous suspensions.³³

1.4.2 Surface Enhanced Fluorescence

The term fluorescence is used to describe the excitation of an electron from the ground state to a higher, excited electronic state followed by the emission of a photon at a lower energy than the incident photon. This process is depicted in Figure 1.6.

Recently, there has been a large amount of interest in combining the use of metallic nanoparticles with fluorophores in the hope of creating a new generation of highly sensitive analytical methods, probes and devices. Metallic nanoparticles exert an influence on the fluorescence emission of nearby molecules in a number of ways. Firstly, they are able to enhance the optical intensity of incident light on the molecules through near-field enhancement, which occurs due to the interaction of the electron clouds present in the metallic nanoparticle with the fluorophore, and can dramatically alter the spectral properties of the fluorophore. Secondly, they are able to modify the radiative decay rate of the molecule, and nanoparticle scattering is able to increase the coupling efficiency of the fluorescence emission to the far field. Furthermore, the quantum efficiency is higher than for an isolated molecule, and photostability is increased. These effects are dependent upon a number of factors, including the metal used, nanoparticle size, the distance between the fluorophore and the nanoparticle surface, and also on the aggregation state of the nanoparticles.³⁴

The behaviour of a fluorophore is strongly dependent on the distance between it and the metal surface. If this distance is less than approximately 5 nm, the fluorescence is strongly quenched, whereas if the molecule is approximately 5-10 nm from the metal surface, the fluorescence can be strongly enhanced.³⁵ Fluorescence quenching is thought to occur through interactions between the analyte dipole and the metal SPR, through a process known as surface energy transfer (SET). This process involves the non-radiative transfer of energy from the dye molecule to slightly lower energy levels of the metallic

particle, this process is shown later in Figure 1.7. The efficiency of this process is inversely proportional to the third power of the distance between the nanoparticle and analyte. At longer distances, this interaction with the SPR can lead to enhancement of fluorescence properties.³⁶

1.4.3 Raman Scattering

The scattering of light accompanied by a change in frequency is known as Raman, or inelastic, scattering. A Raman spectrum shows the scattered light with the new frequencies present. There are two types of Raman lines, the first is Stokes scattering, where the frequency of the photon emitted is less than that of the incident light. The second is Anti-Stokes scattering, where the photon emitted is of a higher frequency than the incident photon.³⁷ These scattering events are depicted in Figure 1.6.

Raman scattering was first observed in 1928,³⁸ this form of scattering can be used to provide detailed information about the chemical and molecular nature of target molecules. It provides far more detailed information than alternative spectroscopies such as absorption and fluorescence,^{39,40} and is therefore ideal for biological detection. Raman spectroscopy is the study of vibrational, rotational and other low frequency modes within a system.

There is a relative difference in the intensity of the Stokes and Anti-Stokes Raman scattered photons. This is explained by the disparity in the number of molecules in the excited state compared with those in the ground state. At room temperature, there are fewer molecules in the excited state, therefore, anti-Stokes Raman bands are less intense than the Stokes Raman bands. There are more molecules in the excited state at elevated temperature, which alters the relative intensities between Stokes and anti-Stokes scattering.³⁷

When monochromatic light is incident upon an analyte, it interacts with the molecule, resulting in polarization of the electron clouds surrounding the nuclei. There is an accompanying transfer of energy from the incoming photons to the electrons, which leads to the formation of a highly unstable species referred to as a virtual state. The light energy is released almost immediately in the form of scattered radiation. If the nuclei begin to move on formation of the virtual state this will lead to molecular energy changes, and the

scattered light will have a different energy to the incident light. Analysis of the scattered light shows that only a very small fraction (1 in $10^6 - 10^8$) of photons have altered energies.³⁷

The first interpretable laser-excited Raman spectrum was obtained in 1970 by Lord and Yu, and showed the Raman spectrum of lysozyme.⁴¹ Most biological molecules have very small Raman scattering cross sections, and therefore exhibit very weak Raman signals, meaning that the original method did not generate much interest as an analytical tool.

1.4.4 Surface Enhanced Raman Scattering (SERS)

Modern interest in Raman spectroscopy as a viable method for molecular sensing can be traced to the work of Fleischmann *et al*, who developed a system based on pyridine adsorbed onto a roughened silver electrode. This process, now known as surface enhanced Raman scattering (SERS) led to an increase in Raman scattering efficiencies by up to 10^6 .⁴² This has led to a wealth of research being carried out using this technique, and SERS has proved successful in a variety of biological applications, such as the ultrasensitive detection of DNA⁴³ and analysis of cells.¹

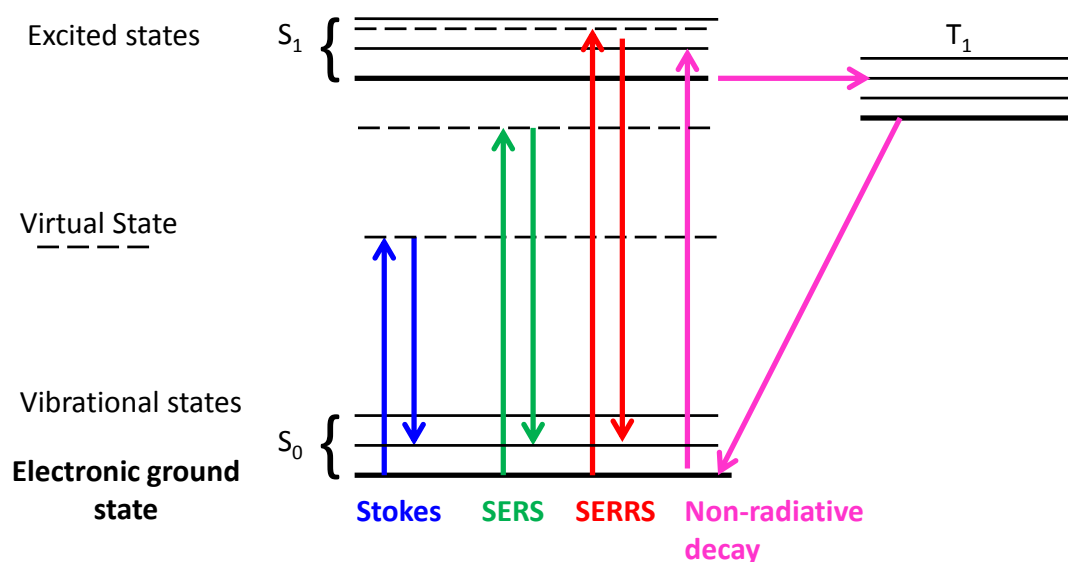


Figure 1.7. Jablonski diagram depicting the Stokes Raman scattering, SERS, SERRS and non-radiative decay processes.

Origin of Enhancement The exact source of Raman enhancement continues to be debated in the literature,⁴⁴ however there are two commonly proposed mechanisms describing the SERS enhancements obtained.

The electromagnetic (EM) enhancement theory proposes that the analyte is in an electric field gradient on the surface, immersed in the LSPR electrons. This field, along with coupling of the analyte with the LSPR causes enhanced scattering. In order to scatter the light, the oscillations of the plasmon must be perpendicular to the metal surface. The magnitude of the enhancement obtained is dependent on the metallic surface (size, shape and intrinsic dielectric property of the metal) and on the frequency and power of the incident light source. The intensity of the incident light will increase by a factor of E^2 , and the scattered light will also be enhanced by a factor of E^2 , leading to an overall signal increase of E^4 . An increase of this magnitude is only attainable under perfect conditions, e.g. where the Raman signal is only slightly different from the incident light.⁴⁵ The EM mechanism is the main contributor to the signal enhancements observed in SERS, with enhancements as high as $10^{10} - 10^{11}$.⁴⁶

Along with the electromagnetic mechanism, another contribution to enhanced Raman is chemical enhancement (or charge transfer). This process involves an interaction between the analyte and the metal surface. If the analyte HOMO and LUMO orbitals are matched to the Fermi level of the metal, it is possible to transfer energy from the metal to the analyte. Energy is then transferred back to the metal and scattered, i.e. there is no interaction with the plasmons. Chemical enhancement is not related to the SERS process itself, but is a result of the increased polarizability of the analyte molecule. This enhancement process is much weaker than electromagnetic enhancement, typically it is thought to contribute only 1-2 orders of magnitude. Unlike EM, this process is dependent upon the analyte used.⁴⁷

The vast majority of evidence currently available suggests that both EM and CE play a role in the SERS process, with EM widely agreed to be the largest contributor.

Over recent years, there has been a move from the use of electrodes to the use of metallic nanoparticles. Furthermore, aggregation of the nanoparticles leads to enhanced electric fields at interparticle junctions, known as "hot-spots", resulting in large enhancements of Raman signals.⁴⁸ The choice of metal is critical, as Raman modes are

excited by visible and near IR frequencies, meaning gold and silver nanoparticles are particularly suitable for application in SERS.

Selection Rules. The SERS surface selection rule describes the effect of the orientation of the analyte molecule adsorbed onto the metal surface on the intensity of the SERS enhancement. It states that when the analyte molecule is perpendicular to the metal surface, the most intense SERS enhancements will be obtained.⁴⁵ Costa *et al* have demonstrated the importance of the molecular orientation of the analyte on the metal surface,⁴⁹ using simazine and atrazine along with silver substrates, and similar findings are discussed later in Chapter 3.

Enhancement Factor (EF). When comparing enhancements obtained from different metallic SERS substrates, SERS enhancement factors (*EF*) are often quoted. The *EF* describes the enhancement obtained with respect to what would be obtained for the same analyte molecule, at the same experimental conditions in the absence of the SERS active substrate. The *EF* can be calculated using Equation 1.3:

$$EF = \frac{I_{SERS}/N_{Surf}}{I_{RS}/N_{vol}} \quad \text{Equation 1.3}$$

where I_{SERS} is the intensity of the SERS signal (typically obtained using the height or area of a characteristic peak), I_{RS} is the intensity of the Raman signal of the same peak for the analyte molecule obtained in the absence of SPR enhancement. N_{Surf} is the average number of adsorbed molecules in the same scattering volume for the SERS experiments. N_{Vol} is the average number of molecules in the scattering volume.⁵⁰

There are a number of limitations associated with the calculation of enhancement factors in this way, the main one being that there are a lot of assumptions made when carrying out the calculation. Many Raman reporter molecules are dyes, when calculating I_{RS} for a dye molecule in the absence of a SERS substrate there is no quenching of the

background fluorescence, which can lead to interference, or in some cases, means it is impossible to extract the Raman peak information, meaning this calculation is not possible. This approach also requires knowledge of the laser focus volume, which is dependent on the wavelength of light used and the lens objective and the medium. A further issue is that Raman signals are much weaker than SERS, meaning that longer integration times often have to be used to obtain signals. Finally, since the SERS effect is distance dependent, for this equation to be accurate, the surface coverage must be sub full monolayer since relative SERS signals from molecules beyond the first monolayer are reduced and the number of contributing molecules are more difficult to estimate.

An alternative to calculating the enhancement factor is to normalize the data obtained with respect to a standard with a known Raman differential cross section ($d\sigma_R/d\Omega$). For a single cross-scattering object this can be defined as:^{46, 51}

$$\left(\frac{d\sigma_R}{d\Omega}\right)_{Label} = \frac{I_{Label} C_{Standard}}{C_{Label} I_{Standard}} \left(\frac{d\sigma_R}{d\Omega}\right)_{Standard} \quad \text{Equation 1.4}$$

Where C_{Label} is the concentration of the nanorod-dye conjugates, I_{Label} is the SERS intensity of the sample, $I_{Standard}$ is the Raman signal of a standard with known concentration ($C_{Standard}$) and known absolute cross section. Both the sample and standard measurements are performed under identical conditions (i.e. laser power and focus, sample volume and integration time). This approach is advantageous as it is based on sample concentrations and does not require knowledge of the laser volume, thus allowing direct comparison of spectral intensities acquired between samples at different laser excitation wavelengths and laser intensities. This approach is discussed in more detail in Chapter 3.

There are a few key limitations of SERS mainly that it can be difficult to relate the spectra obtained to the normal Raman scattering spectrum due to the appearance of new bands and disappearance of existing ones. Furthermore, the spectra can become confused due to contaminants adsorbed onto the metallic surface, making definitive assignment of peaks difficult.⁴⁵ A possible solution is to use a closely related technique known as surface

enhanced resonance Raman scattering (SERRS), which is discussed in more detail in the following section.

1.4.5 Surface Enhanced Resonance Raman Spectroscopy (SERRS)

In the case of resonance Raman spectroscopy the chromophore and laser excitation wavelength overlap. While for SERS of a non-resonant molecule signal enhancements of 10^6 – 10^8 have been reported, signal enhancements of up to 10^6 have been reported as a result of resonant Raman scattering.⁴⁵ Surface enhanced resonance Raman spectroscopy (SERRS) combines the advantages of surface plasmon enhancement with the use of a resonant Raman reporter molecule. When these two effects are combined SERRS enhancements of up to 10^{14} have been reported.^{45, 52-54} The SERRS process has proven to be so sensitive that a number of groups have now reported the detection of single molecules on a nanoparticle surface.^{53, 54}

For SERRS analysis, a laser excitation frequency should be chosen that matches the absorption maximum of the resonant molecule as closely as possible. A formal Jablonski description of SERRS is not widely available in the literature, however, this process is depicted in Figure 1.7. In the case of SERRS, the energy of the virtual state coincides with an excited electronic state, leading to a vibronic state.⁵⁰

A key disadvantage of resonance Raman scattering is that a large proportion of the incident light is absorbed, and can lead to background fluorescence signals which interfere with the Raman spectrum. With SERRS, the absorption of the dye molecules onto a metallic surface means that all fluorescence is significantly quenched (see Figure 1.7). As a result, it is possible to use both fluorescent and non-fluorescent dyes as Raman reporters for SERRS.

SERRS is also able to overcome the main disadvantages of SERS, firstly the signals obtained for SERRS often closely resemble the molecular resonance Raman spectra, and can be less affected by orientation dependence and the selection rules. When comparing Raman spectra with SERRS spectra, the relative intensities of peaks may differ, but the peak positions will only change by a small amount, making peak assignment simpler than for SERS. Contaminants also pose less of an issue as the resonance enhancement does not affect most of them, and thus any signals remain very small compared with those of the analyte molecule.⁴⁵

SERRS and SERS intensities can be further enhanced through aggregation of the nanoparticles. The main reason for this is that at junctions between two or more nanoparticles, local electromagnetic fields overlap, leading to highly intense electromagnetic fields, known as hot spots.

Furthermore, by using nanoparticles such as nanorods, it is also possible to tune the LSPR of the metal to increase overlap with the excitation wavelength of the laser and the reporter molecule resonance, and therefore the EM enhancement is further increased.⁵⁵

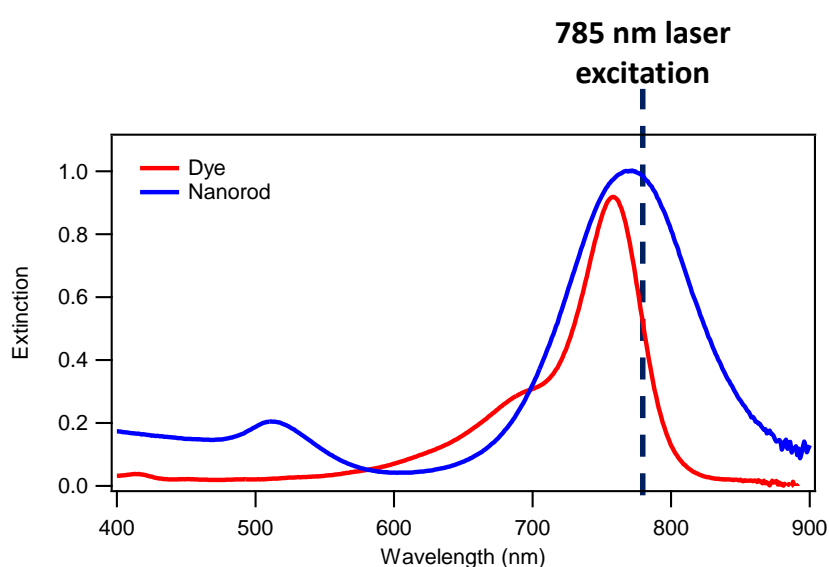


Figure 1.8. Extinction spectra for example dye and nanorod solutions with 785 nm laser excitation line highlighted

The potential to overlap the dye molecular resonance and the nanoparticle λ_L maximum SPR with a laser excitation wavelength is illustrated in Figure 1.8, and should lead to further increases in SERRS signal intensity.

The effect of the SPR position and the laser excitation wavelength used for the optimal design of a SERRS system is still debated in the literature. The Van Duyne group have carried out a series of experiments based on silver nanoparticle arrays and concluded that the maximum SERS enhancement occurs for systems where the SPR is red shifted with

respect to the excitation wavelength.^{9, 56, 57} These nanoparticles are immobilised rather than in solution.

Smith *et al* used unaggregated spherical silver colloid with a benzotriazole dye (λ_{max} 429 nm) adsorbed onto the surface.⁵⁸ The dye itself did not cause aggregation of the colloid. SERRS measurements were performed at various wavelengths, and the results obtained clearly show that the maximum enhancement obtained is at the frequency close to that of the plasmon resonance, and where both the dye and the laser overlap. The study also demonstrated that the SERRS enhancement drops off as the laser gradually moves to the red.

This is in direct contrast to results recently reported by Murphy *et al*, who developed a system based on CTAB stabilized gold nanorods, coated with a layer of polyelectrolyte.⁵⁹ A dye reporter molecule is then adsorbed onto this polyelectrolyte surface, followed by wrapping with another polymer layer to encapsulate the dye. The results obtained here show that the maximum enhancement is obtained where the plasmon resonance is blue-shifted with respect to the laser excitation wavelength, where there was minimal overlap between the adsorption peak and the laser line, with optimal signals reported when the SPR was approximately 50 nm blue shifted from the laser excitation. The authors state that the results imply that the use of nanorods with lower aspect ratios allows optimal sensing. The work in this study was transmission based, rather than a back-scattering configuration, therefore extinction losses along the sample path length are an issue.

Perhaps it may be important to note that the system used by Smith *et al* utilised dyes adsorbed directly onto the nanoparticle surface, while in the system used by the Murphy group, the dyes were spaced approximately 4-5 nm from the metal. The Murphy group also described weak resonance coupling between the rods and dyes, with shifts of less than 5 nm observed.

Additionally, a phenomenon known as the “lightening rod effect” has been described whereby additional high local EM enhancements exist at the corners or tips of nanoparticles,⁶⁰ leading to larger SERRS enhancements than those found for spherical nanoparticles, with nanorods reported to provide enhancements of 10^4 - 10^5 compared to spherical nanoparticles.⁶¹ Unaggregated gold and silver nanorods have been reported to

provide enhancements of 10^7 - 10^9 when the nanorod plasmon is tuned to the laser excitation wavelength compared to when it is off resonance.⁶² This enhancement can be increased further via nanoparticle aggregation, with enhancements of 10^7 - 10^9 reported.^{63,64} The use of unaggregated nanorods for solution based SERRS measurements has not been widely reported in the literature, with most studies relying on aggregation to provide additional signal enhancements in order to obtain bright Raman signals. The use of unaggregated nanorods for such studies is a focus later in Chapter 3.

1.5. Nanoparticle-Enhanced Optical Sensing and Imaging

Since the seminal report by the Mirkin group in 1996,⁶⁵ sensing applications involving spherical metallic nanoparticles have rapidly accelerated. The use of such materials for nanoparticle enhanced imaging techniques is also now widespread. While the work here will focus mainly on nanorods, it is only in the last 10 years that the advantages of working with these structures are beginning to be explored. As a result, the literature in this area is far less developed than for spherical nanoparticles, and has been further hindered by factors including cytotoxicity of the nanorod CTAB stabilizing agent,⁶⁶ along with the relative lack of routes for functionalizing these particles.

Two techniques commonly applied to biosensing applications are SPR extinction measurements and SERS.

1.5.1 Extinction Spectroscopy for Biosensing

As discussed in Section 1.2, the SPR frequency is strongly dependent on the dielectric constant of the surrounding medium. These changes can be the result of aggregation of the nanoparticles, resulting in either a red or blue shift of the SPR, or smaller changes associated with the surface adsorption of target molecules. It is therefore possible to measure either the extinction or scattering of the SPR to allow changes to the surrounding medium to be monitored.⁶⁷

The application of LSPR shifts was pioneered by the Mirkin group, who have successfully demonstrated the detection and sensing of nucleic acids, the process is outlined in Figure 1.9.

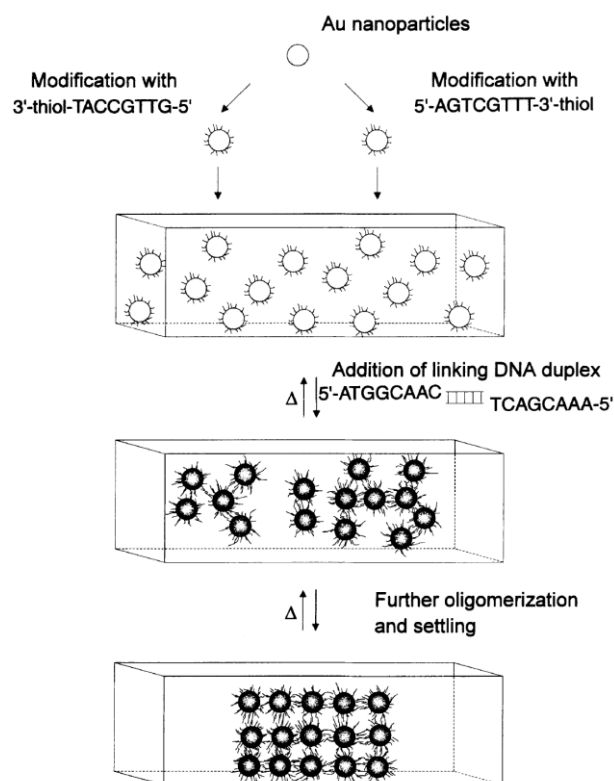


Figure 1.9. Schematic showing the DNA-based colloidal nanoparticle assembly strategy employed by Mirkin *et al.*⁶⁵

This method is based on a sandwich assay, and uses two stock solutions of gold nanospheres, each functionalized with a non-complementary probe sequence of DNA. These are then mixed, and in the presence of target DNA which has sections complementary to both probe sequences, the target DNA hybridises resulting in a relatively controlled aggregation of the nanoparticles. This leads to a shift of the nanoparticle LSPR, which can be visualised by a change in colour of the solution.⁶⁸

Theoretical studies by the El-Sayed group have shown that the sensitivity of LSPR of the λ_L band in nanorods is higher than for nanospheres,⁶⁹ making NRs attractive substrates for these applications. So far gold nanorods have been applied to a number of SPR sensing techniques, for example, gold nanorods of varying aspect ratios were used to create a multiplex sensor, which was able to differentiate between human, rabbit and mouse IgG proteins. Discrimination was based on the differing SPR UV-vis absorbance shifts, with nanomolar limits of detection reported.⁷⁰ Biomolecular protein sensing of the binding of streptavidin to biotin-conjugated gold nanorods, based on SPR shifts as small as

half a nanometre have been measured using dark field microscopy.⁷¹ Dark field microscopy was also used to demonstrate the detection of streptavidin, using gold nanorods conjugated with biotin, with detection limits of 1 nM reported.⁷²

The ultrasensitive detection of protein biomarkers has been achieved using gold nanorods coated with anti-immunoglobulin E (anti-IgE). IgE contains separate antibody and DNA aptamer binding sites, and was immobilized onto a surface coated with aptamers. Detection was carried out via the specific adsorption of anti-IgE coated nanorods, with attomolar detection limits reported.⁷³

The SPR wavelength is also altered depending on the proximity of other nanoparticles, and has been shown to be successful in the detection of DNA, antigens and disease biomarkers.⁷⁴ The detection of target DNA was described by Mann *et al*, who described the specific organization of gold nanorods into 3-D assemblies via DNA hybridisation.⁷⁵ This same technique has been used to identify target DNA, using PCR amplified pathogen genes. The authors reported excellent specificity and discrimination of the target DNA compared with non-specific genes, with nanomolar detection limits achieved.⁷⁶

1.5.2 SERS Spectroscopy for Biosensing

As discussed in Section 1.4.4, SERS is able to give detailed information on the chemical and molecular composition of a target molecule. The electromagnetic field component of SERS is strongly dependent on both the distance between the molecular analyte and the metal surface and the particle radius of curvature,⁷⁷ and thus the shape of the nanoparticle used is critical. It has been shown that the relative SERS enhancements gained offers enhancements of up to $10^4 - 10^5$ when the molecule of interest was adsorbed onto a nanorod surface when compared to the same conditions with spherical gold particles.⁶¹ A further advantage to using gold nanorods for SERS measurements is that it is possible to tune the SPR to the wavelength of the excitation wavelength.

The use of Raman for biosensing applications has become increasingly common in the last decade or so, with detection of a wide variety of analytes, with varying detection limits being reported. A common approach has been to directly detect biomarkers related to diseases such as cancer. The targeting of epidermal growth factor (EGFR) has proven to

be a common approach, in 2008 Nie *et al* described the detection of EGFR on human cancer cells using pegylated quasi-spherical gold nanoparticles functionalized with tumour targeting ligands and detected using SERS.⁷⁸ Another approach reported the detection of carcinoembryonic antigen (CEA), which is a lung cancer biomarker. This was achieved using hollow gold nanospheres (HGNs) and magnetic beads which acted as a supporting substrate for the formation of the immunocomplex, with the limit of detection found to be in the range 1-10 pg/mL.⁷⁹ The same group have also developed a novel microfluidic sensor based on the use of HGNs and magnetic beads, and when applied to enzyme-linked immunosorbent assays (ELISA), they reported a limit of detection for rabbit immunoglobulin (IgG) of 1-10 ng/mL.⁸⁰ Porter *et al* reported the first ever detection in clinical serum samples of the mucin protein, MUC4, which is a biomarker for pancreatic cancer. The assay here used a gold capture substrate, along with 60 nm quasi-spherical gold NPs conjugated with specific antibodies.⁸¹

This strategy has been applied to a wide range of other diseases, for example, Porter *et al* have also successfully developed an assay that detects specific metabolites of vitamin D₃, which has been linked to renal diseases.⁸² The sensitive detection of biomarkers associated of a variety of diseases ranging from Anthrax⁸³ to Alzheimer's disease⁸⁴ have been reported.

SERS is not limited to the detection of diseases, Nie *et al* have developed plasmonic probes applicable to the detection of proteins, cells and intact viruses.⁸⁵ Viruses such as the West Nile virus⁸⁶ and bacteria including *Escherichia coli*⁸⁷ have been detected, and discrimination between cancer cells and healthy cells based on changes to the Raman spectrum as a result of the differences in pH between these cells have been reported.⁸⁸ Intracellular pH sensing in living cells has been reported, using gold nanoshells functionalized with redox active molecules.⁸⁹

The examples above highlight the diverse applications of this technology. Much of the current research focuses on the detection of new analytes, with a drive towards increasing the sensitivity of these assays, as well as developing assays capable of true multiplex detection. Another issue is the detection of analytes in clinical samples, for example, Liz-Marzan *et al* have reported the use of gold nanorods for the direct SERS detection of prions in complex biological media such as serum and blood.⁹⁰

1.5.3 Enhanced Molecular Imaging Applications

Molecular imaging techniques allow either the direct or indirect monitoring and recording of the distribution of molecular and cellular processes *in-vitro* or *in-vivo*. It can be used to visualize molecular or genetic events in live cells, tissues, organs and even whole organisms. The unique optical, electronic, magnetic and structural properties of nanomaterials mean they are of growing interest in this field, either as imaging probes or contrast agents.⁹¹

Raman nanotags have shown a number of promising applications, for example, Wang *et al* reported the use of tags to detect circulating tumour cells (CTCs) in mouse and human blood samples with high specificity to head and neck cancer cells.⁹²

The El-Sayed group were able to directly image the cancer biomarker, epidermal growth factor receptor (EGFR), which is present in larger amounts on cancer cells membranes. The group used spherical gold nanoparticles which were conjugated to anti-EGFR antibodies, and measurements were made using dark-field microscopy.⁹³ The same experiments were also carried using gold nanorods rather than spherical particles, and they were successfully able to image the cancerous cells,⁹⁴ as shown in Figure 1.10.

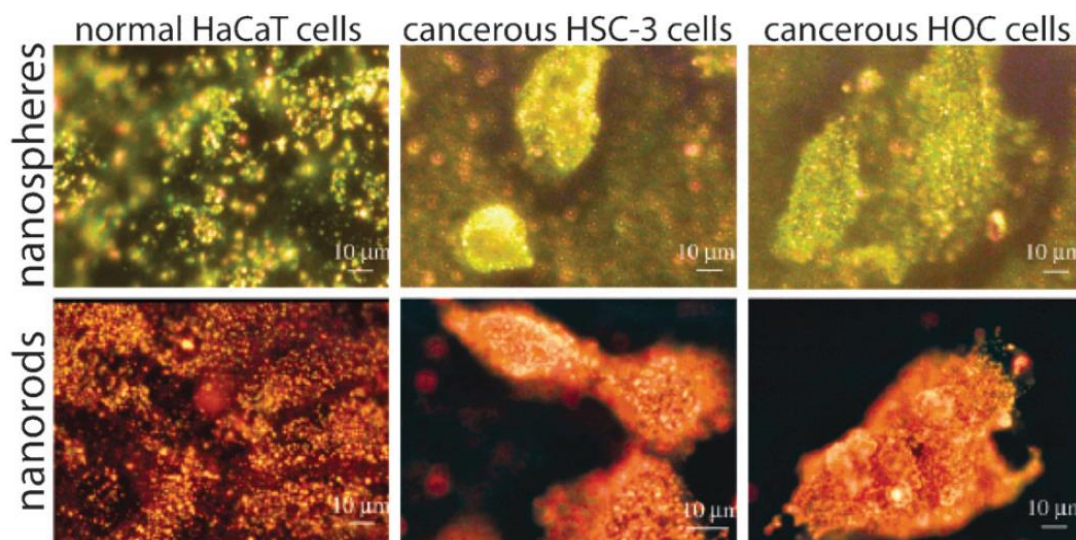


Figure 1.10. Optical dark-field microscopy of normal HaCaT cells and cancerous HSC and HOC cells incubated with anti-EGFR antibody-conjugated gold nanospheres (top row, left to right). The bottom row shows the same type of cells incubated with anti-EGFR conjugated gold nanorods. The anti-EGFR conjugated nanoparticles bound specifically to cancer cells, thereby scattering strongly under dark-field microscopy, and thus enabling detection of malignant cells.⁹⁴

As discussed previously, the ability to multiplex using Raman nanotags is a key advantage, and to date a number of studies have demonstrated this. For example, gold nanospheres have been used to produce ten different Raman scattering nanotags, which were injected subcutaneously into a live mouse. It was then possible to separate the spectral fingerprints of all ten nanotags. Five tags were subsequently injected into the liver and the natural accumulation of the conjugates was successfully determined.⁹⁵

Gold nanorods have been used for *in vitro* and *in vivo* multiplex detection by von Maltzahn *et al*, who were able to utilise the additional resonance enhancement provided by the nanorods due to their LSPR position in the near-IR region.⁹⁶ A further interesting application of gold nanorods was demonstrated by a report describing their use as a substrate for both SERS imaging and photothermal heating. This work was carried out *in vivo* on a mouse using three different nanorod tags, each containing a different dye. These molecules were all found to be identifiable via SERS measurements.⁹⁶

A further growth area of research involves using nanotags to image whole tissues, true *in vivo* SERRS detection has been reported by Qian *et al*, who injected mice subcutaneously and intramuscularly with SERS tags. The nanoparticles were conjugated with tumour-marker specific antibodies and were shown to be able to target tumour biomarkers such as epidermal growth factor receptors on human cells. They were able to detect SERS signals from approximately 1-2 cm depth using 785 nm laser excitation, however, in order to achieve this, a 21 second spectral accumulation time was required.⁷⁸

Whole body imaging is another key area of research, and has been reported using commercial, silica coated SERS labels to image mice.⁹⁷ Wang *et al* have also described the distribution of gold nanoparticles labelled with para-mercaptobenzoic acid (pMBA) in zebrafish embryos.⁹⁸ Furthermore, they were also able to demonstrate multiplexed detection of these probes.

1.6 Multimodal Spectroscopic Techniques

The spectroscopies discussed above are closely related, however, the interplay between each and subsequent exploitation has not been explored to any great extent. Consequently, multimodal spectroscopy is an emerging area of research for nanoparticle enhanced sensing. There are two distinct areas within multimodal research, the first uses the simultaneous measurement by two different optical spectroscopic techniques, for example, fluorescence and SERS. While not the focus here, the second approach is more commonly applied to the combined use of an optical technique with a non-optical one such as atomic force microscopy (AFM), electron microscopy (EM), or magnetic resonance imaging (MRI). Since the focus of this work is to develop nanotags suitable for imaging and tracking via a combination of optical spectroscopies, then this first area will be focussed on briefly here.

The key motivation for developing multimodal spectroscopy is that each individual imaging technique has its own advantages and disadvantages and that by combining the techniques into a single system, it is possible to obtain complementary information not possible with only an individual technique. Secondly, it allows for higher discrimination (spatial, molecular and colocalization) than a single spectroscopic technique. Furthermore, multimodal spectroscopy offers greater potential to carry out very sensitive multiplex sensing, which is the detection and measurement of multiple analytes per sample. Multimodal techniques are information rich, and allow a much better picture to be built up of complex systems.

Multimodal optical approaches, especially at the single nanoparticle level, are still in the early stages of development, however, in the last few years a number of successful examples of their application have begun to emerge using a range of nanoparticles and spectroscopies. A common approach combines optical spectroscopy with photothermal therapy, whereby the nanoprobe targets a specific type of cell and then laser irradiation is used to gradually heat the nanoparticles, leading to the targeted destruction of the cell. Gold nanorods are widely used for this application as they are able to absorb light in the near-infrared region. El-Sayed *et al* reported the imaging and subsequent photothermal therapy of cancer cells *in vitro* using gold nanorods conjugated with anti-epidermal growth factor (anti-EGFR). They demonstrated the binding of the nanoprobe to the cells by

darkfield imaging, and were able to selectively destroy the targeted cells using photothermal therapy.⁹⁴

Photothermal therapy has proven to be a popular approach, and has been combined with a variety of techniques including X-ray computed tomography (CT)⁹⁹ and increasingly with SERS. Sailor *et al* demonstrated the use of gold nanorods stabilized with PEG, and containing cyanine Raman reporter molecules for tumour detection and photothermal treatment.¹⁰⁰ They introduced the probes, along with temperature-sensitive liposomes which contained anticancer drugs. SERS spectroscopy was used to identify the tumour site, based on the cyanine spectra obtained, and then locally heated this area using laser irradiation, as shown in Figure 1.11.

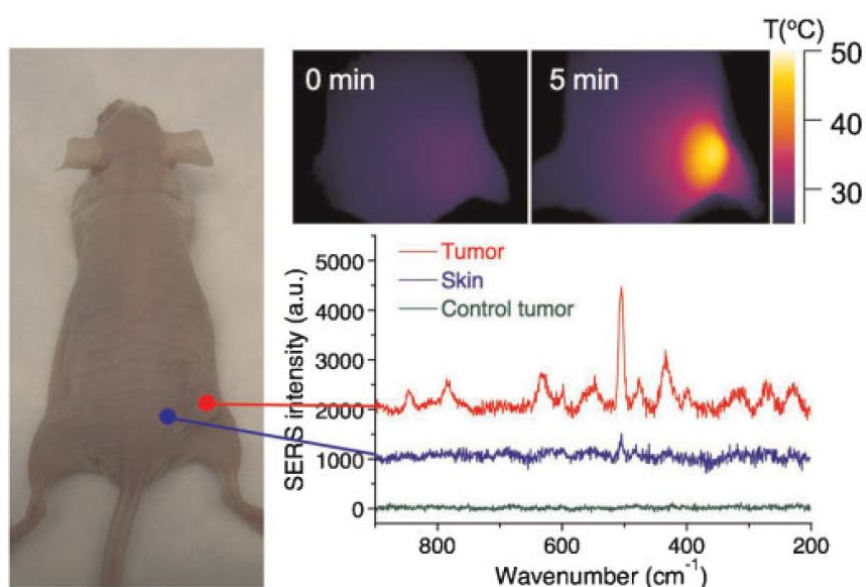


Figure 1.11. Optical and thermal images of a mouse injected intravenously with gold nanorods. Thermal image shows before and after laser irradiation. Also shown are Raman spectra of the tumour region (red trace) and skin near tumour (blue trace)¹⁰⁰

The localized heat triggered release of the drug from the liposomes, and tumour growth was reported to be significantly suppressed. This work was even more significant because it relied on the cooperative effect of two nanoparticle systems (the probes for localized heating and the liposomes for drug release).¹⁰⁰ More unusual alternatives to gold nanorods have been used, such as gold nano-popcorn,¹⁰¹ which consists of a spherical

centre surrounded by tips on the surface. The study showed that Raman signals were amplified by several orders of magnitude (10^9). The nano popcorn was functionalized with anti-prostate-specific membrane antigen (PSMA), resulting in sensitive detection of human prostate cancer cells at the 50 cell level. As with many nanorod based approaches, near-infrared irradiation was used to cause targeted localized heating, leading to cell destruction. By monitoring the SERS intensities it is possible to monitor the progress of the photothermal therapy.

Single-walled carbon nanotubes (SWCNTs) have been used as multimodal agents to provide gene delivery and photothermal treatment. This was achieved by functionalizing SWCNTs with fluorescently labelled oligonucleotides, confocal microscopy was used to confirm the uptake and accumulation of the probes into HeLa cells. Again, NIR irradiation was used to increase the local temperature, causing the cells to rupture and the genes attached to the SWCNTs to diffuse into the nucleus.¹⁰²

An alternative multimodal approach is to couple photoacoustic imaging with SERS. Photoacoustic imaging involves using short laser pulses to detect responsive ultrasonic signals, a key advantage is that it is able to provide high spatial resolution along with enhanced tissue penetration, compared with fluorescence imaging. SWCNTs were used which were conjugated with cyclic Arg-Gly-Asp (RGD), this was used in place of a dye or contrast agent. The peptide conjugated SWCNTs were intravenously administered to mice bearing tumours, and the localization within the tumour was determined using both photoacoustic imaging and SERS.¹⁰³

Combining SERS with fluorescence has proven popular, with a number of studies exploring the preparation and application of substrates. Murphy *et al* have described a route for the one-pot synthesis of spherical silver nanoparticles, inside silica shells, together with iron oxide nanoparticles and Raman reporter molecules. Finally, a fluorophore is attached to the silica shell.¹⁰⁴ Spherical gold-organosilica structures have been prepared via the direct hydrolysis of 3-mercaptopropyltriethoxysilane in aqueous solution in the presence of an Au core. It was then possible to modify the Au core with Raman reporter molecules prior to hydrolysis, and the organosilica shell could also be functionalised with a fluorophore.¹⁰⁵ Silica was also used by Choo *et al* to encapsulate gold nanospheres. The probes were used to detect two breast cancer markers, and to determine the localization of each these within the cells.¹⁰⁶

Heterostructures comprising of DNA-conjugated SWCNTs and quantum dots have been studied using SERS and fluorescence. The heterostructure was compared with both constituents with the aim of correlating structural details and optoelectronic characteristics, allowing researchers to explore photoinduced charge transfer from the quantum dots to the SWCNTs.¹⁰⁷

SERS has also been coupled with other techniques including MRI¹⁰⁸ and LSPR¹⁰⁹ demonstrating its growing importance.

1.7 Research Aims

The overall aim of this work is to perform the controlled assembly of nanorods and dyes, subsequently, the characterization, functionalization and application of these nanotags will be explored. The key aims of this thesis are summarised below:

- Prepare novel nanorod-dye conjugates with control over the dye surface coverage and orientation, and subsequently stabilize these conjugates.
- Perform a systematic SERRS study where both the localized surface plasmon resonance (LSPR) and dye molecular resonance are varied with respect to the laser excitation wavelength, and to determine the resonance coupling observed in these systems. Also to compare the Raman enhancements obtained compared with nanorods to a similar system using quasi-spherical nanoparticles.
- Investigate the controlled side-by-side aggregation of the nanorod-dye conjugates, and subsequent stabilization of these clusters in solution. Perform SERRS experiments to determine the effect of increased cluster size on Raman enhancements.
- Develop novel bright Raman probes, capable of providing SERRS signals at a range of common laser excitation wavelengths (514 - 1064 nm), while remaining hotspot free.
- Test the brightness of these probes via single particle Raman mapping measurements, and correlate these with SEM images to prove conclusively that strong single particle SERRS signals are possible.
- Demonstrate the potential applications of nanorod tags for cellular imaging and biosensing measurements.

- Finally, to develop a methodology to covalently functionalise these nanoparticles with biomolecules such as DNA.

Chapter 2

Experimental

All chemicals were purchased from Sigma-Aldrich, and used without further purification.

All nanoparticle synthesis were performed using Millipore deionized water.

All glassware used in the synthesis and storage of nanoparticles was first soaked in aqua regia for a period of at least 30 mins and then rinsed thoroughly in doubly-distilled water prior to use.

2.1 Nanorod Synthesis.

Nanorod solutions were prepared using a modified version of the procedures developed by Sau and Murphy²⁸ and Nikoobakht and El-Sayed,²⁵ a key difference was that the reaction volume was scaled up to 1 L to give a large volume of stock NRs to avoid problems associated with batch to batch variations. Furthermore, the samples were centrifuged and resuspended four times in 1 mM CTAB to ensure that all excess reactants were removed from the NR stock and to give a fixed CTAB concentration of 1 mM which was critical for the reproducible formation of mixed CTAB-dye layers around the NR surface. Samples were characterised using UV-vis measurements to determine the SPR position, and to calculate the sample concentrations.

Preparation of Seed Solution: A CTAB solution (5 ml, 0.2 M) was mixed with HAuCl_4 (5 ml, 0.01 μM) under stirring, to which freshly prepared, ice-cold NaBH_4 (0.6 ml, 0.01 M) was added, producing a brownish-yellow solution. This solution was kept at 27-30 °C and used immediately following preparation.

Growth Solution: The following procedure was used to prepare two batches of nanorods with a target longitudinal plasmon resonance of 633 nm (Batch 1) and 785 nm (Batch 2). 20 ml of AgNO_3 solution (Batch 1, 5.5 mg and Batch 2, 13.2 mg) was added to

CTAB (400 ml, 0.2 M). Next, HAuCl_4 (400 ml, 1.0 mM) was introduced and the solution gently mixed by inversion. Ascorbic acid (5.6 ml, 0.8 M) was then added resulting in the growth solution changing from dark yellow to colourless. Freshly prepared seed solution (1.6 ml and 1.1 ml for batches 1 and 2 respectively) was added to the growth solution and the reaction allowed to proceed for 48 h in a water bath maintained at 27-30°C. The solution was centrifuged at 8500 rpm for 45 min and resuspended in 1 mM CTAB at half the original reaction volume i.e. 500 ml. This last step was repeated a further 3 times and the rod stock solution stored until use.

Batch 1 had λ_T at 516 nm and λ_L 618 nm, while Batch 2 had λ_T and λ_L at 511 and 770 nm respectively.

Chapter 4: Nanorods prepared as above, using 13.5 mg AgNO_3 and 1.05 ml seed solution. The nanorods prepared had $\lambda_T = 511$ nm and $\lambda_L = 802$ nm.

Chapter 5: Nanorods were prepared using 13.5 mg AgNO_3 and 1.1 ml seed solution. The nanorods prepared had $\lambda_T = 510$ nm and $\lambda_L = 815$ nm.

Chapter 6: Nanorods were prepared using 13.2 mg AgNO_3 and 1.15 ml seed solution. The nanorods prepared had $\lambda_T = 511$ nm and $\lambda_L = 786$ nm.

2.2 Preparation of Nanorod-Dye Conjugates.

1 M dye stock solutions were first freshly prepared in MeOH, and further diluted in Millipore water immediately prior to addition of the desired volume of dye to 6 ml of stock NR solution to give a bulk dye concentration of 0.5, 1, 5, 10, 20 or 50 μM . Samples were left to equilibrate overnight at 27 °C. Next, PSS coating was carried out, 1.2 ml of 10 mg/ml PSS in 5 mM NaCl was added dropwise to the rapidly stirring NR-dye solution, and stirring continued for a few minutes. The samples were then centrifuged at 8,500 rpm for 20 mins and resuspended in 6 ml water, this was repeated a further three times to remove bulk dye. Additional characterisation of the particle concentrations and aggregation state of the NR-

dye conjugate concentrations was performed using a NanoSight LM20 and accompanying NTA software as well as UV-vis and SEM.

2.3 Preparation of Citrate Capped Spherical Gold Nanoparticles.

Gold nanoparticles were prepared by a variation of the Turkevich method.¹¹⁰ 100 mg of HAuCl_4 was added to 500 ml water, heated to boiling and then reduced using 105.7 mg of sodium citrate tribasic dihydrate to afford colloidal gold with a diameter of 38 nm.

2.4 Preparation of Citrate Capped Spherical Gold-DTTCI

A 1 M stock solution of DTTCI was prepared in MeOH, and further diluted in Millipore water immediately prior to addition of the desired volume of dye to 6 ml of stock citrate-capped gold to give bulk dye concentrations of 0.05 or 2 μM . Samples were left to equilibrate overnight at 27 °C.

2.5 Aggregation of Citrate Capped Spherical Gold-DTTCI

Aggregation of the spherical gold-DTTCI conjugates was carried out using MgSO_4 , which was gradually added while carefully monitoring the Raman response from the conjugates to produce the largest possible signal intensities.

2.6 Controlled Aggregation of Nanorods

Variation by Volume of Citrate Added: Various volumes, ranging from 220 μl to 300 μl of sodium citrate tribasic dihydrate (1.75 mM) were added to 2 ml of stock nanorod solution. UV-vis measurements were recorded 1 min and 60 min after addition.

Time-Dependence Measurements: 300 μl of sodium citrate tribasic dihydrate (1.75 mM) was added to 2ml of stock nanorod solution, and monitored by UV-vis over a period of 24 h.

2.7 Preparation of Nanorod Clusters for SERRS Analysis

This section describes the preparation of four samples used in Chapter 4, which were characterised by UV-vis, SEM, and Zeta potential measurements, prior to SERRS analysis. The preparation of these samples utilises all of the steps previously outlined, i.e. the dye loading and clustering of the nanorods. The samples are also stabilised using a polyelectrolyte coating, which has a number of roles, including the prevention of any further aggregation.

Four samples were prepared using the nanorod stock solution with $\lambda_L = 802$ nm

- A) **Stock Nanorods** 6 mL of nanorod stock solution in 1 mM CTAB (i.e. not containing DTTCl) were PSS coated as described below.

- B) **Unaggregated Nanorods-DTTCl** A nanorod-DTTCl solution was prepared as described above, briefly, 660 μ l of 10 μ M DTTCl was added to 6 ml of stock nanorod solution in 1 mM CTAB. This was allowed to equilibrate overnight prior to PSS coating. PSS (1.2 ml, 10 mg/ml 5 mM NaCl) was added dropwise to the rapidly stirring nanorod-DTTCl mixture. Stirring was continued for 15 min, after this time the sample was centrifuged at 6500 rpm for 15 min and resuspended in 6 ml Millipore water.

- C) **Low Aggregation** Low aggregation (i.e. a UV absorbance blue shift of the longitudinal band by 10 nm) was achieved by firstly preparing a nanorod-DTTCl solution as described previously. This solution was allowed to equilibrate overnight before controlled aggregation was carried out. Aggregation was achieved by addition of 540 μ l of 1.75 mM sodium citrate solution to the nanorod-DTTCl solution. After 30 mins, a 10 nm shift had been achieved (verified by UV-vis measurement) and the sample was PSS coated as described above, although unlike for other samples, the aggregated solution was not stirred upon addition of PSS, and instead gently swirled for 10 min to prevent further aggregation due to stirring.

(D) **Higher Aggregation** A higher level of aggregation (i.e. a UV absorbance blue shift of the longitudinal band by 54 nm) was achieved by firstly preparing a nanorod-DTTCI solution by addition of 660 μ l of 10 μ M DTTCI to a 6 ml solution of 1 mM CTAB stock nanorods. This solution was allowed to equilibrate overnight before controlled aggregation was carried out. Aggregation was achieved by addition of 660 μ l of 1.75 mM sodium citrate solution to the nanorod-DTTCI solution. After 1h, a 54 nm shift had been achieved (verified by UV-vis measurement) and the sample was PSS coated as described previously.

2.8 Preparation of Universal SERRS Tags (USTs)

Universal SERRS tags were prepared as follows, 1 M dye stock solutions were prepared in MeOH, and further diluted in MilliPore water immediately prior to use. 4 ml of DCI and IR1048 were premixed prior to addition to 40 ml of NR solution. 4 ml of DTDCI was introduced either along with DCI and IR1048 (i.e. 0 h delay) or following 1 or 14 h equilibration of these dyes with the NRs (1 or 14 h delay). Following the addition of DTDCI, the samples were allowed to equilibrate for a further 14 h. After this time, the samples were PSS wrapped as before (Section 2.2), one key difference is that following polymer wrapping, the samples were centrifuged and resuspended in 25 ml distilled water five times to ensure the removal of any excess dyes from the solution.

2.9 Cell Preparation

Dendritic cells were obtained from BALB/c mice as previously described.¹¹¹ The cells were counted using a haemocytometer and diluted to obtain a 5×10^4 cells/ml concentration. The cell suspension was then replated into five 35 mm Grid-50 μ -dishes (ibidi, Germany) (0.4ml/dish). Lipopolysaccharide (LPS, from Salmonella) [Sigma-Aldrich, UK] was added at 1 μ g/ml to induce dendritic cell activation and cells were left to incubate overnight at 37°C. The nanoparticle test solutions were then added to the cell dishes according to Table 1 at the approximate final concentration of 100 pM in the cell suspension and the dishes incubated for two hours at 37°C.

Sample no.	Solution added
1	-
2	NR
3	USTs

After two hours, the medium was gently removed from the cell dishes and 400µl of paraformaldehyde 4% fixation buffer [Sigma-Aldrich, UK] was added to each dish and left overnight to fix the cells. Cells were then washed with 0.5x HBSS buffer [Life Technologies, UK] and air-dried before mapping.

2.9.1 Cytometry Studies

Dendritic cells were prepared as described in Section 2.9. The cells were incubated with either i) nothing, ii) 50 pM USTs iii) 100 pM USTs or iv) camptothecin (Camptothecin is an apoptosis inducer, and was added to the cells at 0.5 µl of 10 mM stock per 1 ml of cell suspension). All samples were prepared in duplicate. Samples were then left to incubate for 24 h at 37 °C and 5% CO₂. Cells were then harvested from plates and stained with Annexin-FITC and Propidium Iodide kit (eBioscience, UK) according to the manufacturer's instructions. Samples were analysed using BD FACSCanto™ flow cytometry equipment and BD FACSDiva™ software.

2.10 Preparation of Alternative UST Combination

A second batch of USTs were prepared using an alternative dye combination, this was 10 µM DCI, 10 µM MGITC and 10 µM NIR-797. The nanorods used here had $\lambda_L = 770$ nm. The sample was prepared as described in Section 2.8, with, all three dyes premixed and added simultaneously prior to equilibration for 14 h. The samples were then PSS wrapped as before.

2.11 Multilayer Polymer wrapping of PSS NRs.

A range of polymers were investigated in the design of multilayer wrapping for nanorods, including PSS, PDDAC, PAH, PGlu, PLI and PAA. Different combinations of multilayer polymer wrappings were found to be successful, and were used over the course of the project, including PAH-PAA and PDDAC.

For PAH-PAA wrapping, this was carried out as follows: 160 mg of PAH was dissolved in 16 ml of 5 mM NaCl. The solution was added dropwise to 80 ml of rapidly stirring PSS-wrapped NRs (containing dye). The mixture was stirred for a further 15 minutes, and the sample was centrifuged at 7,500 rpm for 40 minutes and then resuspended in 40 ml H₂O.

Following this, 61 µl of PAA was dissolved in 8 ml of 0.1 M NaCl, and added dropwise to the PAH wrapped NRs. The mixture was stirred for 15 minutes, and centrifuged at 6,750 rpm for 30 minutes. The sample was resuspended in 40 ml H₂O.

For PDDAC wrapped samples, 30 µl PDDAC was dissolved in 970 µl 5 mM NaCl. This solution was added dropwise to 5 ml of rapidly stirring PSS-wrapped NRs. The mixture was stirred for 15 minutes, and then centrifuged at 7,500 rpm for 12 minutes, and resuspended in 5 ml H₂O.

2.12 DNA Sequences Used Throughout Chapter 6

Name	Abbreviated name	Sequence
Probe1-5'C12-amine	P1	5'-NH ₂ -(CH ₂) ₁₂ -GTG TTA GCC TCA AGT G-3'
Probe2-amine-3'C6	P2	5'-GTC TAT GCG TGA ACT G- (CH ₂) ₆ -NH ₂ -3'
Comp1and2:	C1and2	5'-CAG TTC ACG CAT AGA CCA CTT GAG GCT AAC AC-3'
Control-T32	Control	5'-TTT TTT TTT TTT TTT TTT TT- 3'
Comp-Probe1-3'T15-amine	C1	5'- CAC TTG AGG CTA ACA C - T ₁₅ - NH ₂ -3'
Probe1-5'C12-amine-3'Cy5	P1-Cy5	5'-NH ₂ -(CH ₂) ₁₂ -GTG TTA GCCTCA AGT GT - Cy5 -3'
Probe1-5'C12-amine-3'FAM	P1-FAM	5'- NH ₂ -(CH ₂) ₁₂ -GTG TTA GCCTCA AGT GT – (6-FAM)-3'
Comp-Probe1-5'FAM	C1-FAM	5'- (6-FAM) - CAC TTG AGG CTA ACA C - 3'
Probe2-amine-3'C6-5'Cy5	P2-Cy5	5' - Cy5 - GTC TAT GCG TGA ACT G -(CH ₂) ₆ -NH ₂ -3'

All DNA was purchased from IDT and were HPLC purified prior to shipment. On arrival, the DNA was resuspended in TE buffer to give a 100 μM stock solution.

2.13 DMTMM Synthesis.

DMTMM was prepared as previously described by Kunishima *et al.*¹¹² Briefly, 2-chloro-4, 6-dimethoxy-1,3,5-triazine (CDMT) (0.386g, 2.2 mM) was dissolved in THF. N-methylmorpholine (NMM) (0.202g, 220 μ l, 2.0 mM) was dissolved in THF and added. The reaction mixture was stirred for 30 minutes at room temperature. The white solid formed was collected by filtration and washed with THF and air dried.

2.14 Conjugation of DNA to PAA wrapped NRs.

100 μ l 1.5 M NaCl was added to 1 ml PAA wrapped NRs, along with 100 μ l 10x PBS (pH 7.5). To this, 10 μ l of 25 μ M DNA was added, and the mixture was shaken for 15 minutes. 10 μ l of DMTMM (13.0 nM) was added, and the mixture was shaken overnight. Excess DNA was removed by centrifuging the samples twice at 7,000 rpm for 10 minutes and resuspending in 1 ml 1x PBS (pH 7.5).

2.15 Preparation of Poly(allylamine hydrochloride) (PAH) Stabilized Quasi-Spherical Gold Nanoparticles.

76.6 mg of HAuCl₄ was added to 380 ml water, along with 36.4 mg PAH dissolved and sonicated in 20 ml H₂O. The mixture was heated to 98 °C for 10-15 minutes until the colour changes to deep red.

2.16 Polymer Wrapping of PAH Au nanoparticles.

300 mg of PSS was dissolved in 30 ml 5 mM NaCl and added dropwise to 150 ml of PAH stabilized Au nanoparticles under rapid stirring. The mixture was stirred for a further 15 mins. Excess polymer was removed by centrifugation at 4,250 rpm for 1 hour, and the sample was resuspended in 150 ml H₂O.

300 mg of PAH was dissolved in 30 ml 5 mM NaCl. The PAH was added dropwise to the PSS wrapped nanoparticles with rapid stirring. The sample was stirred for a further 15 minutes, and excess polymer removed by centrifugation at 4,100 rpm for 1 hour and resuspended in 150 ml H₂O.

The PAH wrapped nanoparticles were coated with PAA by dropwise addition of a solution of PAA (226 μl in 30 ml 50 mM NaCl) to the rapidly stirring nanoparticle solution. The sample was centrifuged at 3,800 rpm for 1 hour, and resuspended in 125 ml H_2O .

2.17 Conjugation of DNA to PAA Functionalized PAH Au.

100 μl of 0.15 M NaCl was added to 1 ml PAA functionalized PAH Au, along with 100 μl 10x PBS (pH 7.5). To this, 10 μl of 25 μM DNA was added, and the mixture was shaken for 15 minutes. To this, 50 μl of DMTMM (13.0 nM) was added, and the mixture was shaken overnight. Excess DNA was removed by centrifuging the samples twice at 3,300 rpm for 10 minutes and resuspending in 1 ml of 1x PBS (pH 7.5).

2.18 Bioactivity of DNA Only in Solution

The bioactivity of the DNA in solution was confirmed by carrying out melting curve analysis. Probe 1 and Probe 2 (1 nM) were hybridised to target DNA (0.1 μM) in 0.3 M PBS.

UV-visible melting experiments were carried out using a Varian Cary Bio 300 spectrometer, and recorded at 260 nm. The temperature was programmed to a heat/cool rate of 1 $^{\circ}\text{C}$ per minute.

General Conditions:

2.19 Raman Analysis

Cyclohexane was used to optimise the signal collection as well as to provide an intensity reference for data normalization.

- For data in Chapters 3 and 4, normalization was carried out with respect to the 802 cm^{-1} cyclohexane peak ($\pm 2 \text{ cm}^{-1}$).
- For data in Chapter 5, this was carried out with respect to the 1029 cm^{-1} cyclohexane peak ($\pm 2 \text{ cm}^{-1}$).

All spectra were processed and background corrected using Grams/AI software (version 7.0)

514 nm

Measurements were performed using a Renishaw *InVia* Raman inverted microscope system, equipped with 20 x long working distance objective. The laser excitation source is an Ar⁺ laser with 514.5 nm excitation, with a power of 5 mW used for analysis. The laser was set to line focus, and utilised an 1800 gr/mm grating. Samples were analysed using disposable microcuvettes, with a sample volume of 500 µl used for analysis. A signal collection time of 10 s per spectra was used.

532 nm

Measurements were performed using a Renishaw Probe system, equipped with a 50 x long working distance objective, with 532 nm excitation. The laser power used for excitation was 35 mW. Samples were analysed using disposable microcuvettes, with a sample volume of 500 µl used for analysis. A signal collection time of 10 s per spectra was used.

633 and 785 nm

Measurements were performed using a Renishaw *InVia* Raman inverted microscope system, equipped with a 20x long working distance objective. Two excitation sources were used at 632.8 nm and 785 nm along with an 1800 or 1200 gr/mm grating respectively. The typical laser power at 633 nm was 1.0 mW while for 785 nm laser powers of 12.0 mW and 1.2 mW were used depending on the nanotag signal intensity obtained. Samples were analysed through transparent bottom micro-titre plates with 300 µl of the nanorod conjugate solution placed in each well. A signal collection time of 10 s per spectra was used. For experiments involving the controlled aggregation of quasi-spherical nanoparticles 1 µl of 1M MgSO₄ was added to 500 µl of colloid followed by mixing

1064 nm

Analysis was carried out using a Real Time Analyzer FT-Raman spectrometer. The laser excitation source was an Nd:YAG laser, with 1064 nm excitation, a laser power of 220 mW was used for analysis. Samples were analysed in glass vials, with a sample volume of 100 μ l used for analysis. A sulphur standard was run to confirm the correct functionality of the laser.

A signal collection time of 10 s per spectra was used.

2.20 Raman Mapping of Individual USTs

Correlated Raman and SEM mapping measurements were achieved on a conductive indium tin oxide (ITO) coated glass slide that had been cut to a \sim 7 mm length square. The slide was prepared by first washing with acetone and methanol in an ultrasound bath, N₂ drying followed by 3 mins in an oxygen plasma chamber to create a negatively charged surface. Next, the slide was coated with first PDDAC and then PSS polyelectrolyte layers. A metallic TEM finder reference grid (400 mesh, H7 Maxtaform) was then placed onto the ITO surface and immobilized with nail varnish at opposite edges. The USTs (with an outer wrapping of PDDAC) were then immobilized electrostatically on the ITO surface by covering a dilute solution (OD \sim 0.1) for a period of time (\sim 10 s to several minutes) to get different surface coverage densities. The slides were then rinsed with water and gently dried in N₂ to remove excess solution.

Raman mapping was carried out using a confocal WITec Alpha300 R instrument with 532, 633 and 785nm excitation lasers available. All maps were acquired using a 100x objective (Olympus MPlan, NA = 0.9) resulting in a theoretical spatial resolution ranging from approximately 360 to 530 nm depending on the laser used. For the correlated SEM and Raman mapping of individual particles a step-size of 250 nm was used and other parameters such as integration time are stated in the data descriptions. As well as selecting a specific square (\sim 80 microns in size) within the reference grid, to further aid in collocating the SEM and Raman measurements, areas up to \sim 20 x 20 μ m in size were selected for optical mapping close to defects in the ITO layer caused during the layer deposition. WITec project 2.10 software was used for further data processing.

Following SERS mapping, SEM measurements (FEI Quanta 250) were performed operating in low vacuum mode to minimize charging interference. Multiple images of an optically scanned area were acquired at high resolution and subsequently stitched together using an Image J plugin.¹¹³ This allowed accurate comparison of optical and electron microscope areas, several microns in size.

2.21 Raman Mapping of USTs in Cells

Cells were prepared and immobilised onto glass etched 50 μm reference grids (Ibdi) as described in Section 2.9.

Raman mapping was carried out using a confocal WITec Alpha300 R instrument with 532, 633 and 785nm excitation lasers available. All maps were acquired using a 100x objective (Olympus MPlan, NA = 0.9). The step size used for analysis was 0.5 μm . WiTec project 2.10 software was used for further data processing. The conditions for each wavelength are described below:

532 nm laser power 0.57 mW 0.5 s integration time

633 nm laser power 0.54 mW 0.5 s integration time

785 nm laser power 0.67 mW 0.5 s integration time

2.22 Confocal Fluorescence Mapping

For confocal fluorescence mapping, coverslips were mounted onto the cell samples using VectaShield® mounting medium with DAPI [Vector Labs, UK]. Samples were mapped using the Leica SP5 confocal microscope.

2.23 Fluorescence Measurements

Characterisation of individual dyes and also of the formation of dye-CTAB bilayers was performed using a Varian Cary Eclipse Fluorescence Spectrophotometer. The instrument was switched on and allowed a few minutes to warm up prior to use, and the emission and

excitation slits were set to 5 nm. A fresh disposable cuvette was used for each measurement.

For analysis of samples containing DTDCI, fluorescence measurements were carried out at 615 nm excitation, and scanned from 620 to 800 nm, with a detection voltage of 650 V.

For analysis of samples containing DTTCl, fluorescence measurements were carried out at 750 nm excitation, and scanned from 760 to 860 nm, with a detection voltage of 680 V.

2.24 Scanning Electron Microscopy (SEM)

SEM images of all samples, with the exception of the USTs in Chapter 5, were obtained using an FEI Sirion 20 ultra-high resolution Schottky field emission scanning electron microscope with FEI software. Si wafer substrates (5 x 5 mm; Ted Pella Inc.) were first rinsed sequentially with methanol and distilled water and dried in a stream of N₂. Next, the Si wafers were treated in an O₂ plasma cleaner for approximately 60 s and then immediately covered with a ~ 10 mg/ml solution of poly(diallyldimethylammonium chloride) in 1 mM NaCl for 30 mins to create a positively charged surface. Each wafer was washed with distilled water and dried under a stream of N₂ before 20-30 µl of nanorod sample was dropped onto the wafer and stored in a humidity chamber for a further 30 mins to prevent the droplet drying, before removing the sample solution, water rinsing and N₂ drying. The deposition methodology was designed to ensure that the sample distribution was representative of the bulk solution rather than distorted by drying-induced aggregation.

2.25 Zeta Potential

Zeta potential measurements were carried out on a Malvern Zetasizer 2000 using Zetasizer 2000 advances software. All settings remained at the instrument default. The machine was allowed a few minutes to equilibrate following being turned on, and was rinsed through with Millipore water. Approximately 3 ml of standard was injected, and measured to check the reliability of the instrument. If satisfactory, 3 ml of sample was injected and the zeta

potential measured. Following each measurement, the instrument was purged with 5 mL of Millipore water and 10 ml of air.

2.26 Extinction Measurements

These were taken on one of two instruments depending on the wavelength range required, the first was a Varian Cary 3000 Bio UV-Visible spectrophotometer with Win UV scan application version 2.00 software. Before spectral acquisition, the lamp was left on for a period of at least 10 mins to allow warm-up and equilibration. The range of wavelengths scanned was 200-900 nm.

The second instrument used was a Thermo Spectronic Unicam UV300 spectrophotometer with Vision 32 software. The wavelength range scanned using this instrument was 400-1100 nm. As before, the lamp was left on for a period of 10 min prior to use.

All samples were analysed using disposable plastic microcuvettes.

Chapter 3

Preparation and Characterization of Monodisperse Stable Nanorod-Dye Conjugates with Controlled Resonance Coupling

Understanding and controlling the interaction between the localized surface plasmon resonance (LSPR) of gold and silver nanoparticles and light-absorbing molecular dyes is a rapidly emerging research area.¹¹⁴ Hybridization between plasmonic and molecular resonances can give rise to a variety of distinct optical properties which depend on the surface density and assembly behaviour of the dye adsorbed on the nanoparticle surface, the relative spectral overlap of both constituents as well as the distance between the dye layer and nanoparticle surface. A number of experimental¹¹⁵⁻¹²⁴ and theoretical¹²⁵⁻¹²⁷ investigations have been reported recently characterising hybrid dye/metal nanoparticle structures. Of particular interest is the development of nanoparticle-enhanced spectroscopies including surface-enhanced Raman spectroscopy (SERS),¹²⁸ resonance energy transfer,¹²⁹ plasmon-enhanced fluorescence¹³⁰ and fluorescence quenching.¹³¹

Surface-enhanced resonance Raman scattering SE(R)RS or SERRS, is a process that can occur when the laser excitation wavelength, the nanoparticle localized SPR and the dielectric constant of the molecular chromophore in contact with the nanoparticle surface all spectrally overlap to some extent.^{132, 133} The relative importance of the multiplicative contributions to the overall SERRS signal from both the local electromagnetic field associated with LSPR and the molecular resonance Raman enhancement is an issue that continues to be debated in the literature. In addition, further enhancement of the Raman signal from colloidal suspensions of gold and silver nanoparticles is typically achieved via nanoparticle aggregation. The formation of hot-spots within small clusters of gold quasi-spherical nanoparticles has enabled single molecule SERRS measurements to be demonstrated.¹³⁴ However, aggregation also makes profiling the LSPR contribution to the enhanced SERRS response much more complex, with parameters such as cluster size and stability, distribution in size, relative nanoparticle orientations and spacing within each

cluster, location of probe molecules and changes in particle concentration all important. Consequently, the design of stable colloidal suspensions of bright SERRS-active probes which can be potentially used across a wide range of sensing and imaging applications has continued to be an area of intense research.¹³⁵

A significant advantage of gold nanorods is the ability to selectively tune the LSPR excitation across most of the visible and near-infrared (NIR) regions of the electromagnetic spectrum.²⁶ In contrast, monodispersed gold quasi-spherical particles are limited to resonance wavelengths of ~510-600 nm and aggregation is necessary to achieve significant SERS enhancements at common laser excitation wavelengths such as 633 and 785 nm. Furthermore, the nanorod-dye conjugate system also enables resonance coupling between the rod LSPR and dye to be explored over a range of wavelengths and a small number of studies have recently been reported by Wang *et al*¹²²⁻¹²⁴ and others^{121, 136, 137} using extinction and fluorescence spectroscopy measurements.

However, even fewer investigations of the SERRS properties of gold nanorod-dye systems have been reported to date. Recently, von Maltzahn *et al*⁹⁶ compared a series of NIR dyes via the formation of mixed polyethylene glycol-dye monolayers on the nanorod surface to establish the brightest probe candidate for SERRS imaging in cells at 785 nm. Pal *et al*¹³⁸ performed SERRS measurements at 633 nm on rod aggregates prepared by drop-casting on a glass surface while Cai *et al* have modelled the Raman spectrum of 3,3'-diethylthiatricarbocyanine iodide (DTTCI) enhanced by nanorod films.¹³⁹ Gabudean *et al* have recently demonstrated the dual use of metal-enhanced fluorescence and SERS on nanorods.¹⁴⁰

As discussed in Chapter 1, there are a number of advantages to working with nanorods over their quasi-spherical counterparts. In this Chapter, the novel preparation of nanorod-dye conjugates will be explored. The ability to tune the LSPR of gold nanorods will be exploited, and along with the molecular resonance of the dye, will be adjusted with respect to two common Raman laser excitation wavelengths. A systematic study of different rod and dye combinations will be carried out.

3.1 Scaled up nanorod preparation

The typical seed-mediated nanorod synthesis described in the literature is for a total reaction volume of approximately 10 ml.^{28, 141, 142} In order to gain increased control over the final aspect ratios obtained, and to avoid the complications associated with batch-to-batch variations, it was essential to scale up the synthesis to approximately a 1 L total reaction volume, which yields approximately 400 ml of nanorods of desired concentration (~ 1 nM). Nanorods have successfully been prepared with varying aspect ratios as described in Section 2.1, a small selection are shown in Figure 3.1.

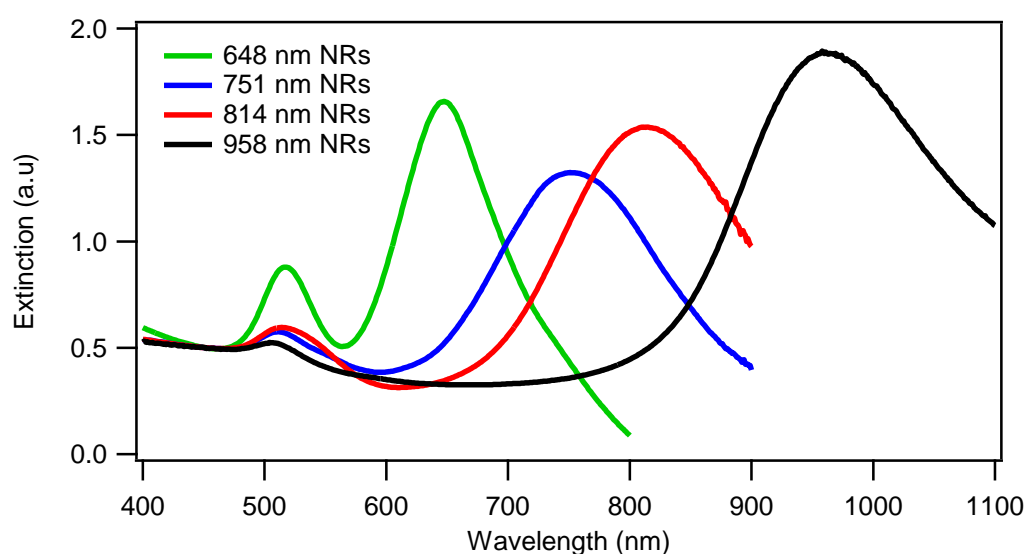


Figure 3.1. Extinction spectra of various scaled up nanorod preps with λ_L ranging from 648-958 nm.

Control of the final aspect ratio was obtained by varying both the concentration of silver nitrate and the volume of seed solution added to the growth solution. It is known that by increasing the volume of seed solution added, the length on the nanorods is decreased,²⁸ and a reduction in the amount of silver nitrate leads to a decrease in the length of the nanorods obtained.²⁵ This synthesis method produces nanorods with λ_T typically 510 - 515 nm and λ_L 620-900 nm.

3.2 Design and Preparation of Nanorod-dye Probes

With the aim of performing a systematic study of the SERRS properties of different gold nanorod (NR)-dye conjugates, NRs and dyes were selected which had resonances closely matching one of two common Raman excitation wavelengths (633 and 785 nm) these were then selectively combined to create a range of NR-dye conjugates. An outline of the strategy used for the preparation of stable and SERRS-active NR-dye conjugates is shown in Figure 3.2.

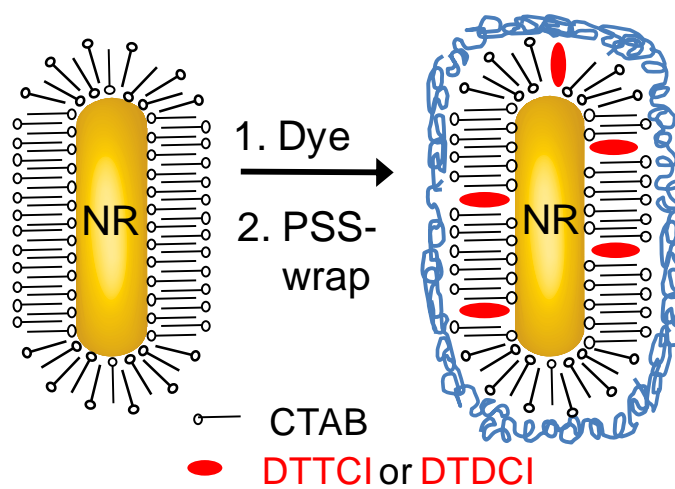


Figure 3.2. Schematic describing the simple two-step preparation of NR-dye conjugates. A mixed CTAB-dye layer is first formed, before stabilizing with a PSS polyelectrolyte wrapping.

During NR synthesis, the surfactant hexadecyltrimethylammonium bromide (CTAB) is used to maintain colloidal stability and as a shape directing agent to encourage the growth of rods. However, the presence of the CTAB bilayer also complicates subsequent surface functionalization, which has previously hindered the use of NRs for SERS-based applications. A further problem is that CTAB has a fairly weak affinity for the gold <110> longitudinal face, and a net desorption from the rod surface starts to occur when the bulk concentration of surfactant is lowered below ~ 0.5 mM, resulting in colloidal instability when the samples are cleaned following synthesis. Control of the CTAB concentration is achieved by performing a minimum of four repeat centrifuge and resuspension washing steps following NR synthesis, to give a fixed concentration of 1 mM.

The first step in Figure 3.2 depicts the addition of a reporter dye, either 3,3'-diethylthiatricarbocyanine iodide (DTTCI) or 3,3'-diethylthiadicarbocyanine iodide (DTDCI), to form a mixed layer of CTAB and dye.

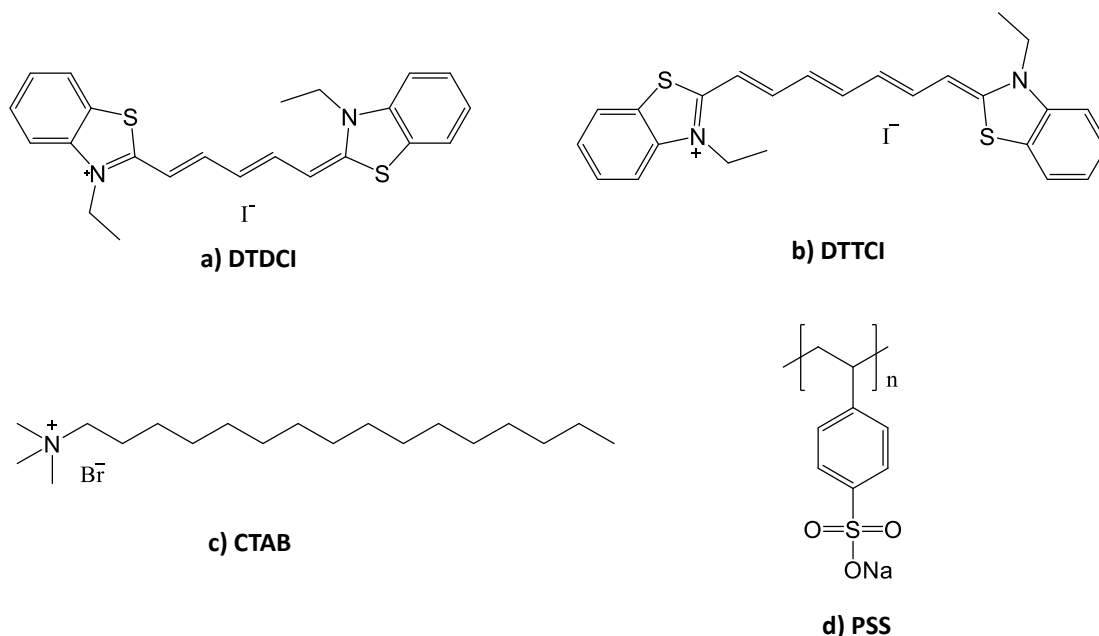


Figure 3.3. The chemical structures of (a) DTDCI dye and (b) DTTCI dye, (c) CTAB surfactant and (d) PSS.

The structures of DTDCI and DTTCI are shown in Figure 3.3(a) and (b), both dyes are structurally very similar, differing only in the length of the polymethine chain. In addition, both dyes are hydrophobic and both contain a quaternary ammonium. Figure 3.3(c) shows the structure of CTAB, which also contains a quaternary ammonium. The hydrophobicity of the dyes allows them to effectively compete with CTAB to form the mixed dye-surfactant layers discussed previously.

Rather than replacing the CTAB, it has been shown by one previous group¹⁴³ that it is possible to sequester hydrophobic molecules into the CTAB bilayer with high efficiencies. A further advantage of this approach is that by maintaining the CTAB bilayer, the orientation of the dye molecule with respect to the nanoparticle surface is controlled, even at very low dye fractional surface coverages.

The dyes DTDCI and DTTCI were chosen as Raman reporter molecules due to the fact that they are both strongly absorbing (λ_{\max} = 646 nm and 754 nm respectively) close to the 633 and 785 nm laser excitation wavelengths, as shown in Figure 3.5(a)

The second step in preparing NR-dye conjugates involves wrapping the positively charged assembly with a layer of negatively charged polyelectrolyte poly-(sodium 4-styrenesulfonate) (PSS) (structure shown in Figure 3.3(d). The polymer wrapping has a number of roles: it encapsulates the conjugate and enables the subsequent removal of any excess dye and CTAB from the bulk solution. It also stabilizes the conjugate, resulting in reproducible SERRS signals when comparing repeat preparations as well as after several months' storage. Furthermore, the polyelectrolyte coating can also act as a starting platform for further surface functionalization.¹⁴⁴

Different combinations of NRs and dyes were prepared as summarised in Figure 3.4 to observe and quantify the effect of altering the NR plasmon resonance and the dye molecular resonance.





	λ_{\max} 618 nm		λ_{\max} 770 nm
DTDCI	646 nm	DTDCI	646 nm
<hr/>			
	618 nm		770 nm
DTTCI	754 nm	DTTCI	754 nm

Figure 3.4. Schematic overview of the various NR-dye combinations prepared.

The extinction spectra for the NR and dye stock solutions are shown in Figure 3.5(a) and (b) respectively.

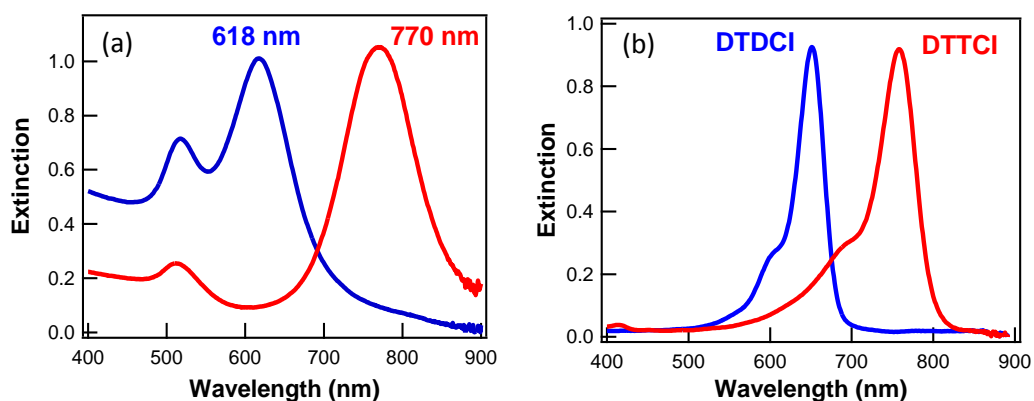


Figure 3.5. Extinction spectra of (a) nanorod stock solutions used and (b) 5 μM DTDCI and DTTCI in MeOH.

The first NR stock solution featured transverse and longitudinal plasmon peaks at 516 nm and 618 nm respectively, along with an average rod length of 32 nm and an aspect ratio of 2.6. The second NR sample had transverse and longitudinal peaks at 511 nm and 770 nm respectively, and an average length of 47 nm and an aspect ratio of 4.3. These nanorod stock solutions were chosen as they provide good overlap with the laser excitations of the Raman instruments used (633 and 785 nm). The particle concentration of both stock solutions was fixed at approximately 1 nM, based on extinction coefficients at the λ_L of the longitudinal surface plasmon resonance (LSPR) of 2.5×10^9 and $4.6 \times 10^9 \text{ M}^{-1}\text{cm}^{-1}$ respectively.¹⁴⁵

3.3. Sequestration of Dyes into CTAB Bilayer

The formation of a mixed CTAB-dye layer is further supported by the experimental observation that the dye absorbance spectrum displays increased stability in 1 mM CTAB solution, compared to water only where the dye molecules form aggregates.

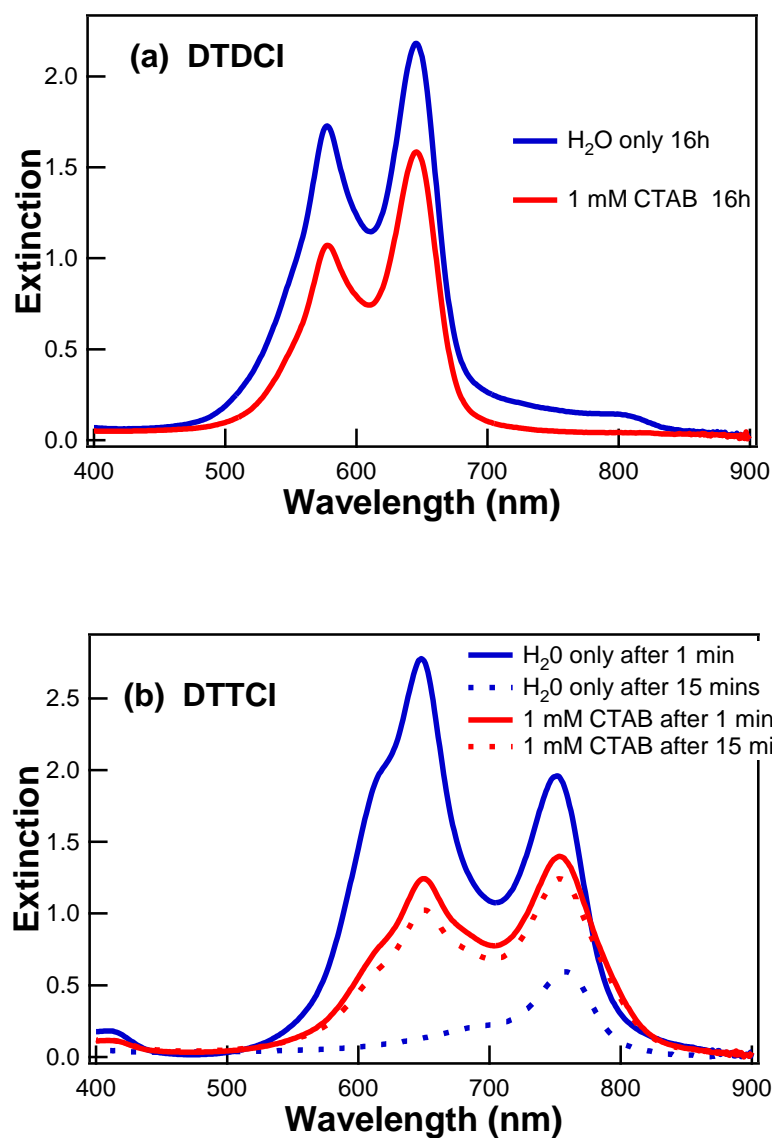


Figure 3.6. UV-vis spectroscopy measurements of 2 μ M (a) DTDCI and (b) DTTCl dye solutions prepared in both water only and 1 mM CTAB solution.

In particular for DTTCl, there is a significant difference in the dye spectral properties as a function of time comparing samples prepared in the presence of CTAB, which display increased stability, with those prepared in water, which have a greater tendency to form dye aggregates.

Adsorption of the dye into the CTAB bilayer was further confirmed using fluorescence spectroscopy, and is demonstrated by a quenching of the fluorescence signal

as the dye molecule comes into contact with the metal surface of the nanoparticle. The data obtained is shown in Figure 3.7:

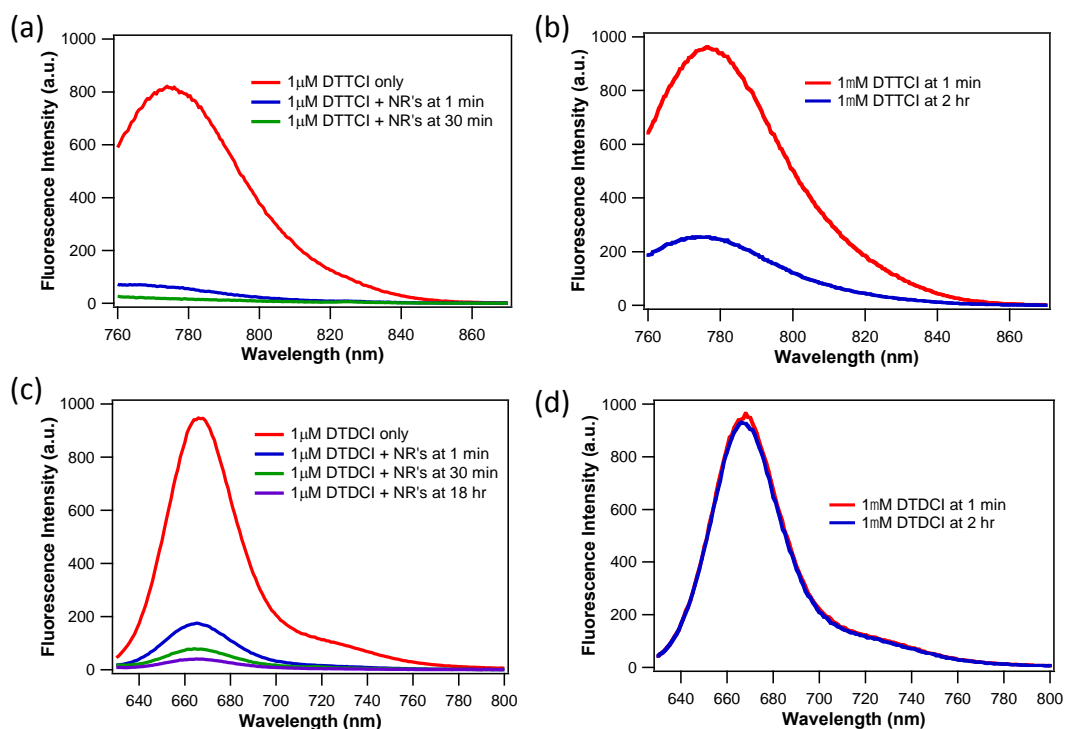


Figure 3.7. Fluorescence spectra obtained for a) a 1 μM DTTCI solution and a second solution containing 1 μM DTTCI and 1 nM gold nanorods ($\lambda_L = 770$ nm). Measurements are taken 1 min and 30 mins after mixing. b) An identical 1 μM DTTCI solution in 1 mM CTAB, with measurements taken at 1 min and 2 hours. For a) and b), the excitation wavelength used was fixed at 750 nm. c) a 1 μM DTDCI solution and a second solution containing 1 nM nanorods ($\lambda_L = 770$ nm). The sample was monitored at 1 min, 30 min and 18 hours following preparation. d) 1 μM DTDCI only in 1 mM CTAB. For c) and d), the excitation wavelength was fixed at 615 nm.

Figure 3.7(a) shows the fluorescence spectra obtained for a 1 μM solution of DTTCI, and for a second solution containing 1 μM DTTCI in the presence of 1 nM gold NR solution ($\lambda_L = 770$ nm). The measurement was taken one minute after addition of the dye to the NR solution, and 30 minutes after addition. It can be seen that there is a dramatic loss in signal very quickly, with a quenching of approximately 80% within the first minute. Figure 3.7(b) shows an identical concentration of DTTCI, this time in the presence of 1 mM CTAB, with no nanoparticles present, under these conditions there is a much slower quenching of the

fluorescence signal. The excitation wavelengths for samples containing DTTCI was fixed at 750 nm.

Figures 3.7 (c) and (d) show the same experiment repeated with DTDCI, the same NR stock solution is used to obtain the spectra shown in Figures 3.7(a) and (c). The fluorescence is this time quenched more slowly, and repeat measurements were taken at 1 minute, 30 minutes and 18 hours after addition of the dye to the NR solution. Figure 3.7(d) shows very little change in signal is observed after 2 hours.

The difference between the adsorption behaviour of the two dyes is attributed to DTDCI being more hydrophilic than DTTCI. Differences in the dye aggregation behaviour will also occur as a result of differing solubilities in water. While the fluorescence intensity of both dyes demonstrated significant quenching within minutes of the addition of the dye to the NR solutions, when preparing conjugates for SERRS or UV-vis measurements, each sample was left overnight to reach a steady state surface coverage prior to PSS coating.

3.4. SEM Analysis of Conjugates

A key concern throughout the preparation of the NR-dye conjugates was to ensure that no significant level of particle aggregation occurred following the addition of dyes and during the polymer wrapping stage. This was an important consideration, as even a very small fraction of aggregates in the bulk solution can potentially have a significant effect on the SERRS intensities measured, and can also cause a shift of the nanorod longitudinal surface plasmon resonance (LSPR). Furthermore, in order to quantitatively compare different conjugate solutions, the particle concentrations were kept constant throughout the preparation and analysis process. A number of complementary techniques were used to monitor the conjugate monodispersity and particle concentration, including the analysis of extinction spectra, the application of NanoSight video tracking analysis³³ and scanning electron microscopy (SEM), see Figure 3.8.

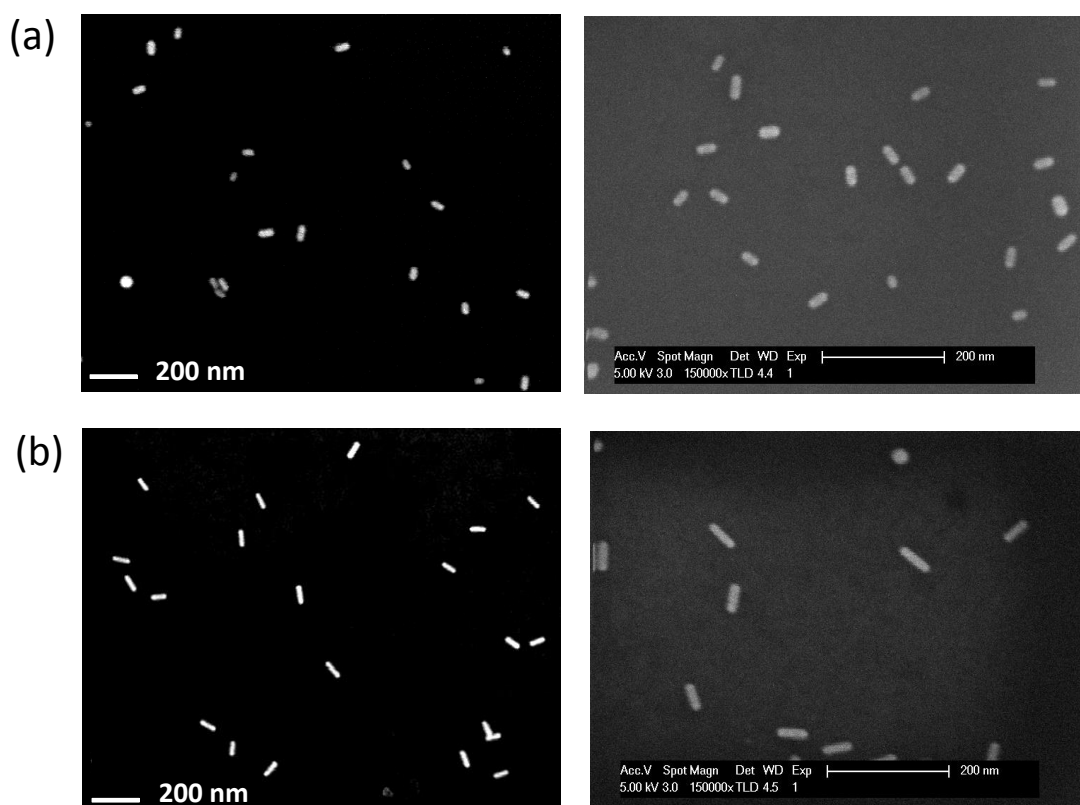


Figure 3.8. Representative SEM images of PSS wrapped nanorod-dye conjugates prepared using a) 618 nm λ_L nanorod and b) 770 nm λ_L nanorod stock solutions.

SEM images were used to calculate the average nanoparticle size and to confirm that adsorption of the dyes and subsequent PSS wrapping did not lead to significant aggregation.

3.5 Observation of Resonance Coupling

In order to investigate the coupling of the nanoparticle plasmon resonance with the dye molecular resonance, a series of nanorod-dye conjugates were prepared where both the NR and dye have closely overlapping resonances, or the NR and dye have different resonances (as shown previously in Figure 3.4). A fixed volume of each NR stock solution was used for each preparation, to which a range of bulk dye concentrations (0.5-50 μM) were added. The samples were left overnight to allow equilibration of the dye with the CTAB bilayer. The conjugates were then polymer wrapped, followed by centrifugation and

resuspension in water. The centrifugation step was repeated three times to ensure the complete removal of any excess bulk dye from the conjugate solutions. The conjugates were then characterized using UV-vis spectroscopy, as shown in Figure 3.9. The repeat centrifugation steps ensure that there is no contribution from any remaining free dye, which will be at least two orders of magnitude lower than the UV-vis detection limit of $\sim 0.5 \mu\text{M}$ for each dye. This means that any spectral shift observed is due to dye adsorbed onto the NR surface rather than free dye in solution.

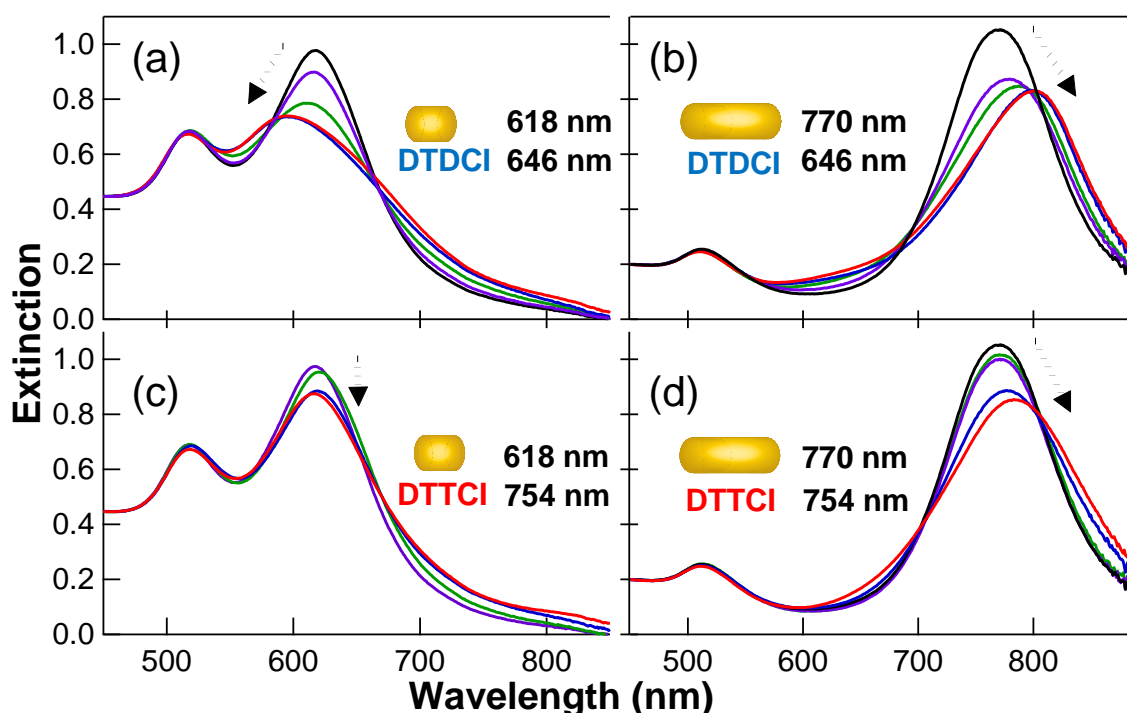


Figure 3.9. Extinction spectra of PSS-wrapped nanorod-dye conjugates prepared at a number of dye concentrations (0, 0.5, 1, 5 and 10 μM) and a fixed nanorod concentration. a) 618 nm NR with DTDCI; b) 770 nm NR with DTDCI; c) 618 nm NR with DTTCI; and d) 770 nm NR with DTTCI. (The arrow indicates the direction of longitudinal plasmon shift).

All four combinations of nanorods and dyes resulted in dampening and a spectral shift of the longitudinal plasmon peak, with both effects increasing with higher dye concentrations. Figure 3.9 shows that the relative positions of the dye and rod resonances are important, both the size and direction of the LSPR shift depends on the relative absorbance wavelengths of the dyes and the NRs. Figure 3.9(a) shows DTDCI adsorbed onto

NRs with $\lambda_L = 618$ nm, the longitudinal plasmon shows a blue shift of approximately 24 nm. However, when DTDCI is adsorbed onto a 770 nm NR, the plasmon shifts by ~ 32 nm, this time the direction of the shift is red. When DTTCl adsorbed onto the 618 nm NR sample, the longitudinal plasmon undergoes a small red shift of ~ 3 nm. When the same dye is adsorbed onto a 770 nm NR sample, the direction of shift remains the same, however, the longitudinal plasmon now shifts by ~ 20 nm for a 10 μ M bulk dye concentration. It can be seen that in all cases, the size of shift is dependent on the bulk dye concentration, with increased dye surface coverages leading to increased plasmon shift and dampening of the longitudinal surface plasmon of the NRs. In all cases, no significant change was observed in the transverse plasmon band.

The results show a blue shift when the nanorod LSPR is blue shifted with respect to the dye molecular absorbance, and a red shift when the nanorod LSPR is red shifted with respect to the dye, which is in agreement with previous findings by the Wang group.¹²²⁻¹²⁴ Several recent studies have reported the observation of Rabi splitting, which is where the SPR band develops into two bands. This effect seems to be associated with the interaction of dye molecule aggregates with the nanoparticle surface, and is strongest in systems where the dye molecular resonance and the nanorod SPR have the largest overlap, and also at larger dye fractional surface coverages.^{120, 123, 146} Only a hint of plasmon band splitting is observed in Figure 3.9, this is attributed to increased control over the dye assembly around the nanorod involving a relatively uniform dispersion of non-aggregated single dye molecules. Maintaining a stable CTAB bilayer around each rod limits the extent to which both the DTTCl and DTDCI dyes assemble into J-aggregates. In water, both dyes quickly self-assemble, while in 1 mM CTAB solution, the dye spectra are much more stable, as shown in Figure 3.6. It has also been reported in the literature that the strongest resonance coupling, determined by the size of plasmon shift, where a large shift correlates to strong plasmon coupling, will occur when the plasmon resonance of the nanoparticle is close to the molecular resonance of the dye.^{122, 147} This holds true for DTTCl, where the largest coupling is found when the dye is adsorbed onto a NR with LSPR at 770 nm. DTDCI, however, does not conform, with the largest coupling measured when the dye molecular resonance does not match the longitudinal SPR.

3.6 SERRS Characterization of Nanorod-Dye Conjugate Formation

The nanorod-dye combinations summarized in Figure 3.4 were prepared by exposing a fixed volume of nanorod stock solution to dyes, to give bulk dye concentrations ranging from 0.5-50 μM . The samples were polymer wrapped and centrifuged to remove excess dye as discussed previously (Section 3.5). The SERRS signals of each of these conjugates were then systematically acquired at both 633 and 785 nm excitation frequencies. A combination of extinction spectral monitoring, SEM and dynamic nanoparticle imaging and tracking measurements were performed for each of the samples to ensure that the nanorods were monodispersed with negligible levels of particle aggregation. Furthermore, in order to promote a direct comparison of spectral intensities acquired at different laser excitation wavelengths and laser intensities, the intensities of the SERRS spectra obtained were normalized with respect to a cyclohexane reference standard acquired under identical conditions to the sample measurement.

Although structurally very similar, the SERRS profiles of DTDCI and DTTCI are significantly different, as shown in Figure 3.10.

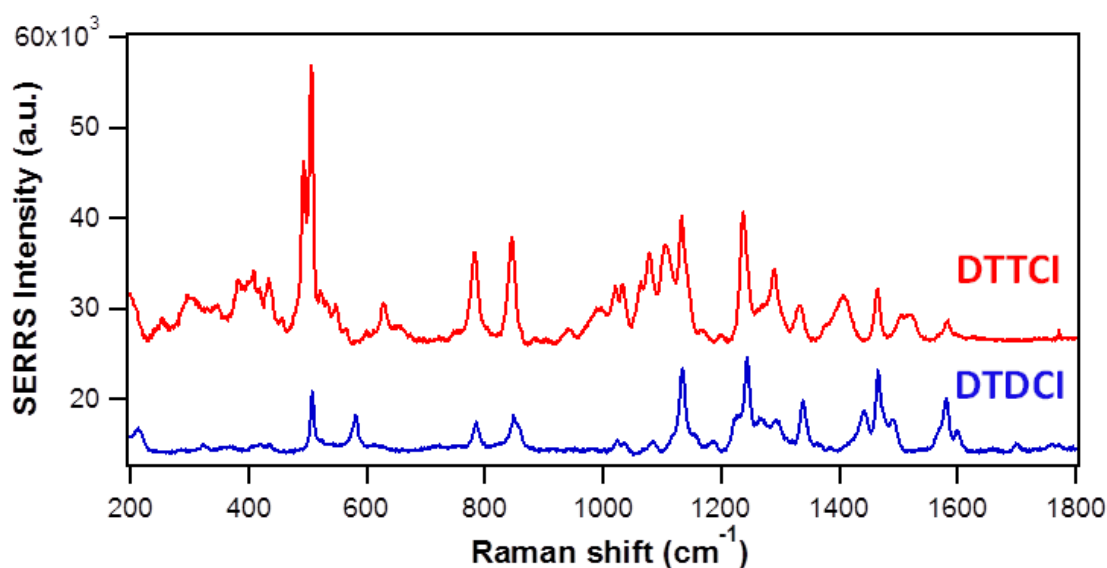


Figure 3.10. Representative extended SERRS spectra of conjugates prepared using 5 μM DTTCI and 20 μM DTDCI dyes plus nanorods ($\lambda_L = 618 \text{ nm}$) and then PSS-wrapped. Laser excitation wavelength = 785 nm. The spectra have been vertically offset to allow comparison.

Figure 3.11(a) and (b) show the SERRS profiles obtained for increasing concentrations of DTTCI and DTDCI adsorbed onto nanorods with a longitudinal SPR at 770 nm respectively.

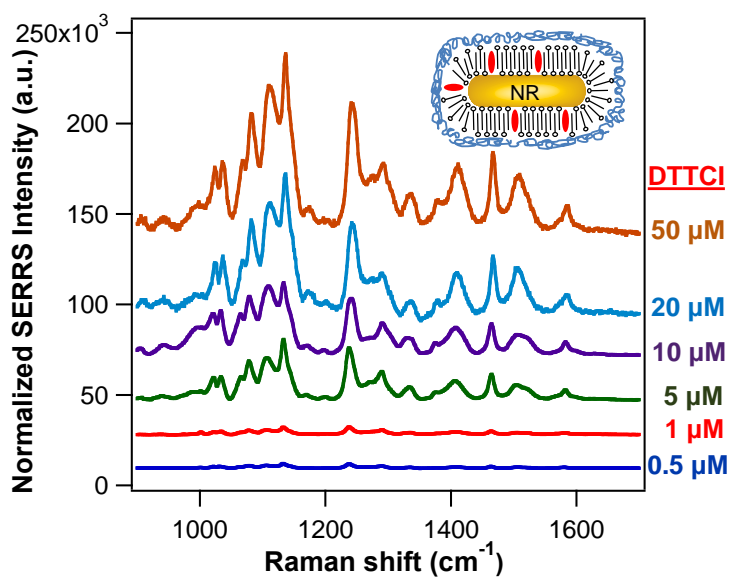


Figure 3.11a. SERRS spectra obtained for a series of PSS-wrapped rod-dye conjugates, using a fixed concentration of NRs ($\lambda_L = 770$ nm) and concentrations of DTTCI ranging from 0.5-50 μM . A bulk CTAB concentration of 1 mM is maintained throughout. Laser excitation = 785 nm. The spectra have been vertically offset to allow comparison.

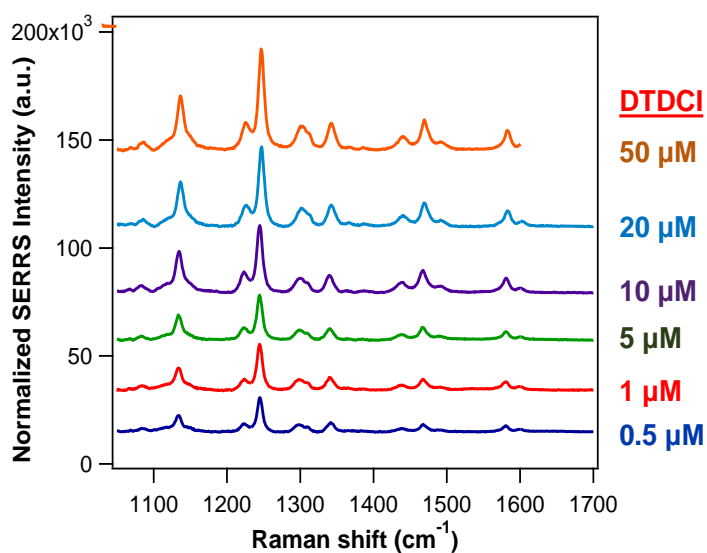


Figure 3.11b. Representative SERRS profiles of nanorods ($\lambda_L = 770$ nm)-DTDCI conjugates, prepared using bulk dye concentrations ranging from 0.5-50 μM , at a fixed nanorod concentration of ~ 1 nM. Laser excitation wavelength = 785 nm. The spectra have been vertically offset to allow comparison.

The data clearly shows that the SERRS response increases as a function of increased dye concentration associated with greater surface coverage of dye. At bulk dye concentrations above approximately 20 μM , there is no significant increase in SERRS intensity, which suggests that maximum dye loading has been achieved at the steady-state conditions employed. In addition, Figure 3.11 shows that the relative peak intensities did not change as a function of dye concentration. This suggests that the dye orientation on the nanoparticle surface is maintained, unlike the data shown later in Figure 3.19, where the spectral profile changes as a function of dye surface coverage in the absence of CTAB. It is also important to point out that no difference in the spectral profile was observed when comparing suspensions before or after PSS wrapping. In the case of DTDCI, similar behaviour was observed, with no significant increase in SERRS signal at concentrations approaching 50 μM .

The change in SERRS intensity was fitted to a Langmuir adsorption isotherm (see Figure 3.12). The Langmuir plots were obtained by first extracting the Raman intensity of a given peak for each dye for a range of bulk dye concentrations (1 - 50 μM). Next, the ratio (dye concentration/peak intensity) was plotted against the dye concentration (not shown). The resulting slope was linear fitted to obtain the signal intensity corresponding to the maximum surface coverage. Dividing the peak intensity by the maximum Raman intensity gives a value for theta. The Langmuir equation states that theta is equal to $(K_{\text{ads}} * \text{Concentration}) / (1 + K_{\text{ads}} * \text{concentration})$, where K_{ads} is the equilibrium affinity constant.

The Langmuir adsorption isotherm in Figure 3.12(a) for DTTCl gave an equilibrium affinity constant of $K_{\text{ads}} = 1.07 (\pm 0.1) \times 10^5 \text{ M}^{-1}$. The value for DTDCI in Figure 3.12(b) was found to be $K_{\text{ads}} = 1.84 (\pm 0.4) \times 10^5 \text{ M}^{-1}$. These numbers are approximately an order of magnitude higher than the value obtained by Alkilany *et al* for the partitioning of 1-naphthol into the CTAB bilayer.¹⁴³ It would have been preferable to also measure the ratio of dye molecules free in the bulk solution to that adsorbed on the nanorod surface using UV-vis spectroscopy, however, the tendency of the free dye molecules to aggregate over longer periods of time, especially for DTTCl, prevented sufficiently accurate measurements.

In both cases, it was difficult to prepare conjugates with dye concentrations higher than 50 μM as it was increasingly difficult to remove all excess dye, and the increased number of centrifugation steps led to a decrease in the stability of the conjugates and loss of particles.

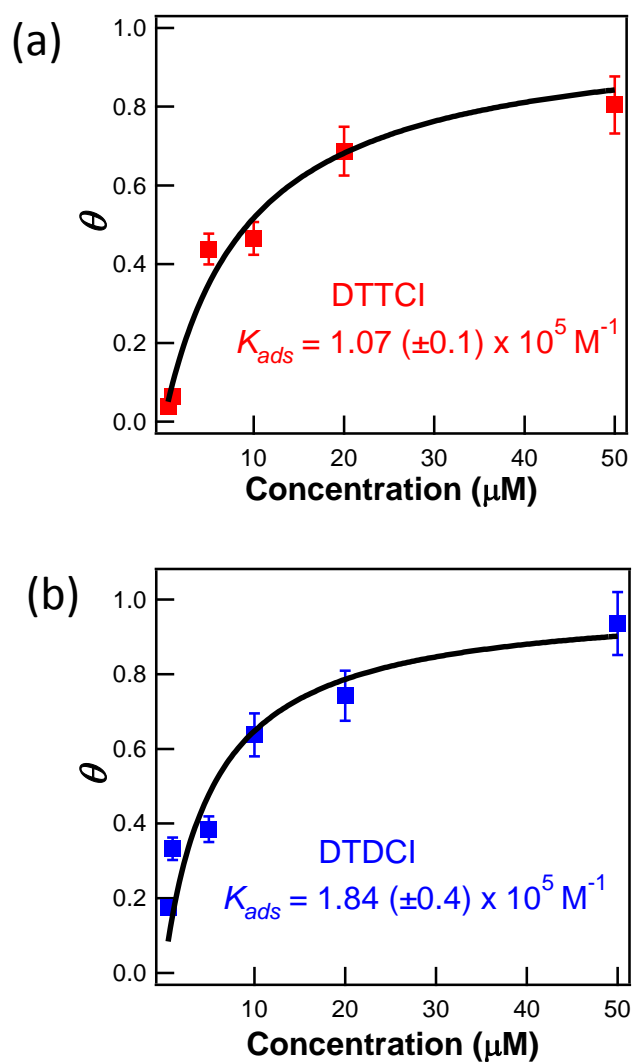


Figure 3.12. Plot of the relative surface coverage of (a) DTTCI and (b) DTDCI for a fixed concentration of NRs ($\lambda_L = 770 \text{ nm}$). Plots were obtained by (a) subtracting the intensity minimum at $1195 (\pm 5 \text{ cm}^{-1})$ from the maximum intensity at $1241 (\pm 3 \text{ cm}^{-1})$ and (b) subtracting the intensity minimum at $1195 (\pm 5 \text{ cm}^{-1})$ from the maximum intensity at $1245 (\pm 3 \text{ cm}^{-1})$ followed by applying a Langmuir fit analysis. In both cases, the solid line represents a Langmuir fit analysis.

3.7 SERRS Control Measurements

Control measurements acquired in the absence of dye molecules for both the stock nanorods in 1 mM CTAB and for PSS-wrapped rods were performed to assess the background contributions from the CTAB and PSS polymer wrap. The results obtained are shown below.

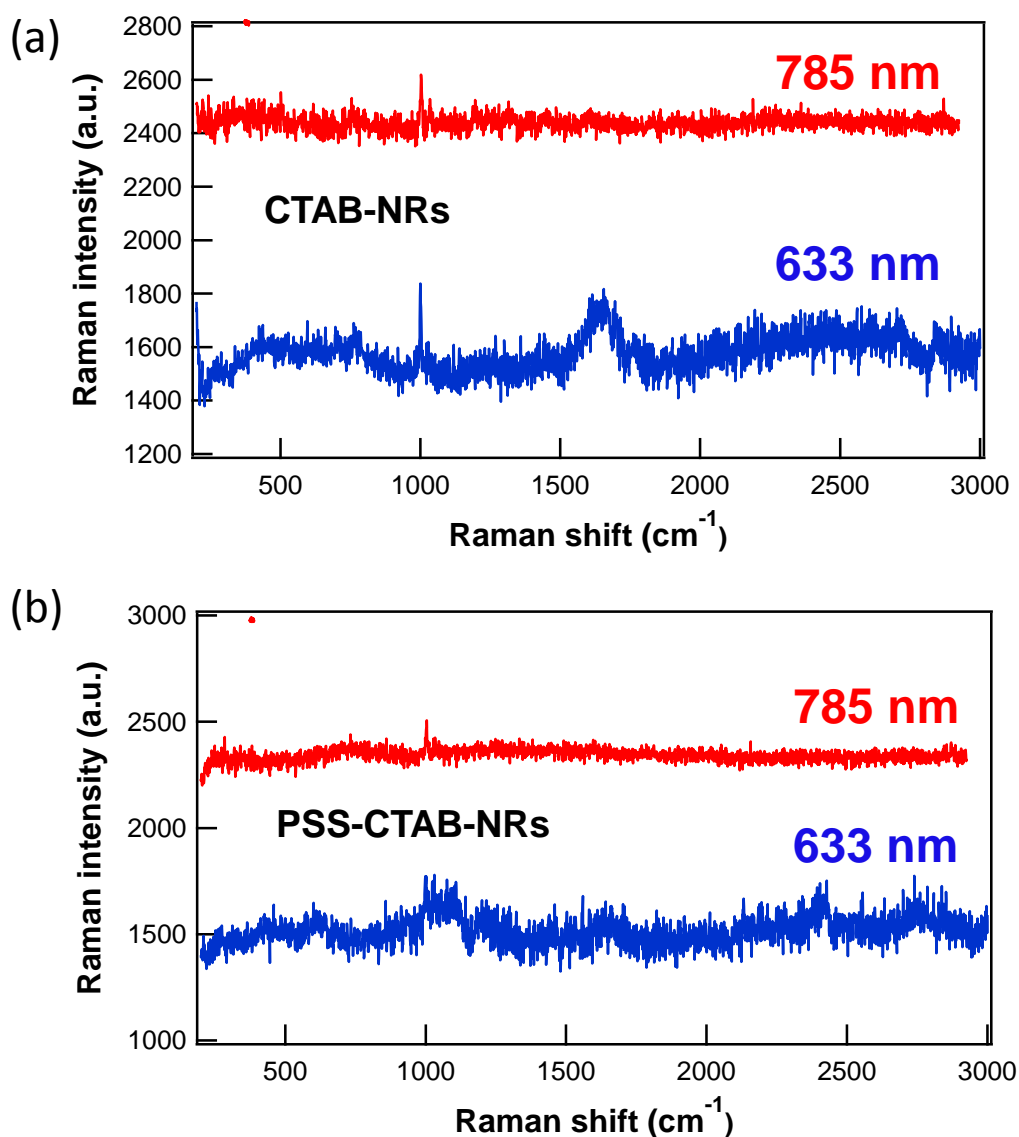


Figure 3.13. Control Raman measurements acquired in the absence of dye molecules for (a) stock solution of NR's in 1 mM CTAB and (b) PSS wrapped nanorods. In each case, the laser powers and integration times (10 s) and also the rod concentrations were maintained at the same values used for the acquisition of the SERRS spectra of the samples containing dyes. The nanorod λ_L was 770 nm.

The data in Figure 3.13 was obtained at identical laser powers, integration times and particle concentrations to the Raman spectra shown for samples containing dyes. It can clearly be seen that both the PSS and CTAB have negligible contributions to the SERRS spectral profiles for the nanorod-dye conjugates prepared.

In order to obtain the resonance Raman spectra for both DTTCI and DTDCI, the dyes were deposited onto a planar gold film to quench the fluorescent background signal.

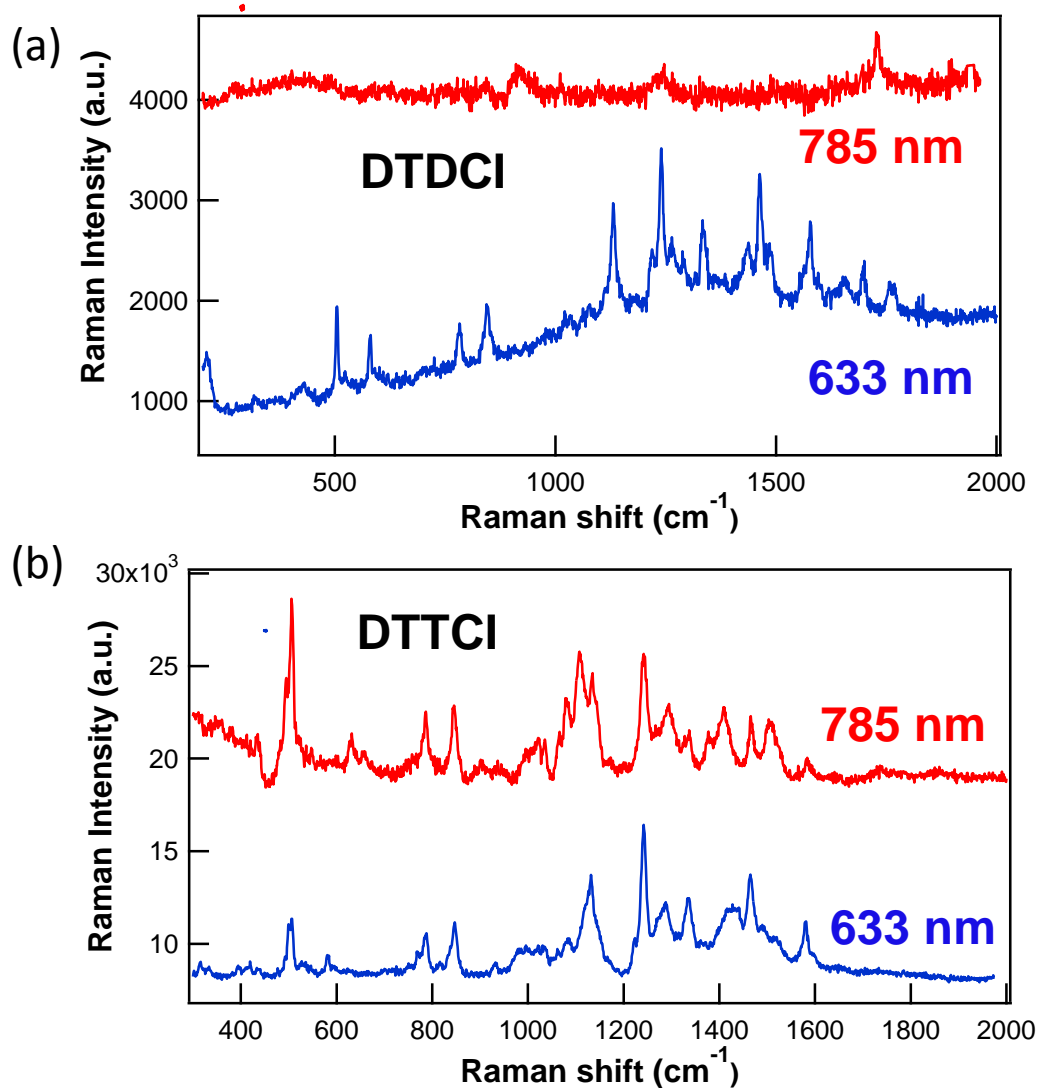


Figure 3.14. Control Raman measurements obtained for (a) DTDCI and (b) DTTCI dyes deposited (by simple solution evaporation) on a planar gold film. The acquisition conditions used are as follows: DTDCI at 785nm laser power 60 mW, 60s acquisition time. DTTCI at 785nm excitation, laser power 1.2 mW, 10 s acquisition time. DTDCI and DTTCI at 633nm excitation, laser power 1.0 mW, 30s acquisition time.

Significantly greater laser powers and accumulation times were required than for the solution based measurements. For DTDCI, no distinct spectrum was obtained at 785 nm compared to 633 nm excitation, suggesting that in Figure 3.11(b), there must also be a significant plasmon enhancement contribution to the overall SERRS signal. For DTTCI, resonance Raman spectra at both excitation wavelengths were obtained. The poorer signal-to-noise for the resonance Raman measurements indicate that the overall enhancement is due to a combination of molecular and plasmon resonance contributions.

3.8. SERRS Study of Different Nanorod-Dye Combinations

A comparison of the normalized SERRS intensities acquired for each different nanorod-dye combination is shown in Figures 3.15 and 3.16. The nanoparticle concentration was carefully controlled and the bulk dye concentration was fixed at 5 μM during conjugate preparation. Each sample was analysed at 633 and 785 nm excitation.

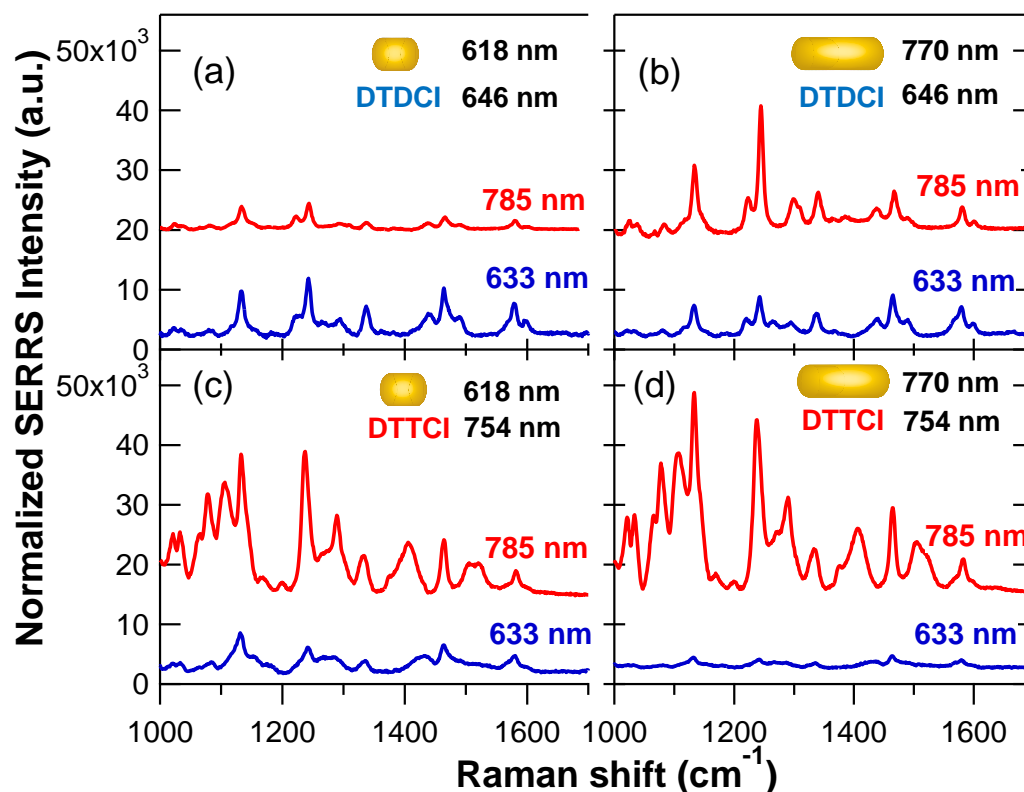


Figure 3.15. Normalized SERRS spectra obtained at an excitation wavelength of 785 nm (red traces in top half) and 633 nm (blue traces in bottom half). All data shown is for conjugates prepared using a 5 μM bulk dye concentration: (a) 618 nm NR, DTDCI; (b) 770 nm NR, DTDCI; (c) 618 nm NR, DTTCl; and (d) 770 nm NR, DTTCl. All spectra are normalized with respect to a cyclohexane standard acquired under identical conditions to enable relative comparisons.

This approach is advantageous as it allows a number of observations to be made regarding the relative importance of the excitation wavelength, nanorod longitudinal plasmon resonance and dye resonance to the overall SERRS signal obtained, while avoiding the additional complexities associated with nanoparticle aggregation, which is usually required to enhance the SERRS signals of colloidal solutions of quasi-spherical particles.¹³² The results were found to be highly reproducible, with small differences between aliquots

of the same batch. Repeat preparations of a number of batches were made, and again, results were found to be reproducible, with less than 10% variation between samples. Furthermore, for samples stored for upwards of eight months, it was found that no significant changes in the SERRS spectral intensities occurred.

The intensities of all of the SERRS spectra reported were normalized with respect to a cyclohexane reference acquired under identical conditions (i.e. laser power and focus, sample volume and integration time) as the sample measurement. This was to promote a direct comparison of spectral intensities acquired between samples at different laser excitation wavelengths and laser intensities.¹⁴⁸

3.8.1 Changing laser wavelength

It is expected that the largest SERRS enhancements will be obtained when both the dye and nanorod resonances overlap with the laser excitation wavelength.^{132, 148, 149} This is clearly seen in Figure 3.15(a), where both the DTDCI dye and nanorod resonances overlap with the 633 nm laser, resulting in a SERRS intensity approximately 2.8 times greater than the normalized signal obtained when the measurement is repeated at 785 nm excitation. In Figure 3.15(d), where the nanorod and DTTCI dye resonances overlap with the 785 nm laser, the relative differences in normalized SERRS spectra between 633 and 785 nm excitation is even greater. The increased contrast observed between the two different SERRS measurements in (d) compared to the smaller difference between the two spectra in (a) is not what would be predicted based on each dyes absorption spectrum (shown in Figure 3.5), with the DTTCI having a broader absorption spectrum, which partially overlaps both laser wavelengths. Instead, these results show that the plasmon field contributions to the overall SERRS enhancement is greater for longer rods excited at 785 nm rather than for shorter rods excited at 633nm.

3.8.2 Changing the dye resonance

The effect of changing the dye molecular resonance can be ascertained by comparing the spectra in Figures 3.15(a) and (c), where the dye-rod conjugates were prepared from the same nanorod stock solution ($\lambda_L = 618$ nm). In each case, the bulk dye concentration was fixed at 5 μ M when the conjugates were prepared, and the particle

concentrations of the monodispersed polymer wrapped conjugates were kept constant. As expected, due to resonance overlap between the dye and the rod, the SERRS signal obtained at 633 nm excitation was higher for the DTDCI in Figure 3.15(a) than for DTTCI shown in (c). However, at 785 nm excitation, the SERRS signal associated with the DTTCI dye in Figure 3.15(c) is more than 5 times greater than the corresponding measurement in Figure (a), and also larger than the DTDCI signal at 633 nm where the rod and dye are both resonant with the laser (Figure 3.15(a)). This may in part be explained by slight differences in fractional surface coverages between the DTTCI and DTDCI dyes on the nanorods.

A similar comparison can also be made between samples prepared using the longer aspect ratio rods ($\lambda_L = 770$ nm) as shown in Figure 3.15(b) and (d). For both dyes, the spectral intensities were greater at 785 nm excitation, even for DTDCI, which suggests that the overlap of the laser and nanoparticle plasmon resonance wavelengths has a relatively larger contribution to the SERRS enhancement than the overlap between the laser and dye molecular resonance wavelengths.

With the exception of sample (a), the data shows that the results obtained for 785 nm excitation were consistently bigger than those obtained at 633 nm excitation. This trend was seen across all dye concentrations prepared (1- 50 μ M).

The results shown in quadrant (b) are more difficult to explain, despite the dye resonance overlapping closely with the 633 nm laser, significant enhancement was obtained at 785 nm excitation. It is also worth noting here that significant resonance coupling was observed in the extinction spectra in Figures 3.9(b) and (d) for both systems.

3.8.3 Quantification of SERRS Intensities

Both dyes used in this study are strongly fluorescent and, as a result, an accurate determination of the *absolute* SERRS enhancement factor was not attempted.^{46, 51} Instead, a relative study has been performed, focusing on the different dye and rod combinations, and a comparison between nanorod and quasi spherical nanoparticles is also discussed in the next section. Furthermore, comparison of the spectra for each dye in Figure 3.10 clearly shows that although DTDCI and DTTCI are structurally very similar, the SERRS spectra are very different. In order to quantitatively compare the relative SERRS intensities for the different combinations in Figure 3.15, separate pairs of representative peaks were selected

for both dyes which could be readily observed at low dye concentrations. For DTDCI, the peak intensity maximum at 1245 cm^{-1} ($\pm 3\text{ cm}^{-1}$) was obtained, and from this, the peak intensity minimum at 1195 cm^{-1} ($\pm 5\text{ cm}^{-1}$) was subtracted. Similarly, for DTTCI, the intensity minimum at 1195 ($\pm 5\text{ cm}^{-1}$) was subtracted from the maximum at 1241 ($\pm 3\text{ cm}^{-1}$). These values were then used as a numerical indicator with which relative SERRS intensities could be compared and the choice of baseline fit was not an additional source of variation. Figure 3.16 summarizes the different selected peak intensity values for each of the spectra shown in Figure 3.15.

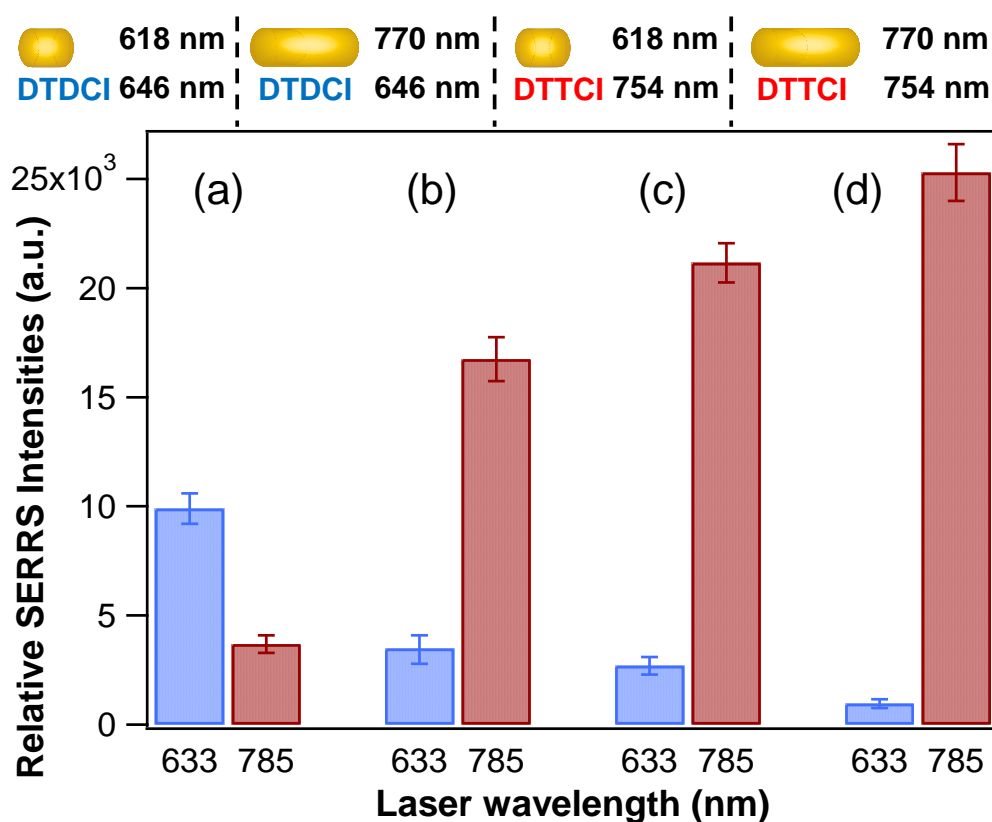


Figure 3.16. Comparison of normalized SERRS intensities for the corresponding spectra and excitation wavelengths shown previously in Figure 3.15(a)-(d). The peak intensity of a representative peak was obtained by finding the maximum peak height at 1245 cm^{-1} ($\pm 3\text{ cm}^{-1}$) and subtracting the minimum at 1195 cm^{-1} ($\pm 5\text{ cm}^{-1}$) for DTDCI. The process was repeated for DTTCI using the maximum peak height at 1241 cm^{-1} ($\pm 3\text{ cm}^{-1}$) and subtracting the minimum peak height at 1195 cm^{-1} ($\pm 5\text{ cm}^{-1}$).

The data in Figure 3.16 shows that for the spectra shown in Figure 3.15(d), a 25 fold increase in SERRS signal was obtained when moving from 633 to 785 nm excitation, while in Figure 3.15(a), only a 2.5 times increase is obtained between both excitation wavelengths.

As discussed in Chapter 1, calculation of enhancement factors can be difficult, and is not possible in this case, since the dye molecules used are strongly fluorescent, and thus it is not possible to obtain a Raman spectrum for the dye-only solution. The differential Raman cross-section ($d\sigma_R/d\Omega$) can be used as an alternative to enhancement factors, the advantages of this approach are discussed earlier. The differential Raman cross-section for the individual nanorod-dye conjugates was estimated by comparing SERRS intensities to that of the cyclohexane intensity standard at 802cm^{-1} used throughout the study. Details of the calculations are shown below:

Raman cross section values for cyclohexane liquid at 802 cm^{-1} have been reported at the following wavelengths: ¹⁵⁰

Laser Wavelength (nm)	407	488	514.5	647
σ_R ($\text{cm}^2\text{ sr}^{-1}$ molecule ⁻¹) $\times 10^{-30}$	17.6	9.06	5.2	2.1

Table 3.1. Raman cross section values for cyclohexane liquid at 802 cm^{-1} reported at various wavelengths.

No values for σ_R at 633 and 785 nm excitation wavelengths could be found in the literature, therefore fitting the above tabulated entries, assuming a $1/(\lambda^4)$ trend in the differential cross section, produced estimated values of 2.28×10^{-30} and $0.97 \times 10^{-30}\text{ cm}^2\text{ sr}^{-1}$ for 633 and 785 nm respectively.

As described previously in the literature,^{46, 51} the differential Raman cross section ($d\sigma_R/d\Omega$) for a single cross-scattering object can be defined as:

$$\left(\frac{d\sigma_R}{d\Omega}\right)_{Label} = \frac{I_{Label} C_{Standard}}{C_{Label} I_{Standard}} \left(\frac{d\sigma_R}{d\Omega}\right)_{Standard} \quad \text{Equation 3.1.}$$

Where C_{Label} is the concentration of the nanorod-dye conjugates, I_{Label} is the SERS intensity of the sample, $I_{Standard}$ is the Raman signal of the cyclohexane liquid with known concentration ($C_{Standard}$) and known absolute cross section. Both the sample and standard measurements were performed under identical conditions.

The values for the SERS intensities were obtained by performing a Lorentzian fit of the Raman peaks to obtain the area of the 802 cm^{-1} cyclohexane peak and the area of the highest intensity peak for the nanorod-dye conjugates (1081 cm^{-1} for DTTCl and 1133 cm^{-1} for DTDCI) which were fitted with a polynomial baseline.

Using values of $C_{Standard} = 9.26 \text{ M}$, $C_{Label} = 1.11 \text{ nM}$ (DTTCl), $C_{Label} = 1.36 \text{ nM}$ (DTDCI), the following estimates were obtained.

$$\left(\frac{d\sigma_R}{d\Omega}\right)_{NR-DTDCI} = 1.4 \times 10^{-20} \text{ cm}^2 \text{ sr}^{-1}$$

For DTDCI nanorods ($\lambda_L = 618 \text{ nm}$) conjugates prepared at a dye concentration of 50 μM and laser excitation of 633 nm.

$$\left(\frac{d\sigma_R}{d\Omega}\right)_{NR-DTTCl} = 3.8 \times 10^{-20} \text{ cm}^2 \text{ sr}^{-1}$$

For DTTCl nanorods ($\lambda_L = 770 \text{ nm}$) conjugates prepared at a dye concentration of 50 μM and laser excitation of 785 nm.

For DTTCl-rod ($\lambda_L = 770 \text{ nm}$) conjugates prepared at a dye concentration of 50 μM (corresponding to the largest SERRS signal in Figure 3.11(a)) a $(d\sigma_R/d\Omega)$ of $\sim 3.8 \times 10^{-20} \text{ cm}^2 \text{ sr}^{-1}$ was obtained. Similarly, for DTDCI rod conjugate with a $\lambda_L = 618 \text{ nm}$, and a bulk dye concentration of 50 μM , which resulted in the highest SERRS intensity at 633 nm excitation, a $(d\sigma_R/d\Omega)$ of $\sim 1.35 \times 10^{-20} \text{ cm}^2 \text{ sr}^{-1}$ was determined. The ratio between these values is approximately 1 : 1.7, which matches the ratios obtained when comparing Figure 3.16(a) and (d). These differential cross-section values are comparable with the brightest signals reported in a recent study by Amendola and Meneghetti,⁵¹ who quantified the SERS

response for a range of spherical nanoparticle-dye label combinations, which contained a significant subpopulation of nanoparticle dimers. To gain further insight, a direct comparison of the relative brightness of the nanorod-dye conjugates versus labelled spherical nanoparticles is carried out in the next section.

3.9 Comparison of Nanorod versus Spherical shapes

The vast majority of SERS studies to-date have focused on the use of colloidal solutions of quasi-spherical metal nanoparticles, therefore, in order to investigate the advantages of using this NR-dye conjugate system the same dyes were adsorbed onto quasi spherical gold nanoparticles, and the relative SERS responses were compared. Gold nanoparticles with an average diameter of 38 nm were prepared by the well-established citrate reduction method,¹¹⁰ a representative SEM image is shown in Figure 3.17.

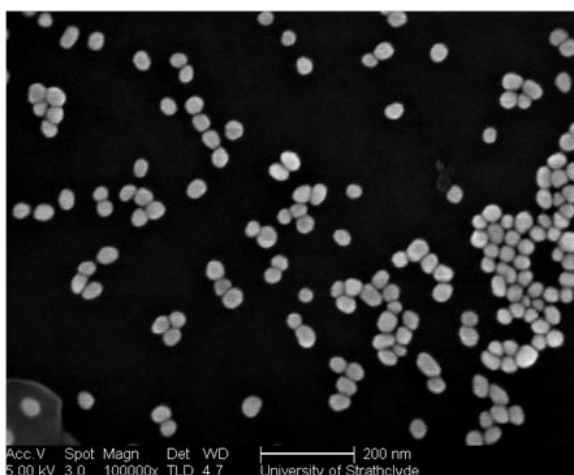


Figure 3.17. Representative SEM image of quasi-spherical gold nanoparticles prepared using trisodium citrate reducing agent.

The creation of a mixed CTAB/dye bilayer on the surface of the spherical nanoparticles was found to be problematic, and the molecular density and organisation is likely to be significantly different between the rod and spherical morphologies. An alternative approach was employed, where the positively charged DTTCl dye was directly introduced to the negatively charged citrate-capped gold nanoparticle solution. The aim

was to establish the *maximum* SERRS signal for the quasi-spherical/dye system, i.e. any further increase in dye concentration does not lead to greater SERRS signal and the level of random aggregation of the spherical particles is also optimised.

The absence of the CTAB bilayer has a significant effect on the adsorption of dye onto the nanoparticle surface and the stability of the conjugate. When DTTCl was introduced to the colloid stock solution, nanoparticle aggregation started to occur at bulk dye concentrations above approximately 0.05 μM , as shown in Figure 3.18.

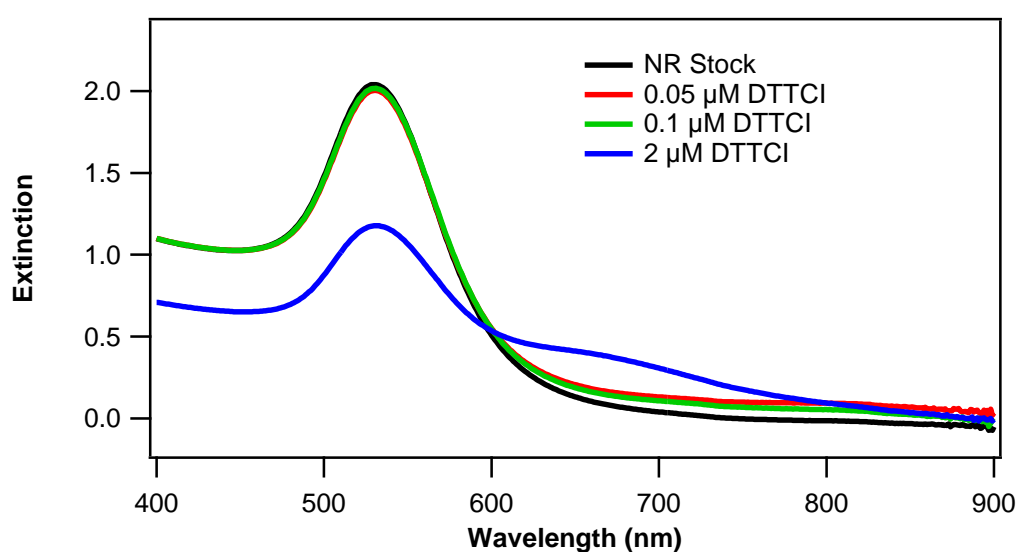


Figure 3.18. UV-vis spectra of quasi-spherical Au nanoparticle stock solution, both before and approximately 1 min after addition of 0.05 μM , 0.1 μM and 2 μM DTTCl.

As well as preventing nanoparticle aggregation when the dye is added, it is likely that CTAB performs a further role in controlling the orientation of the dye molecules on the nanoparticle surface. A range of spherical nanoparticle-dye conjugates were prepared, with DTTCl concentrations ranging from 0.05-2 μM , and the SERRS profiles were obtained at 785 nm excitation.

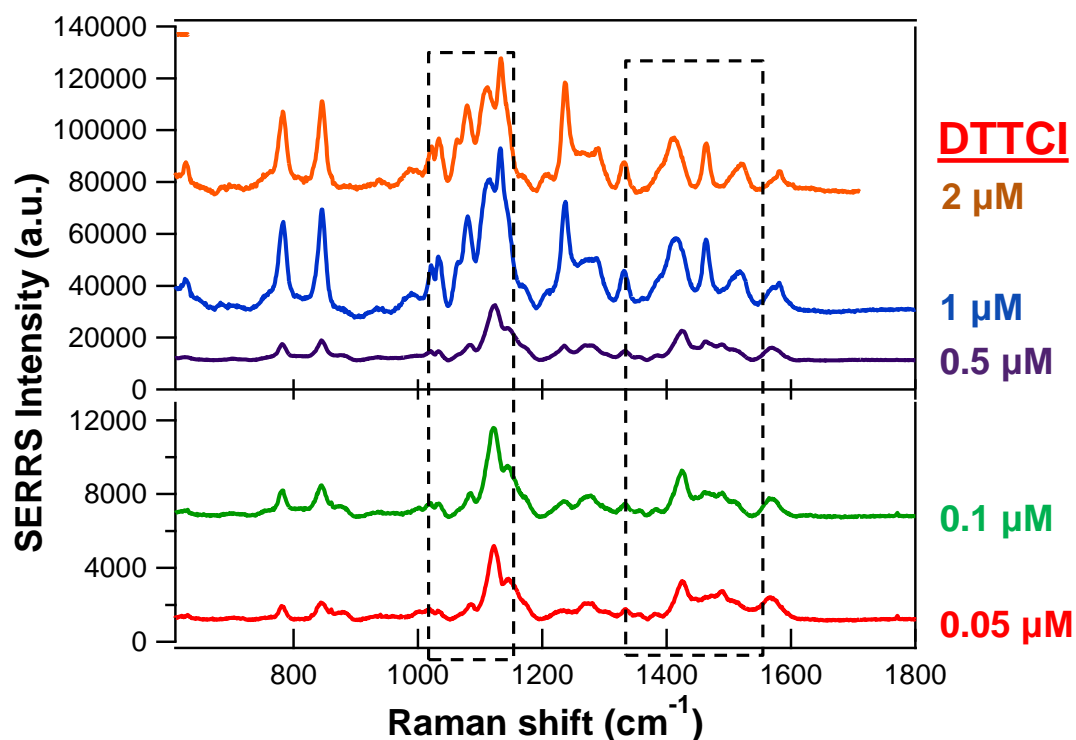


Figure 3.19. Baseline corrected SERRS profiles obtained at 785 nm excitation for Au spheres-DTTCI conjugates, with dye concentrations ranging from 0.05-2 μM . Spectra have been vertically offset to allow comparison.

Comparison of the spectra obtained for conjugates containing less than 1 μM DTTCI with those containing 1-2 μM DTTCI highlights some marked differences in the peak profiles, particularly in the regions highlighted, with differences also observed in the band at approximately 1250 cm^{-1} . It therefore seems likely that the presence of a fixed concentration of CTAB aids in the reproducible formation of these conjugates, even at very low dye concentrations. The normalized SERRS spectra obtained at 785 nm excitation for polymer wrapped DTTCI-NR conjugates and quasi-spherical nanoparticles is shown in Figure 3.20.

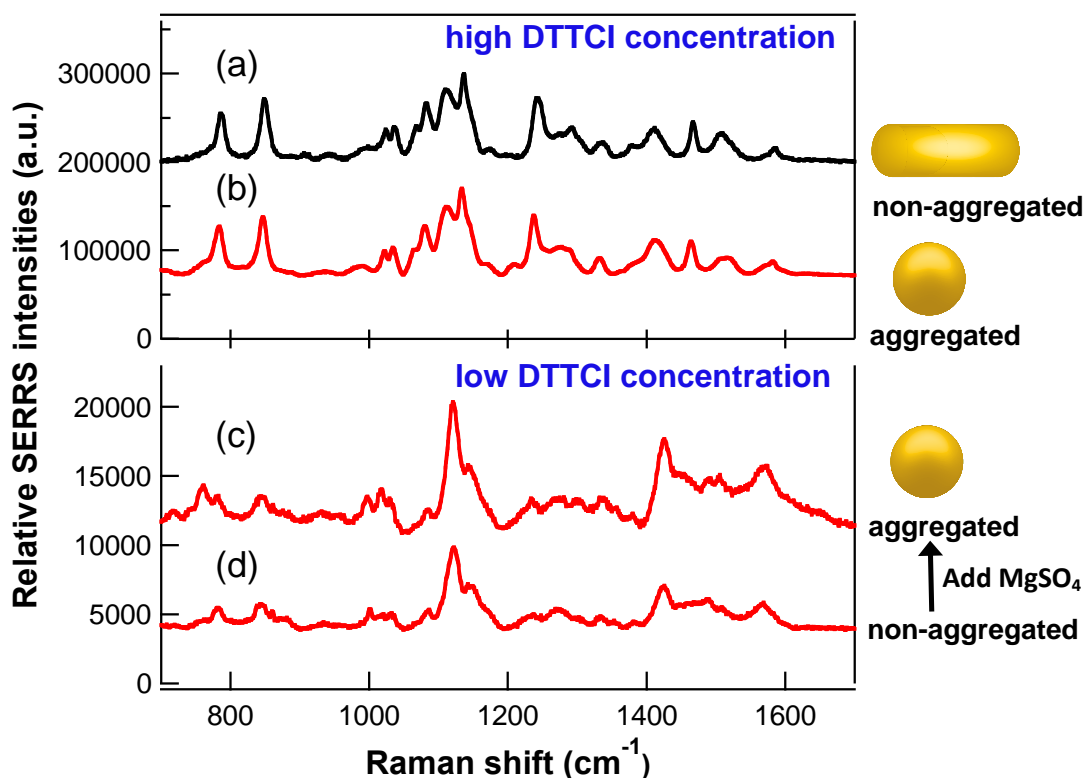


Figure 3.20. Normalized SERRS spectra at 785 nm excitation for (a) monodispersed solution of polymer-wrapped DTTCl-rod conjugates, prepared with a 50 μM bulk dye concentration; (b) aggregated quasi-spherical Au nanoparticles in the presence of 2 μM DTTCl and MgSO_4 , representing the maximum SERRS signal obtainable from this system. Measurements at a lower DTTCl concentration of 0.05 μM are shown for quasi-spherical Au particles (c) following aggregation induced by MgSO_4 and (d) non-aggregated.

As previously discussed, for the spherical gold-dye conjugates, nanoparticle aggregation occurs above approximately 0.05 μM DTTCl, therefore, in order to first compare the signals obtained from unaggregated systems, the dye concentration was fixed at 0.05 μM . The signal obtained for unaggregated quasi-spherical Au-DTTCl conjugates is shown in Figure 3.20(d). MgSO_4 was added to induce aggregation, the maximum SERRS signal obtained was only a relatively modest two fold increase (Figure 3.20(c)). Comparison of the spectra in Figures 3.20(c) and (d) show similar peak profiles, both of which are markedly different from the spectra obtained for the nanorod-dye complexes. However, when higher DTTCl concentrations are introduced to the quasi-spherical nanoparticle colloid, the resulting SERRS profile was very similar to that of the rod-dye conjugates (compare Figures 3.20(a) and (b)). This emphasizes the role of the CTAB bilayer in controlling

the orientation of the dye on the nanoparticle surface, while the average orientation of the dye on the citrate-stabilized quasi-spherical particles must vary with dye fractional surface coverage. The relationship between the molecule orientation on a nanoparticle surface and the SERS spectral profile has been described previously.^{49, 151}

The maximum signal obtained for an unaggregated nanorod-dye system is shown in Figure 3.20(a), where the nanoparticle concentration is fixed at ~ 1.1 nM. The most intense peak in a) is ~ 24 times larger than the most intense peak measured for the unaggregated quasi-spherical particles in (d). The role of nanoparticle aggregation as a means to increase SERRS signal is well-established, and the spectrum shown in (b) represents the maximum response obtained following a series of repeat measurements following the aggregation of the quasi-spherical nanoparticles at higher DTTCI concentrations. Comparing (a) with (b), the signal for the unaggregated rods is approximately 10% higher than that obtained for the aggregated spheres. The concentrations of the nanorod (~ 1.1 nM) and quasi-spherical (~ 0.26 nM) stock solutions are not identical, while the surface area of the average spherical particle is ~ 1.8 times greater than that of the nanorods. Furthermore, it is also reasonable to assume a significantly higher dye coverage on the spheres than the CTAB coated rods. Thus, the difference in the total number of dye molecules adsorbed onto a nanoparticle surface will be considerably less than a factor of two. Given that inducing aggregation results in orders of magnitude increase in SERRS response of spherical particles,³³ and the fact that the normalized SERRS signal associated with the monodisperse nanorods-dye conjugates is comparable with the signal from the aggregated spherical system, it can be deduced that the nanorod-dye conjugates are significantly brighter than their spherical counterparts. The role of nanorod aggregation is discussed in more detail in Chapter 4.

3.10 Conclusions

In this first research Chapter, it has clearly been demonstrated that it is possible to adsorb dyes onto nanorod surfaces in a controlled fashion, and subsequently stabilize these conjugates using polyelectrolyte wrappings. This forms the premise for the rest of the work described in this thesis, starting with the exploration of different nanorod-dye combinations.

A series of stable, monodisperse suspensions of polymer-wrapped gold nanorod-dye conjugates were prepared and their optical extinction and SERRS properties were characterized by selectively tuning both the plasmon resonance of the nanorod and the molecular resonance of the dye with respect to the laser excitation wavelengths (633 and 785 nm).

A particular advantage of this approach is its simplicity, with bright Raman signals obtained without the need to aggregate the nanorods. Further advantages are the good control over the surface coverage and orientation of the reporter molecules on the nanorod surface. In comparison, most efforts to produce SERS probes have involved an aggregation step during their preparation which is relatively uncontrolled, with a recent trend in the literature towards achieving greater control as part of the SERS optimization process. The controlled aggregation of gold nanorods, and the SERRS enhancements obtained from these aggregates is investigated in Chapter 4.

It has been clearly demonstrated that these nanorod-dye conjugates are a highly promising new class of SERRS nanotags which offer a number of advantages.

3.11 Future Work

In order to limit all of the potential parameters, the research in this Chapter was restricted to combinations of two nanorods with different longitudinal surface plasmon resonance and two dyes. SERRS analysis was also only carried out at two excitation wavelengths. There is potential to expand the scope of this work and apply this model system to explore a wider variety of dye and rod conjugates, as well as different laser excitation wavelengths. To a certain extent, this was carried out in Chapter 5, however, there is room for more investigation. By doing so, it is likely that our understanding of the relative contributions to the overall SERRS intensities from both the nanorod and dye could be increased.

In order to further our understanding of the dye-rod conjugates discussed here, it would be useful to carry out molecular modelling studies to gain an insight into the interaction between the nanorods and dyes, this would hopefully result in an increased understanding of some of the effects described here. In particular, the simplicity of this system provides an ideal opportunity to address the challenge of achieving a greater

understanding of the SERRS enhancement mechanism from a joint experimental and theoretical perspective, which could promote the rational design of SERRS substrates for use in a wide range of applications.

It would also be of particular interest to design a study looking at real time SERRS analysis of single nanorods to examine the dye adsorption process. This could be achieved using a polarized excitation source to compare SERRS responses across the transverse or longitudinal axis. The results would allow the position of the dye on the nanorod surface to be determined, i.e. does it preferentially occupy a site at the end or the side of the rod, especially during the initial adsorption process. This is an important consideration since it is known the CTAB densities vary in these positions, and SERRS enhancements are strongest at the ends of nanorods.

The conjugates described here could also be utilised in single particle Raman studies, which would allow an even more accurate determination of Raman enhancements, since issues such as particle concentration and monodispersity would not be a factor here.

Chapter 4

Preparation and Characterization of Stabilized Nanorod-Dye Clusters

The results described in Chapter 3 show that it is possible to obtain bright Raman signals from the monodisperse nanorod-dye conjugates. However, it is well known that the formation of hot spots via nanoparticle aggregation leads to increased Raman intensities. The role of controlled aggregation of the nanorod-dye conjugates will be explored in detail in this Chapter.

The geometrical and surface chemical anisotropy of the rod-shape offers potential avenues for assembling more complex nanostructures. Nanoparticle aggregation in the presence of a specific reporter or target molecule is associated with dramatically enhancing the signal obtained in a variety of optical techniques including SE(R)RS.¹⁵² However, controlled assembly within colloidal solutions to create stabilized free-standing clusters ~2-4 particles in size is challenging for spherical particles with the additional engineering required to also incorporate Raman-active molecules within interparticle junctions an added difficulty.

Nanorods can aggregate in a number of ways, they can either line up in a random fashion (therefore, not controlled aggregation), end-to-end or side-by-side. Aggregation of nanorods in an end-to-end fashion is indicated by a red shift of the longitudinal plasmon band. A lot of interest has focussed on the end-to-end aggregation, and assembly has been reported via a number of methods, for example, using thiolated linkers such as biotin disulfide¹⁵³ and thiolated DNA.¹⁵⁴ Assembly in this fashion can be advantageous for some applications as it is well known that nanorods aggregated in this fashion demonstrate larger increases in properties such as SERRS enhancements.¹⁵⁵ This has been viewed as an attractive and relatively simple method of aggregation, due to the fact that the CTAB surfactant has been shown to bind preferentially to the sides of the nanorods,¹⁵⁶ this means there is less of a barrier to the attachment of linker molecules at the ends of the nanorods.

An alternative method to achieve the controlled aggregation of nanorods is to aggregate in a side-by-side fashion. Successful side-by-side aggregation of the nanorods is indicated by a blue shift of the longitudinal band, and a slight red shift of the transverse band due to the decrease in the effective aspect ratio, accompanied by a dampening of the signal as the particle density rapidly decreases. Side-by-side assembly has been described by a number of groups, for example, using biological linkers such as DNA¹⁵⁷ and antibodies,¹⁵⁸ or by charge interactions, for example, using dimercaptosuccinic acid¹⁵⁹ or citrate. However, no control of aggregate sizes in suspension has been demonstrated, with cluster sizes typically larger than dimers and trimers being prepared.

The basis of the approach here is a combination of two factors; i) a higher density of positively charged surfactant, i.e. a more intact CTAB bilayer along the sides of the rods than at the ends and ii) the relatively larger surface area of the sides versus the ends, which can be exploited to aggregate the nanorods in a side-by-side fashion.

4.1 Cluster Assembly

The overall aim was to create SERRS active clusters of nanorods and dyes which are stable in suspension for long periods of time (i.e. days to months). It is also important that there is the potential to further functionalize these clusters. An overview of the formation of these stabilized clusters is shown in Figure 4.1.

The first stage of cluster preparation has been discussed previously (Chapter 3.2). Briefly, nanorods with $\lambda_L = 802$ nm were prepared and centrifuged and resuspended in 1 mM CTAB a minimum of four times to ensure that the concentration of the surfactant was fixed. A Raman reporter, in this case, the dye DTTCl was incorporated into the CTAB bilayer and allowed to equilibrate overnight. As discussed in detail in Chapter 3.2, nanorods with $\lambda_L = 802$ nm and DTTCl (extinction maximum = 754 nm) were chosen as they provide strong overlap with the 785 nm Raman excitation laser, and the dye is able to sequester into the CTAB bilayer to form a mixed layer.

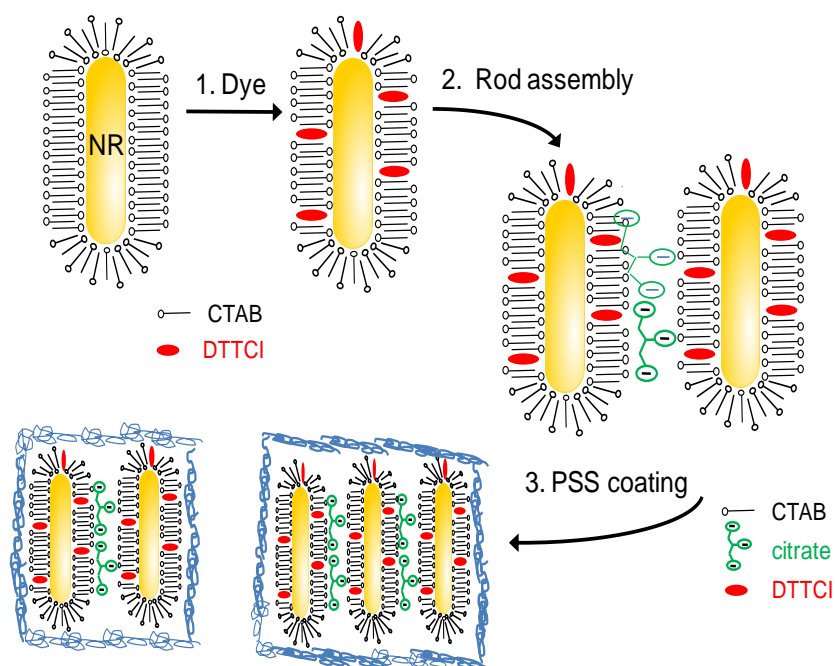


Figure 4.1. Schematic outlining the preparation and stabilisation of self-assembled gold nanorod-dye clusters.

The second stage in cluster formation is the side-by-side self-assembly of the rods into clusters of controllable size. In order to achieve the controlled side-by-side aggregation of the rods, two polyanionic aggregating agents including were investigated. Sodium chloride was found to induce random aggregation, with little control over the final cluster size. Sodium citrate was also investigated and found to aggregate the nanoparticles in the desired manner.

A novel aspect is that the aggregation process can be halted, and clusters can be stabilized using the polyelectrolyte polymer PSS, as shown in stage 3 in Figure 4.1. A further advantage of the polymer layer is that it provides a platform for further surface functionalization (see Chapter 6).

4.2 Controlled Aggregation of NRs

Aggregation can be achieved via an electrostatic interaction using sodium citrate. Two possible routes have been investigated in order to achieve this: 1) controlling the ratio of citrate to nanorod and establishing the immediate resulting plasmon shift and 2) adding

smaller volumes of citrate, but allowing the reaction to proceed over a longer period of time, before halting the aggregation process.

Controlled assembly involves a number of parameters, including the concentration of sodium citrate, CTAB and dye, which are discussed in detail in Sections 4.2.1 - 4.2.4.

4.2.1 Altering the Bulk Concentration of Sodium Citrate Added

The most straightforward method to carry out controlled aggregation is by varying the volume of sodium citrate stock solution added to a fixed concentration of stock nanorods. Figure 4.2 shows the extinction spectra obtained 60 minutes after addition of varying volumes of 1.75 mM sodium citrate to 2 ml of stock nanorod solution.

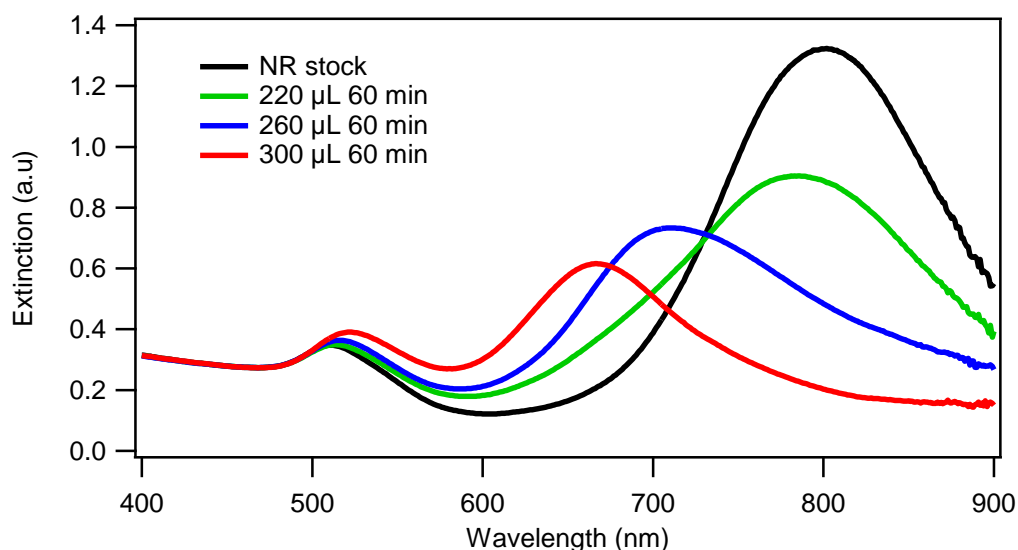


Figure 4.2. Controlled aggregation by varying the volume of 1.75 mM citrate added to 2 ml of nanorod stock solution, spectra acquired after 60 mins.

As the concentration of citrate solution is increased, a corresponding blue shift of the longitudinal band, accompanied by a dampening of the signal is observed. This method does provide control over the size of the initial cluster formed, however, in order to achieve large plasmon shifts, i.e. to form large clusters, increased concentrations of sodium citrate must be used. Figure 4.3 shows the results obtained when 800 μ l of 1.75 mM sodium citrate was added to 2 ml of NRs, and the resulting clusters were PSS wrapped.

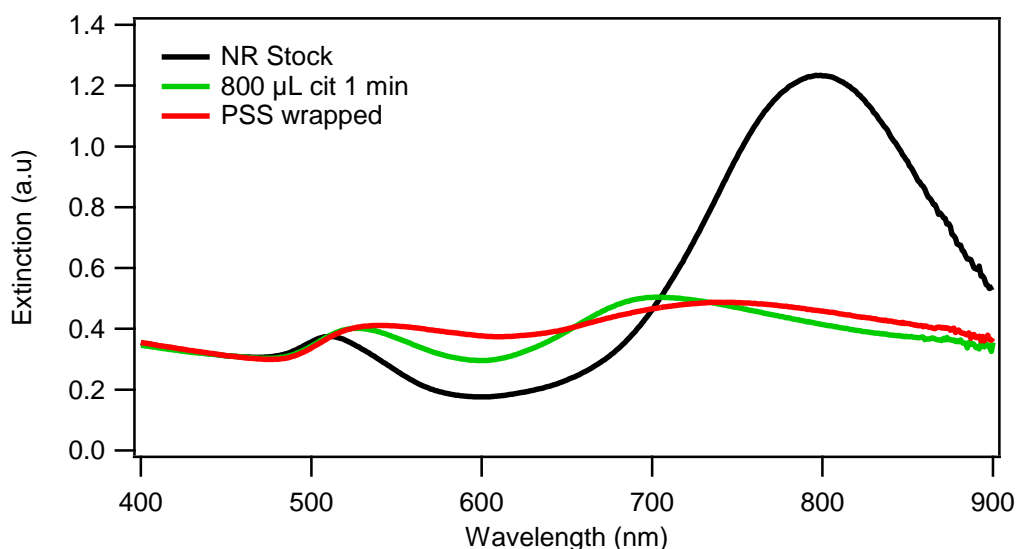


Figure 4.3. Polymer wrapping of cluster following addition of a large volume of citrate.

The results show that the aggregation process is uncontrolled, and due to the higher citrate concentration, continues while the polymer wrapping stage is carried out, leading to a randomly aggregated final product.

4.2.2. Time-dependent aggregation

An alternative method to achieve controlled aggregation of the stock nanorod solution is to add a relatively low citrate concentration and monitor the aggregation process over time, as shown in Figure 4.4.

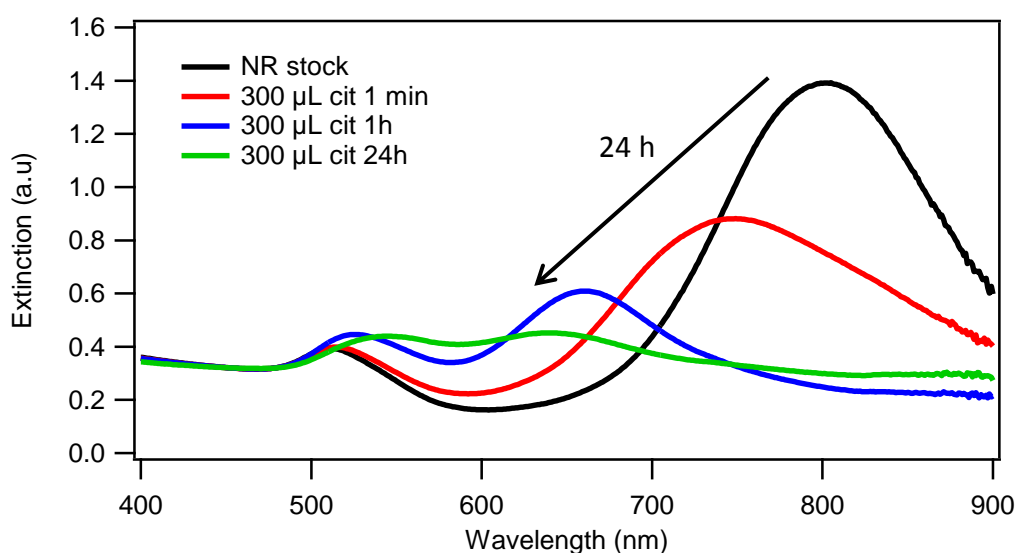


Figure 4.4. Extinction spectra monitoring the controlled side-by-side assembly of gold nanorods upon the addition of citrate anions and measured over 24 hours.

The addition of 300 μl 1.75 mM citrate per 2 ml stock nanorod solution results in a 55 nm blue shift of the longitudinal band within 1 minute of addition. The aggregation process was tracked by measuring the extinction spectra over the course of 24 hours. As can be seen, the aggregation continues gradually over this period, with the longitudinal band blue shifting by 165 nm over 24 hours. This is the preferred method to allow maximum control over the final position of the longitudinal plasmon band, and thereby over the final cluster size obtained. Time-dependent aggregation allows overall control by varying both the initial volume of citrate added and the time the aggregation is allowed to proceed. This allows the kinetics of the aggregation process to be slowed down, and thus, very accurate control over the final cluster sizes obtained by monitoring the process in real time.

4.2.3 Dependence of Aggregation on Bulk CTAB Concentration

In addition to the concentration of sodium citrate, the bulk concentration of CTAB is also a critical factor in the controlled aggregation of these nanorods.

Figure 4.5 and 4.6 compare two sets of experiments where the only difference is the CTAB concentration. Figure 4.5 shows the extinction spectra of nanorods in a 1 mM CTAB solution following the addition of 100 μl of 1.75 mM citrate per 2 ml of stock rod solution.

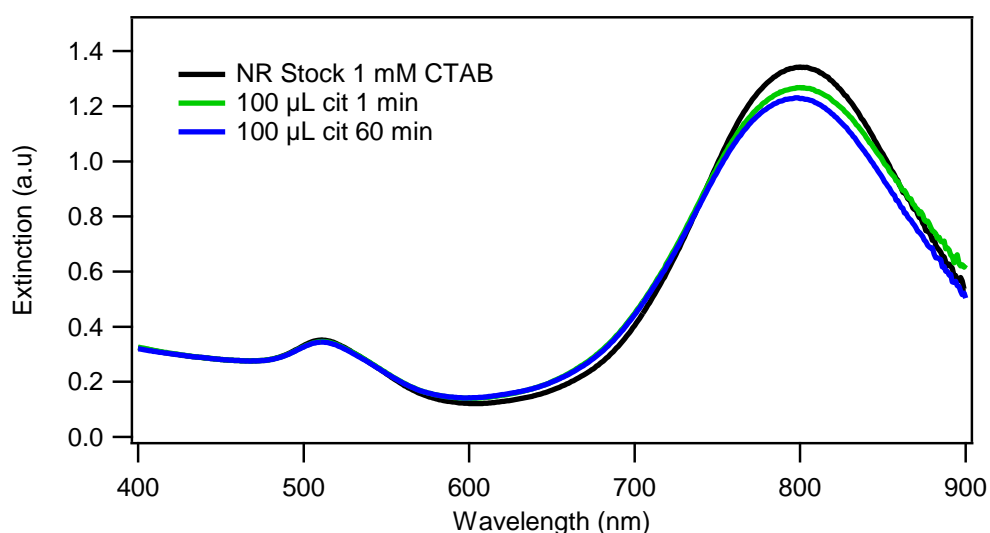


Figure 4.5. Extinction profiles of 1 mM CTAB nanorods following addition of 100 μl 1.75 mM citrate/2 ml stock nanorod solution.

As can be seen in Figure 4.5, no shift of the longitudinal plasmon band is observed following addition of citrate, even when monitored over a period of one hour. However, when the same volume of citrate is added to the same concentration of nanorod stock solution with a CTAB concentration of 0.5 mM, very different behaviour is observed, as shown in Figure 4.6.

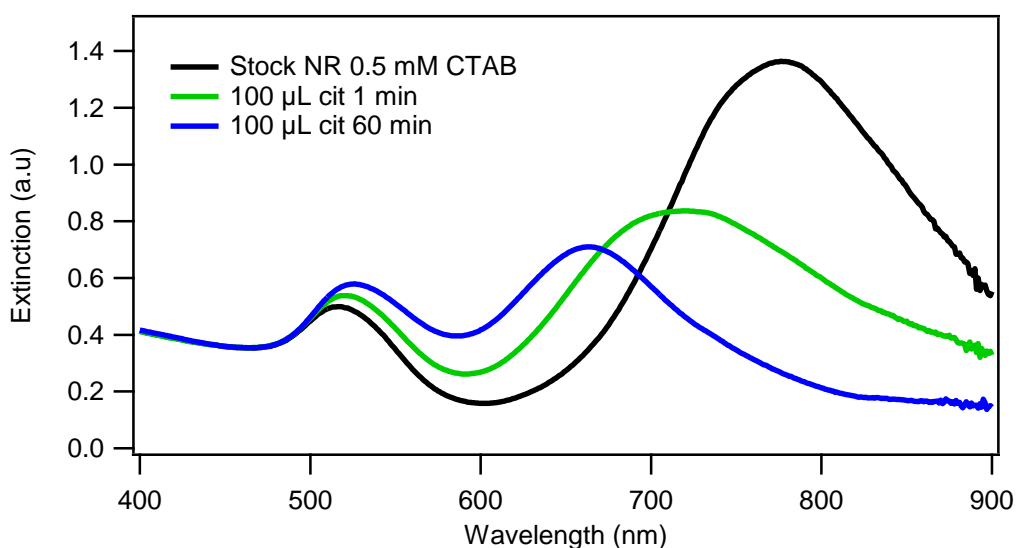


Figure 4.6. Extinction profiles of 0.5 mM CTAB nanorods following addition of 100 µl 1.75 mM citrate/2 ml stock nanorod solution.

There is a large initial shift of the longitudinal band in Figure 4.6, which continues over a period of an hour, indicating that the nanorods in 0.5 mM CTAB solution are aggregated by this volume of citrate, whilst the rods in 1 mM CTAB are unaffected by this concentration of citrate. This suggests that the higher concentration of CTAB stabilises the rods against aggregation, meaning that as the CTAB concentration increases, larger volumes of citrate are required to achieve the formation of clusters. This is in agreement with work carried out to investigate the effect of surfactant concentration on the assembly of gold nanorods onto solid surfaces, which also showed that there was a strong dependence on CTAB concentration.¹⁶⁰

4.2.4 Dependence of the Aggregation Process on Presence of DTTCl

A further parameter affecting the aggregation process is the presence of DTTCl, as can be seen in Figure 4.7, which clearly demonstrates that when a 1 μM bulk concentration of DTTCl is added to a stock nanorod solution in 1 mM CTAB, the aggregation process is drastically affected when compared to the same experiment carried out in the absence of dye. The presence of the dye is shown to cause a large increase in the level of aggregation occurring following the addition of a fixed volume of sodium citrate. It was shown previously in Chapter 3 that monodisperse rod-dye conjugates can be obtained at very high dye concentrations of up to 50 μM . The inclusion of the dye in the CTAB bilayer will have an effect on the charge density of the bilayer, and the fact that the conjugates are stable but undergo different aggregation behaviour is further circumstantial evidence for sequestering of the dye into the bilayer.

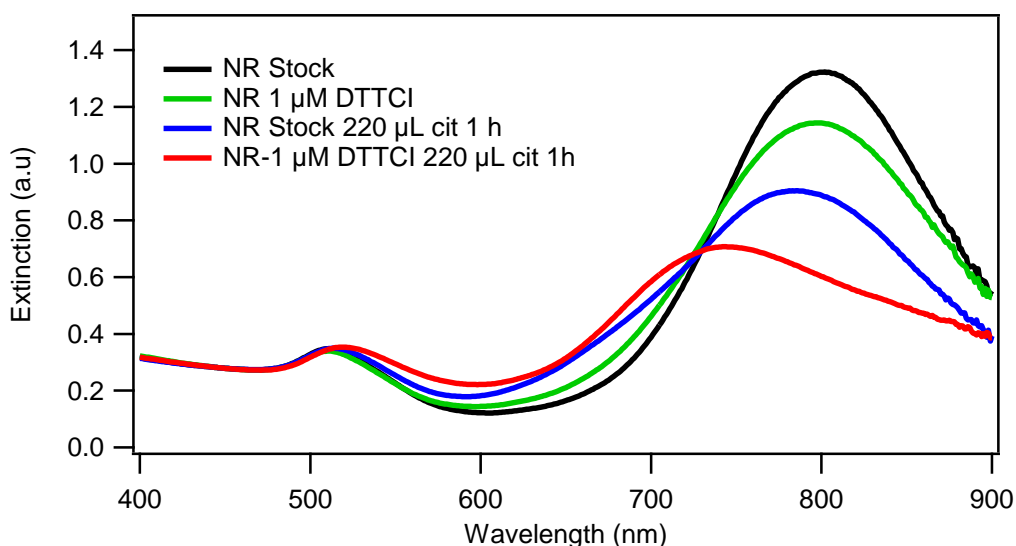


Figure 4.7. Dependence of controlled aggregation on concentration of DTTCl present.

As can be seen in Figure 4.7, a small blue shift of 1-2 nm, and dampening of the longitudinal band is observed for the nanorod samples containing 1 μM DTTCl compared with the stock nanorod solution with no dye, this is due to the adsorption of the dye. The effect of the presence of DTTCl can clearly be seen when these samples are aggregated with the same volume of sodium citrate solution. The results show that the nanorod-dye conjugates undergo a much greater degree of aggregation than nanorod samples with no dye present.

4.3 Polyelectrolyte Wrapping of Clusters

The final stage in cluster formation is the stabilization of the clusters using the polyelectrolyte, PSS. The advantages of polymer wrapping are discussed previously in Chapter 3.2. PSS coating of single nanorods has previously been reported by a number of groups.^{161, 162 94} The success of the wrapping of clusters was verified via zeta potential measurements, as shown in Table 4.1.

Sample	Zeta Potential
NR Clusters	+ 37.4
PSS wrapped clusters	- 44.6

Table 4.1. Zeta potential measurement of PSS coated and uncoated clusters.

There is a distinct change in zeta potential from a positive value for the clusters in CTAB to a negative value for the PSS coated sample, which is expected, as the CTAB is positively charged, while the polyelectrolyte is negatively charged. It has also been shown that the PSS coating does not induce further aggregation of the already formed clusters, as shown in Figure 4.8.

When the sample is PSS wrapped there is a small, approximately 2 nm red shift of the plasmon, this is due to the change in dielectric constant. The shift is negligible compared with the shift in Figure 4.3, and the peak shape remains intact, indicating that by aggregating using smaller concentrations of sodium citrate over a longer period of time, it is possible to control the level of aggregation in the final stabilized product.

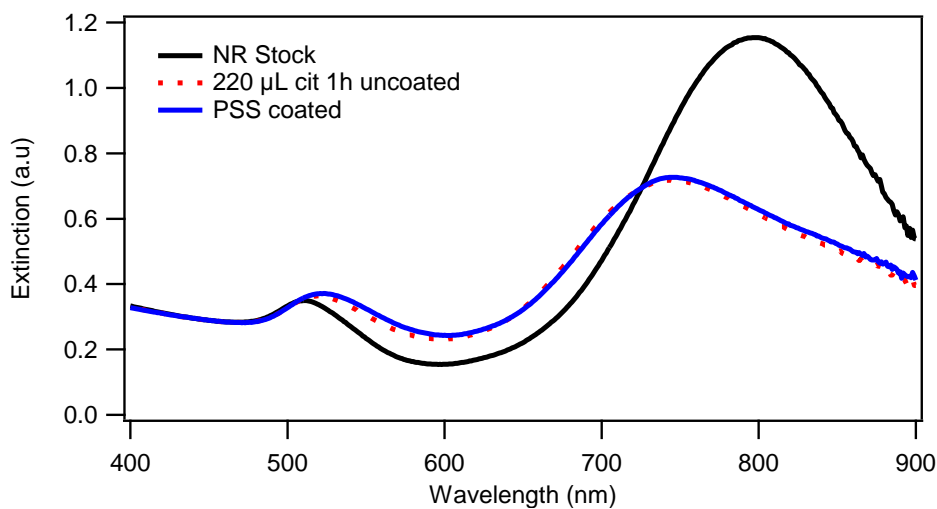


Figure 4.8. Extinction spectra of a solution of nanorod clusters acquired before and after the PSS coating step.

Furthermore, the PSS coated clusters remain stable over an extended period of time. The results in Figure 4.9 demonstrate that the extinction profile of the nanorod clusters remains unchanged over a period of eight months.

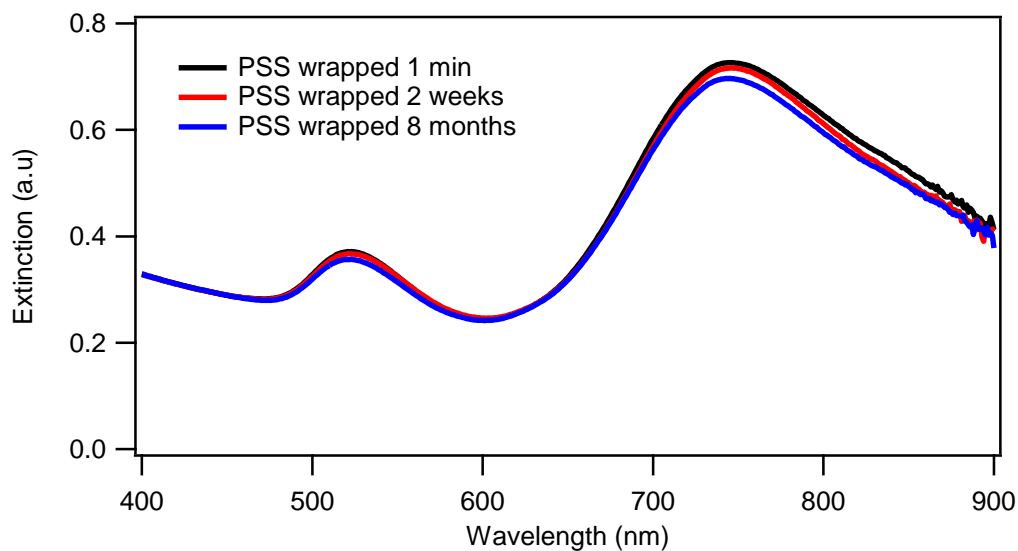


Figure 4.9. UV-vis spectra of a solution of PSS stabilised nanorod clusters acquired at various time intervals.

Figure 4.9 shows that there is no dampening or shift of the transverse or longitudinal peaks over a period of eight months, indicating that no further aggregation has taken place and that the clusters are stable.

4.4 Preparation and Characterization of SERRS Active Clusters

In this section the preparation of a range of clusters with varying levels of aggregation is discussed. The samples were prepared using the same nanorod stock solution, with the CTAB concentration fixed at 1 mM. In addition, a CTAB/DTTCl mixed layer was formed on each sample, except A, where no dye was introduced to the nanorods prior to polymer wrapping. Samples B-D were prepared following overnight equilibration of 1 μM DTTCl with the nanorod samples. Samples A and B were PSS coated without citrate-induced aggregation, while for samples C and D, different concentrations of citrate were added prior to PSS coating. The samples prepared were as follows:

- A – NR stock
- B – NR-1 μM DTTCl
- C – NR-1 μM DTTCl, aggregated to give 10 nm plasmon shift
- D – NR-1 μM DTTCl, aggregated to give 54 nm plasmon shift

All samples were polymer wrapped, and characterized via a series of techniques, including extinction measurements, SEM, NanoSight and SERRS at 633 and 785 nm excitation.

4.4.1 Extinction Analysis

The extinction spectra for each cluster following polyelectrolyte wrapping is shown in Figure 4.10.

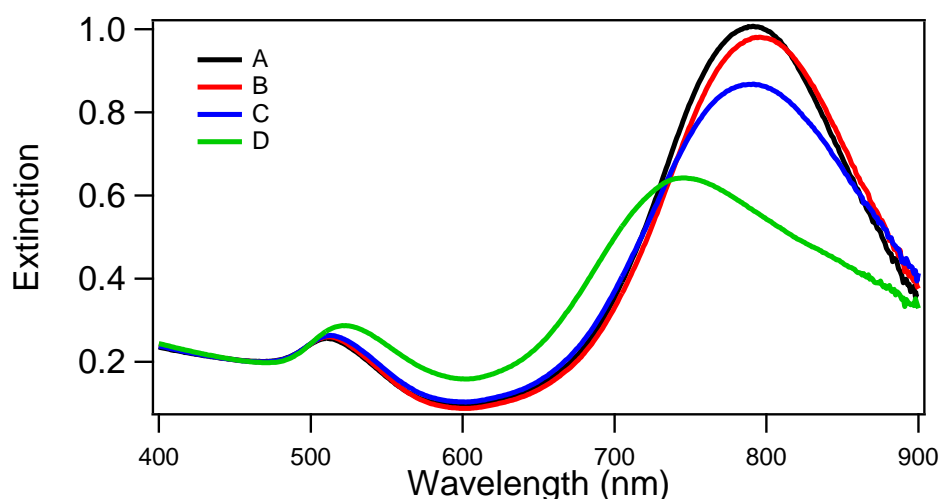


Figure 4.10. Extinction spectra of four PSS-wrapped samples, A-stock nanorods, B-nanorods with 1 μM DTTCl, C-low aggregation and D-more aggregated.

As expected, the extinction spectra of A and B are very similar, a small red shift is observed which is attributed to the adsorption of the dye. A small red-shift also occurs upon PSS coating. Following aggregation of the nanorod-dye conjugates, the longitudinal resonance for sample C is blue shifted by approximately 10 nm due to a low level of aggregation, with a larger shift of approximately 54 nm observed for sample D, where a larger amount of citrate was added.

4.4.2 SEM Analysis

SEM analysis was used to confirm that side-by-side assembly of the nanorods was taking place. Representative SEM images were obtained for both control (sample B, Figure 4.11) and assembled nanorod solutions (samples C and D, Figures 4.12 and 4.13 respectively). Efforts were made to design a methodology for deposition of each sample onto the modified Si substrates for analysis that ensured that the cluster distribution was representative of the bulk solution rather than affected by drying-induced aggregation.

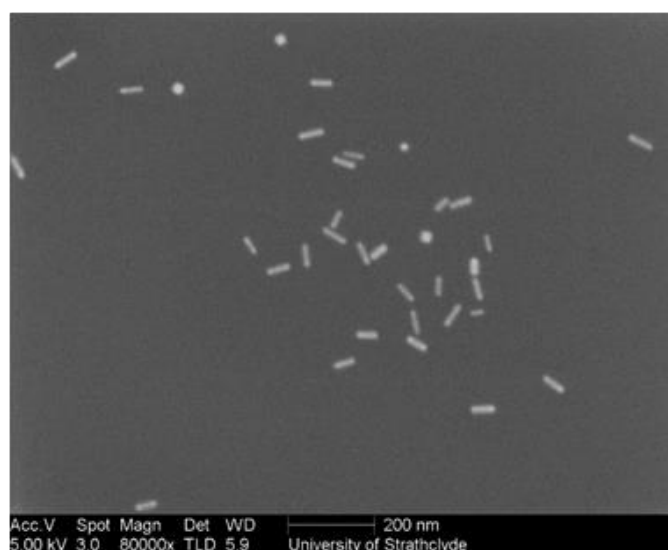


Figure 4.11. Representative SEM image of Sample B indicating the absence of aggregated rod nanostructures.

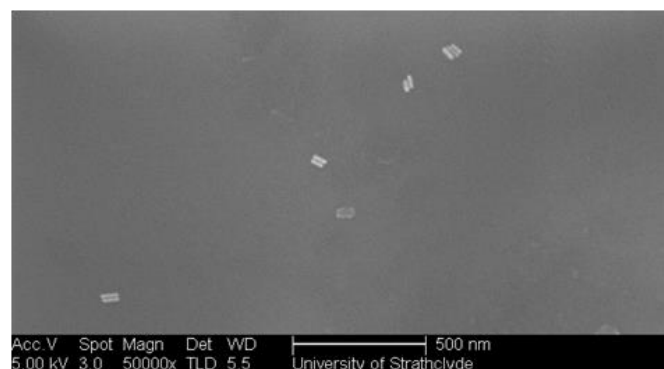
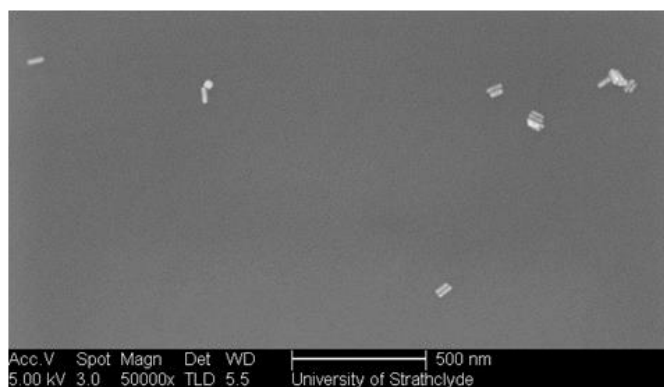


Figure 4.12. Representative SEM images of Sample C showing a low surface density of immobilized clusters typically 2-5 rods in size along with a small percentage of single rods.

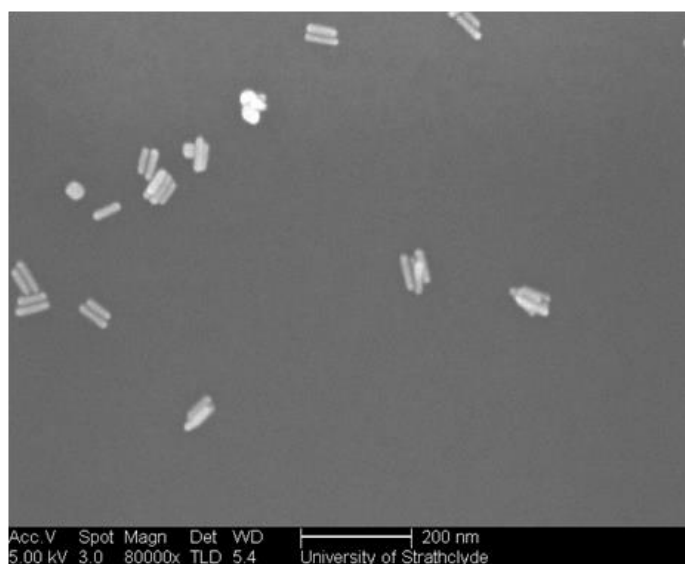


Figure 4.13. SEM image of Sample D providing further evidence for the assembly of rods into small clusters.

Analysis of multiple representative SEM images for each sample gives information on the extent of the nanorod assembly. For each sample, over 500 discrete particles/clusters were counted. For sample C, analysis indicated that 28.0% of particles/clusters were monomers, 46.2 % were dimers and 24.5% were clusters of 3-5 nanorods in size. For sample D, where more citrate was added, the corresponding fractions were 21.8%, 35.3% and 42.5% for monomers, dimers and 3-5 rod clusters respectively. The SEM images also show that the nanorods have aggregated in the desired side-by-side fashion.

4.4.3 SERRS Analysis 785 nm Excitation

The corresponding SERRS data for samples A-D at 785 nm excitation is shown in Figure 4.14.

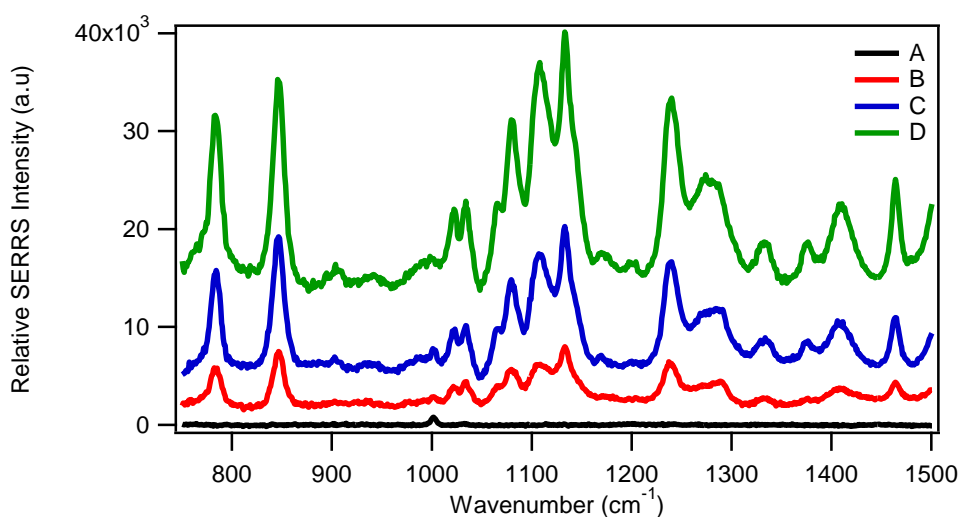


Figure. 4.14. Background corrected SERRS spectra of nanorod cluster samples A-D using an excitation wavelength of 785 nm and an accumulation time of 10 s. The Raman intensities were normalized with respect to a cyclohexane standard to allow direct comparison with SERRS intensities measured at 633 nm in Figure 4.17.

The starting rod concentrations for all samples were kept constant to ensure that comparisons could be made between samples. Sample A has no DTTCl present to prove that CTAB and the PSS do not have a significant contribution to the measured Raman signal. In the presence of DTTCl a large SERRS signal was obtained. Samples B-D also differ in how

strongly the plasmon resonance of the cluster overlaps with the 785 nm laser, as well as the solution particle density, which decreases with increased nanoparticle aggregation. It can clearly be seen that the intensity of each peak increases sharply with increased aggregation. Using the SEM results to estimate relative changes in particle concentration combined with the increased intensity suggests that the average SERRS signal per particle is enhanced approximately 4-fold for sample D compared to sample B.

Quantitative Analysis 785 nm

Quantification of the increase in SERRS intensity for each sample was carried out by focusing on the peak at 1240 cm^{-1} . The peak at 1150 cm^{-1} is larger, however, this overlaps with a small peak due to the plastic of the well-plate used for analysis. This background peak is only appreciable in the 'blank' sample, i.e. sample A, however it was decided to work with the next largest peak in order to eliminate the problem of background interference. Quantitative analysis was carried out on the raw, unprocessed data. The intensity minimum at $1255\text{ cm}^{-1} (\pm 2\text{ cm}^{-1})$ was subtracted from the maximum at $1237\text{ cm}^{-1} (\pm 2\text{ cm}^{-1})$ for each sample. These values were then used as a numerical indicator with which the relative SERRS intensities could be compared. Each measurement was carried out in triplicate, and the results were averaged to give a representative value. The results obtained, along with the associated errors, are shown in Figure 4.15.

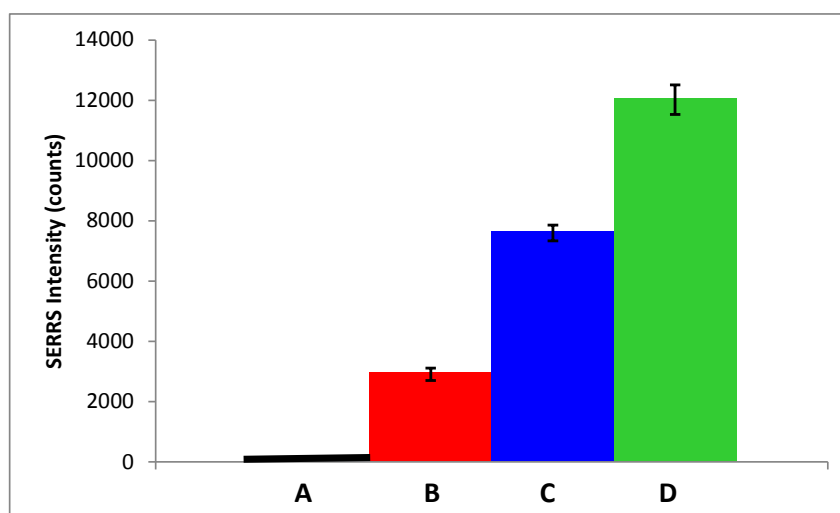


Figure 4.15. Quantification of the increase in SERRS intensity at 785 nm excitation based on the intensity minimum of the peak at $1255\text{ cm}^{-1} (\pm 2\text{ cm}^{-1})$ subtracted from the maximum at $1237\text{ cm}^{-1} (\pm 2\text{ cm}^{-1})$ for each sample.

It should also be noted that as the level of nanoparticle aggregation increases, the particle density rapidly decreases, meaning that the number of particles in the path of the laser has rapidly decreased upon increased aggregation.

4.4.4 SERRS Analysis 633 nm

Samples A-D were also analysed at a SERRS excitation wavelength of 633 nm. The background corrected data obtained was normalized with respect to C_6H_{12} to allow comparison between both sets of results, and is shown in Figure 4.16.

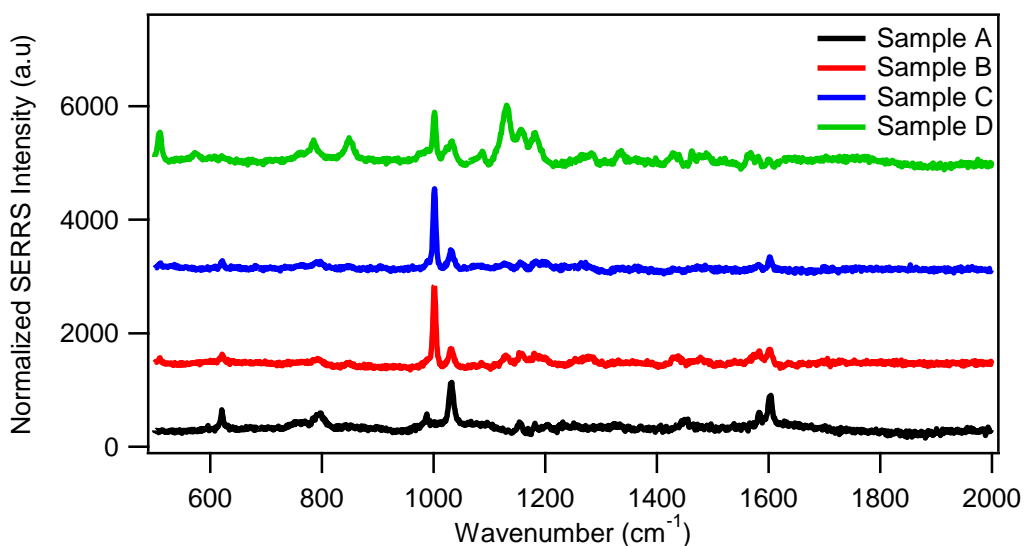


Figure 4.16. SERRS spectra of nanorod cluster samples A, B, C, and D using an excitation wavelength of 633 nm and accumulation time of 10 s. The Raman intensities were normalized with respect to a cyclohexane standard to allow direct comparison with the SERRS intensities measured at 785 nm excitation in Figure 4.15.

The data in Figure 4.16 shows that the Raman intensities obtained are considerably lower than those obtained at 785 nm excitation, the SERRS intensities obtained are in the region of 24 times lower for the 633 nm excitation than at 785 nm. The λ_L of the nanorods and clusters all fall between 800-750 nm, and the dye molecular resonance is at 754 nm, therefore, the samples do not strongly overlap with the laser excitation used. However, the data shows that large SERRS intensity increases are achieved with sample D, which can be

expected, as the longitudinal plasmon is at 750 nm, and has broadened on aggregation, leading to an increased overlap with the 633 nm laser.

Quantitative Analysis 633 nm

Quantitative analysis was carried out as described previously. The results obtained, along with the associated errors are shown in Figure 4.17.

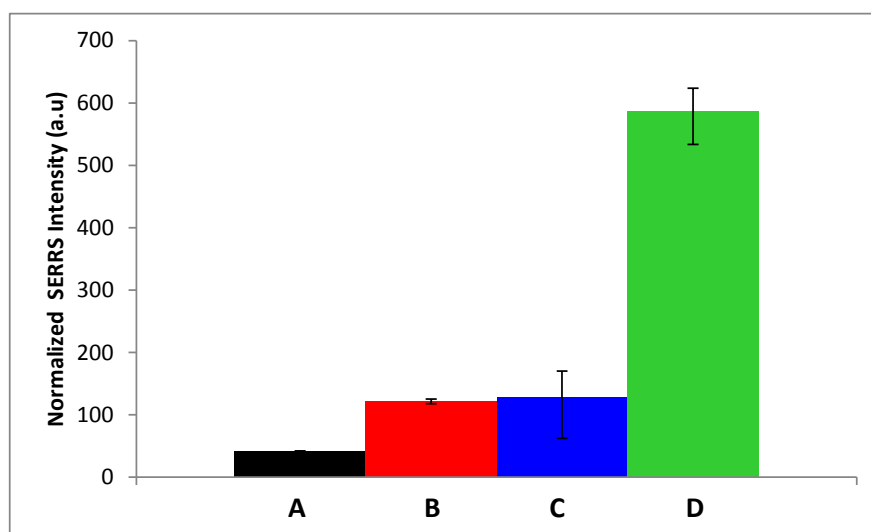


Figure 4.17. Quantification of the increase in SERRS intensity at 633 nm excitation based on the intensity minimum of the peak at 1255 cm^{-1} ($\pm 2\text{ cm}^{-1}$) subtracted from the maximum at 1237 cm^{-1} ($\pm 2\text{ cm}^{-1}$) for each sample.

The data shows that there is no significant difference in the SERRS intensities obtained for the unaggregated DTTCI-nanorod (sample B) and the sample with a low level of aggregation (sample C). There is a roughly five times increase for sample D compared with samples B and C.

4.5 Conclusions

A novel methodology for the solution-based co-assembly of gold nanorods and molecular dyes has been described. By taking advantage of the anisotropy of the nanorods, it was possible to demonstrate the controlled side-by-side assembly of these nanoparticles. Furthermore, these clusters could be stabilized in solution, allowing the first suspension based SERRS study of stabilized nanorod clusters to be performed.

Reasonable control was achieved over the final cluster size in the region of 2-5 nanorods per aggregate, with the clusters shown to remain stable in suspension following storage for eight months.

The aggregation process was found to be strongly dependent on a number of factors including the concentrations of sodium citrate, CTAB and DTTCI.

Finally, the work here correlated the SERRS intensities obtained via bulk solution measurements with the change in extinction, to show that increased levels of aggregation resulted in increased SERRS intensities, with side-by-side aggregation shown to provide up to a five times enhancements of signal.

4.6 Future Work

It would be useful to correlate the accompanying decrease in particle density with the Raman enhancements obtained, and thus, absolute enhancement factors are not reported here. This could be achieved through SERRS measurements of single clusters, rather than bulk solution measurements, which would allow these comparisons to be made.

It may also be interesting to include a wider range of cluster sizes in the study to target other resonances and to evaluate the optimum cluster size for SERRS enhancements. The study could also be further expanded to establish the parameters necessary to prepare clusters of controlled size using nanorods of varying lengths. It is likely that the side-by-side aggregation of shorter nanorods will be more difficult, and thus may require the use of alternative aggregating agents. Further work could also include the aggregation of different nanoparticle shapes, for example, aggregating rods with spheres, as well as different metals, for example, silver aggregating with gold.

Chapter 5

Creating a Universal Nanoparticle SERRS Tag for Imaging at Multiple Excitation Wavelengths Ranging From the Visible to the Near-IR

The nanorod-dye conjugates discussed in Chapters 3 and 4 offer a number of advantages for Raman measurements, mainly the excellent stability, ease of preparation, bright Raman signals without the need for an aggregation step and the potential to functionalize these tags. The data obtained in Chapter 3 demonstrates that it is possible to produce unaggregated conjugates that give bright signals at more than one laser wavelength (for example, DTDCI giving bright signals at 633 and 785 nm excitation). This is an interesting concept that will be explored in more detail in this Chapter. In order to demonstrate how bright these nanoparticle-dye conjugates are, two main concepts will be investigated, the first is the measurement of SERRS from a single nanoparticle, and secondly, the design of tags suitable for imaging applications across multiple excitation wavelengths.

The vast majority of SERRS studies reported in the literature for both bulk solution measurements and cellular imaging use reporters which are restricted to analysis at just one excitation wavelength. The multiplex detection of a mixture of five different individual dye labelled oligonucleotides conjugated to spherical silver nanoparticles and then mixed together has been reported at 514 and 633 nm.¹⁶³ However, these were individual nanoprobe mixed together prior to Raman analysis, furthermore, in order to achieve bright Raman signals, the samples had to be aggregated. Analysis was only reported across a narrow wavelength range.

The Vo-Dinh group have reported the multiplexed detection of probes prepared using gold nanostars and single dyes.¹⁶⁴ The study used four different dye-nanostar conjugates, which mixed were prior to analysis. They were successfully able to use SERRS measurements to quantify the amount of each dye present in the mixture. Analysis here was carried out at only 785 nm excitation.

Very little work has been carried out on systems with multiple dyes co-assembled on the same nanoparticle surface. Le Ru *et al* reported the simultaneous use of two analyte molecules assembled onto silver quasi-spherical colloid.¹⁶⁵ The aim of this work was to improve the sensitivity of single molecule SERRS, which the authors were able to demonstrate. The dyes were chosen as they provide distinct non-overlapping spectra at 633 nm excitation, and thus, analysis was carried out at just one wavelength.

The concept here is to exploit the very bright Raman signals obtained from the nanotags prepared earlier, and to design a single nanoparticle tag that gives large Raman signals at excitation wavelengths ranging from the visible to the near-IR. These tags will be known as Universal SERRS Tags (USTs).

A key question to address here is why would such a system be desirable? There are a number of advantages to this approach, in particular the development of shelf-stable nanotags that are suitable for SERRS analysis across a wide range of excitation wavelengths. Typically Raman reporters are designed to provide bright signals at just one wavelength, and changing the wavelength to be used for analysis means having to rethink the nanoparticle and dye combinations to be used. These tags will also be bright enough to circumvent any of the issues typically associated with the aggregation of nanoparticles for SERRS. It is also envisaged that this class of tags will be particularly useful for co-localization studies involving other dye or nanoparticle molecular probes. Furthermore, the surface chemistry of these tags has been designed to keep in mind the need for simple functionalization methods, which will be discussed in more detail in Chapter 6.

For these tags to be successful there are a range of requirements that must be met, firstly, they must be stable in complex environments, a key initial application for the USTs will be for cell analysis, and therefore, the conjugates must be stable in high salt concentrations. Secondly, the tags must be easy to make and reproducible. Thirdly, it must be possible to biofunctionalize these systems. For the tags to be described as Universal SERRS tags, it is necessary to demonstrate the ability to image at all of the common Raman excitation wavelengths available (514, 532, 633, 785 and 1064 nm). Finally, successful demonstration of the USTs suitability is desired for imaging based applications, preferably at the single particle level.

5.1 Selection of Dyes for Universal SERRS Tags

In order to create tags suitable for multi-wavelength Raman analysis a range of candidate dyes were screened for investigation, the structures of each dye are summarised below.

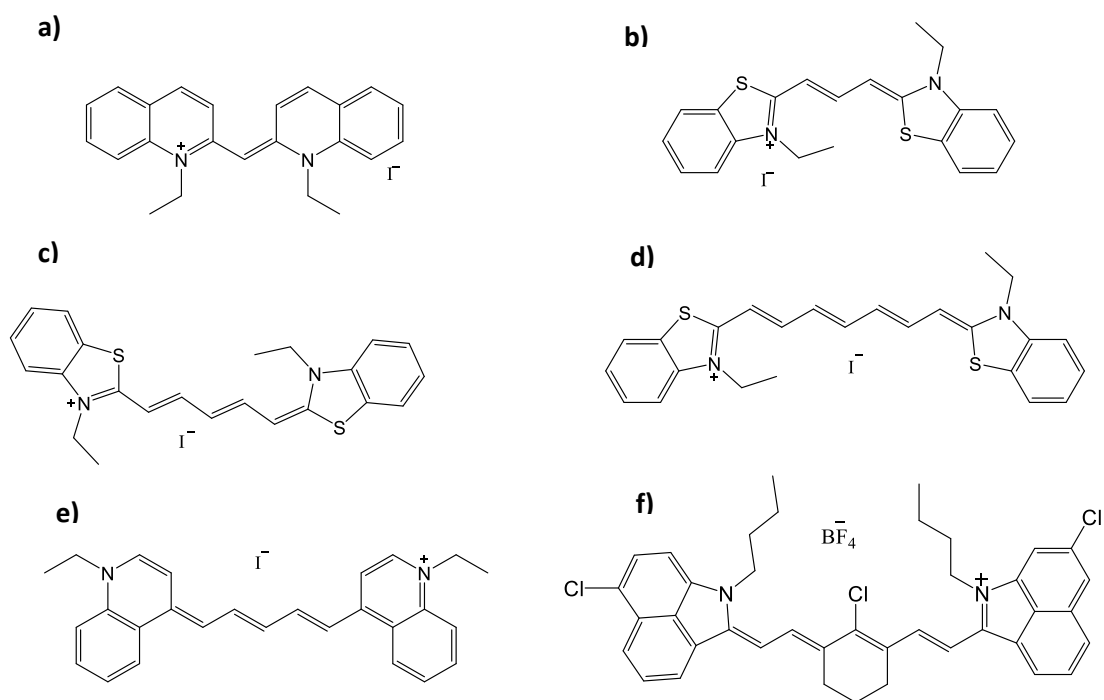


Fig 5.1. Structures of all dyes a) DCI, b) DTCl, c) DTDCI, d) DTTCl, e) DDCI and f) IR1048.

Each dye used in this study is structurally similar, they have a quaternary ammonium group, and are hydrophobic, and thus are expected to have a similar affinity for the CTAB bilayer as discussed previously. The dyes used in Chapter 3 (DTDCI and DTTCl) are evaluated here, along with several others.

In order to determine the wavelength range covered by each dye a 10 μ M solution of each dye in 1 mM CTAB was prepared, and the extinction spectra were measured as shown in Figure 5.2.

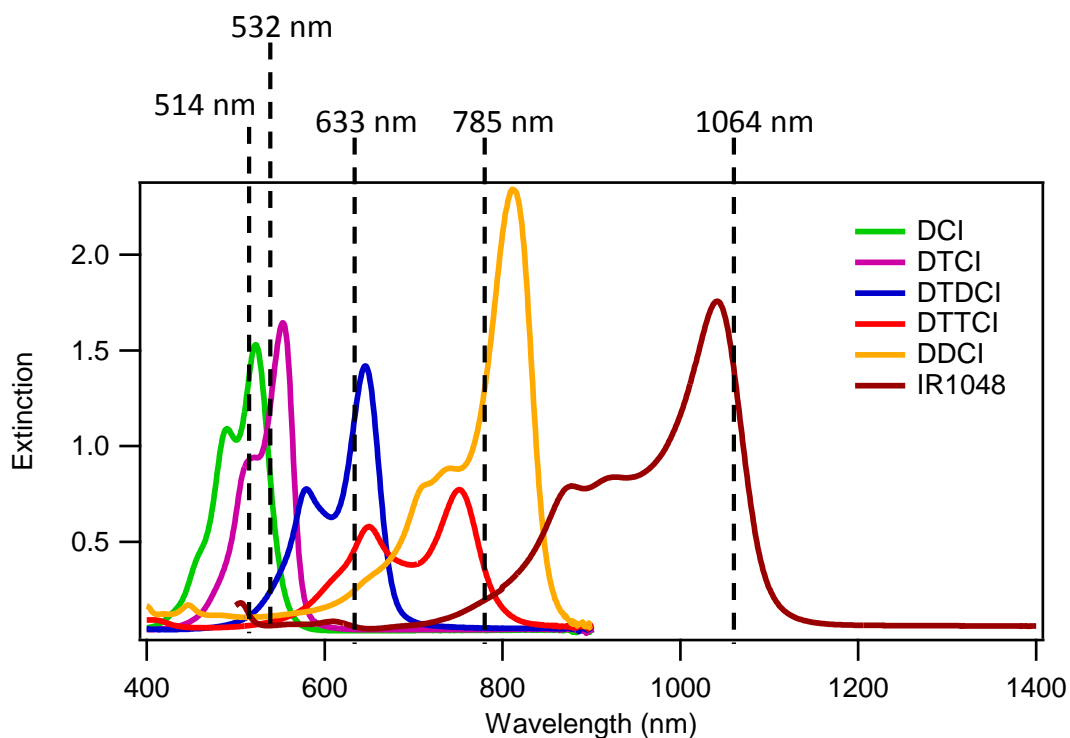


Figure 5.2. Extinction spectra of 10 μM dye solutions in 1 mM CTAB. The positions of common Raman laser excitation wavelengths are also shown.

The extinction spectra show that the absorbance maxima for the dyes selected for comparison cover a broad range of wavelengths, from 524 nm to 1048 nm. Some of the dyes have fairly broad absorption profiles, meaning these dyes may be active across multiple laser excitation wavelengths, this leads to the possibility of utilising combinations of dyes to create tags that are Raman active across all available laser excitation wavelengths.

5.2. Characterization of Individual Nanorod-Dye Conjugates

In order to determine which dyes were most suitable for use as Universal SERRS Tags, a range of nanorod-dye conjugates were prepared and characterized using extinction measurements to investigate plasmon-dye interactions and ensure the samples remain unaggregated, as well as Raman measurements to evaluate the usefulness of each dye at all of the laser excitation wavelengths available (514, 532, 633, 785 and 1064 nm).

All samples used throughout this Chapter (with the exception of Section 5.7) were prepared using a stock nanorod solution in 1 mM CTAB with SPR $\lambda_L = 815$ nm. Dyes were introduced and allowed to equilibrate for 14 hours, following this, the NR-dye conjugates were PSS wrapped and centrifuged and resuspended in distilled water a minimum of three times to remove excess dye as discussed previously (Chapter 3.2). This ensures that only dye present in the CTAB bilayer contributed to resonance coupling and Raman signals

5.2.1 Extinction Spectra of Individual-Dye NR Conjugates

NR-dye conjugates, with a bulk dye concentration of 10 μ M were prepared for each dye.

The extinction spectra for the polymer-wrapped stock nanorods and each NR-dye conjugate are shown in Figure 5.3. As in Chapter 3.5, successful incorporation of the dye is indicated by a shift and dampening of the longitudinal plasmon band. As can be seen, for each different NR-dye combination the resulting plasmon shift varies. The effect of each dye on the plasmon shift of the λ_L peak is summarised in Table 5.1.

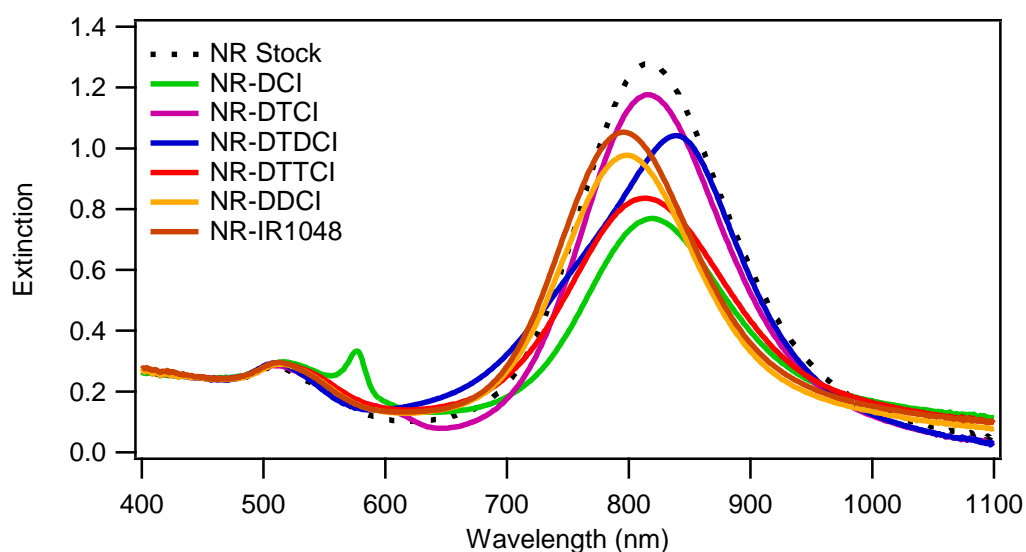


Figure 5.3. Extinction spectra of PSS-wrapped NR-dye conjugates. Samples were prepared using NRs with $\lambda_L = 815$ nm and 10 μ M bulk dye concentrations. All samples were centrifuged three times following polymer wrapping and resuspended in distilled water to remove any excess dye present.

Dye	Dye λ_{\max}	Transverse peak position (λ_T)	Longitudinal peak position (λ_L)	λ_L shift
NR Stock		510	815	
DCI	524	516	818	3nm red
DTCI	560	512	816	1nm red
DTDCI	655	510	839	24nm red
DTTCI	765	515	817	2nm red
DDCI	814	515	799	16nm red
IR1048	1048	514	796	19nm blue

Table 5.1. Resonance coupling between NRs with $\lambda_L = 815$ nm and each dye, bulk dye concentration is 10 μ M. All samples have been PSS-wrapped and centrifuged to remove any excess dye present.

The effect of dye molecular resonance and nanoparticle plasmon resonance on resonance coupling is discussed in depth in Chapter 3.5. NR-dye conjugates prepared using DCI and DTCI undergo small λ_L plasmon shifts, and therefore are amongst the weakest plasmon coupling here. As in Chapter 3, DTDCI again experiences the strongest plasmon coupling, which is again unexpected as the dye molecular resonance and NR LSPR are far apart (see Chapter 3.5 for further discussion). For these NRs, with a longitudinal LSPR at 815 nm, samples prepared using DTTCI change only slightly, with a λ_L shift of only 2 nm. DDCI and IR1048 both result in larger plasmon shifts, as would be predicted based on previous studies.^{122, 147}

It is also interesting to note that for the sample prepared using DCI, a third peak appears at 577 nm, this is not the absorbance maximum for a dye-only solution (which occurs at 524 nm). The peak is present in samples prepared using different dye concentrations, as shown in Figure 5.4.

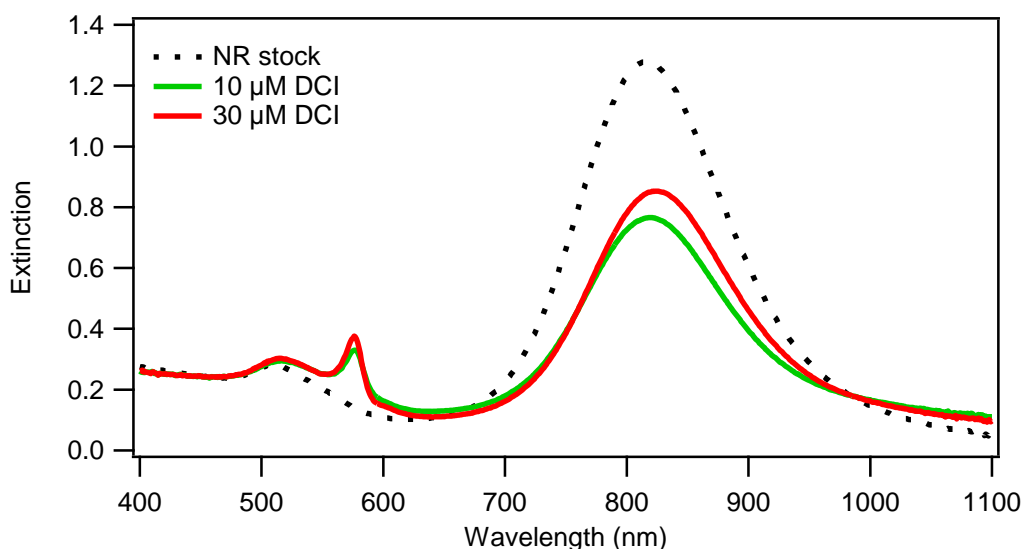


Figure 5.4. Extinction spectra of PSS-wrapped NR Stock, and NR-dye conjugates with 10 μM and 30 μM DCI. Samples have been centrifuged and resuspended three times to remove any excess dye present.

The samples prepared containing 10 μM dye were centrifuged three times following PSS wrapping, while the samples prepared using 30 μM DCI were centrifuged five times, to ensure that any excess dye was removed from the solution. The extinction spectra show that the conjugates prepared using 30 μM dye undergo a larger plasmon red shift than those prepared with the lower dye concentration. The peak associated with DCI is present for both samples, indicating that it is associated with dye adsorbed onto the nanoparticle surface.

5.2.2 Raman characterization of Individual Nanorod-Dye Conjugates at a Range of Common Excitation Wavelengths

The PSS-wrapped samples of each individual dye-NR conjugate described earlier were analysed at all available Raman excitation wavelengths (514, 532, 633, 785 and 1064 nm). Three different instruments were used for analysis (633 and 785 nm measurements were performed on the same instrument), the experimental conditions used are discussed in Section 2.19. All data was collected at an integration time of 10 seconds. All data was normalized with respect to the cyclohexane peak at 1029 cm^{-1} ($\pm 2\text{ cm}^{-1}$). This allows comparison of data collected at different laser excitation wavelengths.

Any excess dye present was removed via multiple centrifuge and resuspension steps to ensure that Raman spectra obtained were from dyes present in the CTAB bilayer, and there was negligible interference from free dyes in solution. The results obtained for each sample at every wavelength are shown in Figures 5.5-5.10.

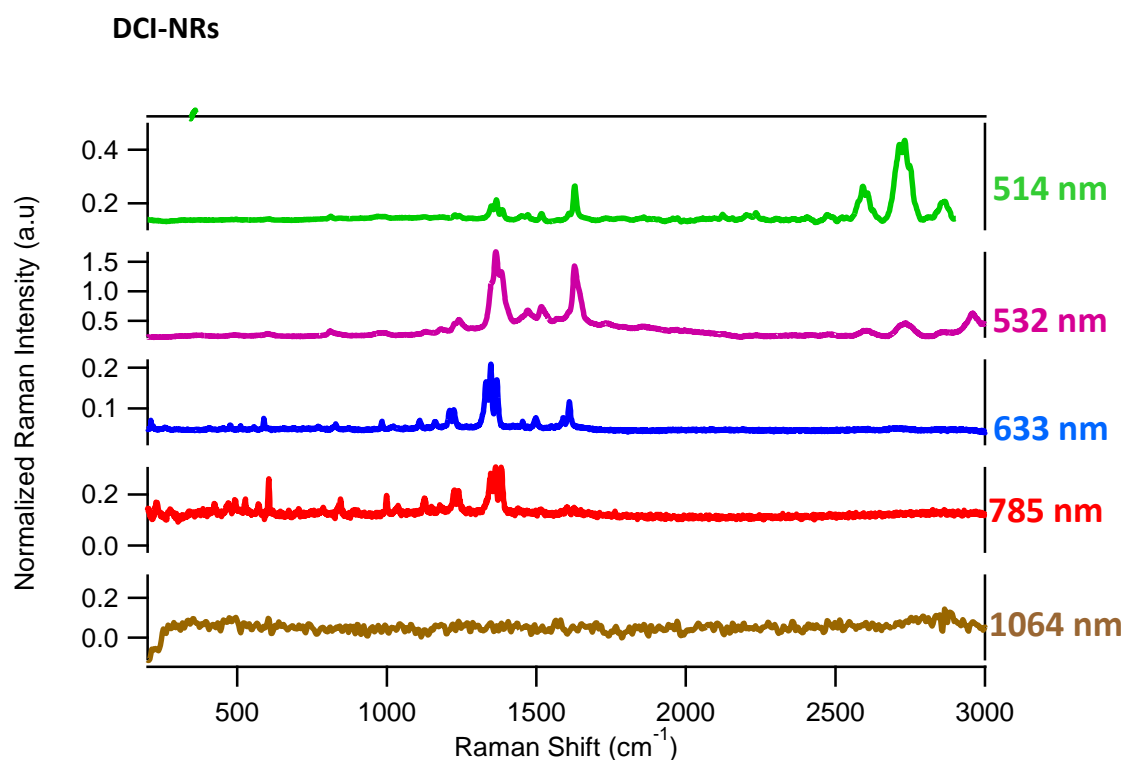


Figure 5.5. Raman analysis of NR-dye conjugates prepared with $10 \mu\text{M}$ DCI (dye absorbance maximum 524 nm) at laser excitation wavelengths ranging from 514-1064 nm. Samples have been polymer wrapped and centrifuged three times to remove any excess free dye. Data has been baseline corrected and normalized with respect to the C_6H_{12} peak at $1029 \text{ cm}^{-1} (\pm 2 \text{ cm}^{-1})$

As shown previously in Figure 5.2, DCI has an absorbance maximum at 524 nm, suggesting that this dye should give good SE(R)RS signals at 514 and 532 nm. The data in Figure 5.5 demonstrates that this is indeed the case, however, a strong signal is also obtained at 633 nm excitation, and a small Raman signal can be seen at 785 nm excitation. The strong signals and fairly simple Raman profile shapes mean that DCI seems to be a promising dye for Raman experiments, although this is complicated somewhat because the spectral shape obtained can be seen to vary at every wavelength analysed here, even between 514 and 532 nm excitations.

The second dye to be analysed is DTCl, the data obtained was normalized as before and is shown in Figure 5.6.

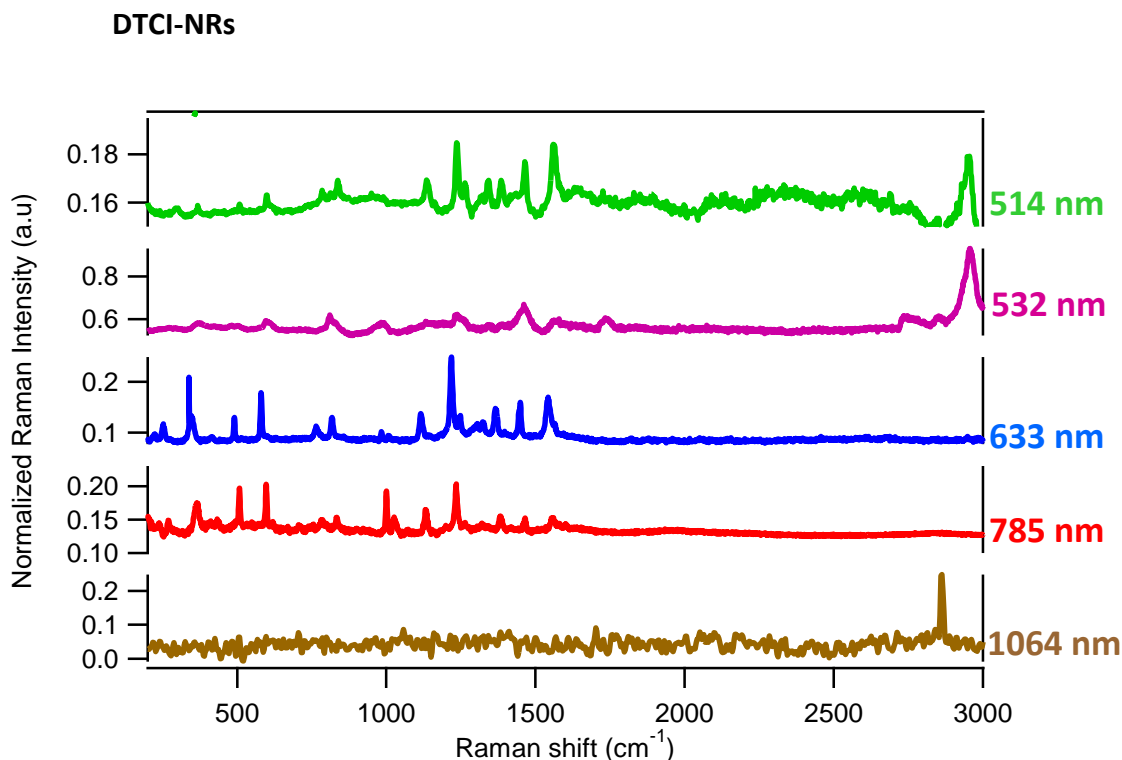


Figure 5.6. Raman analysis of NR-dye conjugates prepared with 10 μM DTCl (dye absorbance maximum 560 nm) at laser excitation wavelengths ranging from 514-1064 nm. Samples have been polymer wrapped and centrifuged three times to remove any excess free dye. Data has been baseline corrected and normalized with respect to the C_6H_{12} peak at 1029 cm^{-1} ($\pm 2 \text{ cm}^{-1}$).

The absorbance maximum for DTCl is 560 nm, and the extinction spectra in Figure 5.2 shows a strong overlap at 514 and 532 nm, suggesting that this dye should perform well at these laser excitations. The structure of DTCl is very similar to DCI, which may suggest that this dye will display similar Raman behaviour, however, it can be seen in Figure 5.6 that DTCl has a strong signal at 514 nm, with signal intensities comparable to DCI at this wavelength, but no signal was obtained at 532 nm excitation. DTCl also displays a reasonably strong SE(R)RS response at 633 nm. The lack of response at 532 nm excitation would not be predicted based on the absorption behaviour of the dye. The data obtained for conjugates prepared using DTDCI and DTTCl is shown in Figures 5.7 and 5.8 respectively.

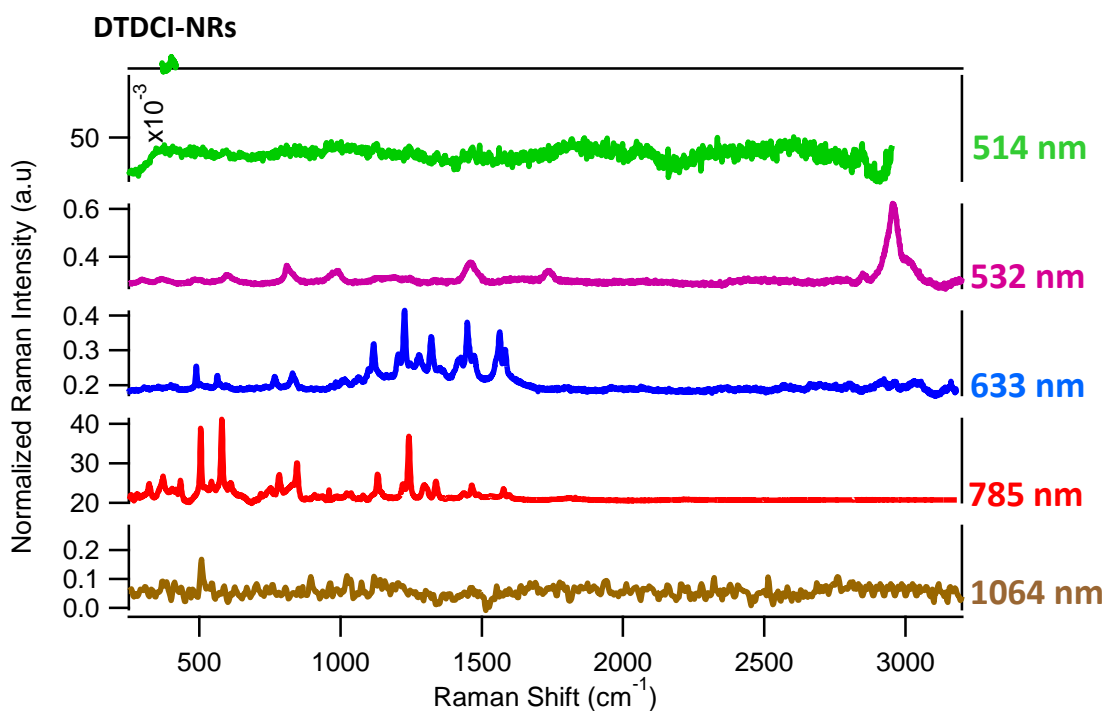


Figure 5.7. Raman analysis of NR-dye conjugates prepared with 10 μM DTDCI (dye absorbance maximum 655 nm) at laser excitation wavelengths ranging from 514-1064 nm. Samples have been polymer wrapped and centrifuged three times to remove any excess free dye. Data has been baseline corrected and normalized with respect to the C_6H_{12} peak at 1029 cm^{-1} ($\pm 2 \text{ cm}^{-1}$) to allow comparison between data obtained at different excitation wavelengths.

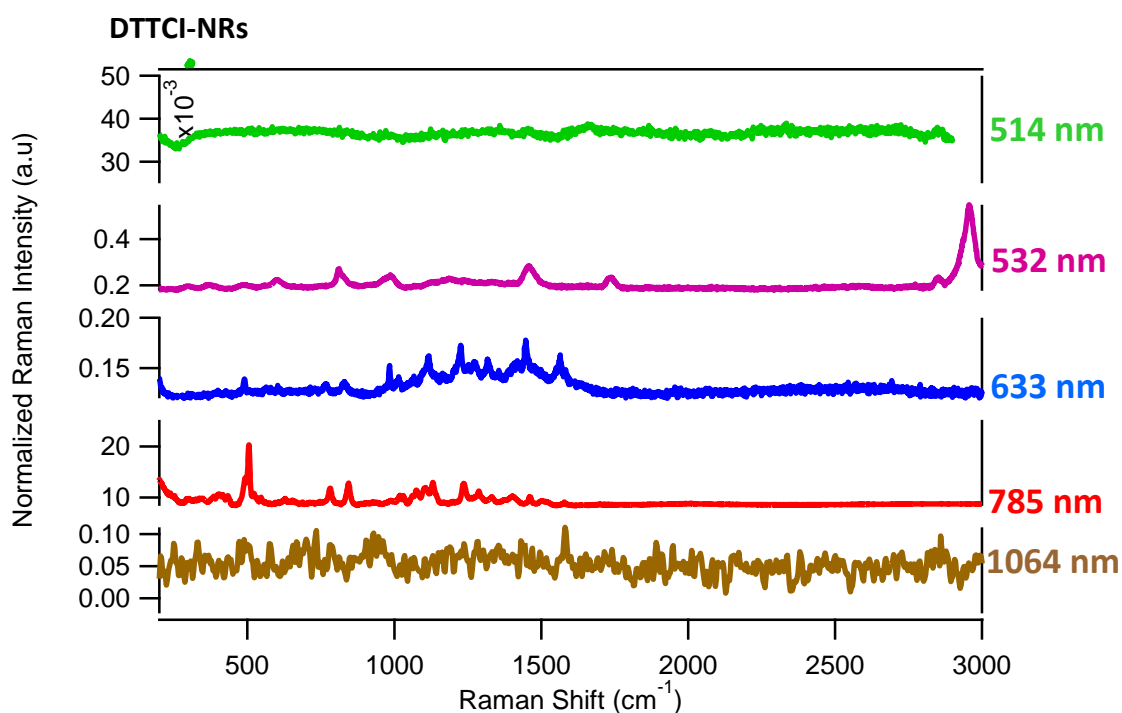


Figure 5.8. Raman analysis of NR-dye conjugates prepared with 10 μM DTTCI (dye absorbance maximum 765 nm) at laser excitation wavelengths ranging from 514-1064 nm. Samples have been polymer wrapped and centrifuged three times to remove any excess free dye. Data has been baseline corrected and normalized with respect to the C_6H_{12} peak at 1029 cm^{-1} ($\pm 2 \text{ cm}^{-1}$) to allow comparison between data obtained at different excitation wavelengths.

DTDCI and DTTCl were studied extensively in Chapter 3. DTDCI was shown to provide large Raman signals at 633 and 785 nm excitations when combined with a nanorod with λ_L at 770 nm. While DTTCl was found to demonstrate large signals at 785 nm excitation, with smaller signals at obtained at 633 nm. The samples in this Chapter are prepared using nanorods with λ_L at 815 nm, this change in LSPR may alter the SE(R)RS behaviour of the dye. For DTDCI, however, it can be seen that in this case, the rod-dye conjugate still displays very high signal intensities at 633 and 785 nm excitations, with no signal obtained at other laser excitations. The signal obtained at 633 nm is stronger than that obtained for the previous two dyes, DCI and DTCl at this wavelength.

In the case of conjugates prepared using DTTCl, the data in Figure 5.8 shows that when adsorbed onto the longer rods with LSPR at 815 nm, the conjugates display the same behaviour, with no signal observed at the other laser excitations. The signal intensities obtained at 785 nm appear to be weaker for DTTCl than for DTDCI shown in Figure 5.7, this may be a result of the poor coupling now demonstrated by DTTCl and the λ_L 815 nm NRs, with only a 2 nm plasmon shift (see Table 5.1), compared to previously in Chapter 3 with the λ_L 770 nm NRs. The conjugates prepared here using DTDCI undergo a plasmon shift of 24 nm, despite there being negligible overlap between the dye and the nanorod λ_L , this was also observed in Chapter 3, and again here, conjugates prepared using this dye display bright Raman signals.

Figure 5.9 shows the SE(R)RS profiles obtained for a stock solution of NR-DDCI, the data obtained demonstrates that DDCl is a very poor dye for Raman purposes, with only a very weak spectrum obtained at 785 nm excitation, and no signal at all other excitation wavelengths. The poor performance of DDCl is unexpected, as the dye is structurally similar to the previous dyes investigated, meaning that there should be good partitioning of the dye into the CTAB bilayer. The NR-DDCl conjugates displayed large plasmon shifts (see Table 5.1), indicating that DDCl is present in the bilayer. Furthermore, the final λ_L position for this dye-rod combination was 799 nm, providing very good overlap with the 785 nm excitation wavelength, making the poor performance of this dye at this wavelength all the more unexpected.

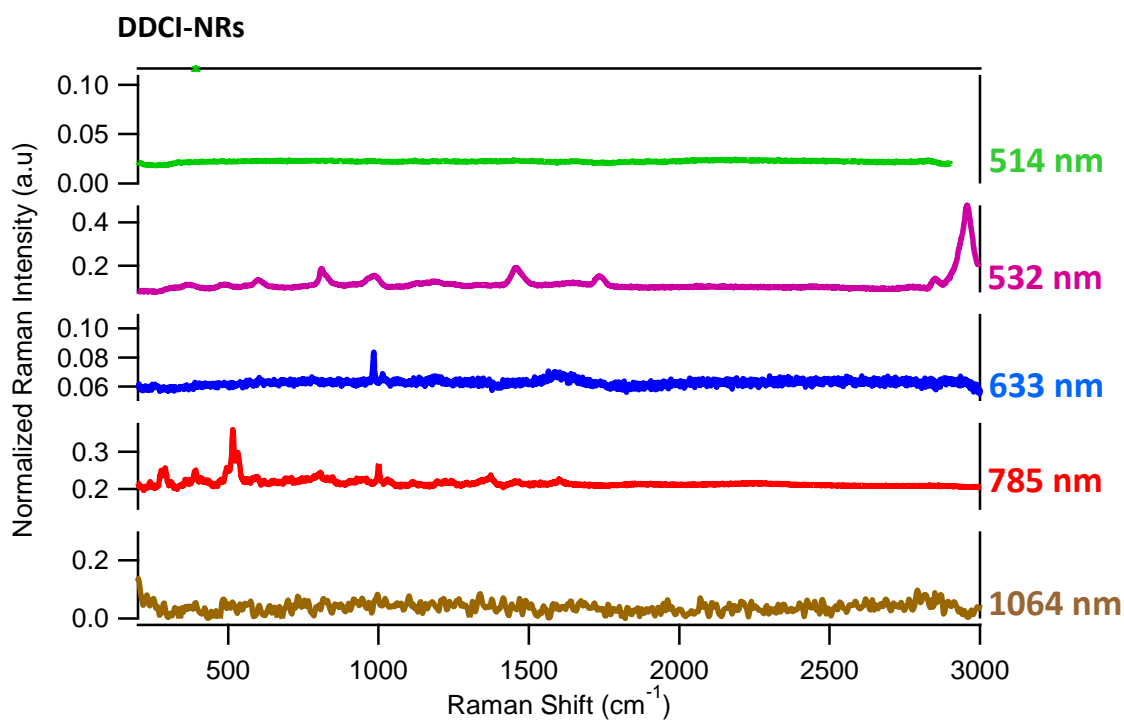


Figure 5.9. Raman analysis of NR-dye conjugates prepared with 10 μM DDCI (dye absorbance maximum 814 nm) at laser excitation wavelengths ranging from 514-1064 nm. Samples have been polymer wrapped and centrifuged three times to remove any excess free dye. Data has been baseline corrected and normalized with respect to the C_6H_{12} peak at $1029\text{ cm}^{-1} (\pm 2\text{ cm}^{-1})$ to allow comparison between data obtained at different excitation wavelengths.

The final dye investigated here is IR1048, the SE(R)RS data obtained is shown in Figure 5.10. IR1048 also displays weak Raman signals across all wavelengths from 514-633 nm, which may be expected as the dye absorbance maximum is 1064 nm, and therefore does not experience any overlap in this range. A weak signal is observed at 785 nm, however IR1048 provides the strongest SE(R)RS signals at 1064 nm excitation of all of the dyes investigated.

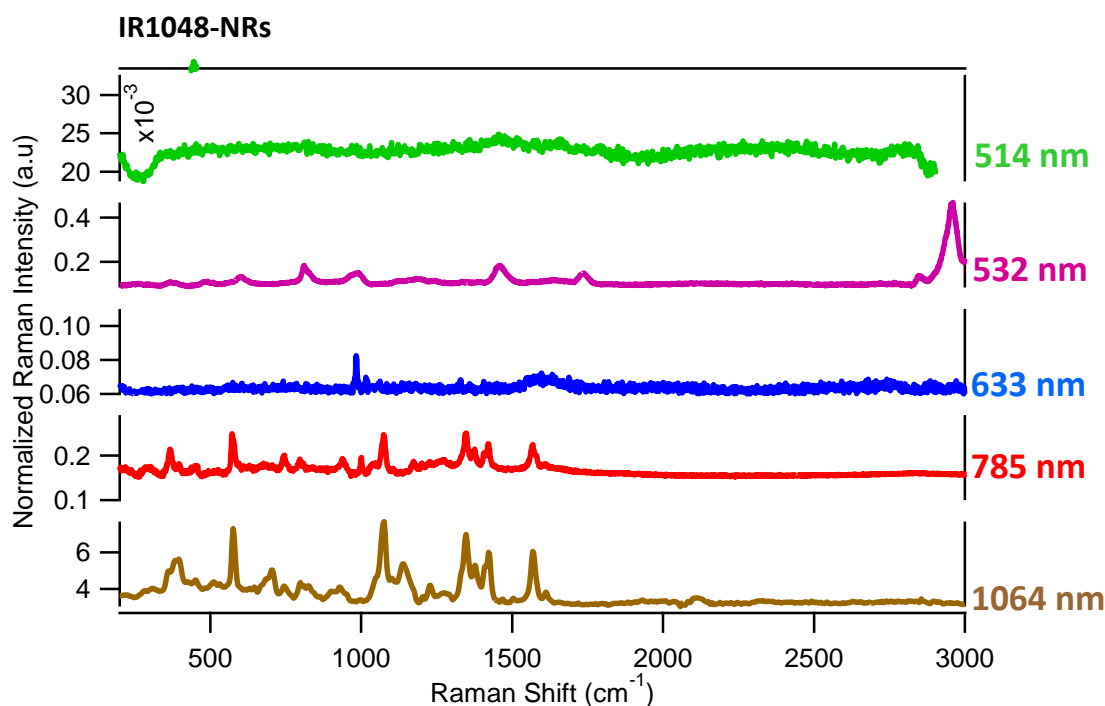


Figure 5.10. Raman analysis of NR-dye conjugates prepared with 10 μM IR1048 (dye absorbance maximum 1048 nm) at laser excitation wavelengths ranging from 514-1064 nm. Samples have been polymer wrapped and centrifuged three times to remove any excess free dye. Data has been baseline corrected and normalized with respect to the C_6H_{12} peak at 1029 cm^{-1} ($\pm 2\text{ cm}^{-1}$) to allow comparison between data obtained at different excitation wavelengths.

The compiled results of the SE(R)RS experiments are outlined below:

Dye	Dye abs	λ_L	514nm	532nm	633nm	785nm	1064nm
DCI	524	818	Strong	Strong	Yes	Weak	No
DTCI	560	816	Weak	No	Yes	Weak	No
DTDCI	655	839	No	No	Strong	Strong	No
DTTCI	765	817	No	No	Weak	Yes	No
DDCI	814	799	No	No	No	Weak	No
IR1048	1048	796	No	No	No	Weak	Strong

Table 5.2. Performance of individual dyes at all Raman wavelengths. The strongest performing dye at each wavelength is highlighted.

No one dye displays strong Raman signals across all excitation wavelengths, and that dye performances vary widely. DCI is effective across the widest range of excitations, with strong signals at 514 and 532 nm, with signal also obtained at 633 nm excitation, while IR1048 for example is only active at 1064nm excitation.

5.3 Preparation of Universal SERRS Tags

Since no individual dye investigated here gives coverage across the full range of Raman excitation wavelengths, a new strategy must be devised for the preparation of the USTs, as outlined in Figure 5.11.

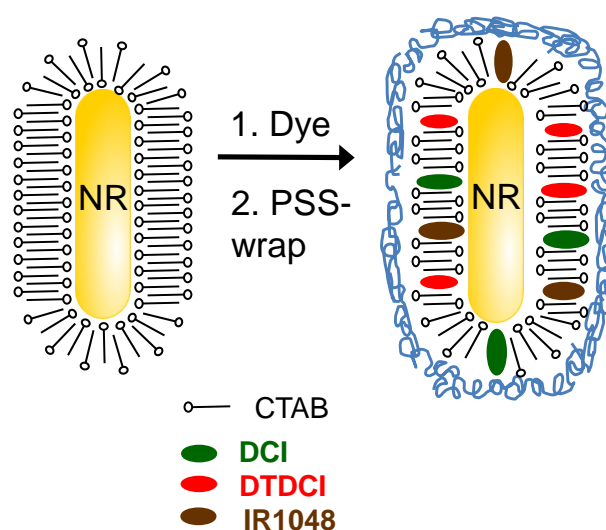


Figure 5.11. Schematic outlining the preparation of Universal SERRS Tags. A nanorod stock solution is prepared and resuspended in 1 mM CTAB solution as before. The first step is to introduce multiple dyes, in this case, three, and allow these to equilibrate for 14 h prior to PSS wrapping as before.

The proposed solution is to use multiple dyes to prepare the Universal SERRS Tags, rather than one individual dye in the preparation of the NR-dye conjugates. Each dye will be sequestered into the CTAB bilayer as before, and the conjugate will be stabilized using PSS. Based on the data in Figures 5.5-5.10 and Table 5.2, it was hypothesised that the combination of DCI, DTDCI and IR1048 would be the most likely to provide signal over the full range of Raman excitation wavelengths selected.

5.4 Addition of Dyes When Preparing Universal SERRS Tags

Universal SERRS Tags were prepared using the same NR stock as previously in this Chapter, with $\lambda_L = 815$ nm, and 10 μM DCI, 10 μM DTDCI and 10 μM IR1048, i.e. a 30 μM bulk total dye concentration. As demonstrated earlier in Chapter 3, Figure 3.12, the maximum surface coverage for DTDCI and DTTCl was found to occur at bulk dye concentrations above 50 μM . The data also showed that at 30 μM bulk dye concentrations, approximately 75-80 % of the available sites were occupied. The hydrophobicity and size of the dyes used to prepare the USTs varies, therefore at 30 μM bulk dye concentration, it is possible there will be competition between the dyes due to the high level of occupation of the available sites. In this section, the importance of the order of addition of DCI, DTDCI and IR1048 will be demonstrated.

5.4.1 All Three Dyes Added Simultaneously

Figures 5.12 and 5.13 show the extinction and Raman results obtained when all three dyes were introduced simultaneously. The dyes were premixed prior to addition to the nanorod stock solution and then allowed to equilibrate for 14 h after which the sample was polymer wrapped using PSS as before. The USTs were then centrifuged and resuspended in distilled water five times to ensure removal of any excess dye.

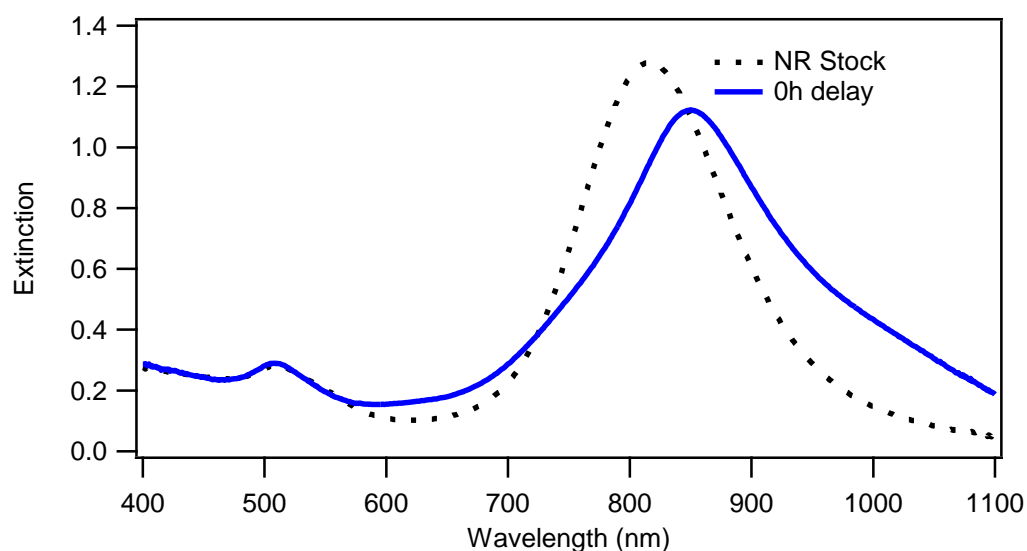


Figure 5.12. Extinction profiles obtained for the PSS wrapped NR stock solution, $\lambda_L = 815$ nm and for the Universal SERRS Tags, where 10 μM DCI, IR1048 and DTDCI are simultaneously introduced to the nanorod stock solution, the sample was then allowed to equilibrate for 14 h prior to PSS wrapping.

The LSPR peak for the USTs is significantly broader than the stock NR solution, this was not seen for the individual dye-rod conjugates in the previous section. Furthermore, the stability of the conjugate was found to be good, and the ratio of dampening of the λ_L peak to the broadening of the spectrum is not typical of nanorod aggregation (see Chapter 4).

When the extinction spectrum of the USTs where the dyes are added simultaneously is compared with the spectra for 10 μM DCI only, it can be seen that the peak at 577 nm is not present, this suggests that DCI may not be present in the USTs. Repeat preparations of this sample all showed the same peak shape. This observation along with the broadening of the extinction spectrum may be a result of aggregation of the dye molecules.

The sample was analysed at all available Raman excitation wavelengths, the normalized spectra are shown in Figure 5.13.

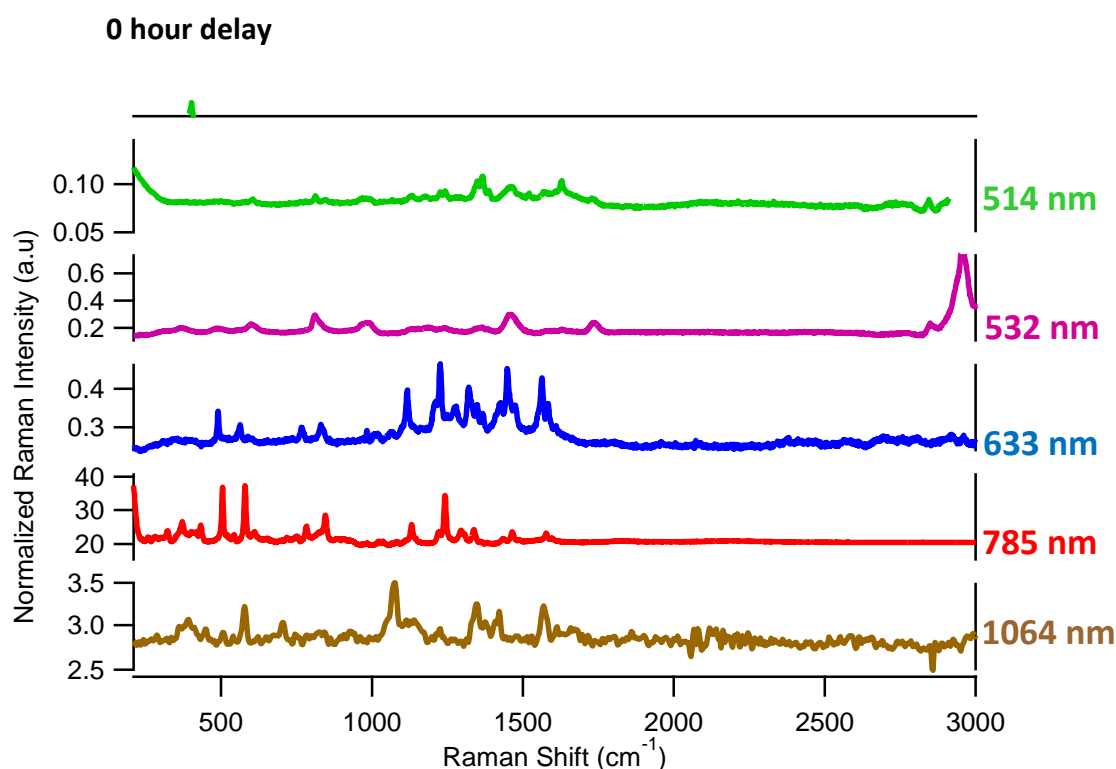


Figure 5.13. Raman analysis of PSS-wrapped Universal SERRS Tags prepared using NRs with $\lambda_L = 815$ nm, and 10 μM DCI, 10 μM DTDCI and 10 μM IR1048. Dyes were added at the same time and allowed to equilibrate for 14 hours prior to PSS wrapping. Data has been baseline corrected and normalized with respect to the C_6H_{12} peak at $1029 \text{ cm}^{-1} (\pm 2 \text{ cm}^{-1})$ to allow comparison between data obtained at different excitation wavelengths.

The SE(R)RS spectra show that there is a limited signal at 514 and 1064 nm, and no signal was obtained at 532 and 785 nm excitation. A strong signal was obtained at both 633 and 785 nm. Considering also the extinction spectra in Figure 5.12, this suggests that the amount of DCI and IR1048 present in the UST was limited. Repeat preparations of this sample produced the same Raman profiles, suggesting that competition between the dyes was preventing DCI and IR1048 from partitioning into the CTAB bilayer as effectively as DTDCI. In an attempt to increase the amount of these dyes present, a time delay step was introduced, whereby DCI and IR1048 were premixed and introduced to the NR solution and allowed to equilibrate for a time prior to the introduction of DTDCI.

5.4.2 Dyes Added Sequentially with Time Delay

Two further Universal SERRS Tags samples were prepared by premixing DCI and IR1048 and adding to the NR stock solution. This mixture was allowed to equilibrate for either one hour or 14 hours prior to the addition of DTDCI. Following addition of DTDCI, the NR-dye mixtures were left for a further 14 h, after which the samples were PSS wrapped and centrifuged five times as before.

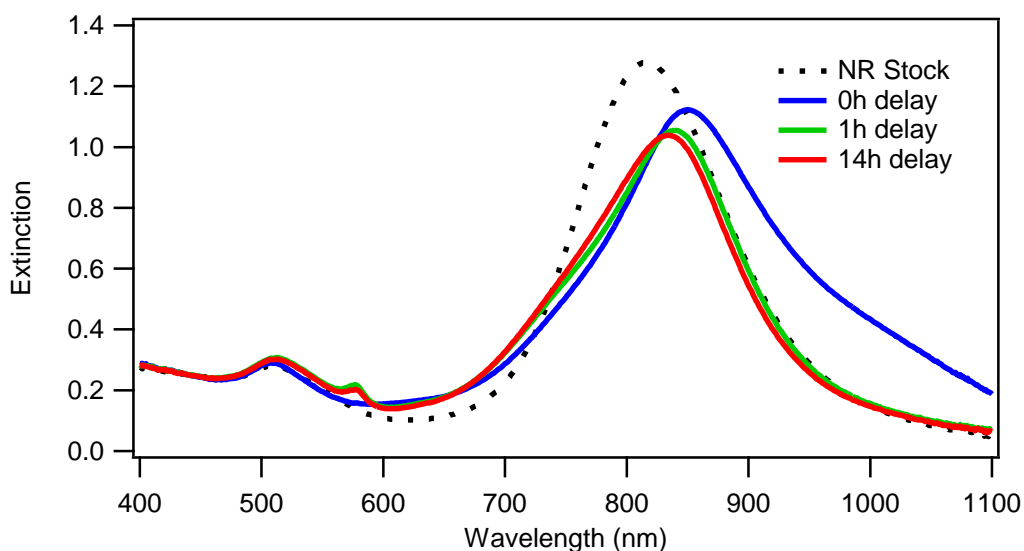


Figure 5.14. Extinction profiles obtained for the PSS wrapped NR stock solution, $\lambda_L = 815$ nm and for the Universal SERRS Tags, where 10 μ M DCI and IR1048 are introduced to the nanorod stock solution, and then 10 μ M DTDCI is added following 0, 1 and 14 hours. All samples were then allowed to equilibrate for a further 14 h prior to PSS wrapping.

The spectra obtained demonstrate that when a time delay step is included, the peak at 577 nm, which is characteristic of the presence of DCI is now present. The spectra obtained for the one hour delay sample and the 14 hour delay are very similar, and are closer in shape to the spectra of the original stock solution. The plasmon shifts displayed by each sample are listed in Table 5.3.

	λ_T	λ_L	Plasmon shift
NR stock	510	815	
0h delay	508	850	35 nm red
1h delay	512	839	24 nm red
16 hour delay	513	835	20 nm red

Table 5.3. Resonance shifts for PSS-wrapped Universal SERRS Tags samples where the dyes are either added simultaneously or DCI and IR1048 are added together, and allowed to equilibrate for either one or 14 h prior to the addition of DTDCI.

Each sample undergoes a significant red shift, however, the sample with no time delay undergoes a significantly larger red shift than the other two samples. The one hour and 14 hour delay samples undergo a comparable shift (24 nm and 20 nm respectively). Earlier results in Table 5.1, which showed resonance coupling results for stock NRs and 10 μ M DTDCI, where the plasmon shift was only 24 nm suggest that the presence of DCI and IR1048 is having some effect on the final LSPR position of the sample. It should also be noted that the extinction spectra obtained for the UST sample where the dyes were all added simultaneously showed distinct broadening, which wasn't seen for the sample with DTDCI only, or the USTs where the dyes were added sequentially.

The Raman spectra for the time delay samples were again measured at all excitation wavelengths. The background corrected and normalized spectra are shown in Figures 5.15 and 5.16.

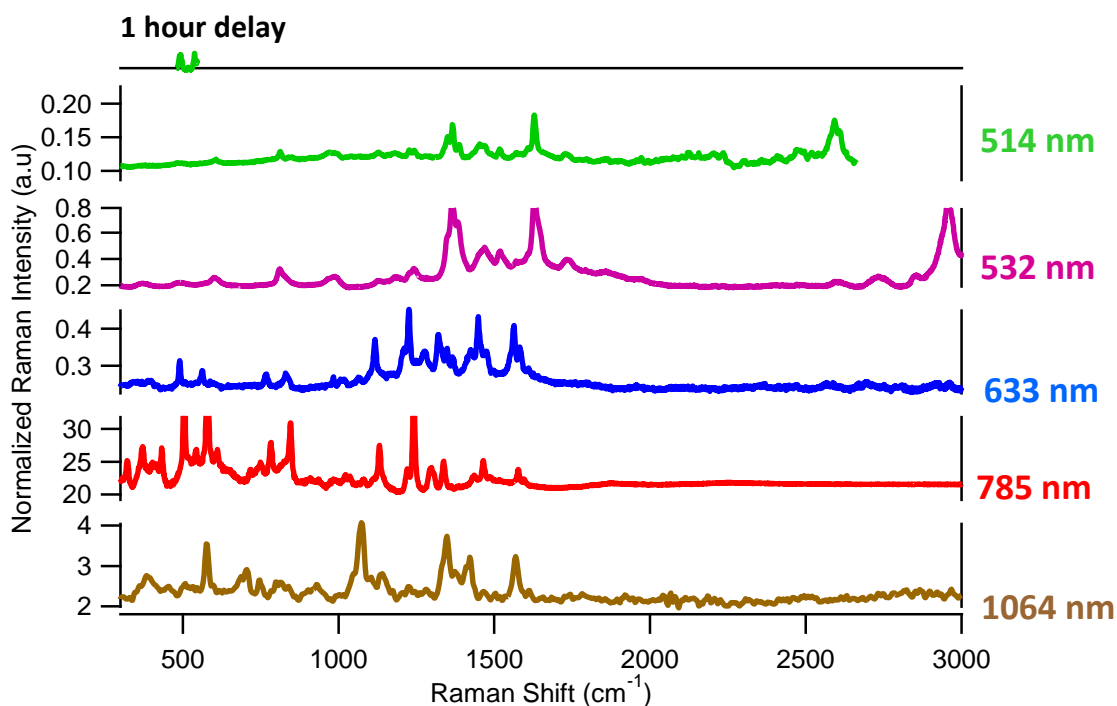


Figure 5.15. Raman analysis of PSS-wrapped Universal SERRS Tags prepared using NRs with $\lambda_L = 815$ nm, and 10 μM DCI, 10 μM DTDCI and 10 μM IR1048. DCI and IR1048 were added together and allowed to equilibrate for one hour, following this, the remaining dye, DTDCI was added and the sample allowed to equilibrate for 14 hours prior to PSS wrapping. Data has been baseline corrected and normalized with respect to the C_6H_{12} peak at $1029 \text{ cm}^{-1} (\pm 2 \text{ cm}^{-1})$ to allow comparison between data obtained at different excitation wavelengths.

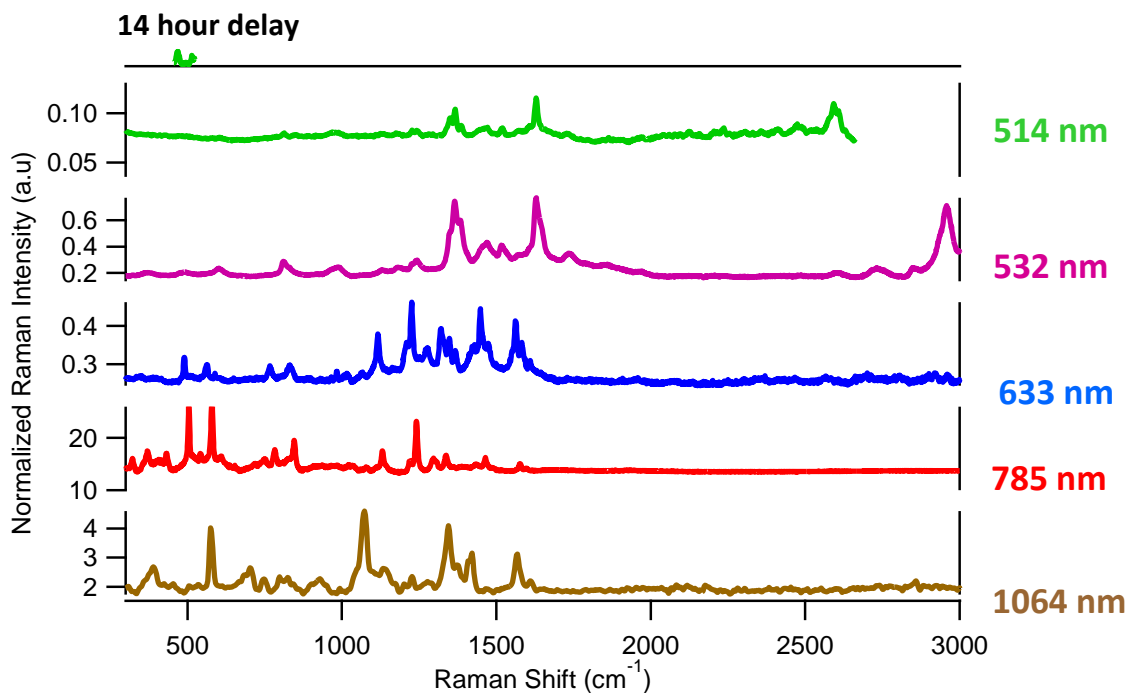


Figure 5.16. Raman analysis of PSS-wrapped Universal SERRS Tags prepared and analysed as in Figure 5.15, however, DCI and IR1048 were added together and allowed to equilibrate for 14 hours, following this, the remaining dye, DTDCI was added and the sample allowed to equilibrate for a further 14 hours prior to PSS wrapping.

For both samples where a time delay step was introduced, strong Raman signals are now obtained at all laser excitation wavelengths. It is also important to note that the spectra for individual dyes can be observed at the relevant wavelengths (compare with spectra obtained for single dye-NR conjugates in Figures 5.5, 5.7 and 5.10). Furthermore, comparison of the data obtained for the 1 and 14 hour time delay approaches shows that there is negligible difference in the intensity of the Raman profiles obtained, suggesting that the additional equilibration time following the addition of the first two dyes has no effect.

Comparison of the data for the time delay UST samples with the individual dye-rod conjugates prepared using 10 μM reveals an interesting trend, the intensity of DTDCI is consistent for the individual dye sample and the UST mixture. However, analysis of the data obtained for DCI and IR1048 reveals that the signal intensities are approximately halved in the mixture compared to the individual dye-rod conjugates dyes (compare with Figures 5.5 and 5.10 at 532 and 1064 nm laser excitations respectively). This suggests that the dye fractional surface coverages are different due to displacement or competition between the dyes.

Since no significant differences were found between the samples prepared following time delays of 1 hour and 14 hours, all subsequent work will be carried out using a 1 hour time delay step.

5.5 Raman Mapping of Single Universal SERRS Tags at a Range of Wavelengths.

The characterization data described in the previous sections focused on bulk solution measurements. Therefore, in order to demonstrate that the Universal SERRS Tags are sufficiently bright that SERRS measurements can be performed at the single particle level, a novel approach was developed, allowing correlated optical and scanning electron microscopy (SEM) imaging of the same surface region where USTs are immobilized. As outlined earlier in the experimental section (see Chapter 2.20) this was achieved by attaching a TEM reference grid onto an ITO coated glass substrate which has been functionalized with a polyelectrolyte layer of the opposite charge to that of the outer layer of the USTs. The USTs used here and in Section 5.6 have been wrapped with a second layer of polyelectrolyte, PDDAC, to provide a positively charged outer layer.

The choice of ITO is important because it is optically transparent with low background Raman signals, while being sufficiently conductive to enable SEM measurements. The ITO surface also minimises surface charging, and can be combined with an SEM instrument operating at low vacuum to allow imaging of these samples. Alternative candidate substrates such as Si wafers have much higher Raman signals that could potentially mask single nanoparticle measurements.

In order to ensure that the same area on the ITO surface could be mapped both with SERRS and SEM, an Au TEM finder grid was first attached onto the PSS-coated ITO surface, shown on Figure 5.17(a). However, with each grid square approximately 70 microns wide, small defects created during the ITO film formation process were sought within a particular square to enable further accuracy in relocating the same surface area while avoiding being close to the grid edges. This is demonstrated in Figure 5.17(b) and (c) where the red square outline highlights the same area ($\sim 13 \times 13$ microns) on both a bright-field and SEM image.

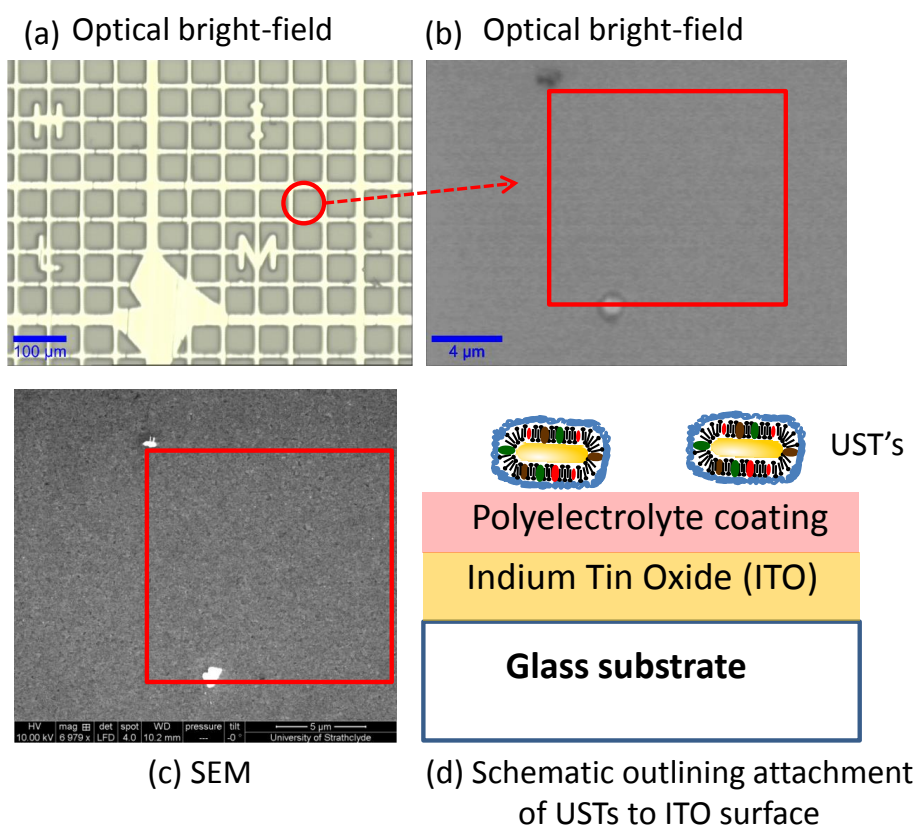


Figure 5.17. (a) Optical bright field image of TEM finder grid attached onto PSS-coated ITO surface. (b) optical bright field image of an area of the grid showing small defects on the surface used to increase accuracy in locating the same areas (c) SEM image of the same area and (d) schematic outlining the attachment of the USTs to the polyelectrolyte coated ITO surface.

The figure above demonstrates that it is indeed possible to identify the same area across at least two different instruments (in this case, the optical bright field from the Raman microscope and an environmental SEM). The next challenge is to prove that it is possible to correlate Raman mapping data for the UST samples with the SEM images obtained of the same area. In order to achieve this, the substrate was coated with USTs, by exposing the ITO surface to a low concentration of USTs for 1 minute, after which time the solution was removed and the surface rinsed with distilled water (Figure 5.17(d)). The UST particle concentration was deliberately kept low in order to promote a low surface coverage density, thus increasing the likelihood of mapping single USTs rather than clusters. An area approximately $13\ \mu\text{m} \times 13\ \mu\text{m}$ was mapped using 532 nm excitation, with a $0.25\ \mu\text{m}$ step size. Laser powers were purposely kept as low as possible, to ensure that the samples were not burned or destroyed, allowing multiple analyses to be carried out on the same area, and at a range of laser excitation wavelengths (see later data in Figure 5.20).

The Raman mapping data obtained was baseline corrected using the WiTec project software (version 2.10). In order to correlate this data with the SEM images, the sum of the area of a representative analyte peak is calculated (in the case of 532 nm analysis, the peak at $1360\ \text{cm}^{-1}$), this is then used to generate a false colour image of the area analysed, where bright areas indicate regions of high signal intensity.

After SERRS mapping the same area was examined using an SEM capable of low vacuum operation. When combined with the ITO substrate, this minimises the substrate surface charging. Images at high resolution are required in order to visualize individual nanorods, therefore, a number of repeat images were acquired covering the optically mapped area. The SEM images were then stitched together using an ImageJ plugin application,¹¹³ thereby allowing accurate comparison of optical and electron microscope areas, several microns in size.

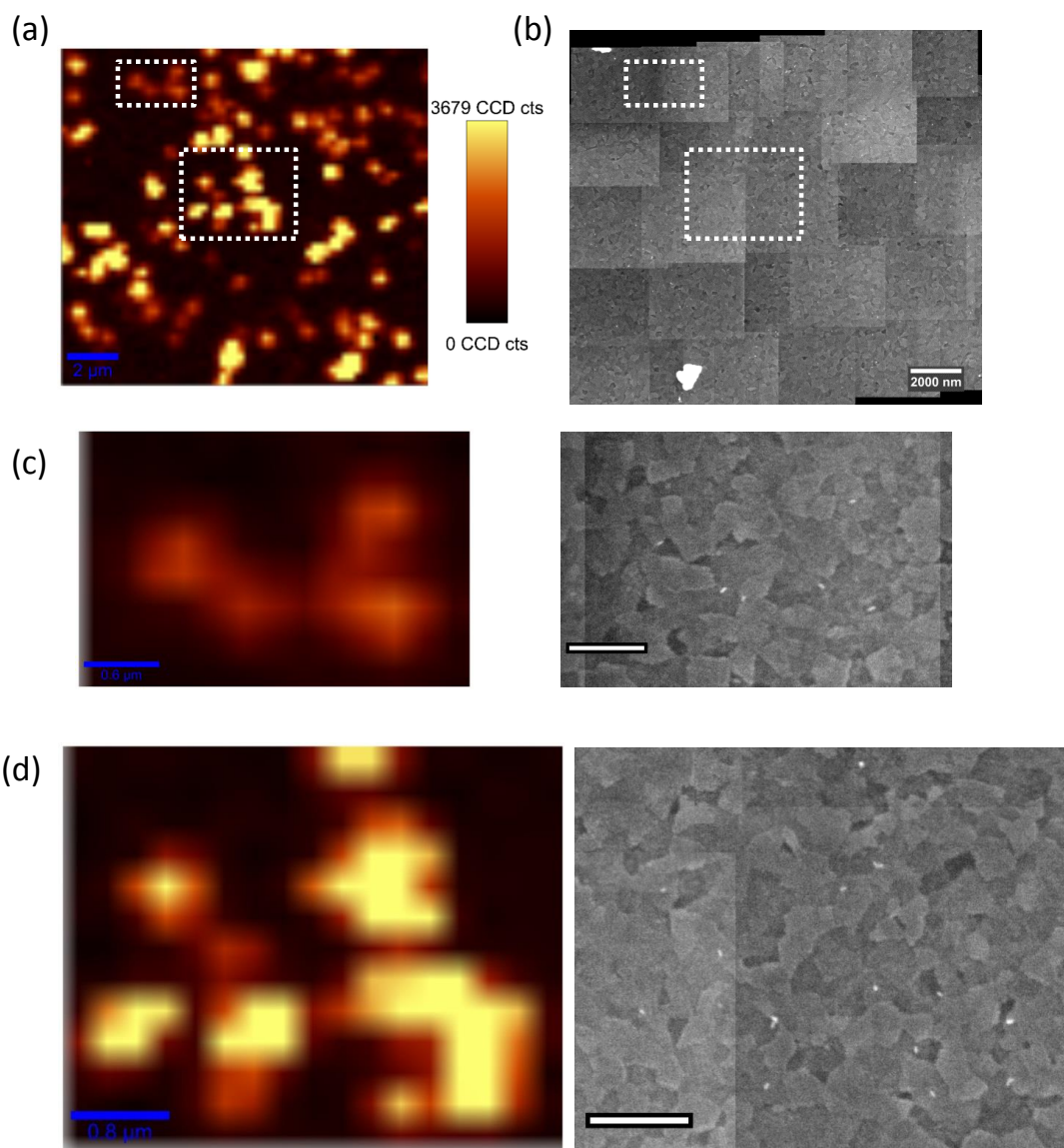


Figure 5.18. (a) Raman false colour map obtained for an area approximately $13\ \mu\text{m} \times 13\ \mu\text{m}$ (scale bar = $2\ \mu\text{m}$), along with (b) corresponding SEM image obtained by stitching together images of smaller areas (scale bar = $2\ \mu\text{m}$), (c) Zoomed in view of area shown in top box in (a), and corresponding area shown in SEM. White spots are nanorods (scale bar $0.6\ \mu\text{m}$), (d) is a magnified view of the box highlighted in the middle of (a), along with SEM image (scale bars $0.8\ \mu\text{m}$). All Raman data was obtained at $532\ \text{nm}$ excitation, with a laser power of $0.7\ \text{mW}$ and a $1\ \text{second}$ integration time. Data was obtained in $0.25\ \mu\text{m}$ steps.

The data clearly shows that Raman signals are obtainable at the single nanoparticle level with these USTs at $532\ \text{nm}$ excitation. Comparison of the false colour images with the SEM data shows that close to 100% of the USTs on the surface are SERRS active, and that there is a very strong correlation between the bright areas of high intensity Raman signal

with the nanoparticles present on the surface, proving that this approach has been successful.

Example spectra obtained at different areas of the SERRS map in Figure 5.18(d) are shown in Figure 5.19. This figure will also be used to discuss the process of generating false colour images (briefly described earlier) in more detail.

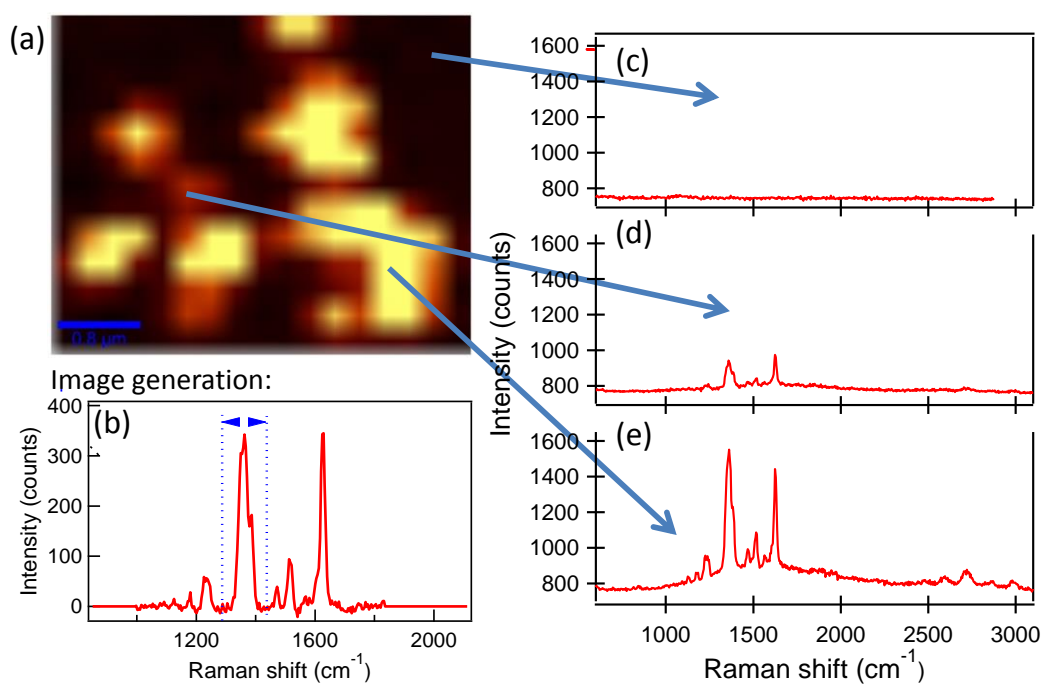


Figure 5.19. (a) Magnified view of Raman false colour map in Figure 5.18(d). (b) shows representative baseline corrected spectrum used for false colour image generation. (c-e) show representative spectra indicating areas of no signal, low and high Raman signal respectively.

An example baseline corrected spectra obtained for this area is shown in 5.19(b), the peak profile is identical to that for DCI only (shown earlier in Figure 5.5). In order to prepare the false colour image, a representative analyte peak must be selected, in this case, the peak at 1390 cm^{-1} was selected, as indicated on spectra (b). The WiTec software was then used to calculate the sum of this peak area for every spectra recorded over the whole area scanned. The software then generates a false colour image, where areas of high signal intensity are represented as bright spots on the image (a). Representative spectra obtained at various points of the image are shown in Figure 5.19(c)-(e). (c) shows a spectrum from an area of the false colour image which is very dark, and it can be seen that there are no peaks

present in the spectrum, comparing this to the SEM data in Figure 5.18(b) it can be seen that there are no USTs present in this area. (d) is taken from an area where the false colour map shows some weak colour, and the here, Figure 5.18(b) shows that there is an isolated nanoparticle. Finally, a spectrum associated with an area that showed higher signal intensity on the false colour image is shown in (e), and it can be seen that this bright area correlates to a spectrum which has a higher intensity Raman signal.

Comparing this data with the SEM image in Figure 5.18(d), it can be seen that in Figure 5.19(c), which shows the spectrum from a dark area of the false colour image, there are no peaks present in the spectrum. This correlates to an area in 5.18(d) where there are no nanorods present. Weak signal is obtained in an area where there is an isolated nanorod present within the beam focus (5.19(d)). The brighter signals in 5.19(e) correlate to an area with a minimum of three nanorods. The theoretical optical diffraction limit is approximately 360 nm at 532 nm excitation, however the intensity of the signal in (e) suggests that the actual spot size is significantly higher than this, resulting in the brighter signal in this area. The data in 5.19(d) shows that it is possible to see an isolated particle, meaning the beam spot must be less than 600-700 μm .

The final challenge here is to take this concept further, and map the same area of the substrate at a range of laser excitation wavelengths. As discussed previously, it is crucial that the laser powers are kept sufficiently low to ensure that the USTs aren't damaged, whilst still allowing the collection of bright Raman signals.

A fresh substrate coated with USTs was prepared as before (Section 2.20), and mapped at all available excitation wavelengths (532, 633 and 785 nm). False colour images were generated as before, however, since different dyes are visible at different excitation wavelengths, then the representative peaks used for analysis were as follows: 532 and 633 both used the peak at 1360 cm^{-1} , 785 nm used the sum of the peaks at $1000\text{-}1750\text{ cm}^{-1}$. The optical bright field image of the area mapped and the corresponding false colour images are shown in Figure 5.20.

USTs at Multiple Wavelengths

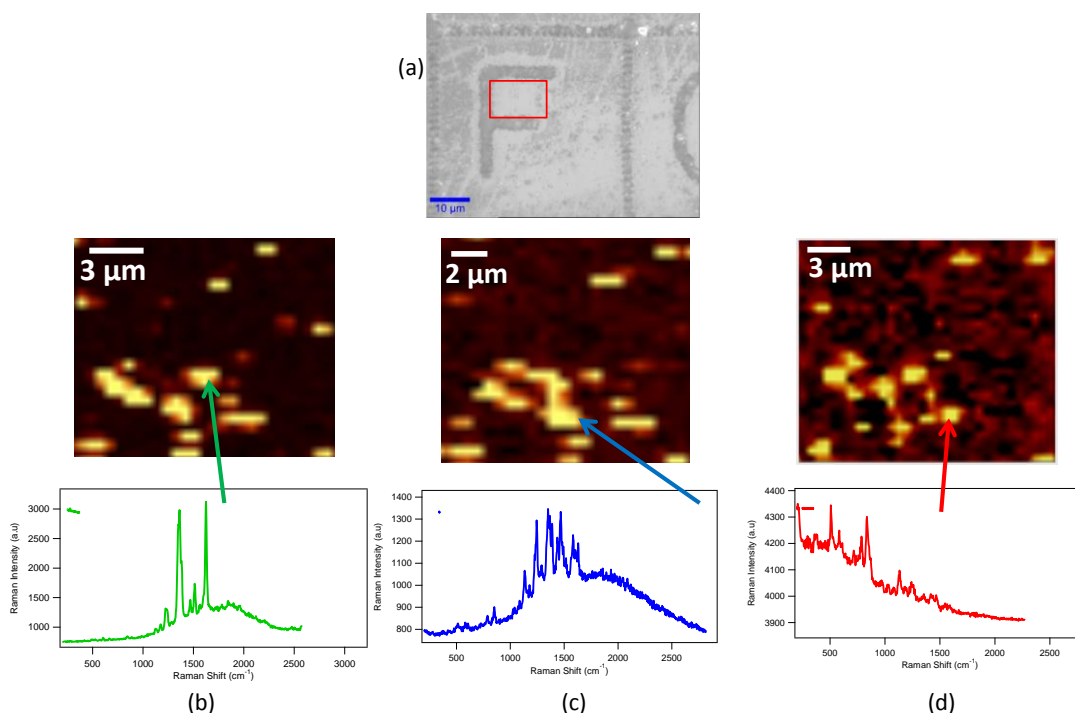


Figure 5.20. (a) Optical bright field image of the area mapped and false colour images obtained for this area at the following laser excitations: (b) 532 nm (laser power 0.6 mW), (c) 633 nm (laser power 0.6 mW) and (d) 785 nm (laser power 0.7 mW). All data was obtained using a 0.5 second integration time and at 0.5 μm steps.

The data obtained at longer wavelengths, in particular 785 nm excitation, is significantly lower in intensity than that obtained at 532 nm, resulting in a higher signal to noise ratio. The data in Figure 5.20(b)-(d) does show a good correlation between the Raman maps obtained at all three wavelengths. As the wavelength changes, variations in spatial resolution and beam spot size, as well as exact positions of the beam spot on repeat maps will all contribute to variations in the resulting images as a function of wavelength. The USTs were designed specifically to give high signal intensities across the excitation range from 514-1064 nm, however, the instrumentation available does not allow mapping over such a wide range. The initial UST design contains three different dyes, DCI, which in bulk solution measurements gives bright signal at 532 nm, DTDCI, which was bright at 633 and 785 nm and IR 1048, which gives high signal intensities at 1064 nm excitation. Since it is not

possible to map at this longer wavelength, then this dye is somewhat redundant for USTs to be used for this purpose.

USTs Prepared Using 2 Dyes

In order to increase the Raman signals over the range to be analysed, a second batch of tags were prepared, using the same nanorod stock solution ($\lambda_L = 815$ nm). However, this batch was prepared using only two dyes, 10 μ M DCI and 20 μ M DTDCI in an effort to boost signal intensities for single USTs at 633 and 785 nm excitations.

Substrates were prepared as described previously, and the same area was analysed at all wavelengths.

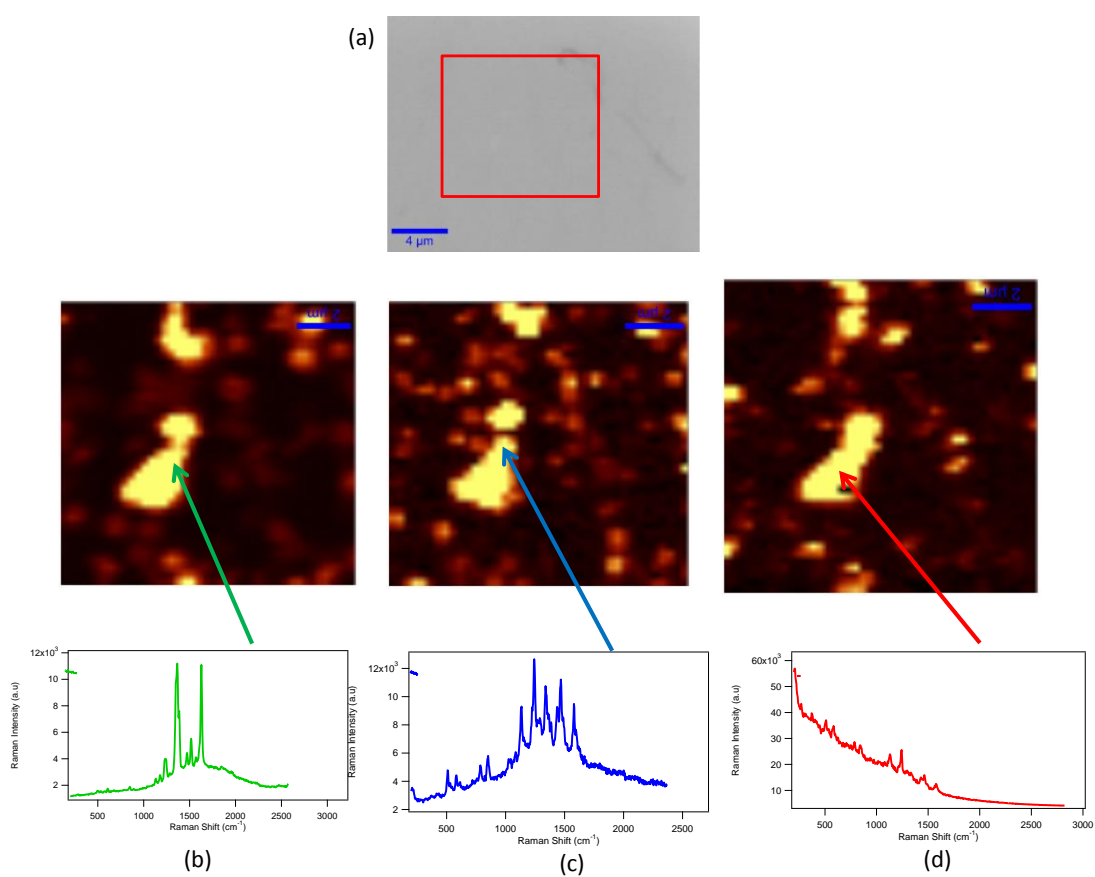


Figure 5.21. (a) Optical bright field image of the area mapped and false colour images correlating to analysis at (b) 532 nm (laser power 0.7 mW), (c) 633 nm (laser power 1 mW) and (d) 785 nm (laser power 1 mW). Typical Raman spectra are also shown for each sample. All data was obtained using a 1 second integration time and at 0.25 μ m steps.

The false colour images at 532 nm were generated as before, using the sum of the area of the peak at 1360 cm^{-1} , however, the data at 633 and 785 nm were now obtained by summing the intensity of the peaks at 950-1750 and 950-1700 cm^{-1} respectively. The correlation between the false colour images obtained at each excitation wavelength is dramatically improved by altering the dye mixture, as a result of increased signal at 633 and 785 nm. The images now match up very closely, suggesting that removing IR1048 and including a higher concentration of DTDCI has increased the amount of this dye in the USTs. One slight anomaly is the black area which appears in the bottom of the bright spot for the data in (d), this may correspond to a different peak profile being obtained for the dye, but more in depth investigations are required to ascertain if this is true.

The USTs prepared have been proven to be bright enough to allow single particle imaging at 532 nm, and suggest a good correlation can be obtained across the range of excitation wavelengths investigated. A final application of these tags will be explored in the following section, where they will be incubated with cells, and the Raman maps of these cells will then be obtained at the wavelengths used previously. Fluorescence measurements will also be taken using a confocal microscope in an attempt to compare these to the Raman maps.

5.6 Universal SERRS Tags used to Map Cells at a Range of Wavelengths.

One of the key applications envisaged for the UST's was to utilise them in cellular imaging based studies. This section describes some initial work demonstrating their suitability for multi-wavelength single cell imaging.

All of the data contained in this section (5.6) was performed in collaboration with Carlota Cunha Matos, a fellow PhD student, who performed the cell incubation, flow cytometry and confocal fluorescence measurements.

Mouse dendritic cells, which form part of the mammalian immune system, were used here as part of a project aimed at tracking the cellular uptake of vaccine-functionalized nanoparticles. However, the cytotoxicity and imaging studies described in this section focus solely on UST's which have been wrapped sequentially with PSS and PDDAC layers, resulting in a positively charged outer surface.

5.6.1 Cytotoxicity Study of USTs

The issue of nanoparticle toxicity is of major concern when incubated with cells.¹⁶⁶ It is well established that freely suspended CTAB is cytotoxic, and as a result, many functionalization approaches are designed to include the complete displacement of CTAB from nanorod surfaces.^{66, 167} However, there are several recent examples in the literature where polyelectrolyte wrapped nanorods (with the stabilizing CTAB bilayer still present) have been found to be non-cytotoxic.^{66, 168, 169}

In order to confirm the uptake of USTs by dendritic cells (DC's), and to ascertain the influence of the nanorods on the viability of these cells, some initial measurements were performed following incubation of DC's for a period of 24 hours with i) nothing (cell buffer only), ii) 50 pM USTs, iii) 100 pM USTs or iv) camptothecin. The latter is an apoptosis inducer, introduced at a suitable concentration to have a significant effect on the cell population.

Figure 5.22(a) shows the confocal image of the cell, this was obtained by staining the fixed cells, which were immobilized on a glass slide, with DAPI, which is a nucleus stain, and measuring the fluorescence at 405 nm excitation. The location of the nanoparticle-dye conjugates within the cell was determined by measuring the fluorescence at 633 nm excitation. This image proves that the USTs are located within the cell and combined fluorescence and SERRS mapping is discussed in the next section.

The percentages of apoptotic and necrotic cells are shown in Figures 5.22(b) and (c) respectively. These were measured by fluorescence activated cell sorting flow cytometry (FACS). The Annexin-FITC stain used in (b) preferentially binds to phosphatidylserine, which is translocated to the extracellular membrane during early-stage apoptosis, and thus becomes accessible to annexin. It is not until late-stage apoptosis, where the cell membrane integrity is lost, that annexin has access to phosphatidylserine in the cell interior, which is not the case here. The viability dye stain Propidium Iodide, used in (c) shows that there is no significant increase in cell death over a period of 24 hours compared to the cell only and camptothecin controls.

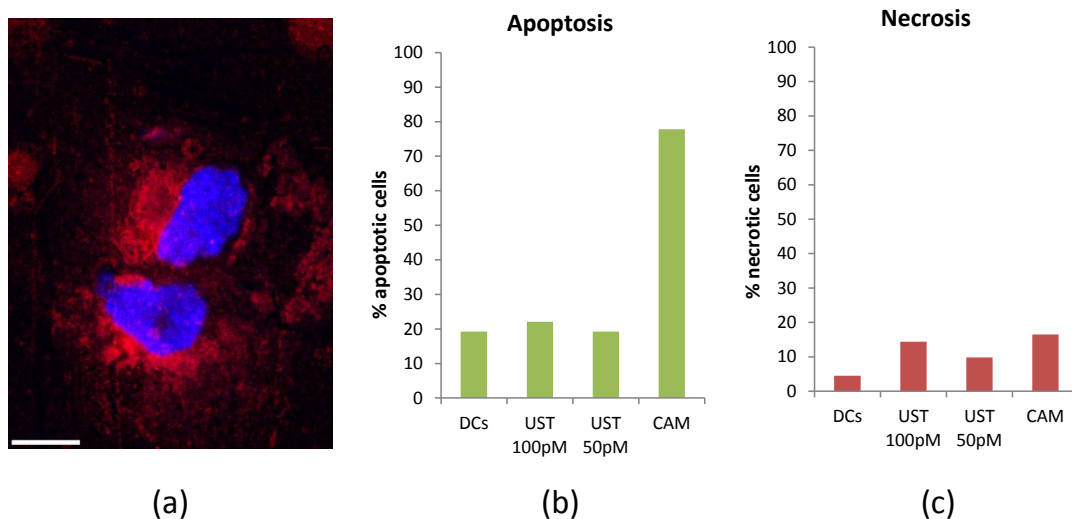


Figure 5.22. (a) Confocal fluorescence image of dendritic cells, where nuclei have been stained with DAPI (blue) and nanoparticle probes are shown in red. Scale bar is 10 μm . Flow cytometry data showing percentage of (b) apoptotic (Annexin-V positive) and (c) necrotic (Propidium Iodide positive) cells after overnight incubation with gold nanoparticle probes. DCs-dendritic cells only; UST-incubated with universal SERRS tags (at 100 and 50 pM in the cell suspension); CAM-incubated with camptothecin (apoptosis inducer).

5.6.2 Cellular Analysis

Following a clear demonstration that the UST's do not have a significant impact on cell viability, joint confocal fluorescence and Raman mapping measurements were performed covering a range of excitation wavelengths. In order to accurately compare the data across two different instrument platforms, it was important to ensure the same cell was mapped at each wavelength. This presents two issues, firstly accurately identifying the same cell for analysis each time, and secondly ensuring the cell is not damaged by the laser during the analysis. A suitable methodology was designed for the preparation of the sample substrates. The cells were fixed onto a commercially available glass bottomed Petri dish, with a 50 μm relocation grid etched onto the glass surface. Using this grid as a reference system, along with a fairly low surface coverage of cells, it is possible to repeatedly map the same cell.

In addition, in order to ensure the cell is not damaged by any of the excitation lasers, it was important to control the laser power at each wavelength. The bulk solution and single nanoparticle measurements carried out on the USTs have demonstrated that

these conjugates are very bright, and thus analysis at relatively low laser powers was possible.

All of the imaging data presented in this section was performed with cells that had been incubated with nanoparticles (or with control solutions) for a total of two hours, rather than the 24 hours used in the cytotoxicity study discussed previously. This was as a result of the previous FACS measurements, which indicated a high uptake of nanoparticles, therefore, a shorter incubation time was required to allow localized differences in particle cellular distribution to be seen more clearly. Further details of the cell substrate preparation are described in Section 2.9, and the optical measurements are described in Section 2.21.

Cells incubated with USTs

The data in Figure 5.23 shows a series of confocal Raman images obtained at a range of excitation wavelengths, while Figure 5.24 shows confocal fluorescence maps of the same cell.

When generating the false colour SERRS maps in Figure 5.23(b)-(d), the approach used previously in Section 5.5, i.e. calculating the sum of the area under the peak(s) of interest, was found to sometimes result in an inaccurate depiction of the areas of high signal intensity within the cell. This was due to background signals originating from the cells. As a result, the imaging data in this sub-section was analysed using a max-min function to produce false colour images, that is, the minimum of the analyte peak subtracted from the maximum. For the data obtained at 532 nm excitation, the area analysed was 1275-1450 cm^{-1} , and for 633 and 785 nm excitations, these were 1397-1549 and 1094-1210 cm^{-1} respectively. When analysis was carried out in this fashion, there was found to be a very high correlation between the data represented in the false colour images and the raw data.

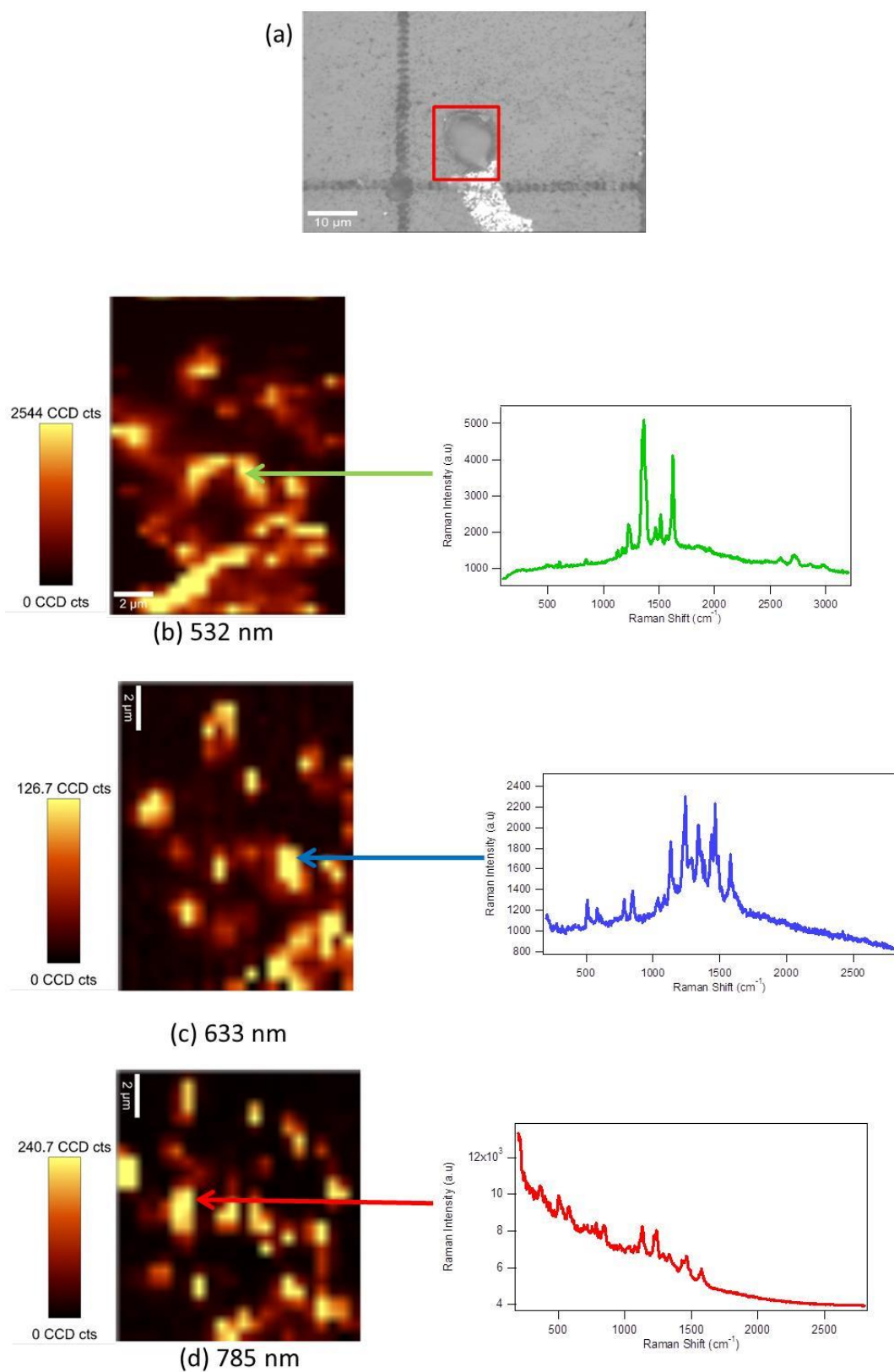


Figure 5.23. (a) optical bright field image of a cell and SERRS analysis of USTs in cells at (b) 532 nm (c) 633 nm and (e) 785 nm excitation wavelengths. Scale bars for each false colour image, along with a typical Raman spectrum obtained at a single bright spot are shown for each image.

The bright field image in Figure 5.23(a) shows a region of high contrast at the very bottom of the image that also appears at all excitation wavelengths which target the nanorod-dye conjugates. This is attributed to a roughened area of the glass substrate, which may promote adsorption of rods during the incubation and cell-washing stages. This is supported by the fact that changing the microscope focus indicated the raised height of the cell with respect to the roughened area of the glass substrate.

Comparison of the SERRS maps clearly demonstrates the uptake of the USTs, with the presence of localized areas of higher signal intensity. Representative spectra for different regions of the maps are also shown alongside each image. These spectra correlate well with the bulk solution analysis of the UST samples shown previously in Figures 5.15-5.16. One complication observed was that at 633 nm excitation, signal is sometimes obtained from both DCI and DTDCI, complicating the resulting Raman spectral profile; this also suggests that there may be some aggregation of the tags within the cell, or that they are at least grouped together in close proximity. Matching areas of higher signal intensity can be found when comparing all three SERRS maps, and differences will result between measurements due to variations in the location of the laser spot, as well as poorer spatial resolution with increasing wavelength. The results also demonstrate that the signal to noise ratio is lower at 633 and 785, compared with the signal obtained at 532 nm. This is not surprising considering the relative intensities observed in the bulk solution measurements.

The corresponding confocal fluorescence imaging maps of the same cell are shown in Figure 5.24.

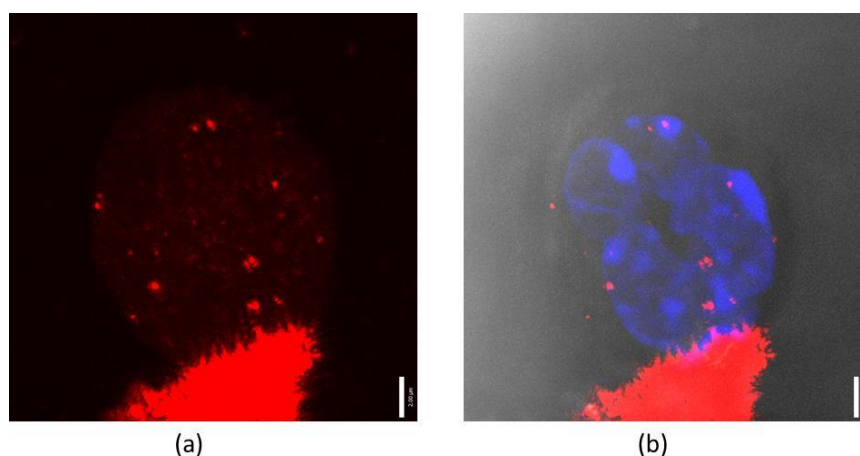


Figure 5.24. Confocal fluorescence images of the same cell shown in Figure 5.23. The blue colour is the fluorescence measured at 405 nm excitation, while the red corresponds to 633 nm laser excitation. (a) 633 nm excitation only, while (b) shows an overlay of images at both excitation wavelengths along with a DIC image of the cell defining the cell outline. Scale bar = 2 μm .

At 633 nm excitation, significant background luminescence was obtained from the rod-dye conjugates, allowing their relative density within the cell to be mapped, showing widespread uptake. Comparing this with the SERRS images shows a good overlap in areas where the signal intensity is highest. An identical scan step size of 0.5 microns was used for both the fluorescence and SERRS mapping, though differences in the instrument design as well as the type and magnification of the objective lens used mean that the spatial resolution of the confocal system appears to be superior to the Raman system.

Joint Raman and fluorescence maps were repeated for a number of selected cells, and similar results were obtained. This clearly demonstrates the potential use of USTs for multimodal optical imaging of cellular environments.

5.6.3 Control Measurements

In addition to incubating the cells with USTs, control measurements were performed using either (i) cells with no nanoparticles present or (ii) cells incubated with polymer wrapped nanorods with no dyes incorporated into the CTAB bilayer. False colour and confocal fluorescence maps were generated in the same manner (i.e. same laser powers, integration times, step size etc) as that used in the previous section.

Cells Only, no Nanoparticles

The images in Figure 5.25 show that the background signal is relatively small when compared to the signal intensities obtained upon incubation with the USTs (Figure 5.23). The Raman spectra at 532 nm show some areas of low signal intensity, which may possibly be coming from the cell itself. The DAPI stain can be easily visualized at 405 nm excitation, but there is very little background at 633 nm.

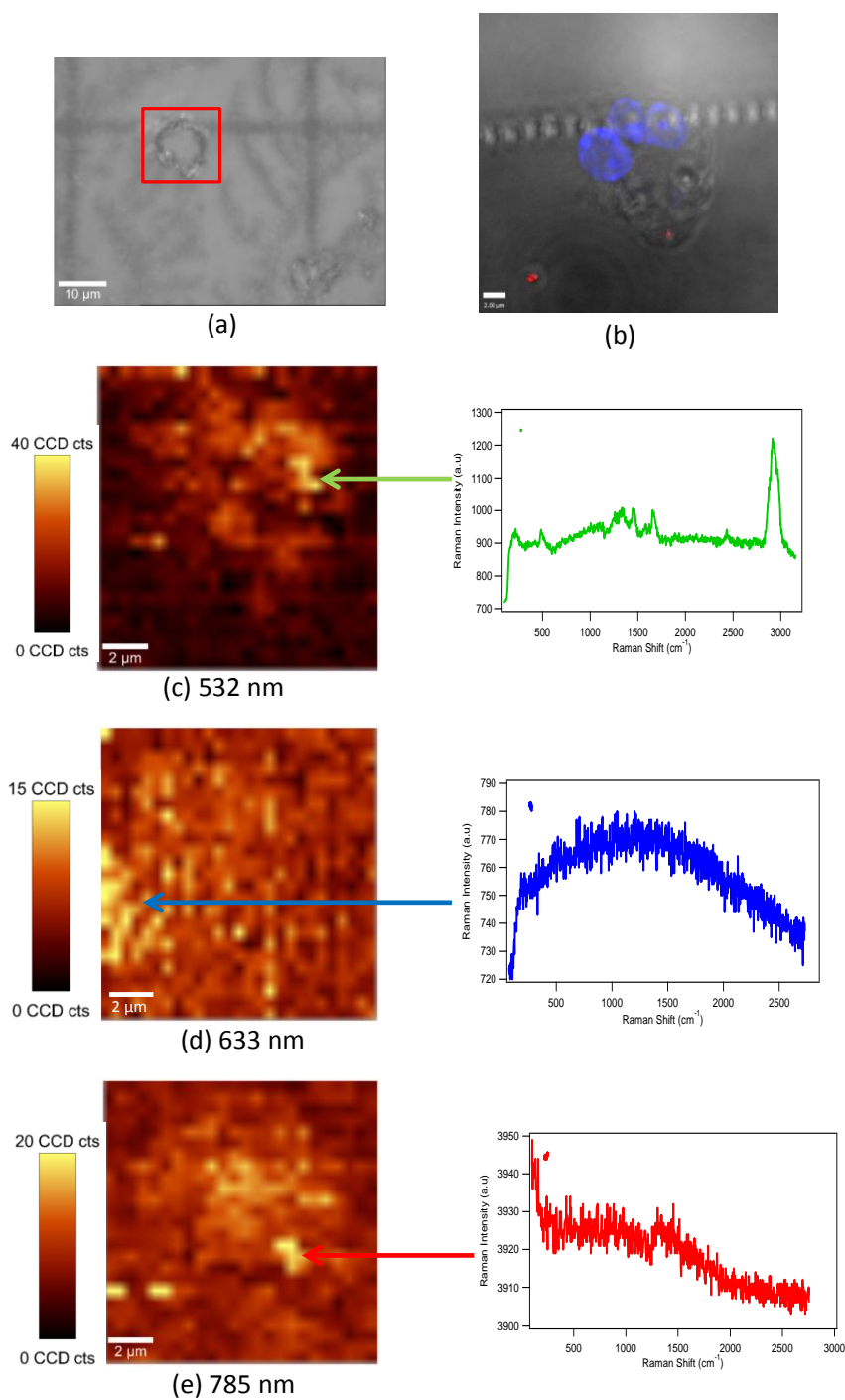


Figure 5.25. Imaging analysis of control sample with dendritic cells only (a) optical bright field image of cell, (b) confocal fluorescence composite of DIC image, plus 405 nm (blue) and 633 nm (red) excitation. SERRS analysis of cells at (c) 532 nm (d) 633 nm and (e) 785 nm excitation wavelengths. Scale bars for each false colour image, along with typical Raman spectrum obtained at a single bright spot are shown for each image.

Cells with Polymer Wrapped NRs, no Dyes Present

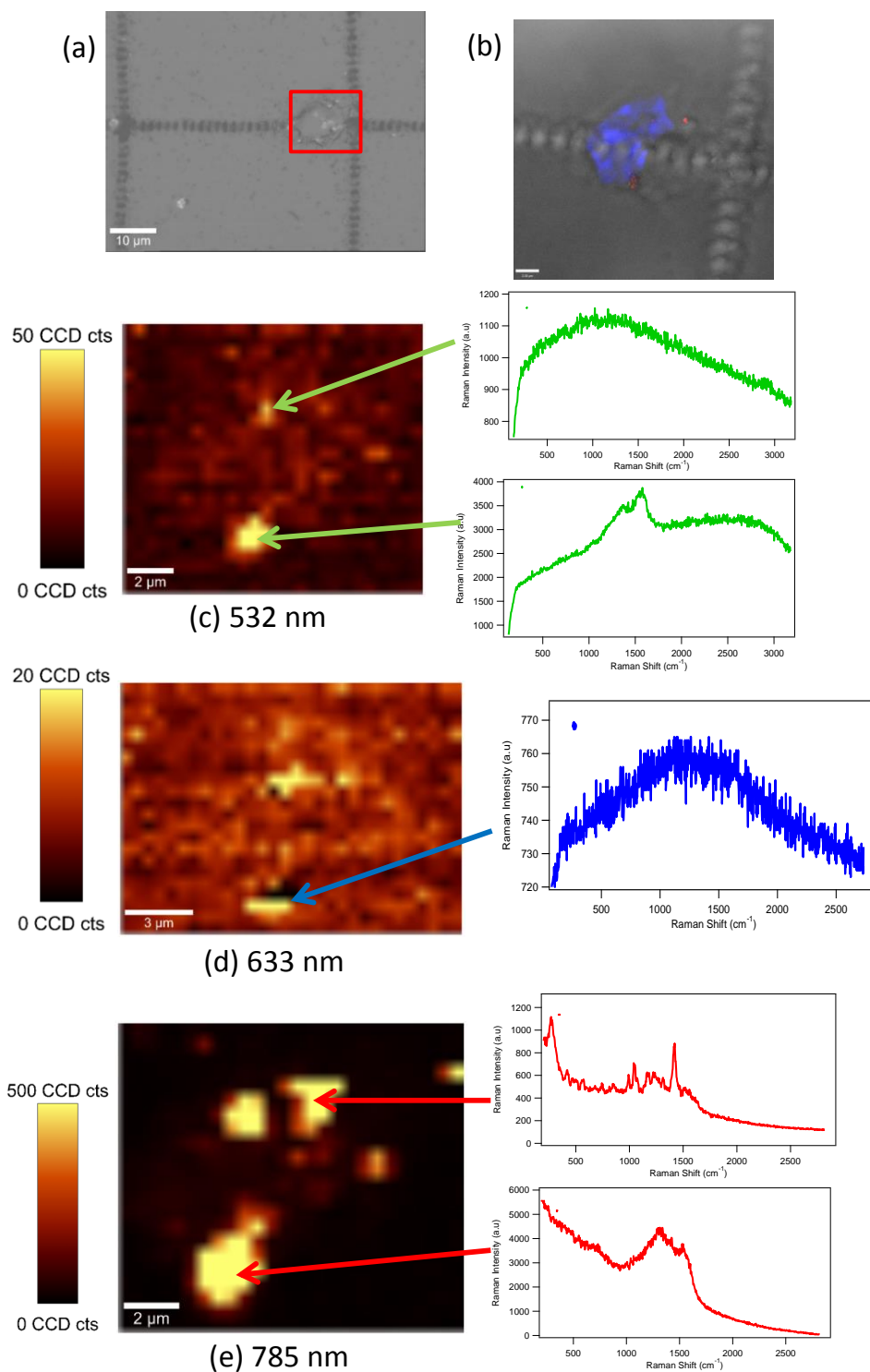


Figure 5.26. Imaging analysis of control sample with dendritic cells incubated with polymer coated nanorods where no dyes are present in the CTAB bilayer (a) optical bright field image of cell (b) confocal fluorescence composite of DIC image, plus 405 nm (blue) and 633 nm (red) excitation. SERS analysis of cells at (c) 532 nm (d) 633 nm and (e) 785 nm excitation wavelengths. Scale bars for each false colour image, along with typical Raman spectrum obtained at a single bright spot are shown for each image.

The control sample data in Figure 5.26 was performed using rods that were wrapped with the same outer layers of polyelectrolytes (PSS and PDDAC), and no dyes were present in the CTAB bilayer. These samples were incubated with dendritic cells for 2 hours.

The control sample data in Figures 5.26 (a)-(e) an increase in background signal, most likely as a result of the SERS effect of the metallic nanoparticles in close proximity to the cells boosting signals arising from areas of the cell itself, even though the nanoparticles are wrapped with two polyelectrolyte layers.. The representative spectra show this increase compared to the previous control sample where no nanorods were present. In particular, the intensities of the background signals obtained at 785 nm excitation have significantly increased, possibly as a result of the overlap of the laser excitation wavelength with the nanorod λ_L . Multiple cells were mapped, and similar results were obtained each time. It is this effect which led to the difficulties in baseline correction described previously in this section.

5.7 Alternative Dye Combination for Universal SERRS Tags to Provide Even Brighter Signal at 785 nm Excitation

The dye combination used in Section 5.4 has proven to be useful for bulk solution measurements across the entire 514-1064 nm wavelength range. However, as highlighted in both the single nanoparticle and cellular imaging sections, the Raman signals obtained when mapping at 633 and 785 nm are relatively low compared to the signals obtained at 532 nm. In order to obtain brighter Raman signals at the longer wavelengths, the dye combination used to prepare the USTs will need to be modified. Since the equipment available does not allow mapping at 514 and 1064 nm, it was decided that the focus should be on boosting the signal intensities at 633 and 785 nm excitations, while maintaining a high performance at 532 nm.

In this final section, an alternative dye combination for use as a UST is briefly introduced and explored.

Characterization of Dyes

DCI has been shown to provide very strong signal intensities at 532 nm, therefore this dye was included in the mixture. A range of other dyes were investigated to improve the signals at 633 and 785 nm excitation, two of these have been selected for further discussion, malachite green isothiocyanate (MGITC) and NIR-797, the structures of these dyes are shown in Figure 5.27, along with the structure of DCI for comparison.

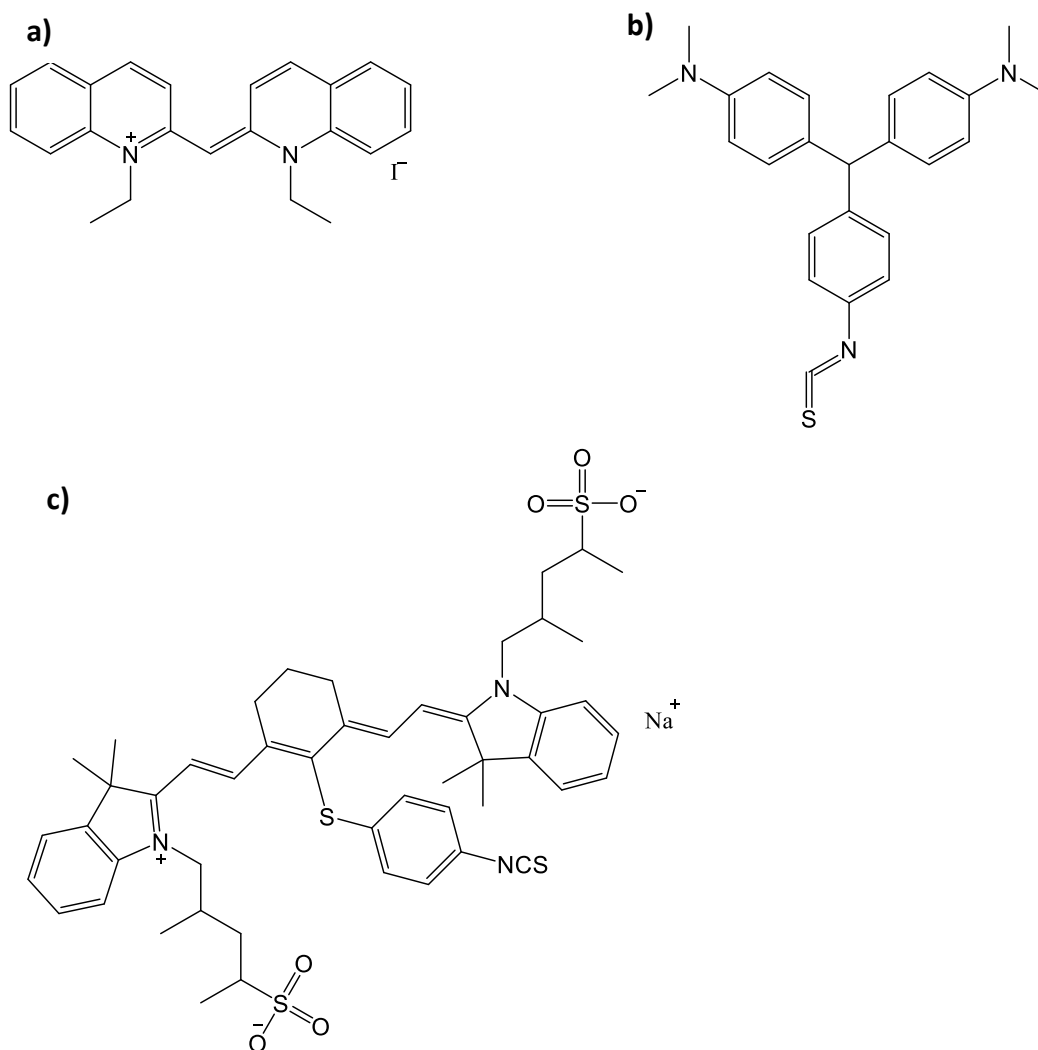


Figure 5.27. Structures of dyes a) DCI b) MGITC and c) NIR-797.

The structures of MGITC and NIR-797 are very different to that of DCI, although as before, the dyes selected are again relatively hydrophobic. One crucial difference to note is that there is no quaternary ammonium group present in MGITC, but that it does contain a

thiocyanate group (SCN). One concern is that the presence of the SCN group may affect the reproducibility of dye loading or displace CTAB, and thus destabilize the colloid.

The extinction spectra for 10 μM dye solutions of each dye in 1 mM CTAB, are shown in Figure 5.28.

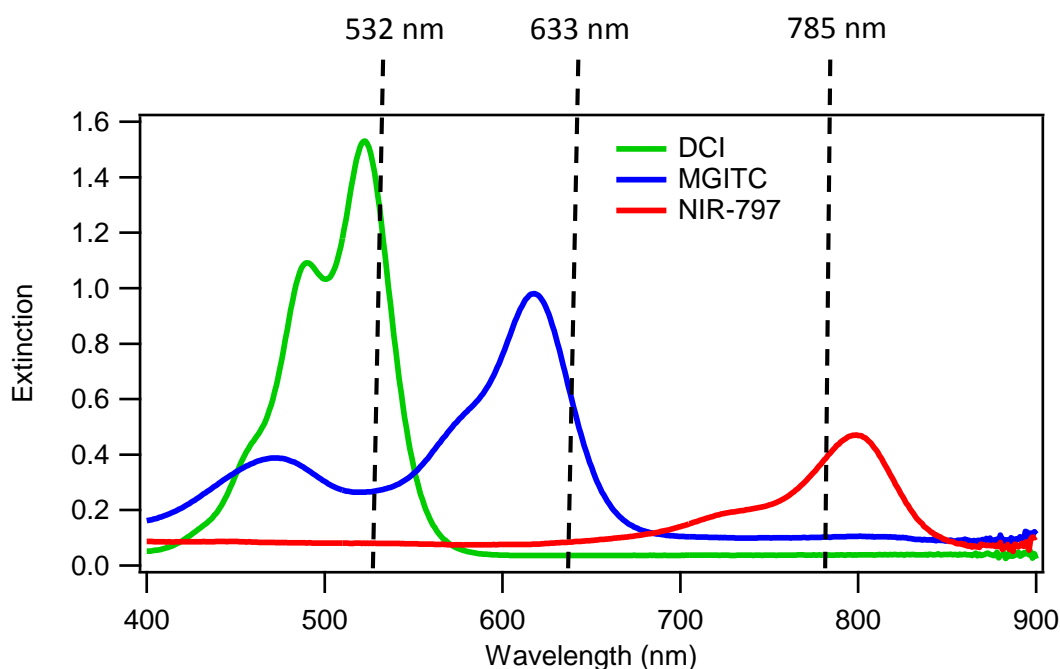


Figure 5.28. Extinction profiles obtained for 10 μM stock dye solutions in 1 mM CTAB solution. Spectra shown are for DCI, MGITC and NIR-797. For comparison, the laser excitation wavelengths are indicated by the dashed lines.

The extinction spectra show a strong overlap between the dyes and the laser excitation wavelengths, suggesting that this combination could give bright Raman signals across this range.

Analysis of Universal SERRS Tags Prepared Using New Dye Combination

In order to evaluate the effectiveness of the new combination of dyes, Universal SERRS Tags in this Section were prepared using a nanorod stock solution with $\lambda_L = 770$ nm and 10 μM each of DCI, MGITC and NIR-797. In this case, all dyes were premixed and added simultaneously and allowed to equilibrate for 14 hours prior to PSS wrapping. As before, the USTs were centrifuged five times and resuspended in distilled water to remove any

excess dye present. The extinction spectra for the polymer wrapped NR stock solution and the USTs are shown in Figure 5.29.

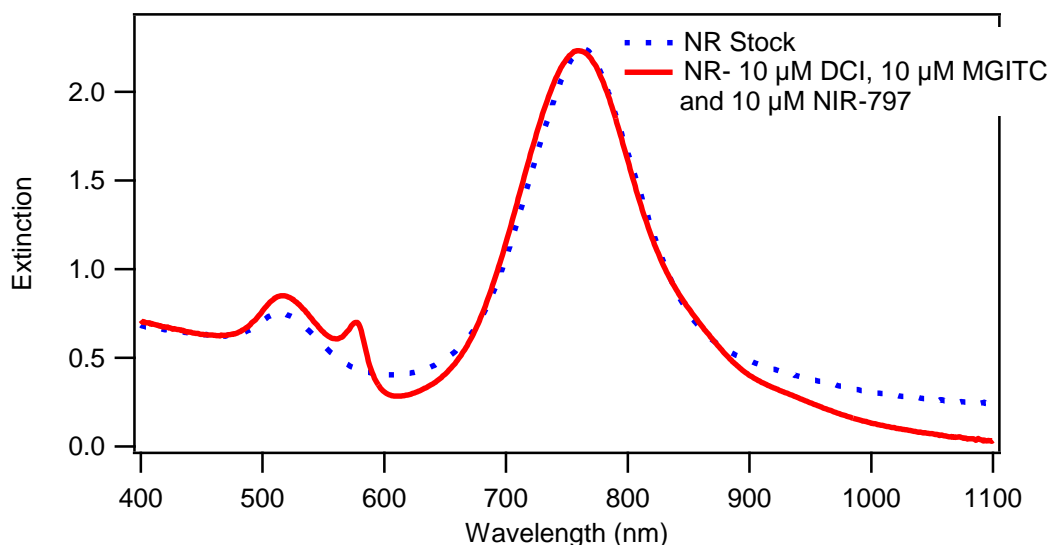


Figure 5.29. Extinction spectra of PSS wrapped stock nanorod solution with $\lambda_L = 770$ nm, and the PSS-wrapped Universal SERRS Tags prepared using this NR stock and a combination of three dyes (10 μ M DCI, 10 μ M MGITC and 10 μ M NIR-797).

There are a few key points to note about these extinction spectra. Firstly, the shape of the spectra for the USTs has remained unchanged, suggesting negligible aggregation has occurred, in fact, the extinction spectra for the USTs is slightly narrower than for the stock NRs. This is likely due to the centrifugation steps removing some larger NRs that may have been present in the stock solution. A second important feature to note is that the peak associated with DCI is present at 577 nm, indicating the inclusion of this dye into the USTs. This is particularly interesting, when compared to the USTs in Section 5.4. where the dyes were added simultaneously, and competition between the individual dyes meant that this peak was not present, and the Raman data in Figure 5.13 showed very limited signal from DCI. Finally, the USTs have undergone a much weaker resonance shift than the earlier examples, in this case the conjugates now undergo only a 6 nm red shift, compared with red shifts of up to 35 nm seen previously in Figure 5.14.

The samples were analysed at all available Raman excitation wavelengths, with the baseline corrected and normalized data shown in Figure 5.30.

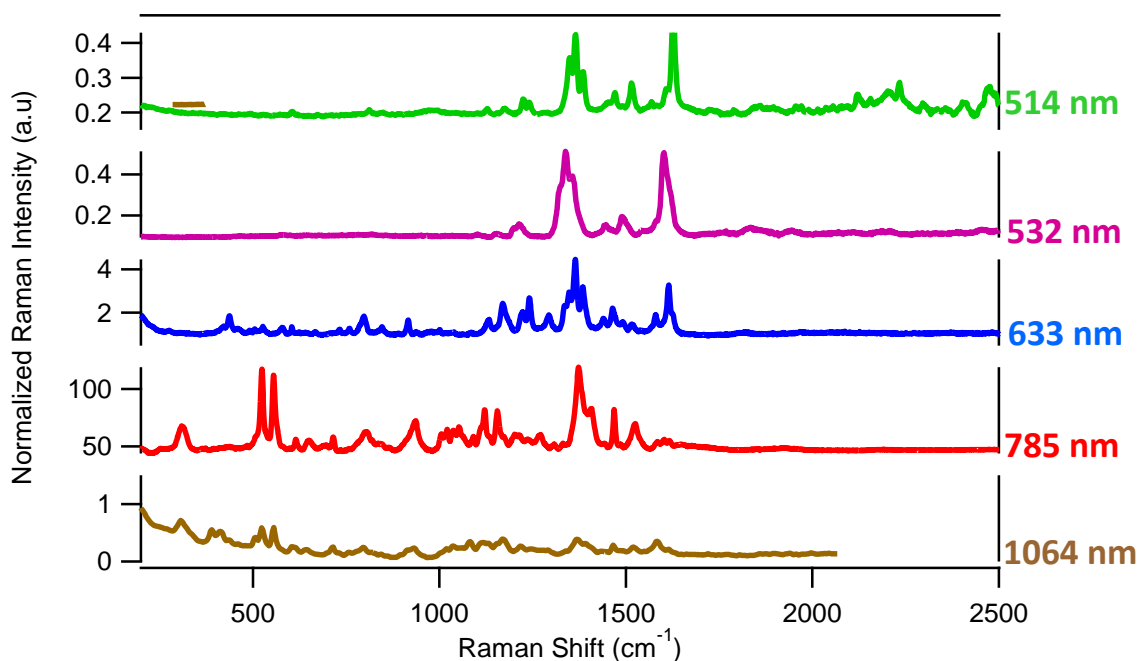


Figure 5.30. Raman analysis of PSS-wrapped NR-dye conjugates prepared using NRs with $\lambda_L = 770$ nm, and 10 μM DCI, 10 μM MGITC and 10 μM NIR-797. Dyes were added at the same time and allowed to equilibrate for 14 hours prior to PSS wrapping. Data has been baseline corrected and normalized with respect to the C_6H_{12} peak at 1029 cm^{-1} ($\pm 2 \text{ cm}^{-1}$) to allow comparison between data obtained at different excitation wavelengths.

Strong Raman signals are obtained at wavelengths ranging from 514-785 nm and a small signal is present at 1064 nm, which is significantly reduced compared with that demonstrated by the previous dye combination. However, since the focus was to develop a dye combination suitable for mapping at wavelengths ranging from 532-785 nm then strong signal intensities at 1064 nm are not crucial. The key aim was to boost the signal intensities acquired at 633 and 785 nm. Comparing the data for the previous dye combination in Figures 5.16 and 5.17, with the data in Figure 5.30. it can be seen that the combination of DCI, MGITC and NIR-797 leads to an approximately 10 fold increase in signal at 633 nm excitation, and signals approximately 4 times brighter at 785 nm excitation, whilst still maintaining the signal at 532 nm. It should also be possible to further increase the signal at 785 nm either by adding more NIR-797 to the dye mixture, (e.g. 10 μM DCI, 10 μM MGITC and 20 μM NIR-797), or by adjusting the dye ratios whilst maintaining the overall bulk dye concentration at 30 μM , for example to 5 μM DCI, 5 μM MGITC and 20 μM NIR-797.

Unfortunately, due to a lack of time, single nanoparticle and cellular mapping studies could not be performed for the USTs prepared using this new dye combination. The normalized SERRS intensities achieved here suggest that this new version of the USTs is highly promising for both of these applications, and that bright Raman signals could be achieved across the wavelength range required.

5.8 Conclusions

This Chapter introduced the novel concept of a universal SERRS tag (UST), where the aim is to develop a SERRS reporter molecule capable of producing bright signals over a range of common excitation wavelengths (514 - 1064 nm). A range of dyes were assessed by successfully preparing a number of polymer stabilized nanorod- dye conjugates. Some were found to provide bright Raman signals across a range of wavelengths, while others were found to be limited in their application. However, no single dye was found to provide bright signals across all of the excitation wavelengths tested.

Three of these dyes were selected (DCI, DTDCI and IR1048) and successfully co-assembled onto the nanorod surface. The conjugates were then stabilized using a polyelectrolyte. SERRS analysis of the bulk UST solutions showed that it was possible to achieve strong Raman signals across all available excitation wavelengths without the need for particle aggregation.

The brightness of the tags was verified via single particle imaging, where the SERRS intensities were correlated with SEM images. The results demonstrated that these monodisperse, unaggregated tags could be seen at the single particle level via SERRS, while remaining hotspot free. The USTs were mapped at three excitation wavelengths (532, 633 and 785 nm).

The potential application of the tags for cellular imaging was investigated by incubating the USTs with dendritic cells. Preliminary studies indicated that the polymer stabilized nanorods are not cytotoxic, and joint Raman and confocal fluorescence mapping studies highlight the suitability of these tags for cellular imaging applications.

The results described here have shown that it is possible to produce shelf-stable nanoparticle-dye conjugates that are suitable for multimodal SERRS and fluorescence analysis across a wide range of laser excitation wavelengths.

5.9 Future Work

The Raman responses for the USTs showed relatively lower signals at 633 and 785 nm excitation. As a result, an alternative dye combination was developed, and bulk solution SERRS measurements show increased signal intensities are obtained at these laser excitation wavelengths. The application of these tags for both single nanoparticle and cellular imaging should therefore be explored further. For example, it would be interesting to investigate the relative SERRS profile variations from particle to particle. Further experiments could address the issue of whether the spectral profile of the USTs changes at different wavelengths when comparing isolated and aggregated nanorods. This would be a useful tool, which could provide an extra layer of information about the USTs local environment.

The range of laser excitation wavelengths covered could potentially be increased by exploring a wider range of dyes, and even nanorods of different lengths (see work in Chapter 3), this could potentially lead to the development of unaggregated tags suitable for use in an even broader range of applications. Further understanding of the fundamental interactions between dyes and nanorods is also required.

As more dyes are introduced, the spectra become more complex, and thus, the use of principal component analysis could be investigated to allow the identification of key components.

Alternative dyes, focusing on further increasing the signal in the wavelength range from 514 – 785 nm could also be investigated. It may be possible to simplify the UST design by exploring dyes with very broad extinction spectra, which would perhaps introduce the possibility of moving to a one or two dye system.

The attachment of fluorescent dyes to the polymer encapsulated nanorods was briefly investigated (data not shown), and provides a route to making these tags suitable for multimodal spectroscopic applications.

Finally, the functionalization of the USTs with biomolecules such as DNA, and subsequent targeting of cells should be a key area of interest for these tags in the future, initial steps to achieve this are discussed in Chapter 6.

Chapter 6

Functionalization of Polymer-Wrapped Nanoparticles

For the polymer wrapped nanorod probes discussed in the previous Chapters to be successfully applied to specific imaging and sensing applications, it is essential that methods for biofunctionalization of them are successfully developed. In this Chapter, initial efforts to establish a novel route for the covalent attachment of DNA are described. Also introduced here is a new route for the synthesis of quasi-spherical polymer stabilized nanoparticles, for which the covalent attachment of DNA will also be investigated.

A vast variety of techniques are described in the literature for functionalizing gold nanoparticles. Perhaps one of the most commonly used is thiol chemistry, which has proven to be an attractive route for the functionalization of gold nanoparticles with thiolated DNA.^{65, 170} This route is challenging for nanorods, as it typically relies on displacement of the CTAB stabilizing surfactant, which can lead to colloidal instability. Furthermore, CTAB is known to be cytotoxic,⁶⁶ and thus the CTAB must be completely removed or coated in some way to prevent any issues arising in cellular work. Thiol chemistry has also successfully been used to modify gold nanorods,^{70, 171} and has also been applied to bimetallic rods comprising of gold and platinum.¹⁷² This route is not an option for the modification of the nanorod probes used here, since the polymer layer wrapping prevents bonding of the thiol group to the gold nanoparticle surface.

Another widely used ligand used for gold nanoparticles is thiolated PEG (PEG-SH), which has the added advantage of being hydrophilic as well as stabilizing.^{173, 174} In the case of nanorod functionalization, this is often achieved using methoxypoly(ethylene glycol) (mPEG), and sometimes in combination with techniques such as dialysis to remove excess CTAB.^{99, 175-177} However, many of the examples in the literature describe the functionalization of nanoparticles with PEG only, with no subsequent route for biofunctionalization.

The growth of silica shells around nanorods has been demonstrated, and was pioneered by Liz-Marzan *et al*, who described the coating of colloidal gold with the coupling

agent (3-aminopropyl)trimethoxysilane, followed by further growth using the Stöber method, allowing control over the thickness of the polymer layer.¹⁷⁸ This technique has been widely reported in the literature,^{179, 180} and the formation of a silica shell around polymer stabilized gold nanoparticles has also been described.¹⁸¹ The Mirkin group have also reported the preparation of silica protected gold triangular prisms.¹⁸²

Polymers are routinely used to stabilise colloidal nanoparticles, there are very few reports of covalent attachment of biomolecules to polymer stabilized nanoparticles. The Murphy group have demonstrated the attachment of biotin, which contains an amine group, to nanorods coated with poly(acrylic acid) (PAA) which has a carboxylic acid moiety. The amide coupling reaction was carried out using N-hydroxysulfosuccinimide (NHSS) along with N-(3-dimethylaminopropyl)-N'-ethyl carbodiimide hydrochloride (EDC HCl) are used as the activating and coupling agents respectively.¹⁸³ The most commonly described methods to functionalize polymer encapsulated gold nanoparticles rely on electrostatic adsorption to attach molecules such as drugs and proteins.¹⁸⁴⁻¹⁹⁰ This technique has also been widely used to attach DNA to these surfaces,¹⁹¹⁻¹⁹⁴ however, to date there are no methods for the covalent conjugation of DNA to polymer stabilized gold nanoparticles of any shape. A number of groups have reported the functionalization of quantum dots via the direct functionalization of stabilizing polymers,^{195, 196} a typical method described in the literature for the functionalization of CdSe/ZnS core shell nanocrystals coated with octylamine-modified polyacrylic acid, which was cross linked with polyethylene glycol-lysine, EDC was then used to couple this to streptavidin or antibodies.¹⁹⁷

6.1 Planned Route for DNA Functionalization of Polymer Wrapped Nanorods

It is apparent that the existing methods for DNA functionalization of nanoparticles are not applicable to covalently attach biomolecules to polymer stabilized systems, and thus initial steps were taken to design a new route to tackle this issue. The schematic in Figure 6.1 outlines the approach investigated for the novel attachment of DNA to the nanorod probes.

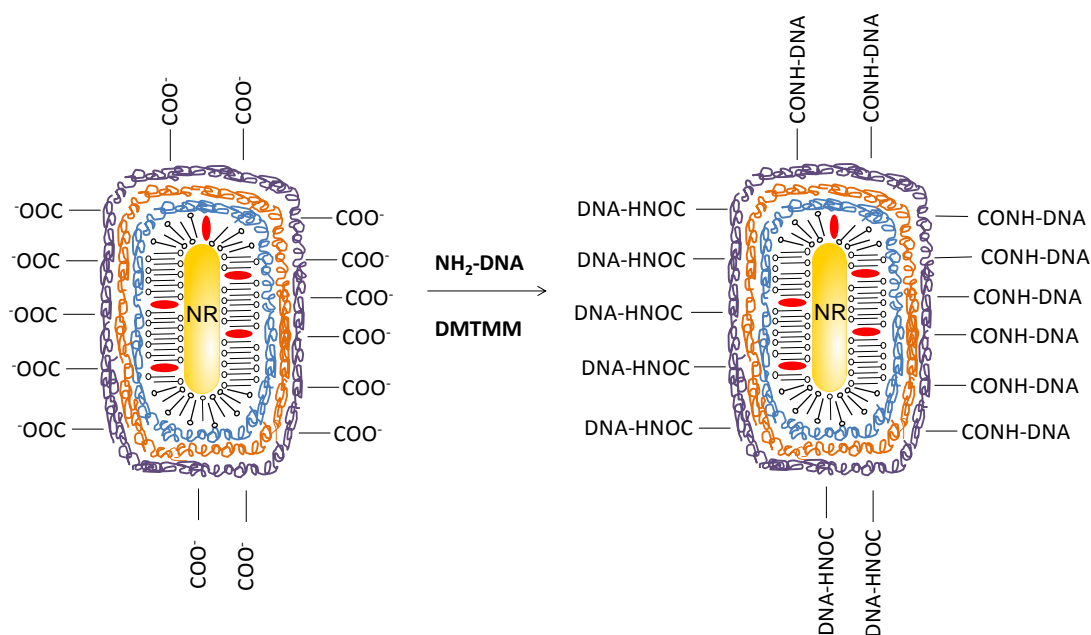


Figure 6.1. Schematic outlining the proposed route for covalent functionalization of polymer wrapped nanorods with DNA.

The PSS-wrapped nanorod-dye conjugates are prepared as described previously (Chapter 2.2). The method proposed here involves the covalent coupling of DNA to a polymer surface through amide bond formation, via coupling of amine terminated DNA to carboxylic acid functionalized nanorods. The steps involved in this reaction are discussed in the following sections.

6.2 Polymer Wrapping of Nanorods

In order to achieve an outer layer of carboxylic acid functionalized groups, a range of polymer layer combinations were assessed, where it became apparent that the affinity of polyelectrolytes for one another varies widely and is not simply dependent on the attraction between positive and negative charges, with a range of polymer combinations found to fail to produce stable conjugates when electrostatically coated in this manner.

Several polyelectrolytes were investigated, including PSS, poly(allylamine hydrochloride) (PAH), poly(acrylic acid, sodium salt) (PAA), poly-L-glutamic acid sodium salt (PGlu), poly-L-lysine hydrochloride (PLL) and poly(diallyldimethylammonium chloride)

(PDDAC). A number of combinations were investigated and found to be unsuccessful, including PSS-PLL, PSS-PAH-PGlu and PSS-PDDAC-PGlu. Attempts to coat CTAB stabilized NRs with PGlu directly were unsuccessful. Direct coating with PAA has been reported previously in the literature,¹⁸³ however, it was not possible to replicate this here. The stability was assessed both visually and via extinction measurements following centrifuge and resuspension of the polymer wrapped nanorods. Many combinations were found to irreversibly aggregate at this stage.

The polymer wrapping procedure is described in detail in Section 2.11. PSS was found to provide the most stable wrapping of the CTAB stabilized NRs. However, since this polymer is negatively charged, and the desired polymer functionality also imparts a negative charge then it was necessary to introduce a three polymer layer system. The first layer wrapping used was PSS, followed by positively charged poly(allylamine hydrochloride) (PAH) and finally, poly(acrylic acid, sodium salt) (PAA). The final polymer layer contains the desired COOH moiety, the use of PAA is also advantageous as it has demonstrated low nonspecific binding of proteins.¹⁹⁸

Following subsequent encapsulation by each polymer layer, the samples were centrifuged at least twice and resuspended in distilled water to remove any excess polymer from the solution. The extinction spectra were monitored following each step to ensure the nanorods had not aggregated, and to resuspend the samples into an appropriate volume of water to keep particle concentrations roughly constant.

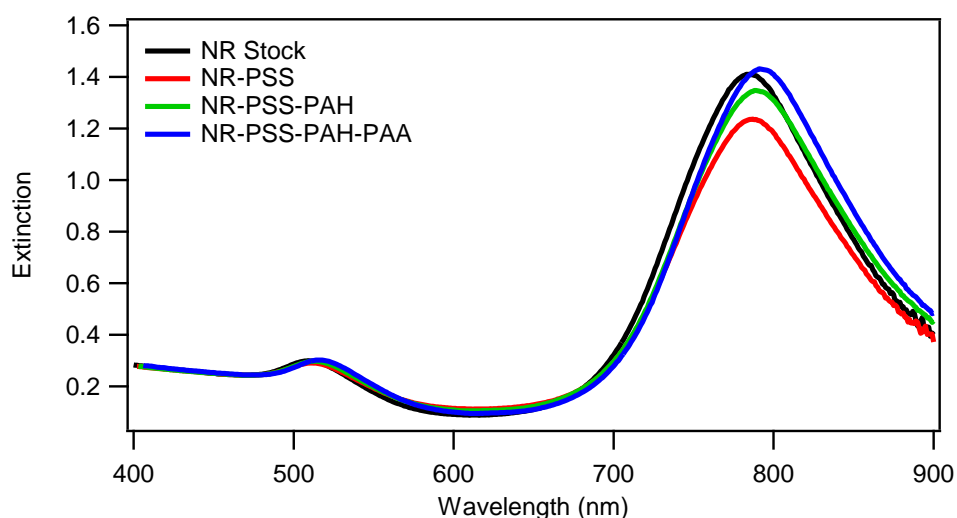


Figure 6.2. Extinction profiles obtained following each wrapping step

The extinction data in Figure 6.2 shows that there is no significant broadening of the spectra following each stage, suggesting that there is negligible aggregation. The λ_L peak undergoes very small red shifts, due to the adsorption of each new polymer layer.

The zeta potential was also measured to ensure successful wrapping and to monitor the stability of the NRs, the results are summarised in Table 6.1.

Layer	Polymer Wrapping	Zeta Potential (mV)
CTAB stabilized NR stock	none	+ 31.6
1	PSS	- 48.4
2	PAH	+ 42.6
3	PAA	- 35.9

Table 6.1. Summary of zeta potential measurements obtained for NR stock and following addition of each polymer layer.

The change in zeta potential from positive to negative confirms that wrapping of each polymer layer has been successful. Zeta potentials above + 30, or below - 30 mV typically suggest very high colloidal stability, each result obtained falls into this category, indicating that the multiple wrapping and centrifuge steps have not impacted on the stability of the nanoparticles.

There are a number of benefits to increasing the number of polymer layers, the main one being the increased stability this imparts onto the conjugate, with three layers more stable compared to one. Furthermore, the thickness of each layer can be tuned simply by altering the concentration of sodium chloride used during the polyelectrolyte self-assembly, with higher salt concentrations leading to thicker polymer layers (see Section 2.11) and increased stability of the conjugates. A further advantage is that it is likely that the increased number of polymer layers means that there is a slower leaching of any dye sequestered in the CTAB bilayer.

6.3 Selection of DNA for Conjugation

The design of the coupling reaction is a key step, which in this case requires a condensation reaction between a carboxylic acid group and an amine group. A full list of the DNA sequences used throughout this work, along with their abbreviated names, are shown in Section 2.12. The primary sequences used in this Chapter are:

Probe 1	5'-NH ₂ -(CH ₂) ₁₂ -GTG TTA GCC TCA AGT G-3'
Probe 2	5'-GTC TAT GCG TGA ACT G-(CH ₂) ₆ -NH ₂ -3'
Target	5'-CAG TTC ACG CAT AGA CCA CTT GAG GCT AAC AC-3'

All three sequences represent a sandwich assay format. Probes 1 and 2 are both 16-mers which are non-complementary to each other, but do bind to separate halves of the 32-mer target sequence.

It was not possible to find a commercial source to purchase DNA with a 5' terminated COOH moiety, possibly as a result of poor DNA stability, thus the system was designed to utilise DNA bearing an NH₂ functional group on the 3' end, with the COOH present on the polymer layer surrounding the nanoparticle conjugate. Probe 1 features a C12 spacer on the 5' end, this should reduce any electrostatic repulsion between the phosphate backbone of the DNA and the negatively charged outer polymer layer surrounding the nanoparticles. It was also thought that non-specific adsorption of target DNA onto the negatively charged PAA surface would be reduced compared to other surfaces.

The second oligonucleotide probe has an amine functional group on the 3' end, it was not possible to purchase this probe with a C12 spacer on the 3' end, and thus a C6 spacer is used instead. The third probe sequence does not require any spacer groups, since this sequence will not be conjugated to any nanoparticles, and will instead be free in solution (See assay design later in Section 6.6).

DNA sequences were also purchased which were modified with either a fluorescein (FAM) or cyanine (Cy) dye. These were utilised in an attempt to prove that DNA attachment to the nanoparticles had been successful.

6.4 Reagent for Coupling Chemistry

Typically when carrying out an amide coupling reaction, N-hydroxysulfosuccinimide (NHSS) along with N-(3-dimethylaminopropyl)-N'-ethyl carbodiimide hydrochloride (EDC HCl) are used as the activating and coupling agents respectively. The Corn group have reported successful coupling of amine terminated DNA onto planar gold surfaces functionalized with carboxylic acid groups introduced to the surface through coating with poly-L-glutamic acid (pGlu).^{199, 200} The same group have also reported the covalent attachment of DNA to silica nanoparticles. The method involves functionalization of silica nanoparticles with 3-aminopropyltrimethoxysilane (APTMS), followed by addition of pGlu, amino-terminated DNA was then coupled using EDC and NHSS.²⁰¹

This use of pGlu to impart a carboxylic acid functionality onto the nanorod conjugates was investigated, however, the resulting nanorod suspension was found to be highly unstable (data not shown), and thus, PAA was used as an alternative.

Silica coating was not considered as an option due to issues associated with trying to control the thickness of the silica shell. Furthermore, the subsequent functionalization of silica is not well described, and thus would have to be explored, thereby increasing the complexity of the system.

There are also a number of disadvantages to using EDC/NHSS, primarily that the reagents are not particularly stable in water, and hydrolyse over time. These reagents are highly pH dependent with coupling typically carried out at pH 7-8, it is therefore necessary to carry out the conjugation in a suitable buffer to ensure maximum efficiency.²⁰² However, the use of buffers in this pH range was problematic for the acid terminated nanorod conjugates, which were found to be very sensitive to pH changes, and displayed poor stability at pH 7-8. All attempts to couple amine terminated DNA to PAA coated nanoparticles failed, mainly as a result of poor nanoparticle stability in the buffered environment required, therefore, the work in this Chapter will focus on the use of an alternative coupling agent, 4-(4,6-dimethoxy-1,3,5-triazin-2-yl)-4-methylmorpholinium chloride (DMTMM).

Mechanism of DMTMM Coupling

Kunishima and co-workers have described the novel preparation and application of DMTMM as an alternative coupling agent to achieve the formation of amide bonds.^{203, 204}

The mechanism for the condensation reaction of carboxylic acids with amines to form amides is shown in Figure 6.3.

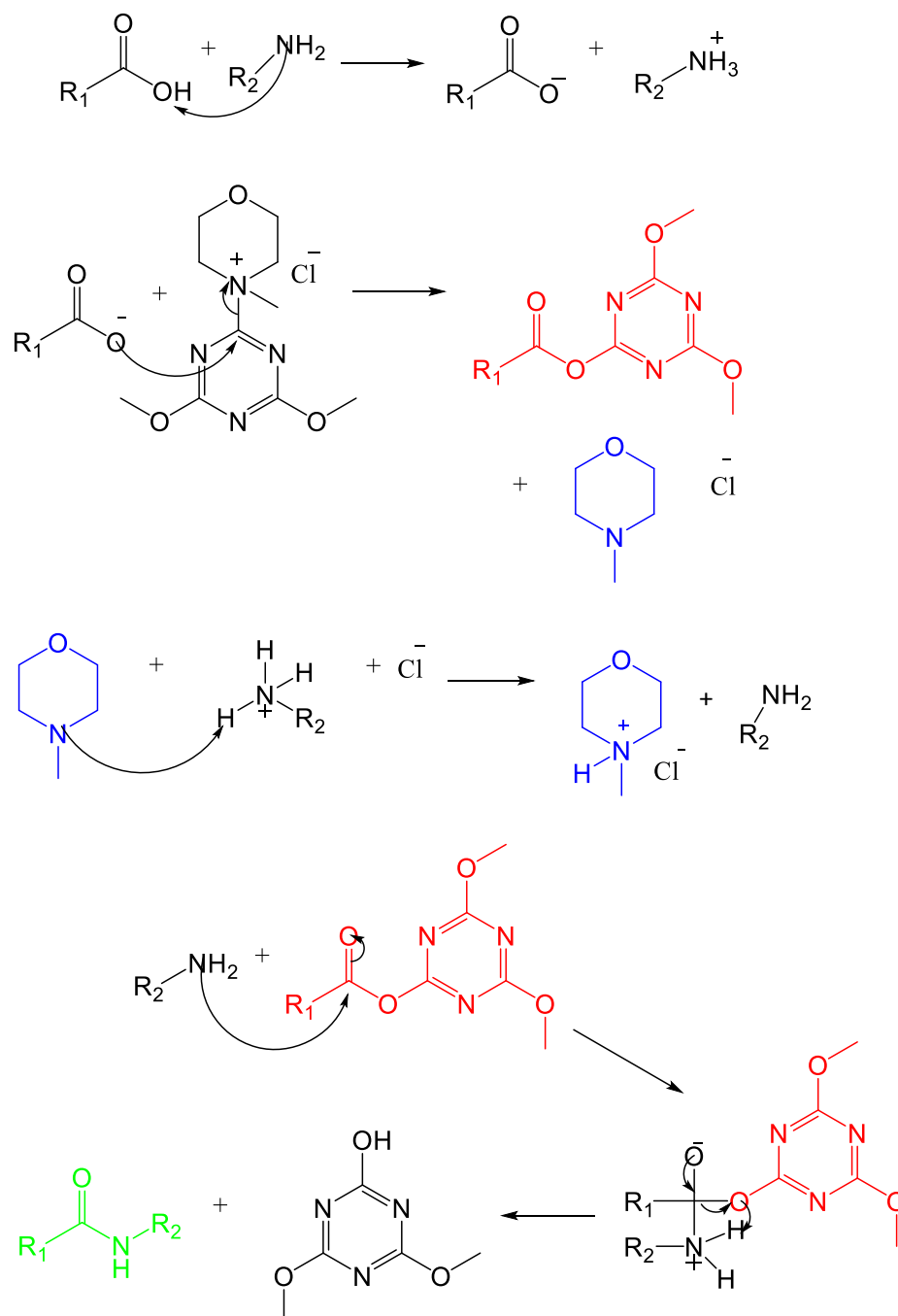


Figure 6.3. Mechanism of DMTMM activated amidation of carboxylic acids

The mechanism shown describes the simple one-step condensation of carboxylic acids and amines to form amide bonds. A key point to note is that in order to increase reaction yields, both the carboxylic acid and the amine should be premixed prior to addition of DMTMM, to facilitate the formation of an ammonium carboxylate salt.²⁰³

The use of DMTMM is advantageous for a number of reasons, reaction efficiencies are high, and Kunishima *et al* have demonstrated that this reagent is applicable to the coupling of both small molecules and polymers.^{112, 203, 204} The preparation of DMTMM is relatively inexpensive and very straightforward, and excess by-products are easily removed from the reaction.²⁰³ This coupling chemistry is compatible with many solvents, including alcohols and tetrahydrofuran, this is not relevant here since biological molecules such as DNA will not survive these conditions. However, it has also been demonstrated that water is a suitable solvent for this reaction,²⁰⁵ making this reagent ideal for applications where stability of the metallic nanoparticles is an issue. DMTMM has also been shown to be effective over a wide pH range, meaning that a variety of buffers can be used.²⁰⁵

The proposed scheme in Figure 6.1. depicts the use of multiple polymer layers around the nanoparticle, with the outer layer being PAA, a further advantage is that the direct conjugation of ligands bearing an amine moiety to poly(acrylic acid) (PAA) has been reported.²⁰⁶

6.5 Covalent Conjugation of DNA to Spherical Nanoparticles

In order to test the conjugation chemistry, the attachment of DNA to spherical nanoparticles was also investigated, as a possible concept for future investigations was to explore sensor designs taking advantage of the extinction properties of larger spherical nanoparticles. Also, a direct comparison of DNA attachment efficiencies with that for nanorods could be performed.

Section 6.2. describes the polymer layers proposed for the nanorod-dye conjugates, with PSS as the first layer based on the electrostatic attraction between the positively charged CTAB stabilizing agent and the negatively charged polymer. In the case of coupling DNA to spherical nanoparticles, a slightly different approach has to be taken, the creation of polyelectrolyte coated nanospheres was first attempted by wrapping the negatively charged citrate capped spherical gold with positively charged polymers. This approach

proved to be problematic, as it was not possible to develop a multilayer coating method that produced a final layer functionalized with carboxylic acid moieties. Furthermore, the citrate-reduced nanoparticles also display very low tolerance to NaCl required for the coating process, resulting in irreversible aggregation, and therefore attempts to polyelectrolyte wrap the citrate capped gold particles were unsuccessful.

As a result, a new route for the preparation of nanoparticles which have a high surface charge density and functional groups which enable the polyelectrolyte wrapping was investigated.

A range of polymers have been used as stabilising agents (and in some cases, joint stabilising and reducing agents) in the synthesis of gold nanoparticles, including polyvinyl acetate (PVA),²⁰⁷ poly(sodium acrylate) (PSA),²⁰⁸ poly(methacrylic acid) (PMAA),²⁰⁹ polyethyleneimine (PEI)²¹⁰ and poly(diallyl dimethylammonium chloride) (PDDAC).²¹¹

The synthesis of PAH Au is described in detail in Section 2.15, briefly HAuCl₄ is dissolved in distilled water prior to addition of PAH, which acts as a joint reducing and stabilizing agent, the solution is then heated to 98 °C for approximately 15 minutes, after which time, the solution turned a deep red colour, indicating successful nanoparticle formation. A range of synthesis conditions were explored, with PAH : HAuCl₄ ratios varying from 0.5 : 2 to 4 : 2, however, control over the particle size was only possible over a very narrow range (with λ_{max} variations of < 5 nm), therefore, to prepare smaller nanoparticles using PAH as the stabilizing agent, it is likely that an additional reducing agent would have to be employed.

Typical extinction spectra obtained for PAH reduced and stabilized gold nanoparticles and citrate capped gold nanoparticles are compared in Figure 6.4.

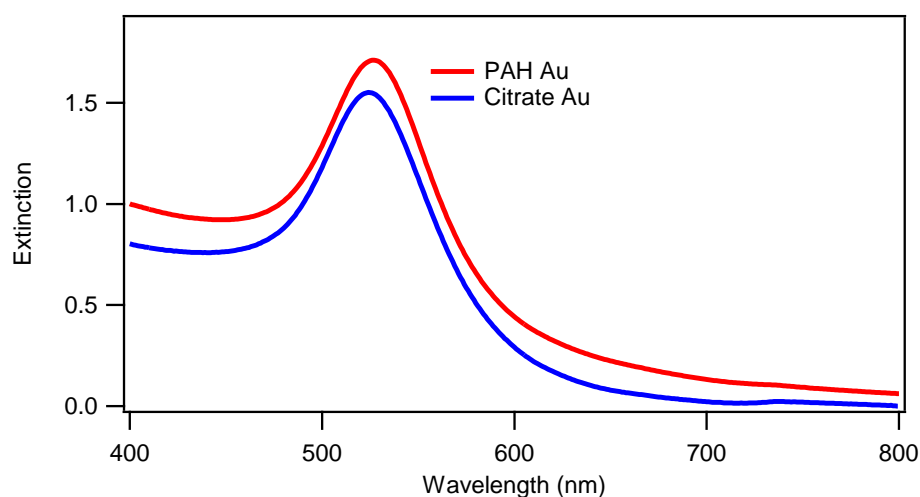


Figure 6.4. Typical extinction spectra obtained for PAH and citrate stabilized gold nanoparticles

The extinction spectra shows the PAH stabilized and citrate capped nanoparticles with a λ_{\max} at 526 nm and 524 nm respectively. Both spectra are fairly narrow with minimal tailing, suggesting a good level of monodispersity. The hydrodynamic diameter of the PAH Au was determined by DLS measurements, which calculated an average diameter size of 54.7 nm, and also gave a low value for the polydispersity index, indicating that the particle sizes measured are fairly consistent. The citrate capped gold shown here was used previously in Chapter 3, where SEM images revealed it has an average particle size of 38 nm. SEM analysis was also carried out to confirm the size and monodispersity of the PAH stabilized nanoparticles, with the results shown in Figure 6.5.

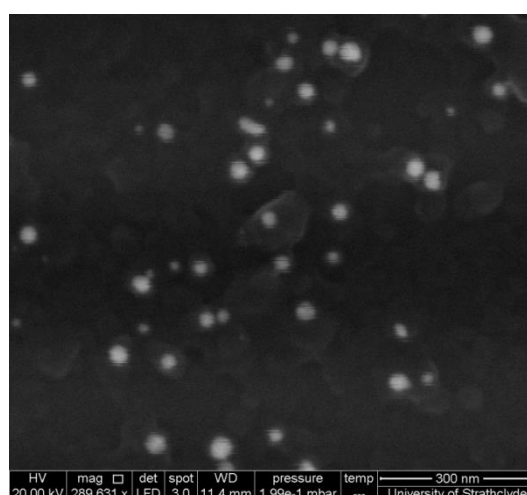


Figure 6.5. SEM analysis of PAH stabilized gold nanoparticles

Samples for SEM were prepared as previously described in Section 2.24, briefly, the wafer was cleaned and coated with a layer of the negatively charged polymer PSS. A dilute aliquot of the PAH Au stock was introduced to the surface and left for 30 minutes, after which it was removed and the surface was rinsed with distilled water. This process ensures that there is no drying induced aggregation on the wafer surface, meaning the SEM images can accurately provide information on the monodispersity of the sample. Analysis of the images confirmed that the average particle size was 34 nm.

Zeta potential measurements for the PAH Au colloid showed that the surface charge was +38.9 mV, the high value obtained verifies that the particles were extremely stable.

There are a number of advantages associated with using PAH as the joint reducing and stabilizing agent, notably that the nanoparticles display increased stability compared to citrate-capped gold. In fact, PAH Au remains stable in salt concentrations (e.g. 40 mM NaCl) significantly above that which would cause aggregation of citrate capped gold. This is a key benefit since polymer wrapping must be carried out in salt solutions in order to ionize the polymer and result in successful encapsulation of the nanoparticles. The thiol-chemistry based methods to couple DNA to nanoparticles typically require the presence of salt in order to increase the packing density of DNA on the particle surface. With particles where salt stability is an issue, steps such as salt ageing (where the salt concentration is gradually increased over time) are necessary, and even then, the stability of the nanoparticles is not guaranteed, with many conjugations failing due to aggregation occurring. PAH Au was found to be stable at salt concentrations above those required for typical conjugation methods.

A further advantage to using PAH is that it is possible to coat the nanoparticles with the same polymer layers as used for the nanorods. The coupling chemistry was then carried out in the same way as for the NRs.

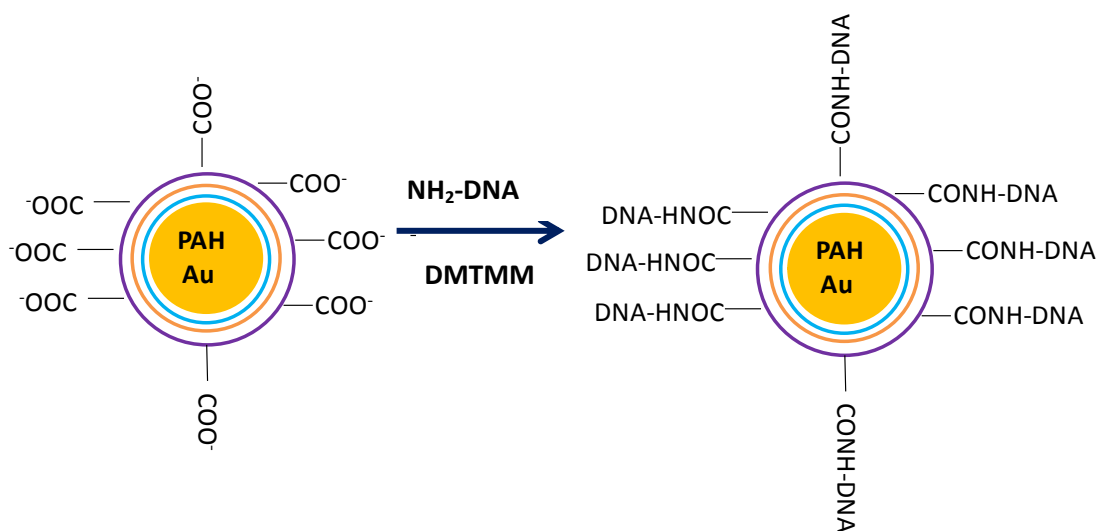


Figure 6.6. Schematic outlining the proposed covalent attachment of DNA to PAH-capped spherical gold nanoparticles.

The use of PAH stabilized Au is critical here, as it allows the use of the same polymer wrapping regime as for the nanorod example shown previously. The coating procedure is described in Section 2.16, a key difference compared with the coating of the nanorod samples is that the salt concentration for the final layer of wrapping must be reduced to 50 mM, (compared to 0.1 M for the NRs) this was found to aid the wrapping process and resulted in a highly stable final product.

Following wrapping with each polymer layer, the sample was centrifuged at least twice, and resuspended in distilled water to remove any excess polymer from the solution. Extinction measurements were taken following each step to ensure the nanoparticles had not aggregated, and to resuspend the samples into an appropriate volume of water to keep particle concentrations roughly constant.

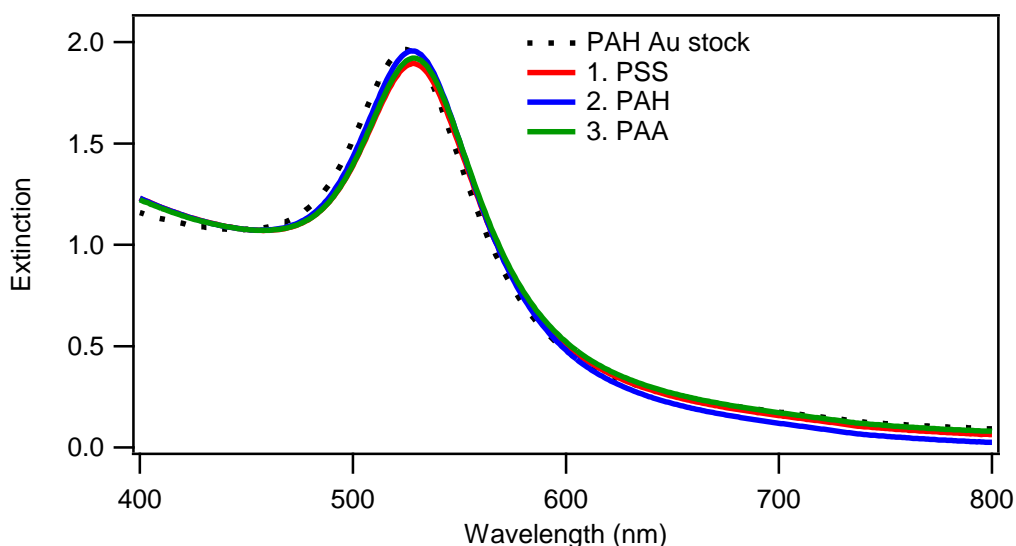


Figure 6.7. Extinction profiles obtained following each wrapping step.

The extinction data in Figure 6.7 shows that there is no significant broadening of the spectra following each additional polymer layer, suggesting that there is negligible aggregation. The λ_{max} position undergoes very small red shifts due to the adsorption of each new layer.

The surface charge was also monitored at each stage via zeta potential measurements, as shown in Table 6.3. As for the nanorod samples discussed previously in Table 6.1, the results show a change from positive to negative on each subsequent wrapping step, confirming the success of each stage and high stability of the nanoparticles following each polymer wrapping step.

Layer	Polymer Wrapping	Zeta Potential (mV)
PAH Au Stock	none	+ 38.9
1	PSS	- 60.0
2	PAH	+ 59.4
3	PAA	- 30.0

Table 6.3. Zeta potentials measured for PAH Au following each wrapping stage.

6.6 Proof of DNA Surface Attachment and Assay Design

Prior to attempting any conjugation of DNA to nanoparticles, it was important to confirm the bioactivity of the DNA in solution. The sandwich assay probe sequences are discussed earlier in Section 6.3, and are represented in Figure 6.8.

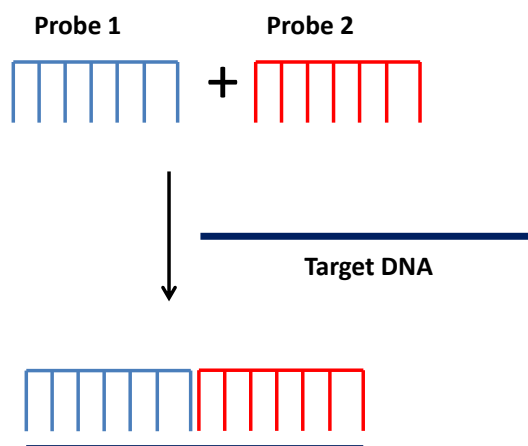


Figure 6.8. Schematic outlining hybridisation process in DNA sandwich assay.

The bioactivity of the DNA was confirmed by performing a melting curve of the hybridising DNA sequences. The melting temperature (T_m) is defined as the point of inflection on the sigmoidal profile, and is representative of the thermal stability of the duplex. The sharp peak obtained proves that the DNA is able to hybridise and then dissociate as the temperature is gradually increased, thereby proving that the DNA is biologically active.

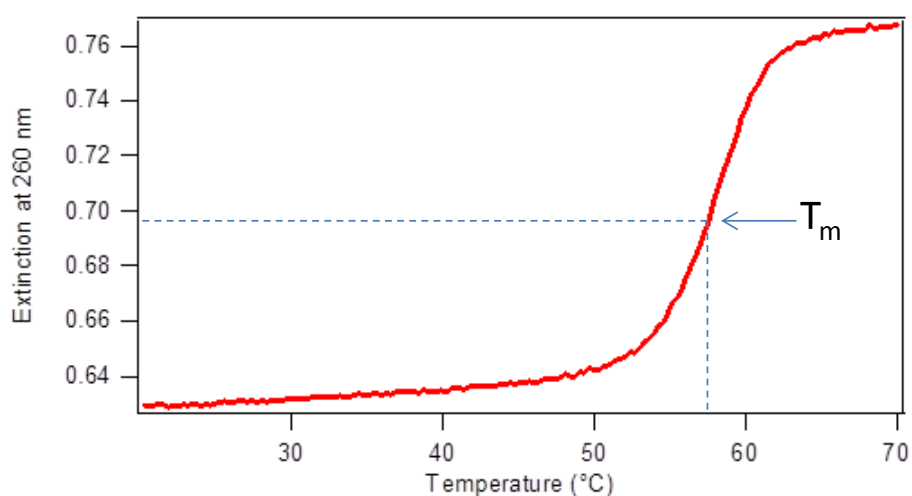


Figure 6.9. UV melting curve obtained for the two DNA probes and the target DNA at 260 nm.

The theoretical T_m for the 32-mer was calculated as 64 °C, while the hybridised DNA shown here has a T_m value of 58 °C. The experimental values obtained are slightly different due to the two 16-mer halves binding to form the 32-mer.

The procedure for conjugation of DNA to polymer coated nanoparticles is described in detail in Sections 2.14 and 2.17. Briefly, the DNA is premixed with the PAA coated nanoparticles for approximately 15 minutes prior to addition of DMTMM. A number of samples were prepared to investigate whether or not DNA attachment was successful, including two different types of control, the first where DNA was added, but no coupling agent was included, and the second, where no DNA was introduced, but coupling agent was present in the reaction mixture. The samples were agitated for 16 hours and then centrifuged and resuspended in 0.3 M PBS prior to analysis.

Visual inspection of the quasi-spherical samples shows that for the control samples, the nanoparticles have settled to the bottom of the eppendorf tube, suggesting aggregation has occurred, while for the sample that contained DNA and coupling agent, the nanoparticles have remained in solution (See Figure 6.10).

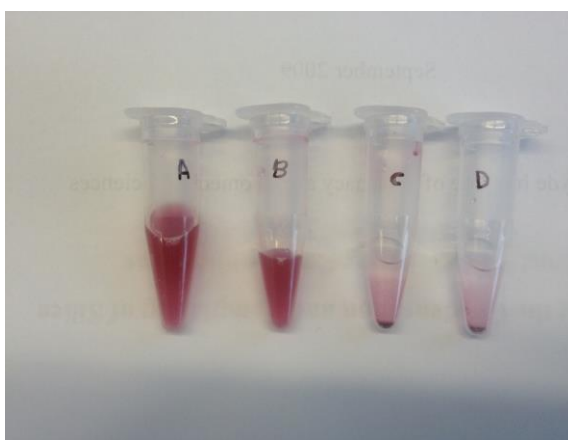


Figure 6.10. Visual analysis of quasi-spherical samples where (a) is PAH Au stock polymer wrapped (PSS-PAH-PAA), (b) DNA conjugation has been attempted (c) Control sample where no DNA was present, and DMTMM was introduced and (d) Control sample where DNA was added and no DMTMM was present.

For the control samples prepared using quasi-spherical colloid, the prolonged agitation and centrifugation resulted in destabilization of the quasi spherical colloid in the

presence of NaCl and buffer. However, the coated nanorod samples were stable in extremely high salt conditions (> 0.3 M NaCl), and aggregation was not observed.

The samples shown above were then analysed via extinction measurements, which confirm the evidence from the visual inspection and show that while the control samples have both aggregated, the sample prepared using DNA and the DMTMM coupling agent is stable.

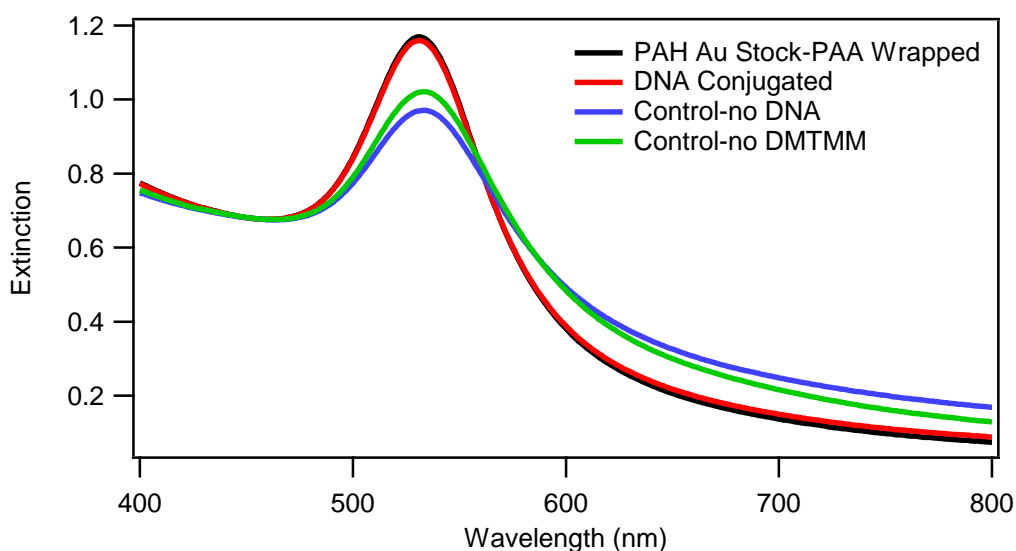


Figure 6.11. Extinction spectra of Stock PAH Au polymer wrapped (PSS-PAH-PAA), sample where DNA conjugation has been attempted, control sample where DMTMM was introduced, but no DNA was added and control sample where DNA was added but no DMTMM was used.

These two pieces of evidence point towards the increased stability of the nanorod and sphere samples where DNA conjugation has been attempted, with the samples found to be stable when undergoing repeat centrifuge and resuspension steps, suggesting that functionalization has been successful. However, alternative methods must be used to confirm this.

One option to prove that DNA attachment to both the nanorods and spheres had been successful is to use dye labelled oligonucleotides. However, the design of the nanorod and nanospheres probes means that the multiple polymer wrapped layers would space this dye at a distance of approximately 10 nm from the metal surface, meaning that confirmation of successful DNA attachment using SERRS analysis is unlikely to be applicable here. This approach was attempted, however, results were found to be inconclusive.

A second method commonly used to confirm the conjugation of DNA is extinction based measurements, i.e. looking for shifts of the nanoparticle SPR following attachment of the DNA. However, the spacing between the metal and the DNA molecule arising as a result of the polymer layers again means that this approach is also unlikely to be successful. This was also investigated, and again the results proved inconclusive.

Another possible route is to use a fluorescent dye attached to the oligonucleotide sequence, when the dye is conjugated to the nanoparticle fluorescence should be quenched. The enzyme DNase I is then introduced, which hydrolyses the DNA, releasing it from the surface. This results in a fluorescence signal, since it is no longer quenched by the metal surface, and thus, it is possible to not only determine if DNA is attached to the nanoparticles, but to also allows quantification of how much is present.²¹² Again, the spacing between the dye and the metal again means that this approach may not be appropriate, and again, no conclusive evidence was found to determine whether or not coupling had been successful. It should be possible to use surface enhanced fluorescence to prove that coupling has occurred, however these experiments were not undertaken due to time constraints.

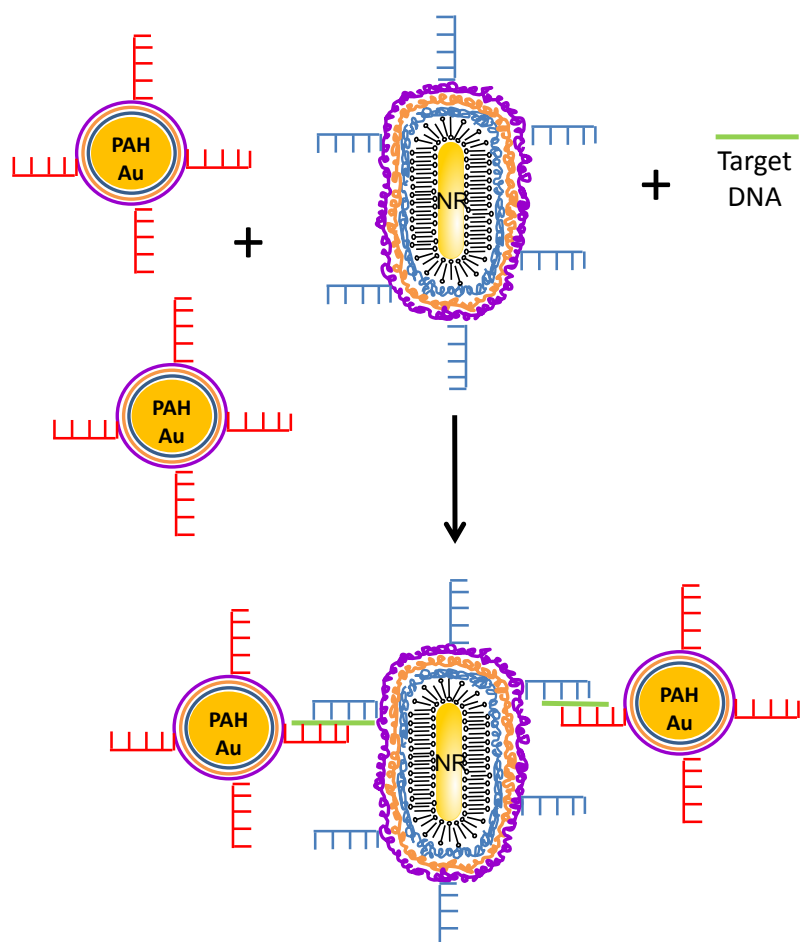


Figure 6.12. Schematic showing proposed DNA sandwich assay using gold nanorods and spheres.

A schematic outlining the proposed sandwich assay to be carried out is shown in Figure 6.12. In this assay format, one strand of DNA is conjugated to the nanorods and another non-complementary strand is hybridised to the spherical nanoparticles. A DNA target sequence which is complementary to both is then introduced, which will cause the sequences to hybridise, resulting in aggregation of the nanoparticles. Due to a lack of time, successful demonstration of this assay was not realised and remains a point for future investigation.

6.7 Conclusions

The main aim of this Chapter was to develop a novel route for the functionalization of polymer stabilized nanoparticles with DNA. The proposed route was to create carboxylic

acid functionalized nanorods and covalently couple these to amine terminated DNA. The work here describes the successful preparation of stable nanorods with carboxylic acid functional groups via multilayer polymer wrapping.

In order to develop a complementary route for spherical particles, the polymer PAH was used as both the reducing and stabilizing agent to create very stable positively charged colloid. The subsequent layer by layer polymer functionalization of these nanoparticles to form highly stable functionalized surfaces was reported.

Preliminary work was carried out using two coupling agents to conjugate bioactive DNA to these nanoparticles. While attempts at EDC/NHSS mediated coupling failed, initial results suggest that a less commonly used coupling agent, DMTMM, was more successful, although conclusive proof was not obtained.

6.8 Future Work

The final Chapter in this thesis is the least developed, however the preliminary results obtained suggest that with time, covalent coupling can be achieved in this manner. Assuming that conclusive proof is obtained then the next step is to optimise the parameters involved in the conjugation to maximise the efficiency of the reaction.

Following successful conjugation an assay such as the one described in Figure 6.12 should be developed, and the limit of detection for this system should be determined. This opens up a route for combined nanorod and spherical nanoparticle assays for optical imaging and SERRS applications. A different class of sensing applications are envisioned for both surface and solution based imaging applications.

It would also be interesting to test the conjugation chemistry for the attachment of various other biomolecules, including amine or carboxylic acid functionalized proteins. If successful then this chemistry could be used to develop probes capable of targeting specific cells or areas within a cell. Combined with the UST concept introduced previously in Chapter 5, this would be a powerful tool for cellular imaging applications.

Chapter 7

Conclusions

The novel preparation of nanorod-dye conjugates capable of producing bright Raman signals whilst remaining unaggregated, and thus hot spot free, has been described. It has clearly been demonstrated that there are a number of advantages to this approach, including conjugate stability even during prolonged storage (> 8 months), control over the dye surface orientation and high levels of reproducibility.

The system described in this thesis can act as a model system to determine the relative dye molecular resonance and nanoparticle LSPR contributions to SERRS enhancements, as well as look at controlled resonance coupling. First two dye and nanorods with two different λ_L positions were picked to closely coincide with two Raman laser excitation wavelengths (633 and 785 nm). The results obtained appear to suggest that the contribution from the dye is dominant. However, for one combination tested, it was found that the highest signal enhancements were obtained off resonance of this dye, indicating that joint experimental and theoretical experiments need to be undertaken to fully understand this effect. A comparison of nanorods versus quasi-spherical nanoparticles showed the nanorod-dye system to be much brighter.

A novel strategy for the side-by-side assembly of the nanorod-dye conjugates was demonstrated by taking advantage of the anisotropy of the nanorods. It was possible to achieve control over the final cluster size, with the polymer-wrapped clusters shown to remain stable in suspension following storage for upwards of eight months. This work also represents the first correlation between the SERRS intensities for stabilized clusters in solution with the change in extinction, with side-by-side aggregation shown to provide SERRS signal enhancements of up to five fold.

The concept of a universal SERRS tag (UST) was introduced. Nanotags were prepared via the co-assembly of multiple different dyes onto the same nanorod. These tags were shown to be capable of producing strong Raman signals across a wide range of common laser excitation wavelengths (514-1064 nm) whilst remaining monodisperse.

Again, following polyelectrolyte wrapping, the USTs were found to be stable for upwards of 6 months without leaching of the dye from the CTAB bilayer with no loss of SERRS intensity.

The brightness of the tags was confirmed via single particle Raman measurements, which were correlated with SEM images to provide conclusive evidence that strong single particle SERRS signals were possible for these tags.

The application of the USTs for cellular imaging was also investigated, and these tags were found to be non-cytotoxic when incubated with dendritic cells. Joint Raman mapping and confocal fluorescence studies have proven that the USTs were localized within the cells, and good image correlation was possible for data obtained at a range of excitation wavelengths. The fact that confocal fluorescence maps of the same cells also correlated well with the SERRS maps highlights the potential of the USTs for multimodal imaging.

A novel methodology to achieve the covalent coupling of biomolecules to polymer-wrapped rods and spherical particles was described. Preliminary data gathered suggested that this route represents a potential method to achieve the functionalization of polymer stabilized nanoparticles.

To conclude, it has been clearly demonstrated in this thesis that the co-assembly of molecular dyes and nanorods represents a very interesting system for a number of reasons. These include enabling fundamental studies of nanoparticle-dye interactions both from a materials and spectroscopic perspective, as well as potentially leading to a host of new applications in the future.

References

1. E. C. Dreaden, Alkilany, A.M., Huang, X., Murphy, C.J., El-Sayed, M.A., *Chem. Soc. Rev.*, 2012, **41**, 2740-2779.
2. E. Boisselier, Astruc, D., *Chem. Soc. Rev.*, 2009, **38**, 1759-1782.
3. E. C. Dreaden, Mackey, M.A., Huang, X., Kang, B., El-Sayed, M.A., *Chem. Soc. Rev.*, 2011, **40**, 3391-3404.
4. T. K. Sau, Murphy, C.J., *J. Am. Chem. Soc.*, 2004, **28**, 8648-8649.
5. M. Grezelczak, Perez-Juste, J., Mulvaney, P., Liz-Marzan, L.M., *Chem. Soc. Rev.*, 2008, **37**, 1783-1791.
6. J. Perez-Juste, Pastoriza-Santos, I., Liz-Marzan, L.M., Mulvaney, P., *Coord. Chem. Rev.*, 2005, **249**, 1870-1901.
7. J. Homola, Yee, S.S., Gauglitz, G., *Sens. Actuators, B*, 1999, **54**, 3-15.
8. D. J. Campbell, Xia, Y., *J. Chem. Ed.*, 2007, **84**, 91-96.
9. K. A. Willets and R. P. Van Duyne, *Annu. Rev. Phys. Chem.*, 2007, **58**, 267-297.
10. M. Hu, Chen, J., Li, Z.Y., Au, L., Hartland, G.V., Li, X., Marquez, M., Xia, Y., *Chem. Soc. Rev.*, 2006, **35**, 1084-1094.
11. J. Yguerabide, Yguerabide, E.E., *Anal. Biochem.*, 1998, **262**, 137-156.
12. T. G. Pavlopoulos, Golich, D.J., *J. Appl. Phys.*, 1988, **64**, 521-527.
13. P. B. Johnson, Christy, R.W., *Phys. Rev. B*, 1970, **6**, 4370-4379.
14. P. Mulvaney, *Langmuir*, 1996, **12**, 788-800.
15. C. L. Nehl, Hafner, J.H., *J. Mater. Chem.*, 2008, **18**, 2415-2418.
16. K. S. Lee, El-Sayed, M.A., *J. Phys. Chem. B*, 2005, **109**, 20331-20338.
17. P. C. Waterman, *Proc. IEEE*, 1965, **53**, 805-812.
18. Y. Sun, Xia, Y., *Analyst*, 2003, **128**, 686-691.
19. B. D. Busbee, Obare, S.O., Murphy, C.J., *Adv. Mater.*, 2003, **15**, 414-416.
20. B. P. Khanal, Zubarev, E.R., *J. Am. Chem. Soc.*, 2008, **130**, 12634-12635.
21. Y. Yu, Chang, S.S., Lee, C.L., Wang, C.R.C., *J. Phys. Chem. B*, 1997, **101**, 6661-6664.
22. N. R. Jana, Gearheart, L., Murphy, C.J., *Adv. Mater.*, 2001, **13**, 1389-1393.
23. Z. Guo, Fan, X., Xu, L., Lu, X., Gu, C., Bian, Z., Gu, N., Zhang, J., Yang, D., *Chem. Commun.*, 2011, **47**, 4180-4182.
24. G. Plascencia-Villa, Bahena, D., Rodriguez, A.R., Ponce, A., Jose-Yacamán, M., *Metallomics*, 2013, **5**, 242-250.
25. B. Nikoobakht, El-Sayed, M.A., *Chem. Mater.*, 2003, **15**, 1957-1962.
26. X. Huang, Neretina, S., El-Sayed, M.A., *Adv. Mater.*, 2009, **21**, 4880-4910.
27. D. A. Zweifel, Wei, A., *Chem. Mater.*, 2005, **17**, 4256-4261.
28. T. K. Sau, Murphy, C.J., *Langmuir*, 2004, **20**, 6414-6420.
29. C. J. Murphy, Sau, T.K., Gole, A.M., Orendorff, C.J., Gao, J., Gou, L., Hunyadi, S.E., Li, T., *J. Phys. Chem. B*, 2005, **109**, 13857-13870.
30. C. J. Johnson, E. Dujardin, S. A. Davis, C. J. Murphy and S. Mann, *J. Mat. Chem.*, 2002, **12**, 1765-1770.
31. M. Liu, Guyot-Sionnest, P., *J. Phys. Chem. B*, 2005, **109**, 22192-22200.
32. C. Wu, Bull, B., Szymanski, C., Christensen, K., McNeill, J., *ACS Nano*, 2008, **2**, 2415-2423.
33. A. W. Wark, Stokes, R.J., Darby, S.B., Smith, W.E., Graham, D., *J. Phys. Chem. C*, 2010, **114**, 18115-18120.
34. M. H. Chowdhury, Ray, K., Gray, S.K., Pond, J., Lakowicz, J.R., *Anal. Chem.*, 2009, **81**, 1397-1403.

35. F. Tam, Goodrich, G. P., Johnson, B. R., Halas, N. J., *Nano Lett.*, 2007, **7**, 496-501.
36. J. R. Lakowicz, *Anal. Biochem.*, 2001, **298**, 1-24.
37. D. A. Long, *Raman Spectroscopy*, McGraw-Hill, New York, 1977.
38. C. V. Raman, Krishan, K.S., *Nature*, 1928, **121**, 501-502.
39. E. B. Hanlon, Manoharan, R., Koo, T.W., Shafer, K.E., Motz, J.T., Fitzmaurice, M., Kramer, J.R., Itzkhan, I., Dasari, R.R., Feld, M.S., *Phys. Med. Biol.*, 2000, **45**, R1.
40. C. H. Liu, Das, B.B., Glassman, L.S., Tang, G.C., Yoo, K.M., Zhu, H.R., Akins, D.L., Lubicz, S.S., Cleary, J., Prudente, R., Celmer, E., Caron, A., Alfano, R.R., *J. Photochem. Photobiol. B: Biol.*, 1992, **16**, 187-209.
41. R. C. Lord, Yu, N.T., *J. Mol. Biol.*, 1970, **50**, 509-524.
42. E. Hao and G. C. Schatz, *J. Chem. Phys.*, 2004, **120**, 357-366.
43. D. G. Thompson, Enright, A., Faulds, K., Smith, W. E., Graham, D., *Anal. Chem.*, 2008, **80**, 2805-2810.
44. M. Moskovits, *Phys. Chem. Chem. Phys.*, 2013, **15**, 5301-5311.
45. E. Smith, Dent, G., *Modern Raman Spectroscopy, a Practical Approach*, J. Wiley, Hoboken, N.J, 2005.
46. E. C. Le Ru, E. Blackie, M. Meyer and P. G. Etchegoin, *J. Phys. Chem. C*, 2007, **111**, 13794-13803.
47. R. Aroca, *Surface-enhanced Vibrational Spectroscopy*, John Wiley & Sons, Chichester, 2006.
48. J. McMahan, Henry, A. I., Wustholz, K., Natan, M., Freeman, R., Van Duyne, R., Schatz, G., *Anal. Bioanal. Chem.*, 2009, **394**, 1819-1825.
49. J. C. S. Costa, R. M. A. Ando, P. H. C. Camargo and P. Corio, *J. Phys. Chem. C*, 2011, **115**, 4184-4190.
50. E. Le Ru, Etchegoin, P., *Principles of Surface Enhanced Raman Spectroscopy and Related Plasmonic Effects*, Elsevier, Amsterdam, 2009.
51. V. Amendola and M. Meneghetti, *Adv. Funct. Mater.*, 2012, **22**, 353-360.
52. K. Kneipp, H. Kneipp, R. Manoharan, E. B. Hanlon, I. Itzkan, R. R. Dasari and M. S. Feld, *Appl. Spectrosc.*, 1998, **52**, 1493-1497.
53. K. Kneipp, Y. Wang, H. Kneipp, L. T. Perelman, I. Itzkan, R. R. Dasari and M. S. Feld, *Phys. Rev. Lett.*, 1997, **78**, 1667-1670.
54. S. Nie, Emory, S.R., *Science*, 1997, 1102-1106.
55. X. Lu, Rycenga, M., Skrabalak, S.E., Wiley, B., Xia, Y., *Annu. Rev. Phys. Chem.*, 2009, **60**, 167-192.
56. A. D. McFarland, Young, M.A., Dieringer, J.A., Van Duyne, R.P., *J. Phys. Chem. B*, 2005, **109**, 11279-11285.
57. C. L. Haynes and R. P. Van Duyne, *J. Phys. Chem. B*, 2003, **107**, 7426-7433.
58. K. Faulds, Littleford, R.E., Graham, D., Dent, G., Smith, W.E., *Anal. Chem.*, 2004, **76**, 592-598.
59. S. T. Sivapalan, DeVetter, B.M., Yang, T.K., van Dijk, T., Schulmerich, M.V., Carney, P.S., Bhargava, R., Murphy, C.J., *ACS Nano*, 2013, **7**, 2099-2105.
60. K. L. Kelly, E. Coronado, L. L. Zhao and G. C. Schatz, *J. Phys. Chem. B*, 2003, **107**, 668-677.
61. B. Nikoobakht, Wang, J. P., El-Sayed, M. A., *Chem. Phys. Lett.*, 2002, **366**, 17-23.
62. C. J. Orendorff, Gearheart, L., Jana, N.R., Murphy, C.J., *Phys. Chem. Chem. Phys.*, 2006, **8**, 165-170.
63. Q. Liao, Cheng, M., Xu, D.S., Ai, X.C., Yao, J.N., Zhang, J.P., *Langmuir*, 2009, **25**, 4708-4714.
64. C. J. Murphy, Gole, A.M., Hunyadi, S.E., Stone, J.W., Sisco, P.N., Alkilany, A., Kinard, B.E., Hankins, P., *Chem. Commun.*, 2008, 544-557.

65. C. A. Mirkin, Letsinger, R.L., Mucic, R.C., Storhoff, J.J., *Nature*, 1996, **382**, 607-609.
66. A. M. Alkilany, Nagaria, P.K., Hexel, C.R., Shaw, T.J., Murphy, C.J., Wyatt, M.D., *Small*, 2009, **5**, 701-708.
67. K. Aslan, Lakowicz, J. R., Geddes, C. D., *Curr. Opin. Chem. Biol.*, 2005, **9**, 538-544.
68. R. Elghanian, Storhoff, J.J., Mucic, R.C., Letsinger, R.L., Mirkin, C.A., *Science*, 1997, **277**, 1078-1081.
69. K. S. Lee and M. A. El-Sayed, *J. Phys. Chem. B*, 2006, **110**, 19220-19225.
70. C. Yu, Irudayaraj, J., *Anal. Chem.*, 2006, **79**, 572-579.
71. G. J. Nusz, Marinakos, S.M., Curry, A.C., Dahlin, A., Hook, F., Wax, A., Chilkoti, A., *Anal. Chem.*, 2008, **80**, 984-989.
72. C. L. Baciou, Becker, J., Janshoff, A., Sonnichsen, C., *Nano Lett.*, 2008, **8**, 1724-1728.
73. H. R. Sim, Wark, A.W., Lee, H.J., *Analyst*, 2010, **135**, 2528-2532.
74. N. L. Rosi, Mirkin, C. A., *Chem. Rev.*, 2005, **105**, 1547-1562.
75. E. Dujardin, Hsin, L.B., Wang, C.R.C., Mann, S., *Chem. Commun.*, 2001, 1264-1265.
76. H. J. Parab, Jung, C., Lee, J.H., Park, H.G., *Biosens. Bioelectron.*, 2010, **26**, 667-673.
77. T. M. Cotton, Kim, J.H., Chumanov, G.D., *J. Raman Spectrosc.*, 1991, **22**, 729-742.
78. X. M. Qian, X. H. Peng, D. O. Ansari, Q. Yin-Goen, G. Z. Chen, D. M. Shin, L. Yang, A. N. Young, M. D. Wang and S. M. Nie, *Nat. Biotechnol.*, 2008, **26**, 83-90.
79. H. Chon, Lee, S., Son, S.W., Oh, C.H., Choo, J., *Anal. Chem.*, 2009, **81**, 3029-3034.
80. H. Chon, Lim, C., Ha, S.M., Ahn, Y., Lee, E.K., Chang, S.I., Seong, G.H., Choo, J., *Anal. Chem.*, 2010, **82**, 5290-5295.
81. G. F. Wang, Lipert, R.J., Jain, M., Kaur, s., Chakraborty, S., Torres, M.P., Batra, S.K., Brand, R.E., Porter, M.D., *Anal. Chem.*, 2011, **83**, 2554-2561.
82. E. J. Dufek, Ehlert, B., Granger, M.C., Sandrock, T.M., Legge, S.L., Herrmann, M.G., Meikle, A.W., Porter, M.D., *Analyst*, 2010, **135**, 2811-2817.
83. K. Ryu, Haes, A.J., Park, H.Y., Nah, S., Kim, J., Chung, H., Yoon, M.Y., Han, S.H., *J. Raman Spectrosc.*, 2010, **41**, 121-124.
84. W. A. El-Said, Kim, T.H., Yea, C.H., Kim, H., Choi, J.W., *J. Nanosci. Nanotechnol.*, 2011, **11**, 768-772.
85. X. M. Qian, Zhouand, X., Nie, S.M., *J. Am. Chem. Soc.*, 2008, **130**, 14934-14935.
86. H. Zhang, Harpster, M.H., Park, H.J., Johnson, P.A., Wilson, W.C., *Anal. Chem.*, 2011, **83**, 1009-1015.
87. B. Guven, Basaran-Akgul, N., Temur, E., Tamer, U., Boyaci, I.H., *Analyst*, 2011, **136**, 740-748.
88. S. W. Bishnoi, Rozell, C.J., Levin, C.S., Gheith, M.K., Johnson, B.R., Johnson, D.H., Halas, N.J., *Nano Lett.*, 2006, **6**, 1687-1692.
89. C. A. R. Auchinvole, Richardson, P., McGuinness, C., Mallikarjun, V., Donaldson, K., McNab, H., Campbell, C.J., *ACS Nano*, 2012, **6**, 888-896.
90. R. A. Alvarez-Puebla, Agarwal, A., Manna, P., Khanal, B.P., Aldeanueva-Potel, P., Carbo-Argibay, E., Pazos-Perez, N., Vigderman, L., Zubarev, E.R., Kotov, N.A., Liz-Marzan, L.M., *Proc. Natl. Acad. Sci. U.S.A.*, 2011, **108**, 8157-8161.
91. W. Cai, Chen, X., *Small*, 2007, **3**, 1840-1854.
92. X. Wang, Qian, X.M., Beitler, J.J., Chen, Z.G., Khuri, F.R., Lewis, M.M., Shin, H.J.C., Nie, S.M., Shin, D.M., *Cancer Res.*, 2011, **71**, 1526-1532.
93. P. K. Jain, Huang, X., El-Sayed, I. H., El-Sayed, M. A., *Acc. Chem. Res.*, 2008, **41**, 1578-1586.
94. X. Huang, El-Sayed, I. H., Qian, W., El-Sayed, M. A., *J. Am. Chem. Soc.*, 2006, **128**, 2115-2120.
95. C. L. Zavaleta, Smith, B.R., Walton, I., Doering, W., Davis, G., Shojaei, B., Natan, M.J., Gambhir, S.S., *Proc. Natl. Acad. Sci. U.S.A.*, 2009, **106**, 13511-13516.

96. G. V. Maltzahn, Centrone, A., Park, J.H., Ramanathan, R., Sailor, M.J., Hatton, T.A., Bhatia, S.N., *Adv. Mater.*, 2009, **21**, 3175-3180.
97. S. Keren, Zavaleta, C., Cheng, Z., de la Zerda, A., Gheysens, O., Gambhir, S.S., *Proc. Natl. Acad. Sci. U.S.A.*, 2008, **105**, 5844-5849.
98. Y. Wang, Seebald, J.L., Szeto, D.P., Irudayaraj, J., *ACS Nano*, 2010, **4**, 4039-4053.
99. G. von Maltzahn, Park, J.H., Agrawal, A., Bandaru, N.K., Das, S.K., Sailor, M.J., Bhatia, S.N., *Cancer Res.*, 2009, **69**, 3892-3900.
100. J. H. Park, von Maltzahn, G., Ong, L.L., Centrone, A., Hatton, T.A., Ruoslahti, E., Bhatia, S.N., Sailor, M.J., *Adv. Mater.*, 2010, **22**, 880-885.
101. W. Lu, Singh, A.K., Khan, S.A., Senapati, D., Yu, H.T., Ray, P.C., *J. Am. Chem. Soc.*, 2010, **132**, 18103-18114.
102. N. W. S. Kam, O'Connell, M., Wisdom, J.A., Dai, H., *Proc. Natl. Acad. Sci. U.S.A.*, 2005, **102**, 11600-11605.
103. A. De La Zerda, Zavaleta, C., Keren, S., Vaithilingam, S., Bodapati, S., Liu, Z., Levi, J., Smith, B.R., Ma, T.J., Oralkan, O., Cheng, Z., Chen, X., Dai, H., Khuri-Yakub, B.T., Gambhir, S.S., *Nat. Nanotechnol.*, 2008, **3**, 557-562.
104. A. Gole, Agarwal, N., Nagaria, P., Wyatt, M.D., Murphy, C.J., *Chem. Commun.*, 2008, **46**, 6140-6142.
105. Y. Cui, Zheng, X.S., Ren, B., Wang, R., Zhang, J., Xia, N.S., Tian, Z.Q., *Chem. Sci.*, 2011, **2**, 1463-1469.
106. S. Lee, Chon, H., Yoon, S.Y., Lee, E.K., Chang, S.I., Lim, D.W., Choo, J., *Nanoscale*, 2012, **2012**, 124-129.
107. H. Kang, Clarke, M.L., Tang, J., Woodward, J.T., Chou, S.G., Zhou, Z., Simpson, J.R., Hight Walker, A.R., Nguyen, T., Hwang, J., *ACS Nano*, 2009, **3**, 3769-3775.
108. M. Mahmoudi, Amiri, H., Shokrgozar, M., Sasanpour, P., Rashidian, B., Laurent, S., Casula, M.F., Lascialfari, A., *Chem. Commun.*, 2011, **47**, 10404-10406.
109. M. Potara, Gabudean, A.M., Astilean, S., *J. Mater. Chem.*, 2011, **21**, 3625-3633.
110. J. Turkevich, P. C. Stevenson and J. Hiller, *Discuss. Faraday Soc.*, 1951, **11**, 55-75.
111. M. B. Lutz, Kukutsch, N., Ogilvie, A.L.J., Robner, S., Koch, F., Romani, N., Schuler, G., *J. Immunol. Methods*, 1999, **223**, 77-92.
112. M. Kunishima, Kawachi, C., Iwasaki, F., Terao, K., Tani, S., *Tetrahedron*, 1999, **40**, 5327-5330.
113. S. Preibisch, Saalfeld, S., Tomancak, P., *Bioinformatics*, 2009, **25**, 1463-1465.
114. H. Chen, Ming, T., Zhao, L., Wang, F., Sun, L.D., Wang, J., Yan, C.H., *Nano Today*, 2010, **5**, 494-505.
115. N. Kometani, M. Tsubonishi, T. Fujita, K. Asami and Y. Yonezawa, *Langmuir*, 2001, **17**, 578-580.
116. A. J. Haes, S. L. Zou, J. Zhao, G. C. Schatz and R. P. Van Duyne, *J. Am. Chem. Soc.*, 2006, **128**, 10905-10914.
117. J. Zhao, Jensen, L., Sung, J., Zou, S., Schatz, G.C., Van Duyne, R.P., *J. Am. Chem. Soc.*, 2007, **129**, 7647-7656.
118. G. P. Wiederrecht, Wurtz, G. A., Hranisavljevic, J., *Nano Lett.*, 2004, **4**, 2121-2125.
119. I. I. S. Lim, F. Goroleski, D. Mott, N. Kariuki, W. Ip, J. Luo and C.-J. Zhong, *J. Phys. Chem. B*, 2006, **110**, 6673-6682.
120. N. T. Fofang, Grady, N.K., Fan, Z., Govorov, A.O., Halas, N.J., *Nano Lett.*, 2008, **11**, 1556-1560.
121. Y. W. Hao, Wang, H.Y., Jiang, Y., Chen, Q.D., Ueno, K., Wang, W.Q., Misawa, H., Sun, H.B., *Angew. Chem., Int. Ed.*, 2011, **50**, 7824-7828.
122. W. Ni, Chen, H., Su, J., Sun, Z., Wang, J., Wu, H., *J. Am. Chem. Soc.*, 2010, **132**, 4806-4814.

123. W. Ni, Yang, Z., Chen, H., Li, L., Wang, J., *J. Am. Chem. Soc.*, 2008, **130**, 6692-6693.
124. W. Ni, Ambjornsson, T., Apell, S.P., Chen, H., Wang, J., *Nano Lett.*, 2010, **10**, 77-84.
125. A. M. Kelley, *Nano Lett.*, 2007, **7**, 3235-3240.
126. D. Gulen, *J. Phys. Chem. C*, 2010, **114**, 13825-13831.
127. S. M. Morton, Jensen, L., *J. Chem. Phys.*, 2011, **135**, 134103-134112.
128. P. L. Stiles, Dieringer, J.A., Shah, N.C., Van Duyne, R.P., *Annu. Rev. Anal. Chem.*, 2008, **1**, 601-626.
129. G. L. Liu, Long, Y.T., Choi, Y., Kang, T., Lee, L.P., *Nat. Methods*, 2007, **4**, 1015-1017.
130. J. R. Lakowicz, Ray, K., Chowdhury, M., Szmecinski, H., Fu, Y., Zhang, J., Nowaczyk, K., *Analyst*, 2008, **133**, 1308-1346.
131. B. Dubertret, Calame, M., Libchaber, A.J., *Nat. Biotechnol.*, 2001, **19**, 365-370.
132. D. Cunningham, Littleford, R. E., Smith, W. E., Lundahl, P. J., Khan, I., McComb, D. W., Graham, D., Laforest, N., *Faraday Discuss.*, 2006, **132**, 135-145.
133. G. McNay, Eustace, D., Smith, W.E., Faulds, K., Graham, D., *Appl. Spectrosc.*, 2011, **65**, 825-837.
134. K. A. Willets, Stranahan, S.M., Weber, M.L., *J. Phys. Chem. Lett.*, 2012, **3**, 1286-1294.
135. I. A. Larmour, Argueta, E.A., Faulds, K., Graham, D., *J. Phys. Chem. C*, 2012, **116**, 2677-2682.
136. B. K. Juluri, Lu, M., Zheng, Y.B., Huang, T.J., Jensen, L., *J. Phys. Chem. C*, 2009, **113**, 18499-18503.
137. A. Yoshida, Uchida, N., Kometani, N., *Langmuir*, 2009, **25**, 11802-11807.
138. S. Pal, Depero, L.E., Alessandri, I., *Nanotechnol.*, 2010, **21**, 425701-425708.
139. H. Cai, Zhu, J., Chen, G., Liu, L., He, G.S., Zhang, X., *J. Raman Spectrosc.*, 2010, **42**, 1722-1727.
140. A. M. Gabudean, Focsan, M., Astilean, S., *J. Phys. Chem. C*, 2012, **116**, 12240-12249.
141. B. Nikoobakht and M. A. El-Sayed, *Chem. Mater.*, 2003, **15**, 1957-1962.
142. B. P. Khanal, Zubarev, E.R., *Angew. Chem. Int. Ed.*, 2007, **46**, 2195-2198.
143. A. M. Alkilany, Frey, R.L., Ferry, J.L., Murphy, C.J., *Langmuir*, 2008, **24**, 10235-10239.
144. A. P. Leonov, Zheng, J., Clogston, J.D., Stern, S.T., Patri, A.K., Wei, A., *ACS Nano*, 2008, **2**, 2481-2488.
145. C. J. Orendorff, Murphy, C.J., *J. Phys. Chem. B*, 2006, **110**, 3990-3994.
146. Y. B. Zheng, Juluri, B.K., Jensen, L.L., Ahmed, D., Lu, M., Jensen, L., Huang, T.J., *Adv. Mater.*, 2010, **22**, 3603-3607.
147. R. A. Jensen, Sherin, J., Emory, S. R., *Appl. Spectrosc.*, 2007, **61**, 832-838.
148. J. Zhao, Dieringer, J.A., Zhang, X., Schatz, G.C., Van Duyne, R.P., *J. Phys. Chem. C*, 2008, **112**, 19302-19310.
149. R. A. Alvarez-Puebla, *J. Phys. Chem. Lett.*, 2012, **3**, 857-866.
150. R. L. McCreery, *Photometric Standards for Raman Spectroscopy. In Handbook of Vibrational Spectroscopy*, John Wiley & Sons, Ltd, 2006.
151. J. R. Lombardi, Birke, R.L., *Acc. Chem. Res.*, 2009, **42**, 734-742.
152. D. Graham, Faulds, K., *Chem. Soc. Rev.*, 2008, **37**, 1042-1051.
153. K. K. Caswell, Wilson, J. N., Bunz, U. H. F., Murphy, C. J., *J. Am. Chem. Soc.*, 2003, **125**, 13914-13915.
154. B. Pan, Ao, L., Gao, F., Tian, H., He, R., Cui, D., *Nanotechnol.*, 2005, **16**, 1776-1780.
155. L. Zhong, Zhou, X., Bao, S., Shi, Y., Wang, Y., Hong, S., Huang, Y., Wang, X., and Z. Xie, Zhang, Q., *J. Mater. Chem.*, 2011, **21**, 14448-14455.
156. B. Nikoobakht, El-Sayed, M. A., *Langmuir*, 2001, **17**, 6368-6374.
157. B. Pan, Cui, D., Ozkan, C. Xu, P., Huang, T., Li, Q., Chen, H., Liu, F., Gao, F., He, R., *J. Phys. Chem. C*, 2007, **111**, 12572-12576.

158. L. Wang, Zhu, Y., Xu, L., Chen, W., Kuang, H., Li, L., Agarwal, A., Xu, C., Kotov, N.A., *Angew. Chem. Int. Ed.*, 2010, **49**, 5472-5475.
159. T. S. Sreeprasad, Samal, A. K., Pradeep, T., *Langmuir*, 2008, **24**, 4589-4599.
160. A. R. Ferhan, Guo, L., Kim, D. H., *Langmuir*, 2010, **26**, 12433-12442.
161. X. Hu, Wenlong, C., Wang, T., Wang, Y., Wang, E., Dong, S., *J. Phys. Chem. B*, 2005, **109**, 19385-19389.
162. C. Wang, Chen, Y., Wang, T., Ma, Z., Su, S., *Chem. Mater.*, 2007, **19**, 5809-5811.
163. K. Faulds, McKenzie, F., Smith, W.E., Graham, D., *Angew. Chem., Int. Ed.*, 2007, **46**, 1829-1831.
164. H. Yuan, Liu, Y., Fales, A.M., Li, Y.L., Liu, J., Vo-Dinh, T., *Anal. Chem.*, 2013, **85**, 208-212.
165. E. C. Le Ru, Meyer, M., Etchegoin, P.G., *J. Phys. Chem. B*, 2006, **110**, 1944-1948.
166. A. M. Alkilany, Murphy, C.J., *J. Nanopart. Res*, 2010, **12**, 2313-2333.
167. K. L. Cheung, Chen, H., Chen, Q., Wang, J., Ho, H.P., Wong, C.K.W., Kong, S.K., *Nanoscale*, 2012, **4**, 4447-4449.
168. L. Xu, Liu, Y., Chen, Z., Li, W., Liu, Y., Wang, L., Liu, Y., Wu, X., Ji, Y., Zhao, Y., Ma, L., Shao, Y., Chen, C., *Nano Lett.*, 2012, **12**, 2008-2012.
169. L. Wang, Liu, Y., Li, W., Jiang, X., Ji, Y., Wu, X., Xu, L., Qiu, Y., Zhao, K., Wei, T., Li, Y., Zhao, Y., Chen, C., *Nano Lett.*, 2011, **11**, 772-780.
170. A. P. Alivisatos, Johnsson, K. P., Peng, X., Wilson, T. E., Loweth, C. J., Bruchez, M. P., Schultz, P.G., *Nature*, 1996, **382**, 609-611.
171. A. Wijaya, Schaffer, S.B., Pallares, I.G., Hamad-Schifferli, K., *ACS Nano*, 2008, **3**, 80-86.
172. B. R. Martin, Dermondy, D.J., Reiss, B.D., Fang, M., Lyon, L.A., Natan, M.J., Mallouk, T.E., *Adv. Mater.*, 1999, **11**, 1021-1025.
173. E. C. Dreaden, Mwakwari, S.C., Sodji, Q.H., Oyelere, A.K., El-Sayed, M.A., *Bioconjugate Chem.*, 2009, **20**, 2247-2253.
174. M. Zheng, Davidson, F., Huang, X., *J. Am. Chem. Soc.*, 2003, **125**, 7790-7791.
175. T. Niidome, Yamagata, M., Okamoto, Y., Akiyama, Y., Takahashi, H., Kawano, T., Katayama, Y., Niidome, Y., *J. Control. Release*, 2006, **114**, 343-347.
176. H. Liao, Hafner, J.H., *Chem. Mater.*, 2005, **17**, 4636-4641.
177. E. B. Dickerson, Dreaden, E.C., Huang, X., El-Sayed, I.H., Chu, H., Pushpanketh, S., McDonald, J.F., El-Sayed, M.A., *Cancer Lett.*, 2008, **269**, 57-66.
178. L. M. Liz-Marzan, Giersig, M., Mulvaney, P., *Langmuir*, 1996, **12**, 4329-4335.
179. S. O. Mulvaney, Musick, M.D., Keating, C.D., Natan, M.J., *Langmuir*, 2003, **19**, 4784-4790.
180. W. E. Doering, Nie, S.M., *Anal. Chem.*, 2003, **75**, 6171-6176.
181. A. Guerrero-Martinez, Perez-Juste, J., Liz-Marzan, L., *Adv. Mater.*, 2009, **22**, 1-14.
182. M. J. Banholzer, Harris, N., Millstone, J.E., Schatz, G.C., Mirkin, C.A., *J. Phys. Chem. C*, 2010, **114**, 7521-7526.
183. A. Gole, Murphy, C. J., *Langmuir*, 2005, **21**, 10756-10762.
184. B. S. Kim, Smith, R.C., Poon, Z., Hammond, P.T., *Langmuir*, 2009, **25**, 14086-14092.
185. H. C. Huang, Barua, S., Kay, D.B., Rege, K., *ACS Nano*, 2009, **3**, 2941-2952.
186. S. Guo, Huang, Y., Jiang, Q., Sun, Y., Deng, L., Liang, Z., Du, Q., Xing, J., Zhao, Y., Wang, P.C., Dong, A., Liang, X.J., *ACS Nano*, 2010, **4**, 5505-5511.
187. S. K. Lee, Han, M.S., Asokan, S., Tung, C.H., *Small*, 2011, **7**, 364-370.
188. K. V. Chakravarthy, Bonoiu, A.C., Davis, W.G., Ranjan, P., Ding, H., Hu, R., Bowzard, J.B., Bergey, E.L., Katz, J.M., Knight, P.R., Sambhara, S., Prasad, P.N., *Proc. Natl. Acad. Sci. U.S.A.*, 2010, **107**, 10172-10177.

189. A. C. Bonoiu, Mahajan, S.D., Ding, H., Roy, I., Tong, K.T., Kumar, R., Hu, R., Bergey, E.J., Schwartz, S.A., Prasad, P.N., *Proc. Natl. Acad. Sci. U.S.A.*, 2009, **106**, 5546-5550.
190. P. S. Ghosh, Kim, C.K., Han, G., Forbes, N.S., Rotello, V.M., *ACS Nano*, 2008, **2**, 2213-2218.
191. A. Kumar, Pattarkine, M., Bhadhade, M., Mandale, A.B., Ganesh, K.N., Datar, S.S., Dharmadhikari, C.V., Sastry, M., *Adv. Mater.*, 2001, **13**, 341-344.
192. C. M. McIntosh, Esposito, E.A., Boal, A.K., Simard, J.M., Martin, C.T., Rotello, V.M., *J. Am. Chem. Soc.*, 2001, **123**, 7626-7629.
193. G. Han, Chari, N.S., Verma, A., Hong, R. Martin, C.T., Rotello, V.M., *Bioconjugate Chem.*, 2005, **16**, 1356-1359.
194. M. Thomas, Klibanov, A.M., *Proc. Natl. Acad. Sci. U.S.A.*, 2003, **100**, 9138-9143.
195. M. T. Fernandez-Arguelles, Yakovlev, A., Sperling, R.A., Luccardini, C., Gaillard, S., Medel, A.S., Mallet, J.M., Brochon, J.C., Feltz, A., Oheim, M., Parak, W.J., *Nano Lett.*, 2007, **7**, 2613-2617.
196. W. W. Yu, Chang, E., Falkner, J.C., Zhang, J., Al-Somali, A.M., Sayes, C.M., Johns, J., Drezek, R., Colvin, V.L., *J. Am. Chem. Soc.*, 2007, **129**, 2871-2879.
197. x. Wu, Liu, H., Liu, J., Haley, K.N., Treadway, J.A., Larson, J.P. Ge, N., Peale, F., Bruchez, M.P., *Nat. Biotechnol.*, 2003, **21**, 41-46.
198. J. Dai, Baker, G.L., Bruening, M.L., *Anal. Chem.*, 2006, **78**, 135-140.
199. Y. Chen, Nguyen, A., Niu, L., Corn, R.M., *Langmuir*, 2009, **25**, 5054-5060.
200. T. H. Seefeld, Zhou, W.J., Corn, R.M., *Langmuir*, 2011, **27**, 6534-6540.
201. W. J. Zhou, Chen, Y., Corn, R.M., *Anal. Chem.*, 2011, **83**, 3897-3902.
202. G. T. Hermanson, *Bioconjugate Techniques (Second Edition)*, Elsevier, Amsterdam, 2008.
203. M. Kunishima, C. Kawachi, J. Monta, K. Terao, F. Iwasaki and S. Tani, *Tetrahedron*, 1999, **55**, 13159-13170.
204. M. Kunishima, Kawachi, C., Hioki, K., Terao, K., Tani, S., *Tetrahedron*, 2001, **57**, 1551-1558.
205. J. M. Pelet, Putnam, D., *Bioconjugate Chem.*, 2011, **22**, 329-337.
206. K. Thompson, Michielsen, S., *J. Polym. Sci., Part A: Polym. Chem.*, 2006, **44**, 126-136.
207. C. Bianchi, Porta, F., Prati, L., Rossi, M., *Top. Catal.*, 2000, **13**, 231-236.
208. I. Hussain, Brust, M., Papworth, A.J., Cooper, A.I., *Langmuir*, 2003, **19**, 4831-4835.
209. I. Hussain, Graham, S., Wang, Z., Tan, B., Sherrington, D.C., Rannard, S.P., Cooper, A.I., Brust, M., *J. Am. Chem. Soc.*, 2005, **127**, 16398-16399.
210. W. Tong, Cao, X., Wen, S., Guo, R., Shen, M., Wang, J., Shi, X., *Int. J. Nanomed.*, 2012, **7**, 1069-1078.
211. H. Chen, Wang, Y., Wang, Y., Dong, S., Wang, E., *Polymer*, 2006, **47**, 763-766.
212. F. McKenzie, Steven, V., Ingram, A., Graham, D., *Chem. Commun.*, 2009, 2872-2874.